# MODELING OF MAGNETIZATION DYNAMICS AND APPLICATIONS TO SPIN-BASED LOGIC AND MEMORY DEVICES

A Dissertation
Presented to
The Academic Faculty

By

Nickvash Kani

In Partial Fulfillment
of the Requirements for the Degree
Doctor of Philosophy in the
School of Electrical and Computer Engineering

Georgia Institute of Technology

December 2017

**MODELING OF MAGNETIZATION DYNAMICS AND APPLICATIONS TO SPIN-BASED LOGIC AND MEMORY DEVICES**

Approved by:


Prof. Azad J. Naeemi, Advisor
School of Electrical and Computer Engineering
*Georgia Institute of Technology*

Prof. Thomas K. Gaylord, Chair
School of Electrical and Computer Engineering
*Georgia Institute of Technology*

Prof. Jeffrey A. Davis
School of Electrical and Computer Engineering
*Georgia Institute of Technology*

Prof. Sudhakar Yalamanchili
School of Electrical and Computer Engineering
*Georgia Institute of Technology*

Prof. Laurence J. Jacobs
School of Civil and Environmental Engineering
*Georgia Institute of Technology*



Date Approved: November 10, 2017

There is always Hope.

*-Saint Walker*

For my family and friends, who give me strength

## ACKNOWLEDGEMENTS

This work would not have been possible without the support of many amazing people. On the professional front, I would like to start by thanking my research advisor, Prof. Azad Naeemi. His patience and guidance during my tenure at Georgia Tech allowed me to broaden my academic interests and develop a unique perspective on spintronic research. The freedom I was afforded has forever changed the course of my studies for the better.

I would also like to thank my reading and defense committee: Prof. Thomas Gaylord, Prof. Jeffrey Davis, Prof. Sudhakar Yalamanchili, and Prof. Laurence Jacobs. I cannot praise these individuals enough for their devotion to the students of Georgia Tech. I would also thank Prof. Jacobs for our weekend meetings and his motivating words. The empathy he offered during the lowest points of my studies allowed me to let go of the bitterness that had built up over the many years. That kindness is something I'll never forget.

I owe the Semiconductor Research Corporation (SRC) much gratitude for providing the financial backing for my research and connecting us to industry experts. I am grateful to the many researchers that offered insight and advice over the course of my research: Dr. Dmitri Nikonov, Dr. Giorgio Bertotti, Prof. Massimiliano d'Aquino, and Prof. Andrew Kent. I would also like to thank Dr. Daniele Pinna. Not only did his research improve my understanding of magnetic systems, but his encouragement to adopt high-performance computing methods greatly accelerated my research allowing me observations that would have been beyond reach using conventional computing methods.

On a more personal level there are many friends I need to thank. My success is the result of support from many individuals leading up to and throughout my academic studies. I'd like to thank Prof. Mohie-Eldin Mohie-Eldin for being a friend to me and my brother for more than a decade. Special thanks to the folks at Hankook Taqueria for all their kind words and delicious food. Prof. Unnikrishna Pillai has and continues to support my academic interests. I would like to thank my friends for listening to my many rants and

helping me keep my sanity during my academic career. Dr. Vachan Kumar and Dr. Ahmet Ceyhan were both my group-mates and good friends. Divya Prasad was a constant source of emotional support. Though he joined the group late in my graduate studies, Victor Huang quickly became an amazing friend and constantly went out of his way to help me any way he could.

I have been blessed to have known Prof. Shaloo Rakheja my entire graduate career. As a graduate student, she was the heart and soul of our group frequently planning events and offering advice. Her subsequent graduation and departure from Atlanta left a void no one will ever be able to fill. Luckily, the two of us managed to stay close for all these years and I count her as my very best friend. Her efforts during my graduate studies, both personally and professionally, are too numerous to count. I have never met anyone more dedicated to her work or more willing to help you succeed. I can't express enough how grateful I am for all the help and support she has given me.

Finally, I would like to thank my amazing family who has shown me nothing but love and support throughout my life. My father, Hossein Kani, continues to work 80 hours a week to ensure we have a home I can always return to. My mother, Mahnaz Kani, has been a constant source of emotional support always managing to put me back together at my lowest moments. My brother, Arash Kani, is the smartest man I know and has always pushed me to be better. He always provided me with a blunt honesty that motivated me to work harder and achieve greater successes while also stepping in to help me when he could. Despite this not being his area of expertise, my brother has read this manuscript cover to cover providing me with invaluable feedback. Lastly, Hope was my pet for most of my life and unfortunately passed away shortly before the completion of my PhD degree. To the world he was just a bird, but he was also my only friend for most of my childhood and I miss him everyday. The hardest part of my academic career and life is attempting to become the man that my family and friends deserve to have in their lives.

## TABLE OF CONTENTS

## LIST OF TABLES

## LIST OF FIGURES

**Summary**

The objective of this research is to develop models to better evaluate the performance and reliability of proposed spin-based Boolean devices. This research will focus on a particular spin-based logic technology called Spin-Switch Logic. There are two primary reversal mechanisms that will be considered for a full evaluation of Spin-Switch technology. Firstly, nanomagnet reversal through the use of spin-transfer torque (STT) is studied. While switching through STT has been analytically solved for the uniaxial nanomagnet case, the biaxial case has yet to be studied on a sufficient scale and is a focus of this research.

Secondly, input-output isolation is achieved through dipolar coupling; hence, the performance and reliability of this type of reversal mechanism is extensively studied. It is shown that dipolar coupling strength is not only a function of geometric and material parameters, but also of reversal speed. If the reversal of a neighboring nanomagnet is very fast, the dipolar field reduces to a constant longitudinal field and can be analytically studied. However, if the reversal of the neighboring nanomagnet is slow, new models are formulated to estimate the region of reliable coupling and delay.

Lastly, a focal point of this research is on the reliability of nanomagnet states in the presence of thermal noise and new models are proposed to estimate the reliability of complex spin-based systems. Not only does the thermal noise affect the probability of magnetization state consistency, it also alters nanomagnet precession during reversal, making the delay a random variable. Hence, models are developed for evaluating the variation in reversal delay through STT for both uniaxial and biaxial cases.

Ultimately, these analytic models are combined to comprehensively evaluate the performance of Spin-Switch technology and identify possible improvements to this technology. While the end result of this research is a thorough analysis of Spin-Switch Logic, the models developed during this research are applicable to a variety of spin-based logic and memory technologies.

# CHAPTER 1
# INTRODUCTION

The study of the interaction between electric currents and the magnetic order in conducting magnetic nanostructures has developed into its own sub-field. In the last several years, novel processing and storage devices using electron spin as the information token have been proposed to augment or eventually replace their charge-based counterparts. Dubbed "spintronics," spin-based devices utilize the spin of electrons and their interactions with magnetic moments to manipulate and share information [1]. While many spin-based devices have been proposed in the past few decades, the physics governing the dynamics of spin-based systems are complex and still not well understood [2, 3]. This thesis is dedicated to the analysis of magnetization dynamics in complex systems through the evaluation of spin-based technologies. Proposed spin-based devices offer a framework for studying the interaction between magnetic moments and/or polarized currents. The models and analyses developed will then be combined and culminate in the complete evaluation of a particular spin-based technology called "Spin-Switch Logic" [4]. While the vehicle of this research is the Spin-Switch Logic evaluation, the models developed are applicable to a range of magnetic systems and research with similar physical foundations.

## 1.1 Magnetic Effects and Literature Survey

Spin-Switch logic is a natural evolution of the spin-based devices that have been proposed prior to its inception. To gain a richer understanding of the device operation and the spin-based effects being discussed in this research, we will first briefly go through the magnetic effects governing the device operation. We will then discuss how these effects are combined to form the core Spin-Switch device.

An example of the overall spin-switch design can be seen in Figure 1.1. This is a

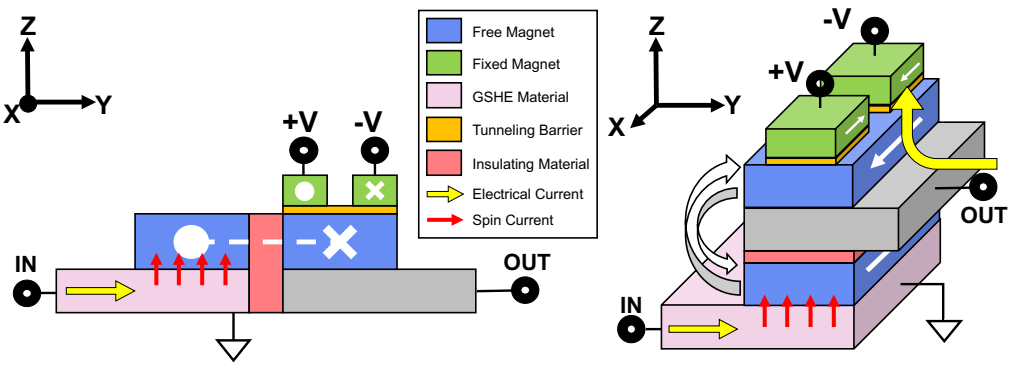


**(a) Lateral Representation**

**(b) Vertical Representation**

Figure 1.1: Visual representation of the Spin-Switch device. (a) the original lateral representation of the device is shown [4]. This layout was considered when the Spin-switch was originally proposed but has since become defunct because the large spacing between the magnetic bodies means a very weak dipolar field. (b) The vertical representation is superior since the spacing between magnetic bodies is reduced by $10\times$. However, the lateral representation is still used when visually prudent.

complex device which incorporates several magnetic effects to perform boolean operation. Four major magnetic effects are utilized during the operation of this device:

- Giant/Tunnel magnetoresistance
- Dipolar coupling
- Spin-transfer torque
- Giant spin-hall effect

In this Section with will provide a qualitative description of these magnetic effects before describing full device operation in Section 1.2. We will also discuss other spin-based devices which utilize these magnetic effects for correct operation.

### 1.1.1 Giant Magnetoresistance Effect

The birth of spintronics can be traced back to the experimental demonstration of the giant-magnetoresistance (GMR) [5]. This effect was discovered independently by Albert Fert's

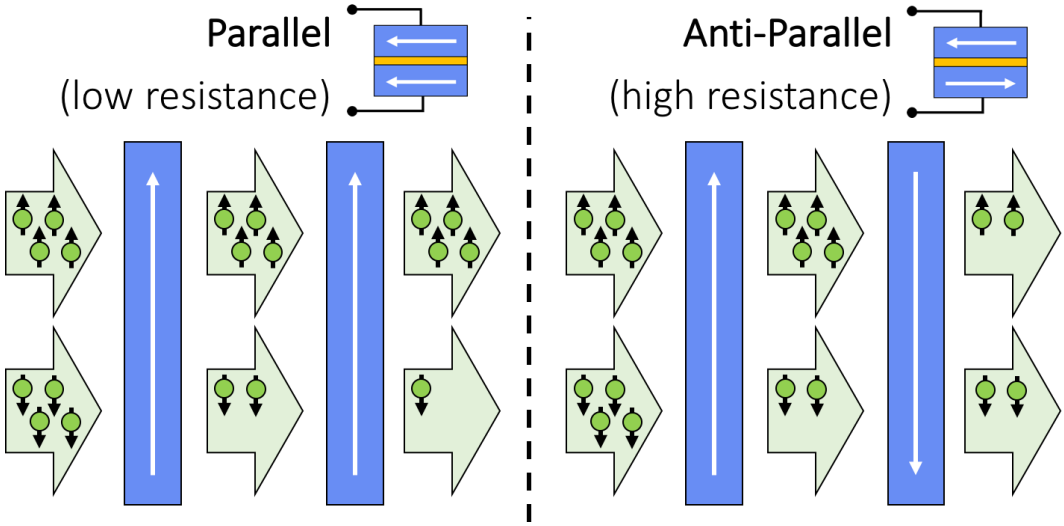


Figure 1.2: Visual representation of giant magnetoresistance effect. The green arrows represent the electrical current flowing through the magnetic layers (represented by the blue rectangles). The GMR effect can be conceptually thought of as a system where nanomagnets filter electrons with opposing spin polarities.

group form Universte Paris-Sud and Peter Grunberg from Festkprperforschung Julich [6, 7]. This phenomenon simply states that for a systems where two-magnetic layers are separated by a non-magnetic metal, the resistance is a function of the orientation of magnetic layers relative to one-another [8]. Resistance is minimized when the nanomagnets are oriented in the same direction and maximized when they are anti-parallel.

This effect can be explained conceptually by assuming that the nanomagnet behaves as a filter [10, 11] as shown in Figure 1.2. When a charge current with an equal mix of electrons at the spin-up and down states passes through a nanomagnet, some of the electrons oriented in the direction of the magnetization will get filtered out. If both nanomagnets are oriented along the same direction, only the electrons with the opposite spin direction will feel this filtration. However, if the nanomagnets have opposing magnetizations, a higher resistance path is created through the partial filtering of both orientations.

Functionally analogous to the GMR effect, the tunnel magnetoresistance (TMR) effect occurs when a thin insulating tunneling barrier is added in between the magnetic layers. Despite their similar functionality, the two effects have largely different physical ori-

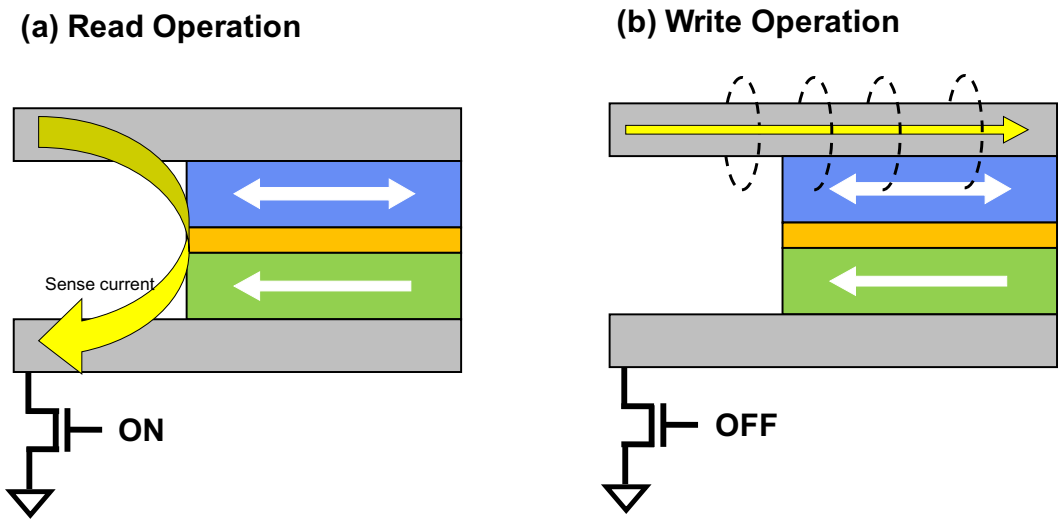


Figure 1.3: Core principle behind the MTJ memory unit. Early units used an Oersted field to write to the free magnet [9]. This Oersted field is generated by sending an electrical current through the bit-line. The state of the MTJ structure is found by turning on the CMOS device pulling one en of the MTJ to ground and sending a sense current through the structure. The magnitude of this current determines if the MTJ structure is in the parallel or anti-parallel state.

gins[12]. In the TMR effect, the change in resistance is a result of spin-dependent tunneling through the tunneling barrier [13, 14]. This magnet-insulator-magnet stack is referred to as a magnetic-tunnel-junction (MTJ) and is an essential component to many of the spin devices [15, 16, 17]. The exact physical model behind the MTJ is beyond the scope of this research. Instead, where necessary, the resistance of the MTJ stack is formulated as:

$$P \equiv \frac{\Delta G}{G} \equiv \frac{TMR}{TMR + 2} \tag{1.1}$$

where $P$ is the polarization of the charge current and $G$ is the conductance of the MTJ stack. $TMR$ is the tunneling magnetoresistance parameter and represents the change in resistance in the MTJ between its parallel and anti-parallel states [18, 17]. This equation denotes the change in conductance and hence, $G + \Delta G$ and $G - \Delta G$ represent the parallel and anti-parallel conductances respectively.

In engineering literature, MTJ's have been mainly proposed as memory devices as seen in Figure 1.3 [19]. Through various methods including the use of pinning layers, it is

possible to fabricate a nanomagnet with a fixed magnetization [20]. The other magnet can be reversed through the use of Oersted fields or spin-transfer torque (STT) [21, 22, 23]. Thus, binary information can be encoded in the MTJ structure as parallel and anti-parallel magnetic states. The state of te MTJ structure is read by sending a sense current through the unit similar to how SRAM units are read [24, 25]. Many researchers have argued that the the benefit of these devices is their inherent non-volatility [26]. However, this non-volatility benefit has not been quantified and it is unclear if it will make up for the larger energy required to read/write to an MRAM cell compared to a classical DRAM or SRAM unit [27].

In the Spin-Switch device, the MTJ effect will be used to determine the polarity of the output electrical current using a special push-pull MTJ structure which is elaborated further in Section 1.2. The GMR effect is largely dependent on material structures and parameters and as such, is difficult to analyze theoretically. Generally speaking, when modeling spin-based devices, the $G$ and $TMR$ parameters are fit to experimental results. For our analysis of the complete Spin-Switch device in Chapter 10, we also use these experimentally simplified models to fully capture MTJ dynamics.

### 1.1.2 Dipolar Coupling

While in the presence of an external field, the magnetization of a magnetic body has a preference to align parallel to the external field direction. Knowing that a magnetic field emits a stray field, it is theoretically possible to control the orientation of neighboring magnetic bodies depending on their relative orientation to the driving magnet and its magnetization as shown in Figure 1.4. It was theorized that many small nanomagnets could be arranged in an array and communicate information along a distance by driving a row magnetic bodies through their respective stray fields [28, 29]. This was the founding principle behind one of the oldest magnetic logic devices dubbed "Nanomagnetic Logic" (NML) [30].

An example NML circuit is shown in Figure 1.5. The bit information is encoded in the

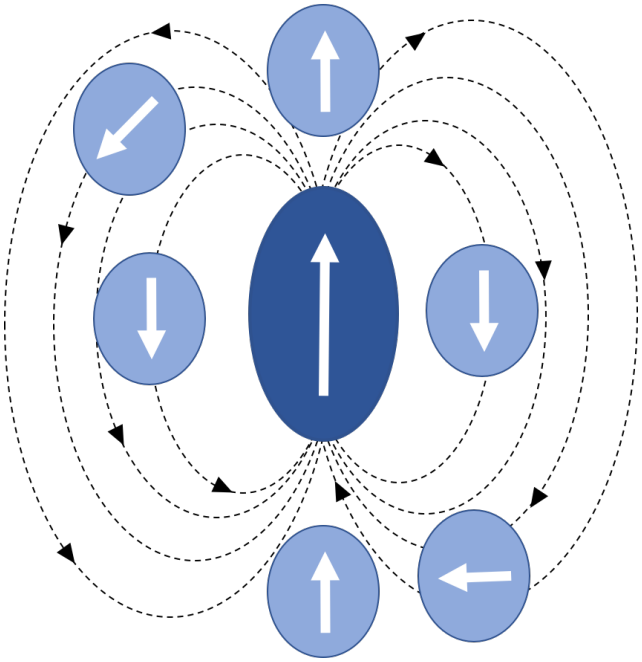

Figure 1.4: Visual representation of coupling between nanomagnetic bodies. The center magnet emits a stray field which overpowers smaller magnets causing their magnetizations to align to the stray field emitted. Dipolar coupling between magnetic bodies is significantly more complex than shown above and will discussed at length in Chapters 5–9.

magnetization state and is communicated through the nanomagnet array [33]. As shown in Figure 1.4, geometry determines if the nanomagnets are coupled in a parallel or anti-parallel manner meaning that the layout magnetic arrays must be precisely controlled to preserve the information being communicated. Logic is performed by bringing the nano-magnet arrays together so that multiple inputs are communicated through their stray fields to a single "key"-magnet. The stray fields from these inputs are summed and the key-magnet aligns with the the majority direction and communicates the result along the output logic array. Hence, the combination of these stray fields forms a majority gate structure.

Figure 1.5 also shows the problem with NML. The previous output of the circuit has as much an influence on the key-magnet as the input arrays. This means that the output may not necessarily reverse with the inputs. There are ways to fix this propagation issue trough the use of novel, non-symmetric nanomagnet shapes, but such schemes results in enormous modeling complexity and are not fully reliable [34, 31]. One can also use magnetostrictive

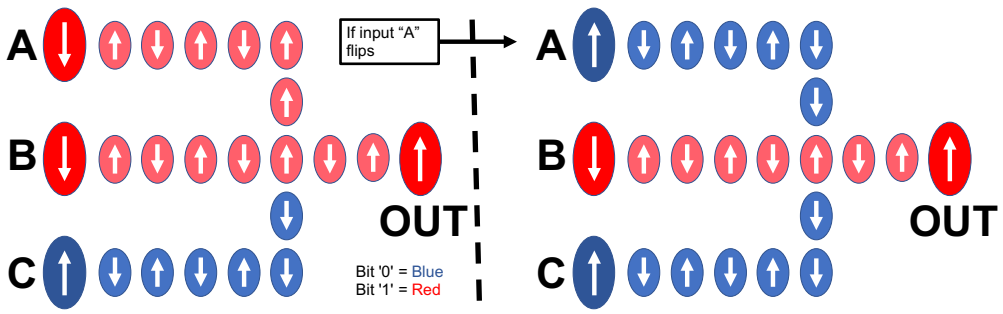


Figure 1.5: Sample circuit of Nanomagnetic-Logic majority-gate [31, 32]. Large magnets are inputs/outputs to the circuit. Red/Blue colors represent nanomagnets carrying bit-wise "0" and "1" respectively. *Left:* shows ideal operation of the circuit. *Right:* demonstrates fundamental problem with this technology which is the progation issue. If one of the inputs change in a manor as shown above, to ensure majority gate operation, the output should change. However, because the output array has an equal influence on the center magnet as the inputs, the output remains the same.

materials to knock the output magnets in a high-energy state before Boolean operation making them easier to reverse [35]. However, the timing complexity and fabrication of such schemes pose a significant challenge [36, 37].

Compared to other reversal effects employed by spin-based logic, the stray-field emitted by a nanomagnetic body is relatively weak. Reversal through magnetic stray field requires the magnetic system can small internal anisotropy fields which can result in magnetization instability [38]. Stray-field interaction is closely linked with magnetization dynamics and as such, will discussed at length in Chapters 5–9.

### 1.1.3 Spin-Transfer-Torque

The GMR effect states that the magnetization of a ferromagnet can polarize an electrical current. Due to the conservation of angular momentum, the reverse is possible as well; as shown in Figure 1.6, a polarized accumulation of electrons may impart a net-angular momentum upon the magnetization of a nanomagnet. This effect is known as spin-transfer-torque (STT) [39].

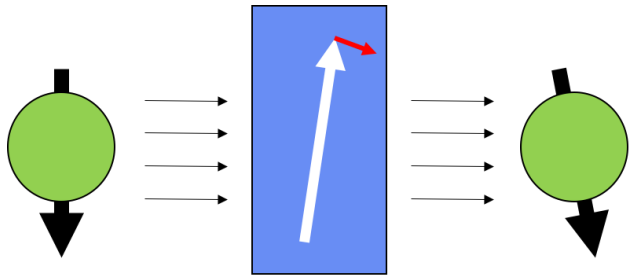

Figure 1.6: Illustration of STT. A polarized electron imparts an angular toque on a magnetic body as it passes through. Assuming a polarized current is large enough, the magnetization of the magnetic body may be reversed.

The magnitude of the STT effect, $\Gamma_s$, is given as [40, 41]:

$$\Gamma_s = -\frac{\gamma\hbar\eta g(\theta)I}{2e}\hat{m}\times(\hat{m}\times\hat{p})\,, \tag{1.2}$$

where $\gamma$ is the gyromagnetic ratio, $\hbar$ is the reduced Planck constant, $\eta$ is the spin polarization, and $I$ is the amplitude of the spin current. for the purposes of this research, the angular dependence of spin torque strength ($g(\theta)$) will always be equal to 1. $\hat{m}$ is the magnetization direction of the nanomagnet while $\hat{p}$ is the polarization of the spin current.

The mathematical treatment of this torque and its interaction with the magnetic body will be espoused on in Chapter 2. The microscopic origin of the STT can be explained as follows. Electrons enter the magnetic body with spins aligned either parallel or anti-parallel to the magnetization. The energy-bands for the electrons with different spin states are different which means that the kinetic energies and wave-vectors of the aligned and not-aligned electrons are different [41, 11, 42, 43, 44]. Therefore the spin-dependent transmission/reflection that depend on potential steps at the interface are different for different spin polarizations. The STT effect can be derived when solving the Schrödinger equation for electron waves at the interface of a non-magnetic metal layer and ferromagnetic layer which demonstrates that the STT is an interface effect and is maximized in thin-film structures [45, 41].

A spin-polarized current can be generated by passing an electrical current though a

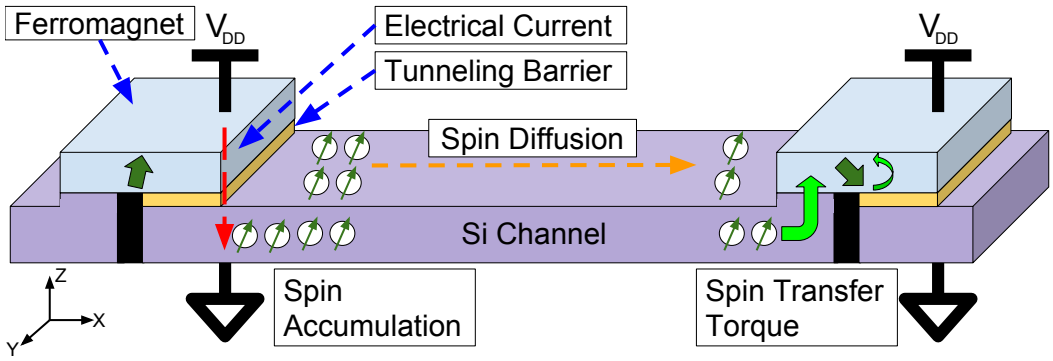


Figure 1.7: Schematic of repeater operation for a ASL circuit. An electrical current is driven through the driving nanomagnet (left) and a net spin current is accumulated below the nanomagnet. This spin current then diffuses through the channel and is then delivered to the receiving nanomagnet. For the purposes of this research, it is assumed that the channel is long/resistive enough so that the leakage current can be omitted. The calculation of the current received by the output magnet through spin diffusion is outline in Appendix B.

metal and the resulting spin accumulation is diffused through the conducting interface [46]. While not a focus of this research, this process is elaborated more in Appendix B. This polarization of electrical current and diffusion of spin current has resulted in the ability for one to use electrical current to reverse magnetic bodies [47, 48, 49]. As such, many spin-base devices can be augmented through the use of STT including proposed MTJ memories [50].

The advent of information being communicated to magnetic states through polarized currents has lead to a technology referred to as All-Spin Logic (ASL) [51]. ASL technology operates by injecting an electrical current through a free magnet and metallic channel. Doing this polarizes the electrical current yielding a net spin accumulation in the metallic channel. This spin accumulation diffuses through the metallic channel imposing a net STT on the output magnet as seen in Figure 1.7 [52, 53]. Because this is a current driven device, logic is achieved by summing the inputs delivering the STT to the output free-magnet. Majority Boolean logic gates, such as AND/OR, are implemented by connecting multiple input nanomagnets to a receiving nanomagnet, where a sum of the input spin currents determines the functionality of the logic gate [54, 55].

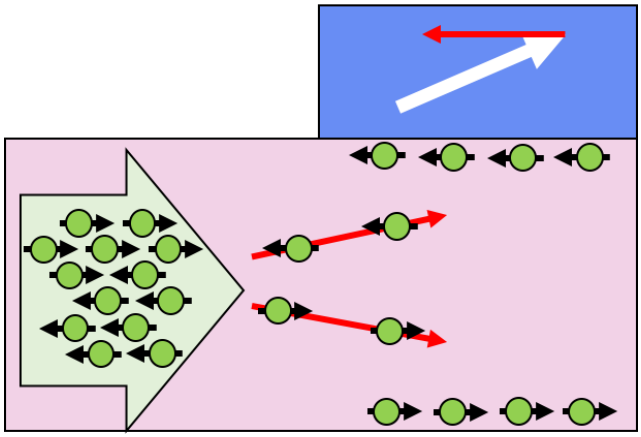

Figure 1.8: Visual representation of giant spin-hall effect. Due to interaction with certain materials, electrons with different spins separate yielding a net spin current perpendicular to the flow of the electrical current.

### 1.1.4 Giant Spin-Hall Effect

ASL logic devices use the MTJ effect to create a spin current by passing a charge current through a ferromagnetic structure, filtering anti-parallel electrons, and thus causing a net accumulation of electrons with a particular polarization. Information is communicated by accumulating the polarized electrons at one end of a interconnect and diffusing this spin current through a metallic interconnect at which point it will hopefully be strong enough to reverse the output magnetic body. While this allows us to communicate between devices, it is also very inefficient. The spin diffusion process requires a large amount of energy since the strength of the spin current exponentially decays as the interconnect length is increased as discussed in Appendix B.

Thankfully, there is another way to generate a spin current through the use of the spin-hall effect [56]. In the Hall effect, one can apply an electrical current through a metal in the presence of a magnetic field and the Lorentz force yields charge accumulation on the boundaries of the metal [57]. Edwin Hall later discovered that the transverse voltage developed is different for magnetic and non-magnetic conductors [58]. This is because the transverse velocity acquired depends on the electrons spin orientation and this effect became known as the anomalous-hall-effect [59, 60]. Later, it was shown that the spin-

orbit-coupling in the band structure of a material can produce a similar effect and became known as the intrinsic spin-hall-effect [61]. A visual representation of the spin hall effect is shown in Figure 1.8. The interaction of electron spins with the materials band structures yields a separation of electrons with different spins and their accumulation on the boundaries of the spin-hall conductor. The Rashba effect is a similar interface-dependent mechanism [62].

In the last decade, several groups have shown experimental proof of the spin-hall effect [63, 64, 65]. Notably, an amplified of version of the spin-hall effect, referred to as the Giant-Spin-Hall-Effect (GSHE), was shown by Luqiao Liu at Cornell University using Tantalum [66]. The exact cause of this effect isn't clear but experimental results show that the GSHE can be modeled as a bulk effect whose magnitude is described by a angle, $\theta_{SH}$, which denotes the magnitude of the spin current over the magnitude of the electrical current per unit length over thickness [67, 68]. A formulation of this effect has been noted as [69]:

$$\frac{J_s}{J_e} = \theta_{SH}\frac{L}{t}\left(1 - sech\left(\frac{t}{\lambda_s}\right)\right), \tag{1.3}$$

where $J_s$ and $J_e$ denote the spin and electrical current-density, respectively. $L$ and $t$ are the length and thickness of the GSHE material, respectively. This effect allows for a large amplification of spin current over charge current. Several recent experimental papers have noted that this amplification is tampered if the GSHE material thickness becomes comparable or smaller to the spin flip length [70, 71]. The last $\left(1 - sech\left(\frac{t}{\lambda_s}\right)\right)$ term is included to account for this negation of the spin-current generation for very thin films [72].

## 1.2 Operation of Spin-Switch Device

In the previous section, we reviewed the different magnetic effects required for the operation of the Spin-Switch device and also reviewed the spin-based logic devices which emerged from the existence of these magnetic effects. Much like how ASL and NML are a

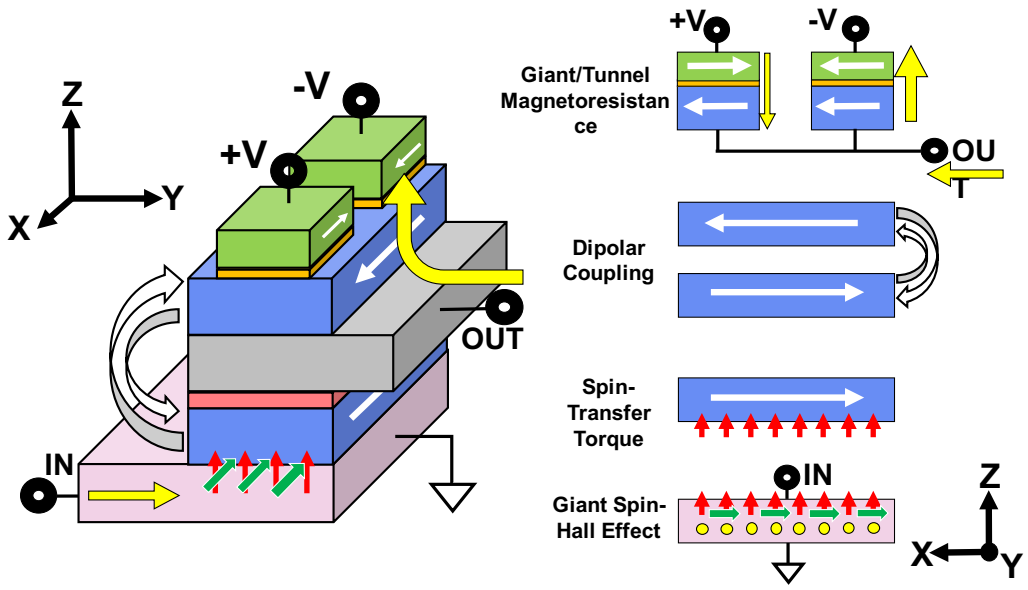


Figure 1.9: Picture of system as well as the overall effects responsible for device operation. The operation of the Spin-Switch can be broken up in four stages. First a electrical current flows through the GSHE material generating a spin current delivered to the bottom nanomagnet. The polarization of this spin current is determined by the direction of the electrical current. This spin current reverses the bottom nanomagnet through STT. The reversal of the bottom nanomagnet causes the reversal of the top magnet through dipolar coupling. Finally, the push-pull dual MTJ stack delivers an output electrical current with polarity dependent on the top nanomagnet.

product of STT and dipolar coupling physical effects, the Spin-Switch is also a result of the summation of STT, dipolar coupling, GMR and GSHE. In this way, it can be argued that the Spin-Switch is simply an evolution of previous devices and more specifically, the Spin-Switch is the next-generative ASL device which communicates through electrical instead of spin current.

The operation of the Spin-Switch is shown in Figure 1.9. First, a net electrical current enters the device through the "IN" contact and flows through the GSHE material. A net spin current is then generated by the GSHE which imposes a spin-transfer torque on the bottom ferromagnet. The direction of the electrical current determines the polarization of the spin current and, by extension, the desired direction of the bottom magnetization. The bottom nanomagnet interacts which the top nanomagnet through complex dipolar interac-

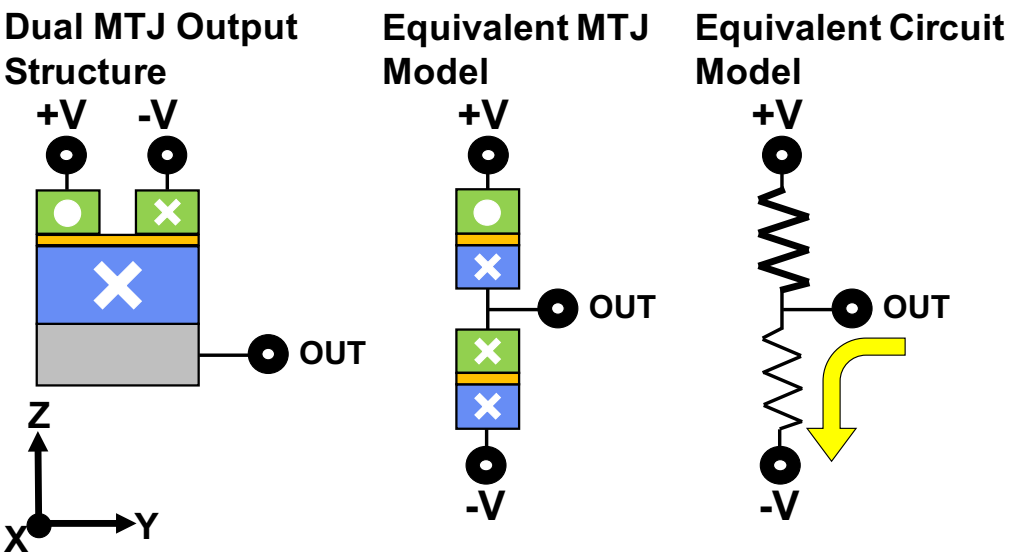


Figure 1.10: Equivalent circuit model of output portion of Spin-Switch structure. The free magnet is shared between the MTJ stacks. This results in one of the supplies having a lower resistance to output than the other. This dual MTJ structure results in a electrical current at the output node whose polarity is controlled by the magnetization of the top nanomagnet.

tions. When the magnetization of the bottom nanomagnet is reversed the magnetization of the top will also change its direction.

The top half of the Spin-Switch architecture is dual push-pull MTJ structure and its equivalent circuit model is shown in Figure 1.10. There are two fixed magnetization ferromagnets with opposing polarities. Each of these fixed magnets forms a MTJ structure with the top ferromagnet. Since the ferromagnet has only one magnetization direction, one of these MTJ stacks will have a lower resistance than the other. By connecting two voltage supplies with opposing polarities to the two MTJ stacks, we ensure the resistance to the output is smaller for one of the power supplies. This means that the direction of current flowing out of the output node is determined by the magnetization direction of the top nanomagnet.

The Spin-Switch can be classified as a current-in/current-out device which communicates information through current direction. Boolean information can be encoded in the direction of the electrical current where -I and +I represent bit “0” and “1” states, respec-

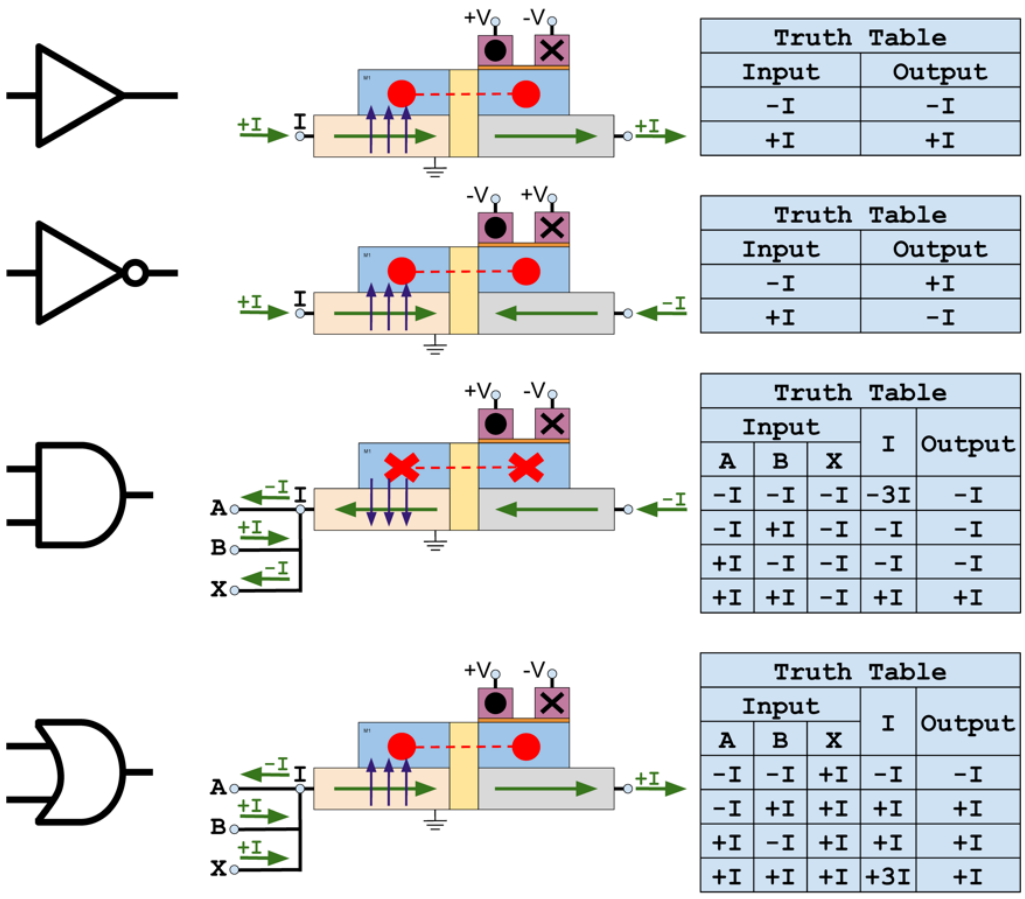


Figure 1.11: Example of Spin-switch performing Boolean operations. We encode bit information as -I and +I which represent bit "0" and "1" states, respectively. Because the Spin-switch is a current-driven device, the summing of the electrical currents at the input node results in majority gate functionality. A majority gate can provide Boolean operations by adding a static input "weight".

tively. Because this is a current based device, multiple device outputs can be connected to a single device input. At this node, the currents will be summed and, assuming a odd number of inputs, the output of the next stage will be determined by the majority current directions of the inputs. Hence, like many other next-generation device technologies, the Spin-Switch may behave as a majority gate. By using an input weight, the Spin-Switch can also perform Boolean operations as shown in Figure 1.11.

## 1.3 Overview of the Thesis

This research was birthed as a direct response to the many cursory modeling manuscripts and proposals regarding spin-based logic devices. The cursory analyses of these works is largely due to the fact that the physical equations governing magnetic behaviors are highly complex and require significant computing resources to analyze. The main focus of this research is on accurate theoretical modeling of physical phenomena governing the operation of spin-based logic and memory devices that are currently being investigated in academia and industry. Specifically, the research focuses on:

1. Reliability of magnetization state (Chapter 3)
2. Reversal through STT (Chapter 4)
3. Requirements for reliable dipolar coupling (Chapters 5–9)
4. Overall Spin-Switch analysis (Chapter 10)
5. Possible improvements to spin-based devices (Chapters 11–12)

to obtain accurate bounds on the performance and energy dissipation of Spin-Switch Logic. Areas 1-3 are required for the accurate analysis of the Spin-Switch device and allow us to conduct to evaluate the theoretical potential of Spin-Switch devices. While we do effectively prove that Spin-Switch technology delivers significantly worse, performance metrics to current CMOS technology, we formulate possible augmentations which can be applied to many types of spin-based technologies bringing their theoretical performance closer to current standards.

The rest of the thesis is organized as follows: Chapter 2 establishes the physical equations governing the magnetization state of the free-magnets in the Spin-Switch system. In Chapter 3 we analyze the stability of magnetization for a biaxial thin film magnetic body. This is an area of research that is crucial for all magnetic technologies. All modern digital circuits are founded on an implicit trust with users that the devices will behave in a

deterministic manner. However, at room temperature, a thin film nanomagnet is under the influence of a stochastic field referred to as thermal noise. Thermal effect turn the magnetization state of the thin-film body into a Brownian motion. Often neglected in literature, we evaluate the stability of a biaxial nanomagnetic system when in the presence of this thermal field and how it may be modeled. It is shown that for long observation times, the analytic models describing the reliability of magnetization in a uniaxial energy landscape is sufficient for the description of reliability in a biaxial system.

In Chapter 4 we investigate reversal delay through STT. Similar to the reliability analysis, previous works found the analytic solutions for STT magnetization dynamics within a uniaxial system [73]. By extension, the delay of reversal for a uniaxial nanomagnet through STT has also been found [74]. However, these analytic models do not apply to biaxial systems [2]. In Chapter 4, analytic expressions are developed which can approximate the reversal delay of a biaxial nanomagnet through STT allowing us to better analyze complex nanomagnet systems. In addition, this chapter also investigates the variability of STT reversal delay due to thermal noise. We propose new methods for analyzing the delay variation of a circuit whose individual components are stochastic variables.

Unlike the previous two areas of interest which have had some analytic analysis in literature, dipolar coupling between magnetic systems has had limited analysis. This is because the stray fields emitted by the magnetic bodies are dependent on the magnetization direction. Because of the infinite possible precessional trajectories and the added stochasticity added to the system by thermal noise, traditional physical models of dipolar coupling are difficult. However, in Chapters 5–9, we exhaustively analyze reversal through dipolar fields culminating in models which outline the correctly define the requirements for coupling in a two-body system.

The qualitative analysis and analytic models of the individual magnetic effects are then combined yielding a full comprehensive analysis of Spin-Switch Logic in Chapter 10. This analysis allows us to outline the material and geometric parameters required for reliable

operation, potential energy and delay parameters for a Spin-Switch device. We show that the minimum energy-delay product (EDP) for Spin-Switch technology is approximately four orders of magnitude greater than modern CMOS standards.

While this result is disappointing for future of Spin-Switch Logic and other spin-based technologies, using the knowledge gained through our previous analysis we are able to conceptualize possible improvements to the Spin-Switch device. In Chapter 11, we propose a latch-less pipelining scheme and discuss the benefits of majority-gate logic. Both these improvements promise to reduce gate count potentially improving the energy consumption of larger chips. In addition, we investigate the possibility of a copper-collector which can increase the amplification offered by the GSHE.

Notably, it has been theorized that more efficient reversals can be achieved if the magnetization is initialized to a high-energy state through the use of a piezoelectric material. A theoretical framework for strain-mediated reversal and its potential benefit to nanomagnet systems is shown in Chapter 12. We demonstrate that while this type of reversal does offer significant energy savings when compared to standard reversals cases but is limited by thermal effects present in the system. Hence, though many magnetic devices can benefit from this technology, it is unlikely this augmentation alone will make spin-based devices more attractive than their CMOS counterparts in terms of energy and delay.

Even with the theorized improvements to the Spin-Switch device, we show that the performance gap between this device and conventional CMOS devices remains very large and hence, the Spin-Switch is unlikely to be a viable replacement for current CMOS logic technology. With this enhanced understanding, we conclude this thesis with a discussion of the future of spin-based technologies.

# CHAPTER 2

# MAGNETIZATION DYNAMICS

The interaction of electron spins with the crystal lattice is a quantum process. However, employing full quantum mechanical models to study the properties of fine ferromagnetic particles is extremely difficult with modern computing systems. As such, we can consider a semi-classical approximation in a continuous medium to represent the characteristics of the magnetic body. Such a theory was first introduced by Landau and Lifshitz while studying the properties of domain walls in larger magnetic systems [75]. However, the magnetic bodies considered in this thesis are very small and under slow reversals with minimal domain nucleation. Such magnetic bodies can be reasonably described by a single-domain model (also described as the Stoner–Wohlfarth model) [76].

## 2.1 Energy Landscape

The precession of the magnetic moment and its interaction with external fields/torques is defined by the shape and magnitude of its energy landscape. The energy landscape is the summation of several distinct energy components. The most significant contribution is by the exchange energy:

$$E_{exchange} = -J\hat{s}_1 \cdot \hat{s}_2, \tag{2.1}$$

where $\hat{s}_1$ and $\hat{s}_2$ are the unit vectors representing the directions of two neighboring spins, and $J$ is the exchange constant. $J$ can be derived analytically using quantum mechanics and is positive for a ferromagnetic material; it is negative for an anti-ferromagnetic material [77, 78]. The exchange energy is a result of overlapping orbits of neighboring electrons because the Coulomb energy is minimized when their orbits are anti-symmetric. This exchange

energy can be written in a continuum representation as:

$$E_{exchange} = \int_V A[(\nabla m_x)^2 + (\nabla m_y)^2 + (\nabla m_z)^2]d^3r \tag{2.2}$$

where $V$ is the volume of the magnetic body. $A$ is the exchange stiffness constant and can be written as $A = \frac{JS^2n}{a}$ where $a$ is the distance between nearest neighbors and $n$ is the number of atoms inside a unit cell. The exchange stiffness constant is commonly used to derive the exchange length which is the typical length scale over which the exchange energy acts. It is given as $l_{ex} = \sqrt{\frac{2A}{\mu_0 M_s^2}}$ where $\mu_0$ is the free-space permeability constant and $M_s$ is the saturation magnetization. For most bulk magnetic materials such as Fe/Co/Ni/Permalloy, the exchange length is on the order of several nanometers.

While the exchange interaction is significant over short distances, it rapidly weakens as the size of the magnetic body is increased when it must compete with the opposing dipolar interaction. The dipolar interaction will attempt to align spins according to their relative position. Without going through the extensive derivation required for analytic evaluation of this interaction, the dipolar energy can be represented as:

$$E_{dipole} = \int_V \frac{1}{2} H_D(r) \cdot \hat{m}(r) d^3r, \tag{2.3}$$

where $H_D$ is the demagnetization field. The treatment of the demagnetization field is discussed in Section 2.1.2.

The magnetic bodies considered in this research have length and width dimensions on the order of 10's of nanometers and are few nanometers thick. Since the magnetic bodies are sufficiently small, the exchange interaction would most likely dominate at these scales and we can reasonably assume the magnetic film to be a mono-domain body[1]. Several works have successfully used this macrospin spin assumption to describe magnet interac-

[1]The one exception is in Chapter 9 where we do show the existence of the mutual coupling effect in multi-domain magnetic systems

tion [73, 79]. The magnetic moment is represented as the vector $\vec{M} = M_s\hat{m}$ where $\hat{m}$ is the direction of magnetization and can be written in both Cartesian and polar coordinates as:

$$\hat{m} = \langle m_x, m_y, m_z \rangle = \langle \cos\theta \sin\phi, \sin\theta \sin\phi, \cos\phi \rangle \tag{2.4}$$

where $\theta$ and $\phi$ are the azimuthal and polar angles, respectively.

Other energies acting upon the the magnetic moment include the the "magneto-crystalline anisotropy energy" and describes the magnetization's preference to align itself along the material's crystalline axis. This is an anisotropy energy and is given as:

$$\epsilon_K(\hat{m}) = -K_u \hat{r}_{free} \hat{m}^2, \tag{2.5}$$

where $\hat{r}_{free}$ is the crystalline axis. This axis is also commonly referred to as the "free-axis". Here, $K_u$ is the uniaxial anisotropy constant.

In a thin film structure, the dipole interactions between spins result in a nanomagnet's desire to align itself along the the longest geometric axis which is referred to as the "shape anisotropy". The shape anisotropy can also be referred to as the "demagnetization energy." For a mono-domain magnetic body, the shape anisotropy has the form:

$$\epsilon_D(\hat{m}) = \frac{1}{2}\mu_0 M_s^2 \left( N_{xx} m_x^2 + N_{yy} m_y^2 + N_{zz} m_z^2 \right), \tag{2.6}$$

where $N_{xx}$, $N_{yy}$, and $N_{zz}$ are the demagnetization coefficients. The assignment of these coefficients is discussed in Section 2.1.2.

Finally, the Zeeman energy which describes the nanomagnet's desire to align parallel to an externally applied magnetic field:

$$\epsilon_{Zeeman}(\hat{m}) = -\mu_0 M_s \vec{H}_{app} \cdot \hat{m}, \tag{2.7}$$

where $\vec{H}_{app}$ is the external field applied on the magnetic body. Knowing all these energy

contributions, we can say that the magnetization energy density of the mono-domain body is:

$$\epsilon(\hat{m}) = \epsilon_K(\hat{m}) + \epsilon_D(\hat{m}) + \epsilon_{Zeeman}(\hat{m}). \tag{2.8}$$

The total magnetization energy has three components, the two anisotropies of the magnetic body and the Zeeman energies imposed by applied magnetic field(s).

### 2.1.1 Abstraction of Energy Landscape

It is often useful to abstract a magnetic body by noting that, for bulk material thin-film nanomagnet systems, $\epsilon(\hat{x}) < \epsilon(\hat{y}) < \epsilon(\hat{z})$; the energy landscape of the nanomagnet can be represented by an easy-axis anisotropy ($K_\parallel$) and out-of-plane anisotropy ($K_\perp$). Using (2.9), the new energy landscape using these two anisotropy values becomes:

$$\epsilon\left(\hat{m}\right) = -K_\parallel m_x^2 + K_\perp m_z^2, \tag{2.9}$$

where

$$K_\parallel = K_u + \frac{1}{2}\mu_0 M_s^2 \left(N_{yy} - N_{xx}\right), \tag{2.10a}$$

$$K_\perp = \frac{1}{2}\mu_0 M_s^2 \left(N_{zz} - N_{yy}\right). \tag{2.10b}$$

This normalization sets $\epsilon(\hat{y}) = 0$ without altering the dynamics of the magnetic body significantly simplifying analysis.

### 2.1.2 Type of Energy Landscapes

To discuss magnetization dynamics, we can represent the energy space of a magnetic body as a series of precessional trajectories as shown in Figure 2.1. The precessional trajectories are the solutions to the LLG equation assuming $\alpha = 0$ and that the magnetization lies on a constant energy orbit [80]. The blue trajectories correspond to the high energy region where

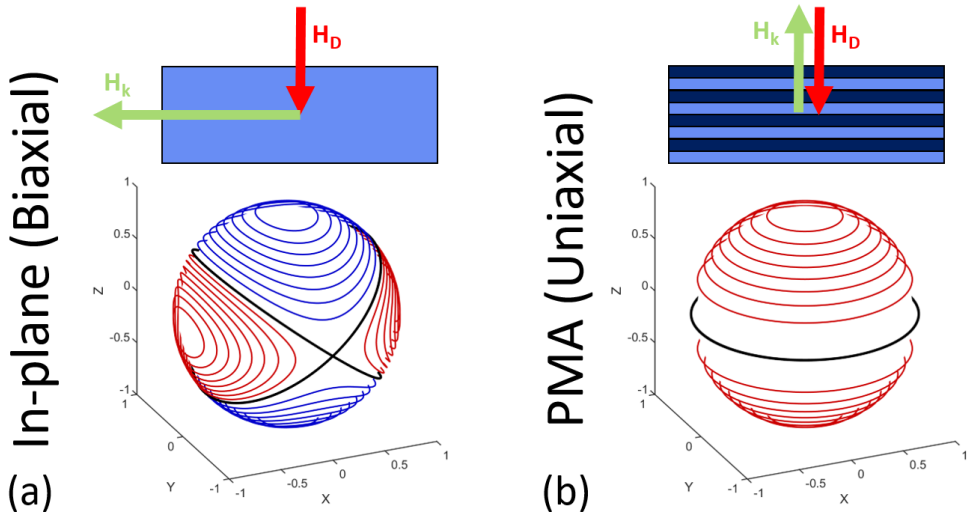


Figure 2.1: Visual representation of energy landscapes for (a) in-plane and (b) PMA nanomagnets. Lines denote magnetization orbits at different magnetization energies. Red lines map energy basin while blue lines map energy pole. Black lines mark energy barrier between regions. Despite having orthogonal free-axis directions, the only difference between the two energy landscapes is the existence of a perpendicular positive anisotropy energy. This perpendicular anisotropy energy creates a biaxial system and significantly alters the precessional mechanics of the nanomagnet. Hence, uniaxial and biaxial nanomagnet systems need to be evaluated separately.

the magnetization precesses and falls away from a high energy pole. The red trajectories denote the precessional trajectories in an energy basin where the magnetization will precess and fall towards an energy minima. The axis of this energy minima is often referred to as the free-axis of the magnetic body and is defined by the direction of the uniaxial anisotropy energy. The separatrix (plotted in black) shows the orbit associated with the energy barrier.

Two types of energy landscapes are considered: uniaxial and biaxial, that account for most nanomagnetic systems currently being researched. In both cases, there is a net negative anisotropy oriented along the free-axis. This anisotropy is largely due to the uniaxial anisotropy energy. In a biaxial energy landscape, a net positive shape anisotropy is oriented perpendicularly to the free-axis. In the uniaxial case, the magnetizations interact more with both dimensions of the energy landscape as compared to the biaxial case.

These two types of energy landscapes correspond to two types of nanomagnets commonly found in experimental studies: in-plane and perpendicular-magnetic-anisotropy (PMA)

[2, 81]. Using simple coordinate transformation, these types of energy landscapes can be applied to these two thin-film nanomagnet bodies as demonstrated in experimental studies.

In-plane nanomagnet systems are commonly created using bulk materials with a rectangular magnetic body to ensure a negative net anisotropy contribution to the free-axis ($\hat{x}$) from both the nanomagnet's shape and magnetocrystalline energies. Because of the thin-film body, the positive shape anisotropy significantly contributes to the out-of-plane axis $\hat{z}$. The uniaxial anisotropy energy accounts for the negative net anisotropy energy along the free-axis ($\hat{x}$). Because this energy landscape contains a positive and negative anisotropy perpendicular to each other, the in-plane nanomagnet is analogous to a biaxial energy landscape.

In the case of PMA nanomagnets, the magnetic body is composed of layered metals whose surface interactions create a net-negative anisotropy along the out-of-plane axis ($\hat{z}$) [82, 83, 84]. Furthermore, assuming a square thin-film body the shape anisotropy energy will also oriented along $\hat{z}$ [85, 86]. Hence, a PMA nanomagnet will have one net anisotropy energy along $\hat{z}$ and assuming correct design, this net-anisotropy will be negative, making $\hat{z}$ the free-axis [87]. It can be concluded that a PMA magnet has a uniaxial energy landscape except that its free-axis is oriented along $\hat{z}$ instead of $\hat{x}$. Figure 2.1 clearly demonstrates the differences between the two type of nanomagnets. Notice that the in-plane and PMA nanomagnet bodies are both subsets of biaxial and uniaxial systems respectively. Magnets with uniaxial energy landscapes can also be fabricated using bulk material shaped into a rectangular prism. By making the nanomagnet width and thickness equal, the shape anisotropies along the two longest axes have no net effect on the precessional dynamics of the system.

*Representation of Energy Landscapes Through Demagnetization Field*

The difference between the uniaxial and biaxial energy landscapes is the inclusion of a perpendicular anisotropy energy. Hence, for the purposes of analysis, we can create these

types of energy landscapes through careful assignment of the three demagnetization coefficients: $N_{xx}$, $N_{yy}$, and $N_{zz}$. For instance, a uniaxial energy landscape is created if there is no net perpendicular contribution from the shape anisotropy. For this case, we define a zero-demagnetization system (0Hd), whose demagnetization coefficients are assigned as $N_{xx} = N_{yy} = N_{zz} = 0$. This means that the energy barrier of the magnetic is equal to the uniaxial anisotropy energy and greatly simplifies our analysis.

A biaxial nanomagnet system can be assigned in two ways. Firstly, we define the simple demagnetization field (SHd) where $N_{xx} = N_{yy} = 0, N_{zz} = 1$ which corresponds to an infinitely long and wide thin film structure. This case is useful because it maintains the energy barrier equal to the uniaxial anisotropy energy simplifying comparisons between SHd and 0Hd systems. Secondly, for realistic thin film geometries, $N_{xx}$ and $N_{yy}$ are non-zero and significantly contribute to the energy barrier of the magnetic. For our benchmarking analyses, we must consider the most realistic cases. Hence, we define the complex-demagnetization field (CHd), where the demagnetization coefficients are determined by geometry [88]. In this case, the coefficients satisfy the condition: $N_{xx} + N_{yy} + N_{zz} = 1$ and each value is inversely proportional to the geometric length of the material body along that corresponding axis.

For the majority of this thesis, we will assume SHd. However, in Chapter 7 we do an analysis of dipolar coupling in both biaxial (SHd) and uniaxial (0Hd) systems. CHd models are used for real-world analyses in Section 7.5 and for benchmarking purposes in Chapter 10.

## 2.2 Landau-Lifshitz Gilbert Equation

The phenomenological equation describing the physics of each magnet under the effects of STT and dipolar coupling field is given by the Landau-Lifshitz-Gilbert equation [41, 75, 89, 90]

$$\frac{d\hat{m}}{dt} = -\gamma\mu_0\left(\hat{m} \times \vec{H}_{eff}\right) + \alpha\left(\hat{m} \times \frac{d\hat{m}}{dt}\right) + \frac{\vec{I}_{s,\perp}}{qN_s}, \tag{2.11}$$

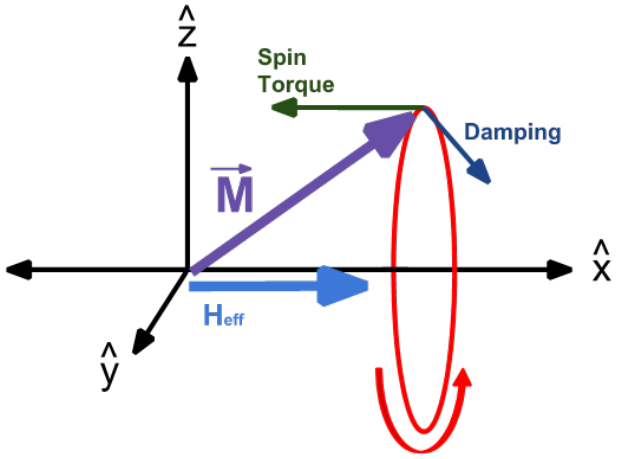


Figure 2.2: Visual representation of the torques acting upon the magnetization of a single-body ferromagnetic system .

where $\gamma$ is the gyromagnetic ratio, $\mu_0$ is the free space permeability, $\alpha$ is the Gilbert damping coefficient, $q$ is the element charge, $M_s$ is the magnetic saturation, and $I_{s,\perp}$ is the spin current. $N_s$ is given as

$$N_s = \frac{2M_sV}{\gamma\hbar}, \tag{2.12}$$

It can be seen that the LLG is the sum of the three torques that act upon the magnetization of the mono-domain as shown in Figure 2.2. The precessional torque cause the magnetization to precess along the constant energy obits discussed in Section 2.1.2. The second term is the damping torque and represents the nanomagnet's desire to find the lowest energy state. This torque is oriented perpendicularly to the precessional orbit and coerces the magnetization to relax towards lower-energy precessional orbits until the magnetic moment reaches its free-axis. the magnitude of this damping term is determined by the $\alpha$ coefficient. For the majority of our analysis, we consider a small $\alpha = 0.01$ which corresponds to a bulk iron body [91]. A small $\alpha$ is beneficial for STT reversal and dipolar coupling, but reduces magnetization reliability when in the presence of thermal noise.

The third term is the STT discussed in Section 1.1.3. The STT imparts an angular momentum on the magnetic moment proportional to the orthogonal component of the spin-polarization axis. Unlike an external field, the STT is a separate torque and not added to

the nanomagnet's energy landscape. For STT reversal, this STT torque term must be larger than the damping torque pushing the magnetization across the energy barrier to the parallel basin. The nuances of STT reversal are described more fully in Chapter 4.

The energies create a gradient system represented by the fields applied to the magnetic moment and is related to the magnetization energy by:

$$\vec{H}_{eff} = \frac{1}{\mu_0 M_s} \frac{\partial \epsilon}{\partial \hat{m}}. \tag{2.13}$$

Therefore $\vec{H_{eff}}$ can be written as

$$\vec{H}_{eff} = \vec{H}_K + \vec{H}_D. \tag{2.14}$$

where $\vec{H}_K$ is the uniaxial anisotropy field and is derived from the Stoner-Wohlfarth model as [76]

$$\vec{H}_K = \left( \frac{2K_u}{\mu_0 M_s} m_z \right) \hat{z}. \tag{2.15}$$

and the demagnetization field ($\vec{H}_D$) is given as:

$$\vec{H}_D = -M_s \left\langle N_{xx} m_x, N_{yy} m_y, N_{zz} m_z \right\rangle, \tag{2.16}$$

where the demagnetization coefficients are assigned values as described in Section 2.1.2.

## 2.3 Thermal Noise

The thermal field describes the susceptibility of the magnetic moment to random thermal fluctuations. As we are considering small, nanometer-scale magnetic bodies, the thermal fluctuations significantly impact magnetization dynamics. The thermal field is Gaussian with a zero mean. That is,

$$\left\langle \vec{H}_{T,i}(t) \right\rangle = 0. \tag{2.17}$$

The correlation between the elements of $\vec{H}_T$ defined over time interval $\tau$ as

$$\left\langle \vec{H}_{T,i}(t)\, \vec{H}_{T,j}(t+\tau) \right\rangle = \frac{2\alpha k_b T}{\mu_0^2 \gamma M_S V} \delta_{ij} \delta(\tau). \tag{2.18}$$

According to the theory developed by [92], the thermal field can be defined as an isotropic vector process field Wiener process $W_k$ [93]. Knowing this, the thermal field $\vec{H}_T$ can be modeled as 3-dimensional Wiener process [94]:

$$\vec{H}_T = \sqrt{\frac{2\alpha k_B T}{\mu_0^2 \gamma M_S V}} \left( \frac{\partial W_X}{\partial t}\hat{x} + \frac{\partial W_Y}{\partial t}\hat{y} + \frac{\partial W_Z}{\partial t}\hat{z} \right), \tag{2.19}$$

The Wiener process is simply a stochastic process whose value at every time increment is a normal variable with a mean of 0 and standard deviation of 1. The integration of the Wiener process is a Brownian motion. Because we're assuming that the thermal noise is uncorrelated at each time interval, the Brownian motion model valid [3]. In addition, this model of thermal noise has been used to accurately describe thermal dynamics of experimental magnetic systems [73, 95]

The treatment of the thermal field with respect to the LLG equation requires a nuanced understanding of stochastic calculus [96]. Differential equations which include a stochastic element can be interpreted using one of two types of calculus: Itô and Stratonovich [97, 98]. Appendix C clarifies the difference between these two form of calculus; the primary difference being the evaluation of the differential equation with respect to the time interval.

Given that the LLG equation and thermal noise both describe a physical process (traversal of the magnetic moment) a Stratonovich interpretation of the LLG would be most appropriate. Fortunately the stochastic version of the LLG equation can be derived by simply adding the thermal field to the effective field of the nanomagnet resulting in the stochastic Landau-Lifshitz Gilbert (sLLG) equation

$$\frac{d\hat{m}}{dt} = -\gamma\mu_0 \left( \hat{m} \times (\vec{H}_{eff} + \vec{H}_T) \right) + \alpha \left( \hat{m} \times \frac{d\hat{m}}{dt} \right) + \frac{\vec{I}_{s,\perp}}{qN_s}. \tag{2.20}$$

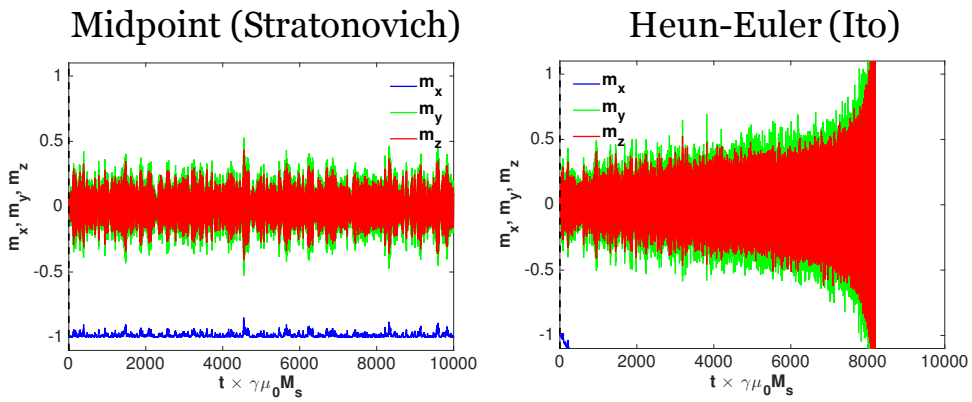


Figure 2.3: Plots taken from [100]. Plots show numeric integration of sLLG (2.20) using two different integration schemes. The difference of these results is due to the fact that certain numerical integration schemes adhere to either Stratonovich or Itô solutions. Hence, using a numeric integration scheme such as the Midpoint method yields perfectly acceptable results when evaluating (2.20). However, the Euler-Heun method, which converges to the Itô solution, outputs unstable results assuming the same parameters.

It can be mathematically proven that this interpretation of the sLLG adheres to the Stratonovich interpretation and is the form most commonly used in literature [3, 99].

This is important to emphasize because the translation of numerical integration schemes which are correct for deterministic differential equations may yield incorrect results when applied to the stochastic case [101]. Figure 2.3 shows what happens when a stochastic differential equation is paired with a numerical integration scheme that does not converge to the same stochastic interpretation. In our research, the Heun method was used to simulate the sLLG [102]. Other works have used Runge-Kutta (RK4) and Midpoint methods for evaluation [103, 104, 105, 106]. While RK4 and Midpoint methods do offer stronger convergence than the Heun method, they also require more computing power. We felt that the trade-off of time-step to calculations per interval favored the usage of the Heun method.

While not used in this research, the Itô interpretation of the sLLG can be solved for through the inclusion of the deterministic drift term. This is useful when there is no choice of numerical technique such as in the case of modeling magnetization dynamics using SPICE simulations. Typical SPICE solvers employ a Euler's method due to its simplicity and hence, the Itô interpretation of the sLLG is necessary when modeling magnetization

dynamics in such an environment.

## 2.4 Simulation Methods and Environment

While I began my research using custom numerical solvers developed in Matlab, it became evident that serial scripting languages are were insufficient for the purposes of my research. Fortunately, the serial CPU processing bottleneck was noticed in the previous decade and massive the GPU unit evolved into a highly parallel many-core processor with significant computational bandwidth. GPU computational cores are simpler than modern CPU cores omitting advanced architecture components such as branch predictors and predictive caches. However, the simpler designs allow for more cores running in parallel thanks to their smaller footprints. Modern high-end GPU architectures contain roughly 3500 CUDA cores which means a significant simulation speedup assuming the programmer can make use of all these cores in parallel. In addition, these simpler cores are designed for numerical processing and contain added floating-point processing units. These evolved GPUs are designed for highly-parallelized data-processing.

CUDA (Compute Unified Device Architecture) is the programming language used to program the GPU device and behavior of the individual cores. CUDA programming is similar to classic embedded device programming where each chip in the embedded device must be programmed separately and operations are performed when these chips communicate with one-another. In CUDA, there is a central kernel function which is distributed to all the cores. The behavior of the kernel function changes based on the Core identification number which allows one to program many cores performing different functions.

CUDA/GPU programming is well suited for our purposes. We limit each CUDA core to solve one instance of the sLLG equation. This means that we can more rapidly perform a Monte-Carlo simulation analyzing the reversal probability for a magnetic body in the presence of thermal noise. We can also solve for the reversal delay of many different magnetic systems when omitting stochastic effects. Or we can perform Monte-Carlo analyses on

many different system at once. The programming and use of many-core GPU architectures fulfilled enormous computational demands of our research.

Custom numerical solvers are written in CUDA implementing the Heun method to solve the sLLG [94, 107]. Most GPUs have a limited amount of memory available and hence, a great deal of effort was dedicated to making this solver as memory efficient as possible. The accuracy of the simulator was verified by comparing results of the simulations against known analytic solutions for the LLG [73]. The results of this comparison are shown in Figure 2.4. [73] solves the LLG equation for a uniaxial (PMA) magnetic body under the influence of STT. The comparison of the analytic equation and numerical integrator shows strong agreement verifying the correct operator of the deterministic portion of our solver. Using similar logic, we compare the analytic and numerical results for the initial angle distribution of a PMA magnet at its steady state. The agreement between the solver and analytic models confirms the correct operation of the stochastic portion of our solver. Using the methods in Figure 2.4, we find that strongly converges to the correct using a 10 fs time-step.

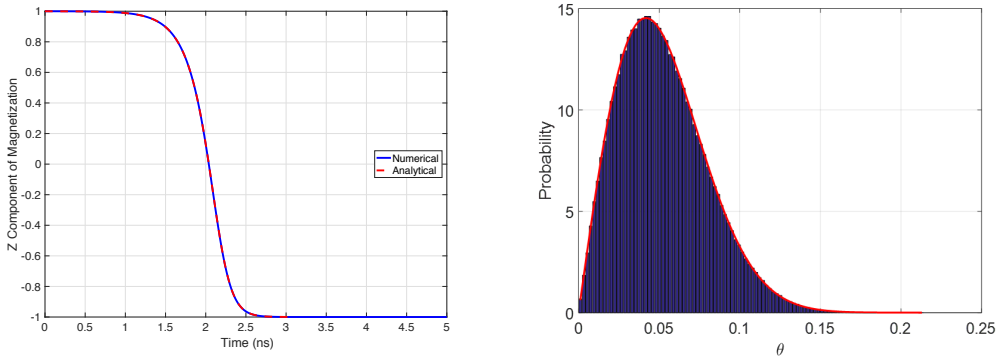


(a) Comparison of Deterministic Results (b) Comparison of Stochastic Results

Figure 2.4: Considering a a $40 \times 40 \times 1nm^3$ PMA magnet with $M_s = 10^6 \frac{A}{m}$, $K_u = 10^6 \frac{J}{m^3}$ and $\alpha = 0.01$. *Left:* Z component of magnetization as nanomagnet is reversed using a -96 $\mu$A spin current. Compares numerical results with solution to LLG equation (4.4) derived in [73]. *Right:* Evaluates the initial angle of the nanomagnet while it is at rest fluctuate around the free-axis due to thermal effects. Compares numerical results with analytic equation (4.7a) derived in [73].

# CHAPTER 3

# THERMAL STABILITY OF MAGNETIC BODIES

Before we can analyze the reversal characteristics of magnetic bodies, we need to understand the reliability of the magnetization state [108]. The interaction of the magnetic order parameter with the underlying thermal fluctuations of the magnetic body has been analyzed extensively in prior literature [109, 110, 111, 112]. Most prominently, W. Brown, in his seminal works in 1963 to 1979, developed the "Brownian motion" model of thermal noise. Using the Fokker-Planck analysis, Brown showed that the probability of the thermal reversal in fine ferromagnetic bodies (i) is a single exponential function with respect to time and (ii) it varies monotonically with the energy barrier of the nanomagnet [113, 92]. Brown's analysis is specifically applicable in cases when the magnetization energy is "independent of the radial angle" [113] implying the absence of demagnetization field caused by the shape anisotropy of the magnetic body. The lack of the demagnetization field decouples the dimensions of the Landau-Lifshitz-Gilbert (LLG) equation and allows analytic solutions of the thermally-induced magnetization reversal probability [73]. However, thin-film biaxial nanomagnets contain both a negative uniaxial anisotropy along its free-axis, and a positive shape anisotropy oriented perpendicular to the free-axis. As such, the magnetization energy depends on both the azimuthal and polar angles of the magnetization vector, which does not allow for the dimensional decoupling of the LLG equation.

While building upon prior works, including those of Brown, in this chapter, we specifically analyze the magnetization reversal probability of thin-film nanomagnets that are characterized with a biaxial magnetic anisotropy. The analysis is conducted for a variety of material parameters of the magnetic body such as the magnetic saturation and the uniaxial energy density. For the first time, we show that for a given energy barrier, the magnetization reversal probability varies non-monotonically with the magnitude of the perpendicular

shape anisotropy. Specifically, we consider two cases of the instability in magnetization resulting from the thermal noise that eventually lead to magnetization reversal within a given time period. These two cases of thermal reversals are defined as follows.

- Case-I: reversal occurs when the magnetization vector crosses the $\hat{x}$ = 0 plane
- Case-II: reversal occurs when the magnetization energy exceeds the energy barrier of the nanomagnet

In Case-I, an increase in the demagnetization field increases the frequency of precessional energy orbits, which makes it more likely for the magnetization to cross $\hat{x} = 0$ plane once the magnetization energy exceeds a particular energy threshold. However, we find that the reversal probability in Case-II also varies non-monotonically with the demagnetization energy. This is because a larger perpendicular anisotropy shapes the energy orbit, minimizing its $\hat{z}$ components, and allows the thermal field to induce a greater torque on the magnetization. Finally we test the limits of this non-monotonic behavior and show that while this behavior is especially present in small timescale (sub-100 ns) measurements, it is diminished at very large timescales.

Note that in this chapter, to ensure simplicity of analysis, we consider a SHd demagnetization field. The physical equations governing the dynamics of a nanomagnet under the influence of thermal noise have been outlined in Chapter 2.

### 3.1 Nanomagnet Model

In this chapter, we consider a single domain thin-film nanomagnet of size 60 nm $\times$ 45 nm $\times$ 2 nm whose magnetization evolves under the influence of thermal noise. We assume a SHd demagnetization field such that the energy barrier for biaxial magnetic anisotropy is given as $E_b = -K_u$. The free-axis is along $\hat{x}$ and the material parameters of the magnetic body are varied to reveal the dynamics of thermal reversal.

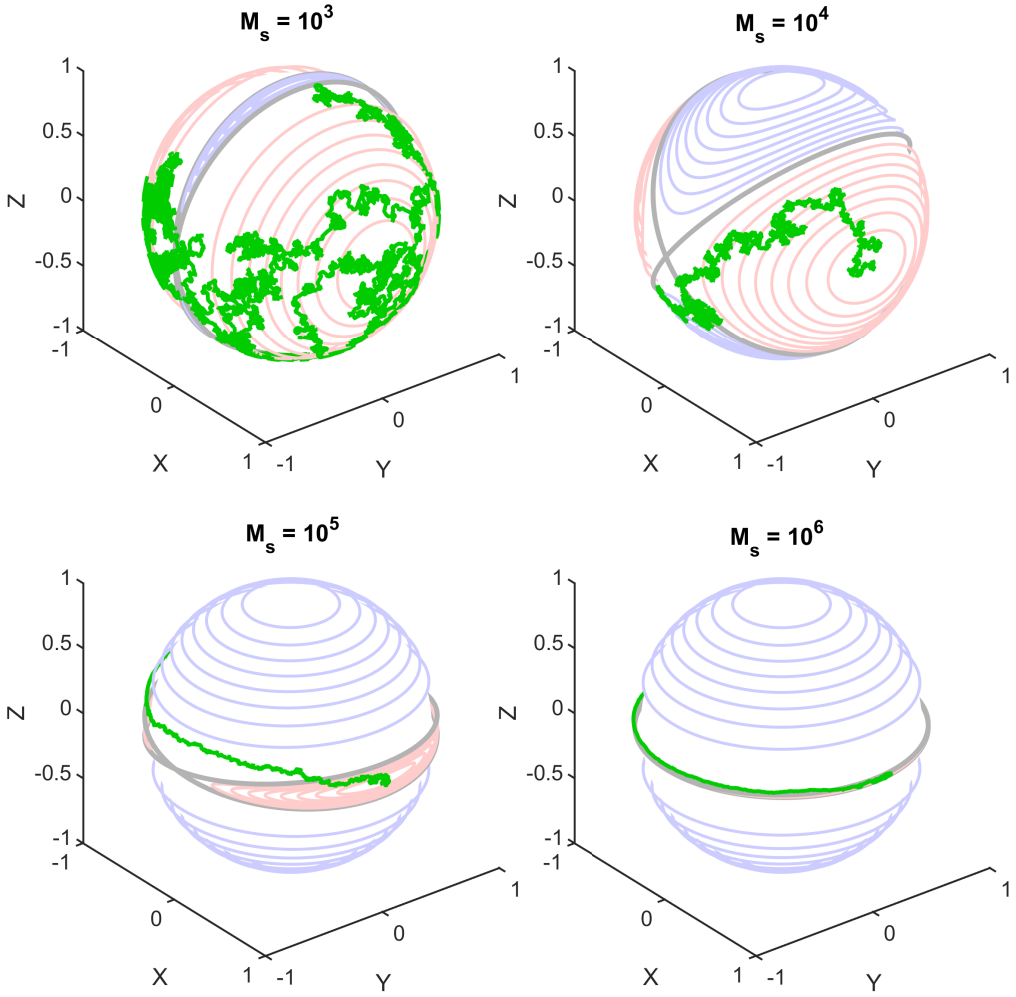


Figure 3.1: Sample reversal trajectories for nanomagnet under the influence of thermal noise. In all cases $K_u = 10^2 \frac{J}{m^3}$. Background light-colored lines denote precessional trajectories for the corresponding $M_s/K_u$ values. Green line denotes sample magnetization trajectory under thermal noise.

### 3.2 Comparison of Case 1 and Case 2 Reversals

The magnetization reversal due to thermal noise in the thin-film nanomagnet is analyzed for two cases and the results are shown in Figs. 3.2 and 3.4. In Case-I, thermally-induced magnetization reversal occurs when the magnetization crosses the $\hat{x}$ = 0 plane within a specific time period for which the probability of reversal is being examined. As evident in Figure 3.2, for a fixed energy barrier, an increase in $M_s$ leads to a non-monotonic trend in the magnetization reversal probability. It is known that a larger $M_s$ increases the thermal

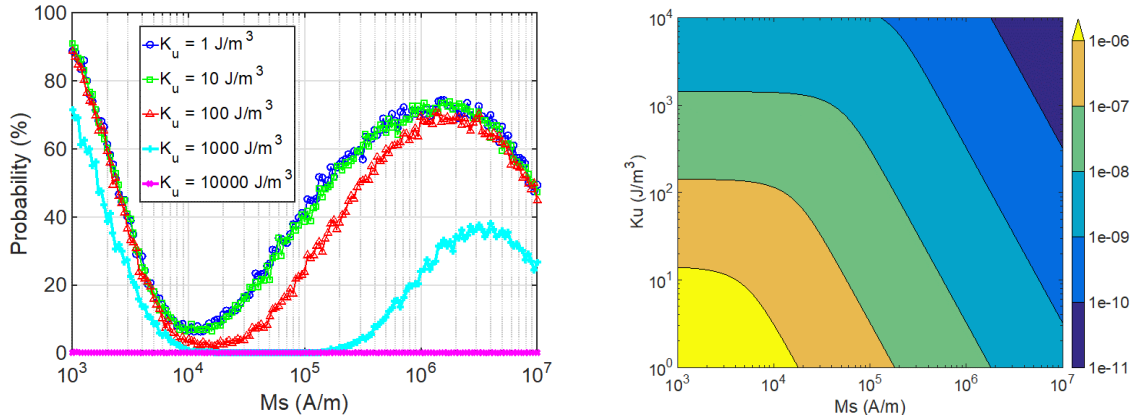


Figure 3.2: (*Left*): Probability that the magnetization will cross the $\hat{x} = 0$ plane at least once within 1 ns. While $E_b$ is solely proportional to $K_u$, it is shown that a larger $M_s$ also increases the probability of Case 1 reversal. (*Right*): Precessional period associated with nanomagnet with corresponding $M_s/K_u$ parameters at the orbit whose associated energy $= -0.01E_b$.

stability of the nanomagnet because the magnitude of the thermal field is decreased; hence, an increase in $M_s$ results in an overall decrease in reversal probability [92]. However, once $M_s$ exceeds a certain threshold, there is an increase in the reversal probability of the magnetization. This increases is partly explained by observing the sample magnetization reversals as plotted in Figure 3.1. In the case of lower $M_s$, the magnetization trajectory may cross the $\hat{x} = 0$ plane due to the random walk of the thermal noise. However, in the large-$M_s$ cases, the thermal noise simply forces the magnetization beyond the energy barrier, where the magnetization will precess across the $\hat{x} = 0$. As shown in the inset of Figure 3.2, for large values of $M_s$, the precessional time period decreases and becomes comparable or even smaller than the observation time. Thereby, it is more likely for the magnetization at a high-energy trajectory to cross the $\hat{x} = 0$ plane during the observation time which leads to a higher probability of reversal. In Case-II, the thermal reversal probability is defined such that the magnetization will cross the energy barrier at least once within a given time period. In this case, the probability of magnetization reversal for various $M_s/K_u$ parameters is plotted in Figure 3.4. Case-I reversals are a subset of Case-II reversals. Similar to Case-I dynamics, the non-monotonic behavior of reversal probability on $M_s$ for a fixed $K_u$ is

also present in the magnetization dynamics of Case-II. This shows that a perpendicular anisotropy not only alters the precessional period, but also brings the separatrix closer to the free-axis and both these aspects contribute to the positive reversal probability trend affecting large-$M_s$ nanomagnets.

### 3.3 Thermal Field Torque Dependence on Perpendicular Anisotropy

In Case-II dynamics, the non-monotonic behavior of magnetization reversal results primarily from the altered thermal-field torque for a precessional orbit at a specific energy $E(\hat{m})$. To illustrate this point, we can assume that the three-dimensional Wiener process in (2.19) is instead a constant vector $dW = [1, 1, 1]$. We then apply the LLG equation (assuming no damping) along each point in the precessional orbit associated with a particular energy to measure the change in magnetization energy due to the thermal field.

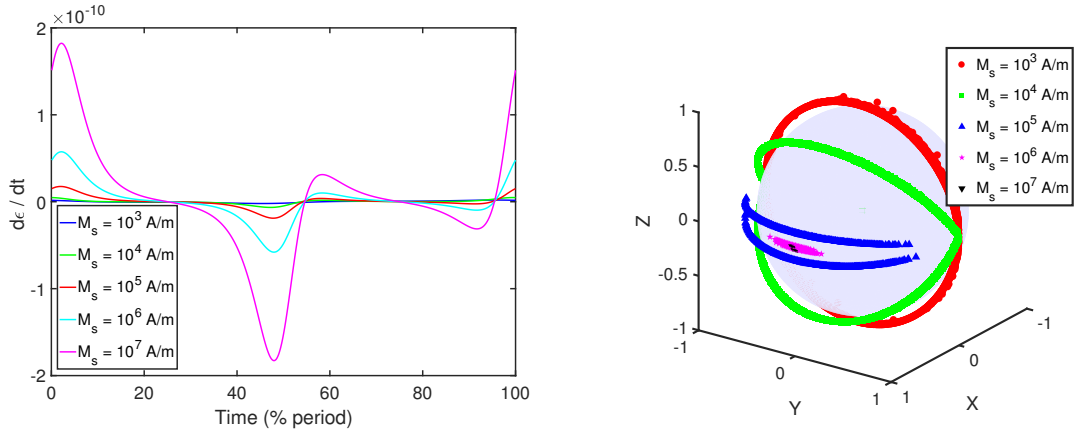


Figure 3.3: (*Left*): Change in magnetization energy due to thermal field assuming Wiener process in thermal field, $dW = [1, 1, 1]$. Change in energy calculated for each point along precessional orbit whose associated energy $= -0.01E_b$. Precessional periods for each $M_s$ value normalized along x axis. Assuming $K_u = 10^2 \frac{A}{m}$ a $dt = 10^{-12}s$. (*Right*): Scatter plot of magnetization position when magnetization energy first exceeds energy barrier for various values of $M_s$.

As shown in Figure 3.3, the thermal-field torque is enhanced when the nanomagnet has a larger perpendicular anisotropy. This is because the perpendicular anisotropy shapes the precessional orbits affecting the $\hat{z}$-components of their trajectories as shown in Figure 3.1.

Spatial distance between the magnetization and free-axis, alters the thermal-field torque imposed on the magnetization. This enhanced torque can cause a greater change in the magnetization energy, thereby increasing the probability for $E(\hat{m})$ to exceed the energy barrier, $E_b$. We also capture the position of the magnetization vector when it first exceeds the energy barrier to further corroborate the results. As shown in the inset plot of Figure 3.3, the point at which the magnetization first crosses the energy barrier is spread evenly along the separatrix for smaller perpendicular magnetic anisotropy (low-$M_s$). However, when the perpendicular anisotropy is increased, the crossover point of the magnetization becomes clustered closer to the free-axis.

### 3.3.1 Effect of Time on Non-monotonic Behavior

The non-monotonicity of magnetization reversal probability on $M_s$ for a fixed $K_u$ is present only when the dynamics at short time-scales (sub-100 ns) are considered. As shown in Figure 3.4, the probability curve tends toward the classical energy-barrier dependent model as the observation time is increased. This suggests that Brown's model is still valid when considering the long-term stability of nanomagnets as in the case of spintronic memory devices. Yet, in many proposals of spintronic logic devices, data retention on short time-scales is relevant. Hence, the non-monotonic behavior of magnetization reversal must be considered to accurately analyze the noise sensitivity and reliability of these logic devices [108].

## 3.4 Analytic Equation for Nanomagnet Retention Time

Note that we are concerned with the long-time behavior of the magnetic body in the magnetic body and as such, Section 3.3.1 demonstrates that a biaxial and uniaxial nanomagnets can be reduced to one another in such systems. The thermal relaxation time is the timescale for which magnetization behavior escapes the initial energy basin and crosses the energy barrier. The thermal relaxation time $\tau$ assuming a large energy barrier is described as[114,

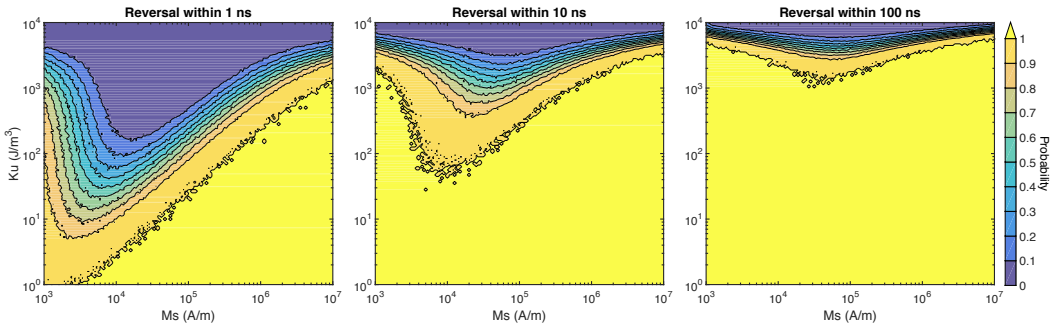


Figure 3.4: Probability that the magnetization energy for a nanomagnet will exceed $E_b$ atleast once within a given time. Three simulation times are considered according to title of plots. While $E_b$ is solely proportional to $K_u$, a larger $M_s$ also increases the probability of Case 2 reversal. The subplots together also demonstrate that the effect of this non-monotonic behavior is diminished as the observed time is increased.

115]:

$$\tau = f_0^{-1} e^{\frac{E_b}{k_b T}}, \tag{3.1}$$

Where $f_0$ and will be discussed momentarily. According to the Arrhenius-Neel theory, the probability of thermal reversal as a function of time becomes:

$$P_{SW} = 1 - exp[t f_0 e^{-\frac{E_b}{k_b T}}]. \tag{3.2}$$

The attempt frequency is difficult to decipher analytically for biaxial nanomagnet systems. Several works have attempted to at apply an analytic treatment to magnetic bodies with various axial landscapes. Most notably Coffey et al. derived several formulations for the thermal reversal probability of uniaxial, biaxial and cubic anisotropic bodies when under the influence of an applied field [116]. However, a single expression is not sufficient for describing all magnetic bodies. Separate expressions are needed for describing the very-low damping (VLD) and intermediate-high damping (IHD) bodies. Other methods such as matrix continued-fraction analyses are possible, but are computationally-expensive defeating the goal of a rapid characterization of spin-based systems using analytic results [96,

117]. However, the uniaxial case can be derived exactly [92, 118]:

$$f_0 = \frac{\gamma\alpha}{1+\alpha^2}\sqrt{\frac{H_K^3 M_s V}{2\pi k_B T}}, \tag{3.3}$$

where $H_K$ here represents the effective anisotropy field along the free-axis. This distinction is important if considering that complex demagnetization energies contribute energy to the free-axis anisotropy of rectangular magnetic bodies. However in the SHd and 0Hd cases, $H_k$ solely consists of the uniaxial anisotropy field.

# CHAPTER 4

# MAGNETIZATION REVERSAL THROUGH SPIN-TRANSFER TORQUE

Before the introduction of STT, most spin-based devices were some variant of magnetic quantum cellular automata (MQCA) which communicated information through stray-field interactions[28]. However, the introduction of STT has resulted in a myriad of proposed devices utilizing spin currents for data processing and communication. In Spin-Switch Logic, the reversal of the bottom nanomagnet is dependent on the spin current delivered by the GSHE material and as such understanding this reversal mechanism is critical for the analysis of this device. In this chapter, we analyze the STT reversal mechanism for deterministic uniaxial and biaxial magnetic bodies. Using these models, we formulate methods to model STT delay variation of uniaxial magnetic bodies under the influence of thermal noise [111].

## 4.1 Critical Current Expression

As shown in Figure 2.2, the a polarized current imparts a STT towards a particular directional state. The STT is a non-conservative force making it significantly different than the torque applied by an external field. To this end, the STT fights against the magnetic body's damping torque. Assuming the STT is large enough, it can overpower the nanomagnet's natural damping torque and reverse the magnetization. Hence, it is first important to know what magnitude STT is required to successfully reverse the magnetization of a magnetic body.

To understand the critical current magnitude requirements, we musty briefly review the critical current models available in literature. It was first noted that the minimum longitudinal spin current required to overpower the damping and drive the magnetization away from

the free-axis can be given as [74]:

$$I_{C1} = \frac{4q}{\hbar}\alpha V\left(K_{\parallel} + \frac{K_{\perp}}{2}\right). \tag{4.1}$$

However, [74] also notes that in certain magnetic systems, the spin current may be sufficient to drive the magnetization away from the low energy state, but insufficient to fully reverse the magnetization. This can be observed from the existence of in-plane magnetic oscillators [119]. This is because as the perpendicular anisotropy is increased, the damping torque at the energy barrier increases faster than the damping torque at the free-axis. It is found that the damping torque at the energy barrier can be larger than at the low-energy position along the free-axis [110]. Assuming a constant $D = \frac{K_{\perp}}{K_{\parallel}}$, it was found that for systems where $D > 5.09$, the critical current required to drive the magnetization across the energy barrier is equal to:

$$I_{C0} = \frac{4q}{\hbar}\alpha V K_{\parallel}\left(\frac{2}{\pi}\sqrt{D\left(D+1\right)}\right). \tag{4.2}$$

The magnitude of these two critical current expressions is shown in the inset of Figure 12.4. Conceptually, $I_{C1}$ and $I_{C0}$ can be thought of as the critical current when the magnetization is close to the free-axis and on top of the energy-barrier, respectively. Hence, assuming that the magnetization is initially at rest along the free-axis, the critical current magnitude required for full reversal can be given as:

$$I_C = max\left(I_{C1}, I_{C0}\right). \tag{4.3}$$

The complete model is necessary when evaluating magnetic bodies with large perpendicular anisotropies. Many spin-based models commonly ignore this and yield less-accurate results.

It is important to note that both these critical current expressions are derived by averaging the damping and spin-transfer torques along the precessional orbit of the energy

landscape. Hence, these expressions are only valid for cases where the magnetization interacts with both-dimensions of the energy landscape. For nanomagnet systems with short precessional periods, like the ones considered in this research, this orbit averaging assumption is accurate. However, if the precessional period is on the order of the nanomagnets reversal time, the analytic expressions may not be valid.

## 4.2 Uniaxial Delay Model

Having defined the minimum current required for reversal, it is now important to find the reversal delay for nanomagnets under the influence of above-critical spin currents. We will begin with the delay expressions of a uniaxial system since such systems have been proven analytically. The physics of PMA-SHd nanomagnet reversal has been exhaustively studied in [109, 120]. The energy landscape of such a magnetic body is greatly simplified because the magnetization energy is dependent on a single dimension of magnetization. This allows analytic solutions of the LLG equation. The implicit analytic equation for the dynamics of the nanomagnet is given as [73]

$$(i-1)\frac{\tau}{\tau_D} = \ln\left(\frac{\tan\left(\frac{\phi_\tau}{2}\right)}{\tan\left(\frac{\phi_0}{2}\right)}\right) - \frac{1}{i+1}\ln\left(\frac{\frac{i-1}{i+1}+\frac{\tan^2(\phi_\tau)}{4}}{\frac{i-1}{i+1}+\frac{\tan^2(\phi_0)}{4}}\right),$$

where $\tau$ is the time it takes for the polar angle of the magnetization to transition from $\phi = \phi_0$ to $\phi = \phi_\tau$. $\tau_D$ is the time scale of the magnetization dynamics and is given as

$$\tau_D = \left(\frac{1+\alpha^2}{\alpha\gamma\mu_0\left(H_k - M_s\right)}\right). \tag{4.4}$$

In (4.4), $i = I/I_{C1}$ is the ratio of the spin current entering the nanomagnet and the critical spin current of the nanomagnet. $I_c^{UNI}$ is mathematically given as [85]

$$I_C^{UNI} = \frac{2eM_sV\alpha}{\hbar}\mu_0\left(H_k - M_s\right), \tag{4.5}$$

where $e$ is the elementary charge. This critical current expression is equivalent to (4.1) without the perpendicular energy component. (4.4) is verified against numerical results in Figures 4.1 & 4.2. (4.4) reduces to the expression derived in the seminal work of J.Z.

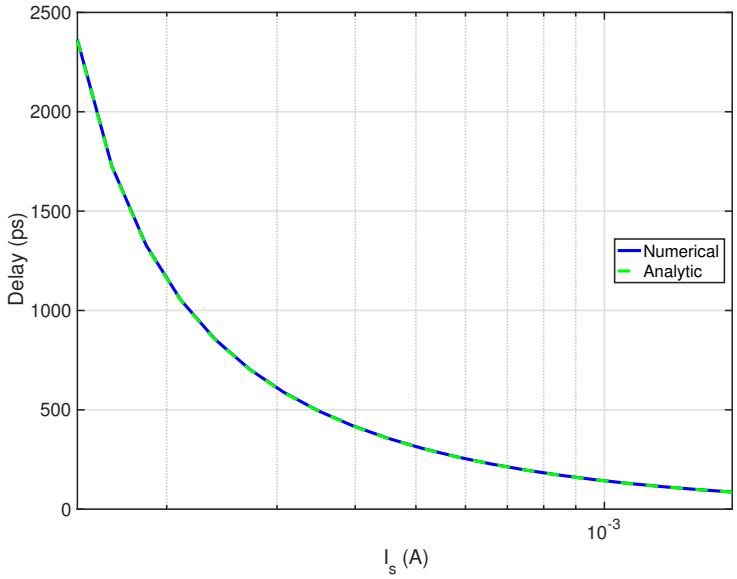


Figure 4.1: Delay of uniaxial nanomagnet using numerical and analytic results. Assuming $40 \times 40 \times 1\text{nm}^3$ with a $M_s = 1\frac{MA}{m}$ and $K_u = 1\frac{MJ}{m^3}$. Figure demonstrates exactness of (4.4) analytic expression.

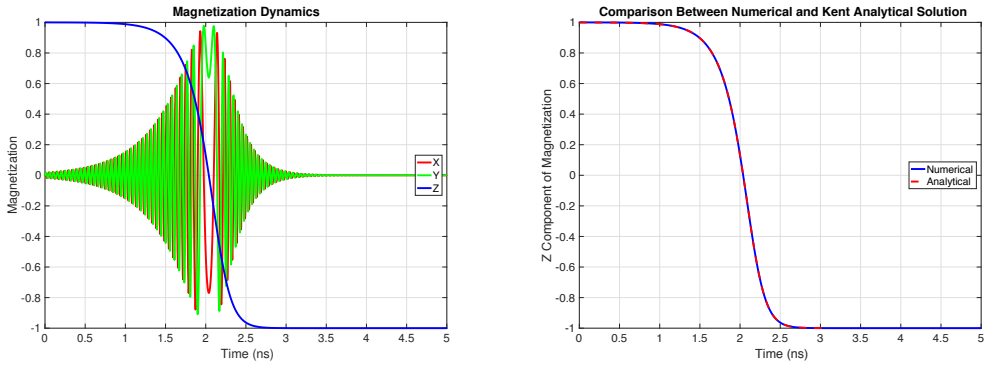


(a) Full magnetization Trajectory

(b) Free-axis magnetization. Numerical vs Analytic.

Figure 4.2: Assuming $40 \times 40 \times 1\text{nm}^3$ with a $M_s = 1\frac{MA}{m}$ and $K_u = 1\frac{MJ}{m^3}$. Figure demonstrates exactness of (4.4) analytic expression.

Sun [74] under the condition that the input spin current of the nanomagnet vastly exceeds its critical current.

## 4.3 Biaxial Delay Model

Currently, there does not exist an analytic delay expression for biaxial systems. In the uniaxial case, the magnetization energy is only a function of one dimension. This allows the two dimensions of the LLG equation to be decoupled. Each dimension can then be directly solved independently [73]. However, in biaxial systems, the magnetization energy is dependent on both dimensions which prevents this dimension decoupling.

Biaxial nanomagnets are required for the optimal operation of the Spin-Switch device and therefore, a biaxial delay expression is required. While an exact analytic expression

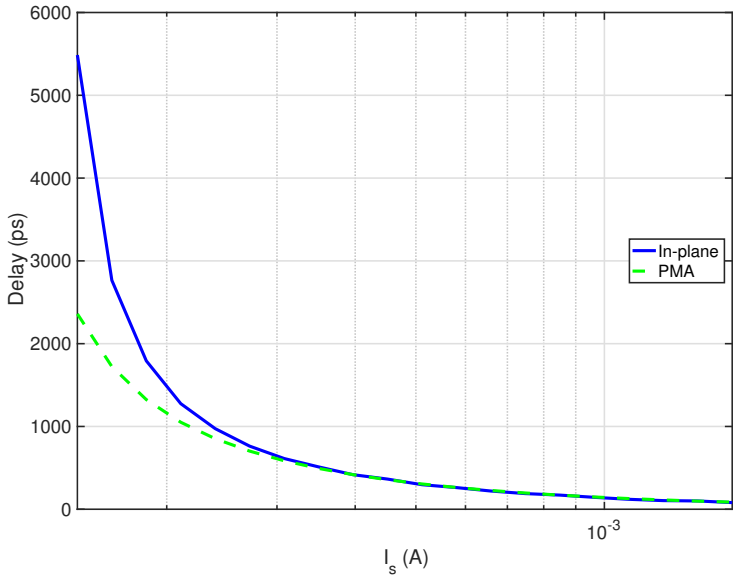


Figure 4.3: Numerical evaluation of 0Hd and SHd nanomagnet bodies. Assuming $40 \times 20 \times 2\text{nm}^3$ with a $M_s = 1\frac{MA}{m}$ and $K_u = 1\frac{MJ}{m^3}$.

can't be derived through a physical basis, we can formulate a rough approximation of biaxial delay through analysis of the differences in precessional dynamics in uniaxial and biaxial cases. We can compare the delays of 0Hd and SHd nanomagnet systems in Figure 4.3.

As evident from Figure 4.3, for very large current magnitudes, the biaxial delay values converge to the uniaxial case. As current increases, the change in magnetization becomes

more rapid reducing the number of precessions during reversal, reducing the interaction with the perpendicular field. This can be seen clearly in Figure 4.4.

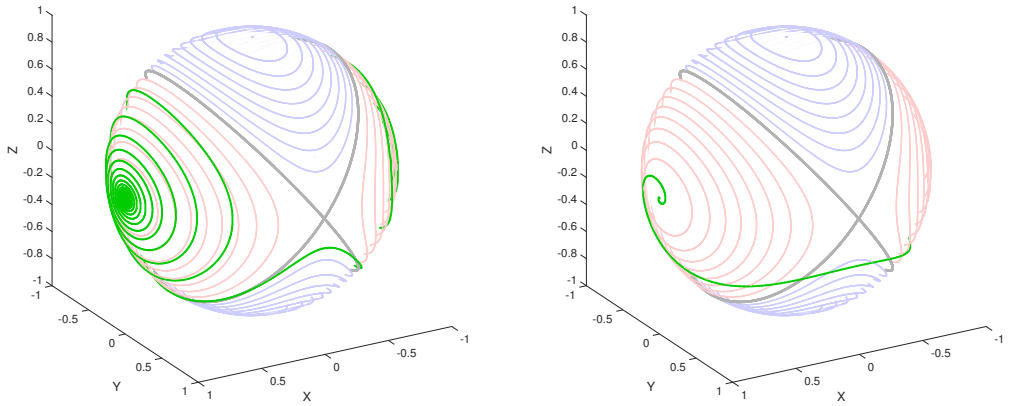


(a) 0.6 mA (b) 6.0 mA

Figure 4.4: Assuming $40 \times 40 \times 1\text{nm}^3$ in-plane SHd magnetic body with a $M_s = 1\frac{MA}{m}$ and $K_u = 1\frac{MJ}{m^3}$. Figure demonstrates difference in precessional trajectory for slow and fast reversal cases..

However, during slow reversals when the interaction with the perpendicular energy is significant, the delays are significantly different. This is due to the fact that the perpendicular anisotropy lowers the damping and increases the average torque on the magnetization as it precesses through the energy basin. Knowing that uniaxial and biaxial delays converge as $I_s \to \infty$ and diverge as $I_s$ approaches its critical current value, we can make the following approximation for the biaxial delay:

$$\tau^{bi} = (\frac{I_C}{I_s - I_C})^X \cdot \tau^{uni} \tag{4.6}$$

where $I_C$ is the critical current of the biaxial magnetic body given by (4.3), $I_s$ is the spin current magnitude and $\tau^{uni}$ is the delay of an equivalent 0Hd uniaxial body given by (4.4). The fitting parameter, $X$, depends on the shape of the energy landscape ($\frac{K_p}{K_u}$). Assuming that the correct fitting parameter is chosen, this model is accurate to within $\pm 10\%$ as shown

in Figure 4.5.

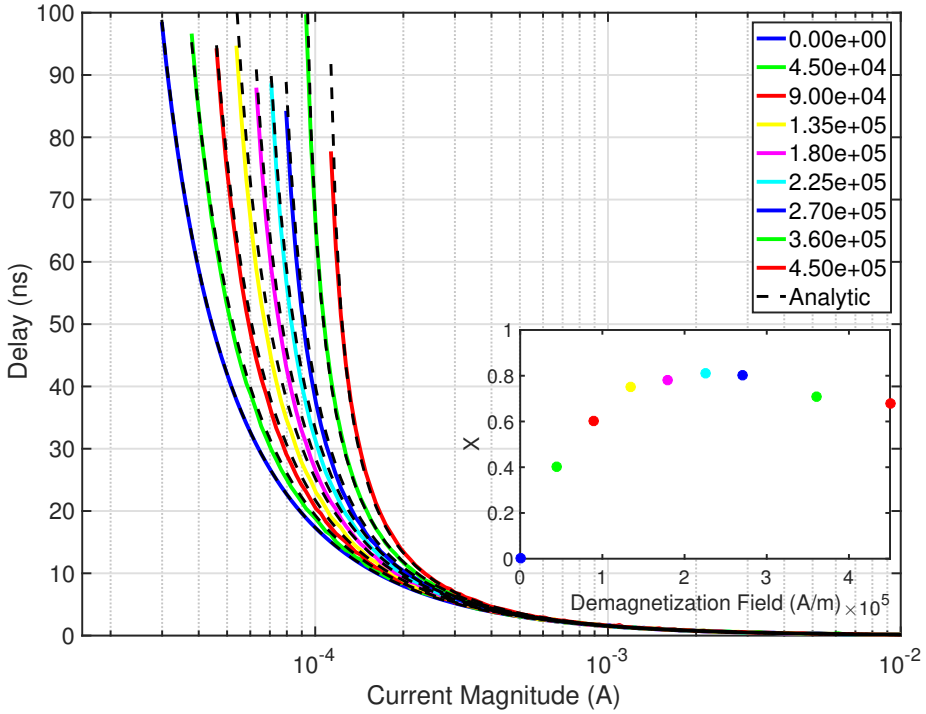


Figure 4.5: Numerical evaluation of SHd nanomagnet bodies for various demagnetization fields. Assuming $60 \times 45 \times 2\text{nm}^3$ magnetic body with a $M_s = 1.7\frac{MA}{m}$ and $K_u = 48\frac{kJ}{m^3}$. Demagnetization Field amplitudes arbitrarily chosen.

Notice that there is a trend to the fitting parameter values. However, further evaluation requires extensive analysis and will be the subject of a future work. Nonetheless, (4.6) is reasonably accurate for most biaxial magnetic bodies and is therefore sufficient for benchmarking of spin-based devices.

## 4.4 Uniaxial Delay Distribution Models

Due to the complex nature of the equation governing the behavior of the nanomagnet body, complete analytic descriptions for the delay distributions of a nanomagnet are unavailable. Previous work has suggested that the effect of thermal noise may be approximated by knowing the initial angle of the nanomagnet and neglecting the thermal noise during reversal [87]. While these models do provide significant insight into the nature of nanomagnet

reversal, numerical simulations presented in this chapter show that these analytic distributions are only accurate for rapid reversal times ($<$ 200 ps). Therefore, for the case when the nanomagnet is under the influence of spin currents comparable in magnitude to the critical spin current for reversal, new types of distribution functions to describe the magnetization dynamics must be sought. Here, we demonstrate the applicability of the Fréchet distribution that contains double exponentials to more accurately capture the evolution of magnetization over a very broad range of time scales. The Fréchet distribution is also compatible with the results obtained in [121, 122] by analytically solving the Landau-Lifshitz-Gilbert (LLG) equation with specific boundary conditions. In this section, we investigate the delay variation in uniaxial systems due to thermal noise and how it may be modeled.

For Sections 4.4–4.6, a PMA magnetic body with material parameters shown in Table 4.1 is considered.

Table 4.1: Simulation parameters of the nanomagnet

| **Parameter** | **Value** | **Units** |
|---|---|---|
| Length, $L_M$ | 100 | $nm$ |
| Width, $W_M$ | 100 | $nm$ |
| Thickness, $t_M$ | 4 | $nm$ |
| Saturation magnetization, $M_s$ | $3 \times 10^5$ [82] | $\frac{A}{m}$ |
| Uniaxial anisotropy energy density, $K_u$ | $6 \times 10^5$ [82] | $\frac{J}{m^3}$ |
| Damping coefficent, $\alpha$ | 0.01 | unitless |
| Temperature, $T$ | 300 | $Kelvin$ |
| Critical spin current, $I_c$ | 1.32 | $mA$ |
| Input spin current, $I_{op}$ | 1.50 | $mA$ |

### 4.4.1 Analytic PDF for Rapid Reversals

Assuming a large energy barrier between the two stable states of the nanomagnet, the probability distribution of the initial angle of the magnetization of the nanomagnet is given as [109]

$$P(\phi) = e^{-\xi\phi^2}, \tag{4.7a}$$

$$\xi = \frac{\mu_0 M_s V H_k}{2 k_B T}. \tag{4.7b}$$

During fast reversals, it is expected that the thermal noise has little effect on the nanomagnet during its transition. Instead, the thermal noise only sets the initial angle, which affects the reversal delay according to (4.4). Using this assumption, three different probability distribution models for nanomagnet switching were derived in [87]. The analytic cumulative distribution functions (CDFs) are given below for completeness:

$$P = \exp\left\{-4\xi\left(\frac{i-1}{2i}\right)^{2(i+1)} \exp\left[-(i-1)\frac{2\tau}{\tau_D}\right]\right\} \tag{4.8a}$$

$$P = \exp\left\{-4\xi \exp\left[-(i-1)\frac{2\tau}{\tau_D}\right]\right\} \tag{4.8b}$$

$$P = \exp\left\{-\frac{\pi^2\xi}{4} \exp\left[-(i-1)\frac{2\tau}{\tau_D}\right]\right\} \tag{4.8c}$$

(4.8a) corresponds to the derivation of the CDF through (4.4) assuming a large energy barrier. The PDFs of the delay can be found by taking the derivative of the CDFs. Note that the CDFs are denoted by "$P$" while PDFs are denoted by "$p$". Assuming $i >> 1$, (4.8a) can be further simplified to (4.8b). Finally, (4.8c) assumes both the initial and final magnetization angles are small.

Figure 4.6 compares the PDFs of (4.8a-4.8c) to numerical results. In [87], it is shown that an $i > 2$ is sufficient to accurately describe the delay variation of the nanomagnet. However, we note that these PDFs only become accurate at much larger values of $i$. This effectively means that the analytic PDFs are accurate only when the reversal time of the nanomagnet is $< 100$ ps. Under such conditions, the electrical current required would vastly exceed the maximum threshold for electro-migration of both the nanomagnet and the non-magnetic metallic channel; therefore, there will be reliability concerns that will

reduce the mean-time-to-failure of the ASL device. Other PDFs are needed to capture the magnetization dynamics accurately for reversal times on the order of several hundreds of picoseconds or nanoseconds.

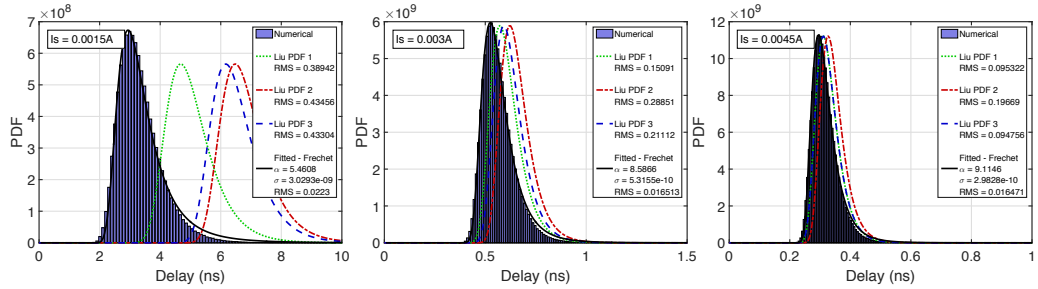


Figure 4.6: Switching delay distributions for a 100 nm $\times$ 100 nm $\times$ 4 nm, PMA-type nanomagnet with $M_s = 3 \times 10^5\ A/m$ and $K_u = 6 \times 10^5\ \frac{J}{m^3}$ under the influence of an anti-parallel longitudinal spin current with magnitude as shown in figure labels. PDFs 1, 2, and 3 correspond to equations (4.8a), (4.8b), and (4.8c) respectively. As you can see, PDFs are only accurate when the input spin current is much larger than the critical current. The Fréchet distribution is also fitted to each of the data sets and very accurately describes all three delay distributions. Each subplot has $10^6$ data points. The normalized root-mean-square (NRMS) values are calculated for each distribution against the numerical data. The maximum of the numerical PDF is used as the normalization factor of the RMS value.

### 4.4.2 Analytic PDF for Near-Threshold Reversals

The analytic solution of the LLG becomes formidable for conditions where the input spin current is comparable to the critical spin current of the nanomagnet. To obtain a PDF that best represents the nature of the delay variation of the nanomagnet, we consider the following situation. It is shown in the previous sub-section that as the spin current is increased, the PDF of the delay tends toward a double exponential function. In addition, it is known that if the spin current drops below the critical current, nanomagnet reversal occurs only when the magnetization angle of the nanomagnet becomes large enough such that the sub-critical current can overcome the reduced energy barrier of the nanomagnet [92]. This process of nanomagnet reversal, primarily through thermal activation, is known to be a single exponential function. Therefore, we seek a PDF solution to describe the nanomagnet reversal that can be seamlessly adjusted from a single- to a double-exponential function depend-

ing on the value of $i$. The Fréchet distribution that meets the above criteria. The Fréchet distribution is mathematically given as

$$p = \frac{\alpha}{s}\left(\frac{\tau}{s}\right)^{-1-\alpha} e^{\left(-\frac{\tau}{s}\right)^{-\alpha}}, \tag{4.9}$$

where $s$ is the scale parameter, $\alpha$ is the shape parameter, and $\tau$ is the delay of the nanomagnet. $\alpha$ and $s$ are treated as fitting parameters [123, 124]. To prove the suitability of the Fréchet distribution, Figure 4.6 shows the best fits of the Fréchet distribution to the delay curves of a nanomagnet driven by various spin currents [125]. The figure clearly shows improved accuracy of the Fréchet distribution to capture the numerical simulation data and the applicability of the Fréchet distribution to nanomagnet delay under various reversal regions. Figure 4.6 demonstrates that the $\alpha$ parameter increases greatly if $i >> 1$. Since a smaller $\alpha$ suggests a larger left lean, this suggests that reversal distributions for nanomagnets under large spin currents have less left lean.

For the remainder of this chapter, the delay of a nanomagnet under the influence of a specific critical field will be represented by a Fréchet distribution that has been fitted to numerical data.

### 4.4.3 Relationship to Error-Rate

Because the delay has been shown to be a random variable, the probability that the nanomagnet delay will exceed some time $t$ will always be nonzero. When designing circuits, this probability can be referred to as the nanomagnets error rate ($er$). Using the Fréchet distribution (4.9) it is possible to derive $t$ as a function of $er$. Mathematically, this relationship is given as

$$t = \frac{s}{\sqrt[\alpha]{-\ln\left[1-er\right]}}, \tag{4.10}$$

where $\alpha$ and $s$ are defined previously in (4.9).

## 4.5 Combination of Reversal Delay Distributions

There is a two-fold complexity associated with spintronic circuit design due to the stochastic nanomagnet behavior as discussed in our prior work [54]. First, the circuit delay exhibits large variability that can increase the effective-delay of the circuit depending on the desired error tolerance. Second, for interconnected logic networks, the delay distributions of individual nanomagnets combine non-linearly increasing the circuit delay complexity significantly [73, 126].

In any complex circuit, devices can be arranged in two ways. They can be operated in parallel, where their outputs arrive at the same time. Alternatively, devices can be cascaded in series, where the output of one is fed into the input of of another.

### 4.5.1 Devices in Parallel

For the case of a circuit with multiple devices in parallel, the output delay (denoted by random variable $Y$) of the circuit is the maximum of the output delay of the devices given as

$$Y = \max\left\{X_1, X_2, X_3, ...X_n\right\}. \tag{4.11}$$

where $X_i$ is a random variable representing the delay of a single nanomagnet. Hence, the CDF of the parallel device circuit becomes

$$P\left(Y \leq x\right) = P\left(X_1 \leq x, ..., X_n \leq x\right) = \prod_{i=1}^{n} P(X_i \leq x) = \left(P\left(x\right)\right)^n, \tag{4.12}$$

where $P$ corresponds to the CDF of the particular device. Knowing this, the PDF of a circuit with multiple devices in parallel can be found using (4.12) and (4.9) and is plotted in Figure 4.7. Assuming a Fréchet distribution, the PDF of multiple nanomagnets in parallel is given analytically as

$$p = n\frac{\alpha}{s}\left(\frac{x}{s}\right)^{-1-\alpha} e^{n\left(-\frac{x}{s}\right)^{-\alpha}}, \tag{4.13}$$

where $n$ is the number of devices in parallel.

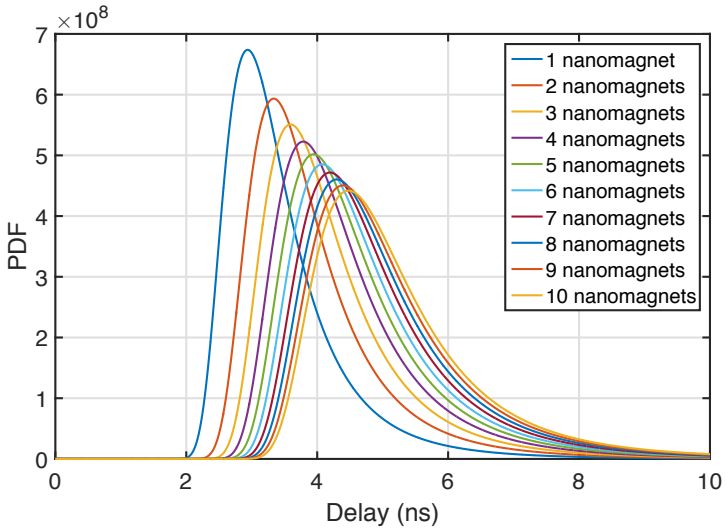


Figure 4.7: Reversal delay of a circuit composed of multiple nanomagnets arrange in parallel. A 100 nm $\times$ 100 nm $\times$ 4 nm, PMA-type nanomagnet with $M_s = 3 \times 10^5\ A/m$ and $K_u = 6 \times 10^5\ \frac{J}{m^3}$ and is under the influence of a $1.5\text{mA}$ anti-parallel spin current. The PDF of a single nanomagnet is estimated by fitting a Fréchet distribution to numerical data. Multi-nanomagnet results are calculated numerically.

### 4.5.2 Devices in Series

For the case of devices connected in series, the output delay (Y) of the circuit is the addition of the device delays connected in series and is given as

$$Y = X_1 + X_2. \tag{4.14}$$

The PDF of Y is given as

$$p_Y(y) = \int_0^y p_{X_2}(y - x)\, p_{X_1}(x)\, dx \tag{4.15}$$

Figure 4.8 shows the PDFs of multiple nanomagnet devices arranged in series. This situation corresponds to a repeater-chain circuit. As the number of devices increases, the distribution of the delay gets more symmetrical and normal, following the central limit

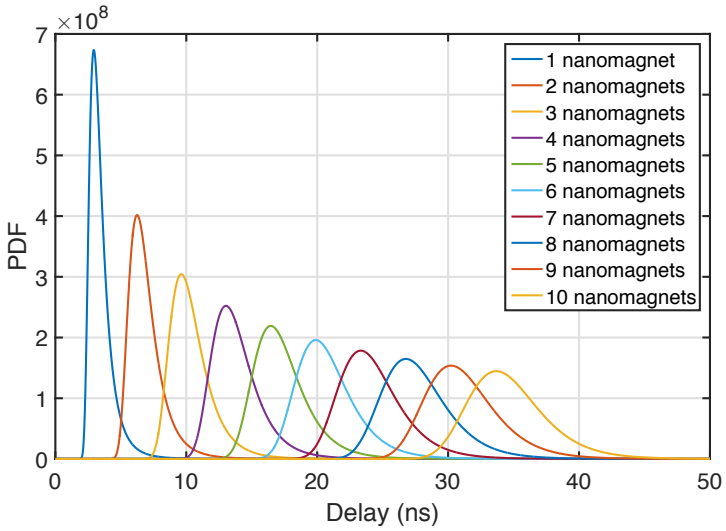


Figure 4.8: Reversal delay of a circuit composed of multiple nanomagnets arrange in series. A 100 nm $\times$ 100 nm $\times$ 4 nm, PMA-type nanomagnet with $M_s$ = $3 \times 10^5$ $A/m$ and $K_u$ = $6 \times 10^5$ $\frac{J}{m^3}$ and is under the influence of a $1.5mA$ anti-parallel spin current. The PDF of a single nanomagnet is estimated by fitting a Fréchet distribution to numerical data. Multi-nanomagnet results are calculated numerically.

theorem [127].

### 4.5.3 Comparison of Device Arrangements

Often when developing spin-based circuits, it is possible to achieve similar functionalities using many devices driven in parallel, or many devices cascaded off each other. A prime example of this is the many variations of VLSI adder designs. Since devices arranged in parallel increase the nanomagnet variation, it can be argued that highly parallel circuits may have longer delays than serialized circuits given a particular $er$. However, Figure 4.9 demonstrates that this is not the case. While the number of devices in parallel does increase the circuit delay, this increase is still dwarfed by the increase in average delay caused by arranging the nanomagnet in series.

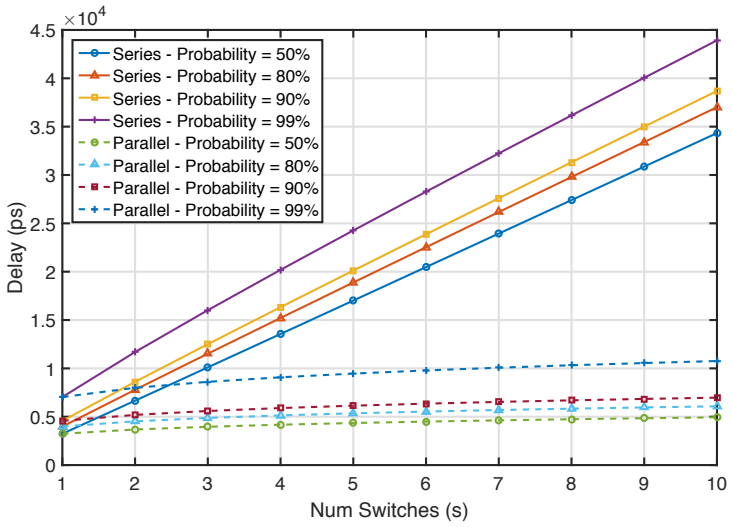


Figure 4.9: The reversal delay of a circuit comprising multiple nanomagnets arranged in series and parallel versus the number of switches. While arranging devices in parallel slightly increases delay of the circuit, this increase is minimal compared to the average delay of the nanomagnet. Multiple error rates are considered.

## 4.6 All-spin Logic Analysis

The previous sections introduced the key concepts required to analyze the delay variation of a complex logic circuit. It would be useful to analyze the effectiveness of thermal variation to a device technology which solely depends on STT. As discussed in Section 1.1.3, all-spin logic (ASL) achieves Boolean logic functionality by summing the inputs delivering the STT to the output free-magnet as can be seen in the inset of Figure 4.10. For this section, a four-input ASL-AND circuit is designed and analyzed. We use the PDF of the nanomagnet delay to analyze the performance of an ASL-AND gate. Due to the summing nature of ASL, the magnitude of the spin current delivered to the output nanomagnet will vary depending on the input values and will alter the delay distributions of the output nanomagnets. An example of a four-input AND (AND4) gate is shown in the inset of Figure 4.10. As mentioned earlier, the summing nature of the inputs in ASL logic naturally creates a majority logic. To create an AND gate from this majority logic, the input of the logic nanomagnet must be weighted such that the input to the nanomagnet is only

positive when all the inputs are positive. In the case of the ASL-AND circuit shown, a fixed magnet generating a constant $-3 \times I_s$ is added such that the output nanomagnet will only receive a $+\hat{z}$-orientated spin current if all the nanomagnet are oriented along $+\hat{z}$. The polarity of this bias can be changed to switch between AND and OR logic. It is assumed that the input nanomagnets have been reversed at time $\tau = 0$ and the voltage supplies at these nanomagnets are turned on at this time [128].

### 4.6.1 Effect of Input Pattern on Nanomagnet Delay

An important aspect of current-based computation is the fact that the input current to the OUT nanomagnet will not be constant. In fact, depending on the logical combination of the input devices, the current being fed into the OUT nanomagnet will vary as shown in Table 4.2. Assuming the inputs of the nanomagnet are equi-probable, the likelihood that the OUT nanomagnet is reversed by a spin current of a particular magnitude is given by Table 4.3. The probabilities of each of these magnitudes follows an ordering, which can be described by Pascal's Triangle.

### 4.6.2 ASL-AND Delay-PDF

At worst, the nanomagnet will be driven by a current magnitude $= I_s$. This corresponds to the case where all the inputs, except one, are oriented along the $+\hat{z}$ direction, and only one of the input nanomagnets is oriented along the $-\hat{z}$ direction. This worst-case scenario is shown in Figure 4.10. However, depending on the input pattern, the driving spin current to OUT is likely larger than $I_s$. For larger spin current magnitudes, the nanomagnet is expected to reverse over much shorter timescales. By calculating the PDFs of nanomagnet reversal at each of the different spin current magnitudes (by fitting the Fréchet distribution to numerical results), the PDFs can be combined to find the input-aware PDF of the circuit delay as shown in Figure 4.10.

This new input-aware PDF has several peaks corresponding to each of the possible spin

current magnitudes during the operation of the circuit. As the number of inputs increases, the number of peaks will also increase, but the area under each of the peaks will decrease since the area of the entire PDF must remain equal to unity. Assuming a very small error-rate, one is mainly concerned with the right-most peak that is associated with nanomagnet reversal under the minimum operating current. This suggests that for a given delay, the circuit reliability is improved as the number of inputs increases. In other words, as the circuit becomes more complex, it tends to operate more reliably given a certain delay [111].

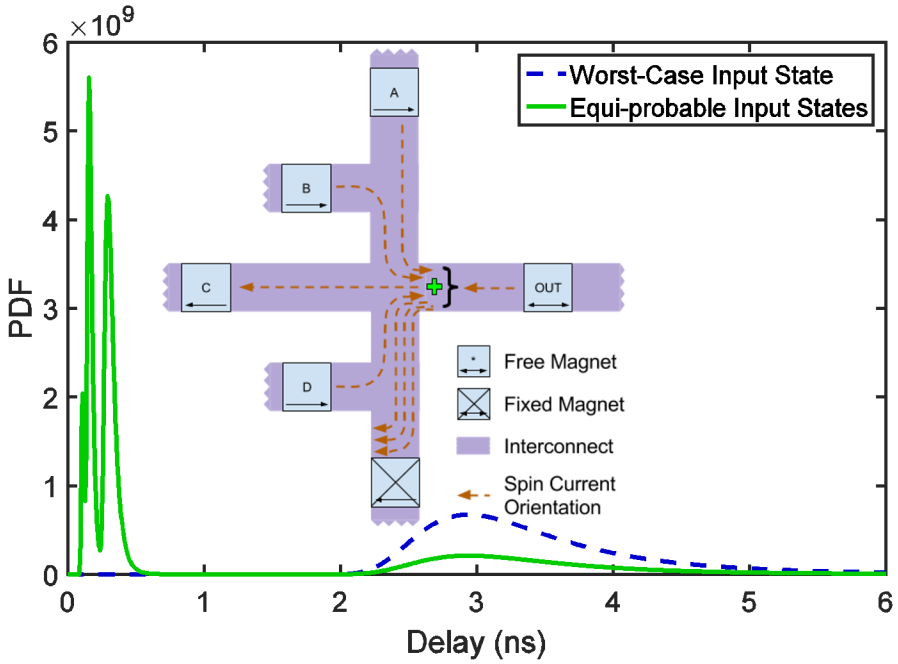


Figure 4.10: PDFs of parallelized AND4 circuit assuming several different types of delay analyses. Baseline PDF simply considers the delay of the AND-gate assuming worst-case input conditions (OUT nanomagnet being driven by $I_s$. Input-probability aware distribution analyzes the OUT nanomagnet reversal considering the variable input spin current magnitudes considering different input combination. Inset: Schematic of parallelized ASL AND4 gate. Blue square represent thin-film nanomagnets while purple bars represent channels. Orange arrows represent spin orientation. Assuming PMA nanomagnets with material parameters shown in Table 4.1.

Table 4.2: Demonstrates the variation of the input spin current to the OUT nanomagnet depending on the input logical combination. Spin current magnitude is normalized against minimum reversal current shown in Table 4.1.

| Inputs | | | | | Outputs |
|---|---|---|---|---|---|
| A | B | C | D | Total Input Current | OUT |
| 0 | 0 | 0 | 0 | -7 | 0 |
| 0 | 0 | 0 | 1 | -5 | 0 |
| 0 | 0 | 1 | 0 | -5 | 0 |
| 0 | 0 | 1 | 1 | -3 | 0 |
| 0 | 1 | 0 | 0 | -5 | 0 |
| 0 | 1 | 0 | 1 | -3 | 0 |
| 0 | 1 | 1 | 0 | -3 | 0 |
| 0 | 1 | 1 | 1 | -1 | 0 |
| 1 | 0 | 0 | 0 | -5 | 0 |
| 1 | 0 | 0 | 1 | -3 | 0 |
| 1 | 0 | 1 | 0 | -3 | 0 |
| 1 | 0 | 1 | 1 | -1 | 0 |
| 1 | 1 | 0 | 0 | -3 | 0 |
| 1 | 1 | 0 | 1 | -1 | 0 |
| 1 | 1 | 1 | 0 | -1 | 0 |
| 1 | 1 | 1 | 1 | +1 | 1 |

Table 4.3: Assuming all logical input combinations are equally possible, table demonstrates the probability that a nanomagnet is reversed with a particular spin current magnitude. Spin current magnitude is normalized against minimum reversal current.

| Current Magnitude | Probability |
|---|---|
| +1 | $\frac{1}{16}$ |
| -1 | $\frac{4}{16}$ |
| -3 | $\frac{6}{16}$ |
| -5 | $\frac{4}{16}$ |
| -7 | $\frac{1}{16}$ |

# CHAPTER 5

# DAMPED MAGNETIZATION REVERSAL THROUGH A SUB-CRITICAL FIELD

The most crucial component of the Spin-Switch is the communication between the input and output magnetic bodies performed through dipolar interaction. A large portion of this research is dedicated to the characterization of dipolar interaction between magnetic bodies. As a starting point, this chapter is dedicated to the investigation of reversal mechanics of a *single*, biaxial magnetic body under the influence of a constant longitudinal field. This analysis will reveal some critical characteristics of field-induced reversal and is crucial for the comprehension of the complex time-variant dipolar case present in the following three chapters.

## 5.1 Above-Critical Damping Reversal

First we consider a constant longitudinal field oriented along the free-axis anti-parallel to the magnetization state. Assuming the external field is large enough, the magnetization will be forced away from its initial state toward the parallel position. This section investigates the magnitude requirements for such a reversal as well as the delay of a damped reversal.

### 5.1.1 Critical Field Expression

To find the critical field requirement for a damped reversal, it is sufficient the analyze only one dimension ($\theta$) of energy landscape of the magnetic body. Setting $\phi = \frac{\pi}{2}$, the total energy density of nanomagnet under the influence of an external magnetic field can be written as

$$E(\theta) = K_{\parallel} - \mu_0 M_s \vec{H}_X \cdot \hat{m}, \tag{5.1}$$

Setting $\frac{\partial E}{\partial \theta} = 0$ ensures that $\theta$ is a pole of the magnetic body. It is also known that the critical field value occurs when $\frac{\partial^2 E}{\partial \theta^2} = 0$ marking the point at which the pole at $\theta$ goes from a stable to unstable as shown in Figure 5.1. Solving for $H_X$, the critical field becomes

$$H_{crit} = \frac{2K_{\parallel}}{\mu_0 M_s}. \tag{5.2}$$

In order to switch a magnet resting along its easy-axis ($\theta = 0, \phi = \frac{\pi}{2}$) with an external field also aligned along $\hat{x}$, the required critical field will be

$$H_{crit} = \frac{2K_{\parallel}}{\mu_0 M_s}. \tag{5.3}$$

### 5.1.2 Analytic Expression for Delay

The analytic delay expression for the switching delay of a nanomagnet considering only uniaxial anisotropy and being driven through an external field can be written as [129, 130]:

$$\tau \approx \frac{\ln \frac{\sqrt{2}}{\theta_0}}{\alpha\gamma \left(H_{EXT} - H_{crit}\right)}. \tag{5.4}$$

This equation follows the asymptotic relationship observed in several experiments [131, 132, 133]. However, because an in-plane nanomagnet with a demagnetization field oriented perpendicular to the free-axis is being assumed, a delay expression which includes a fitting term is necessary and given as [134]

$$\tau \approx \frac{S}{\left(H_{EXT} - H_{crit}\right)}, \tag{5.5}$$

where $S$ is a fitting parameter. This expression is verified with our numerical simulations as shown in Figure 5.2.

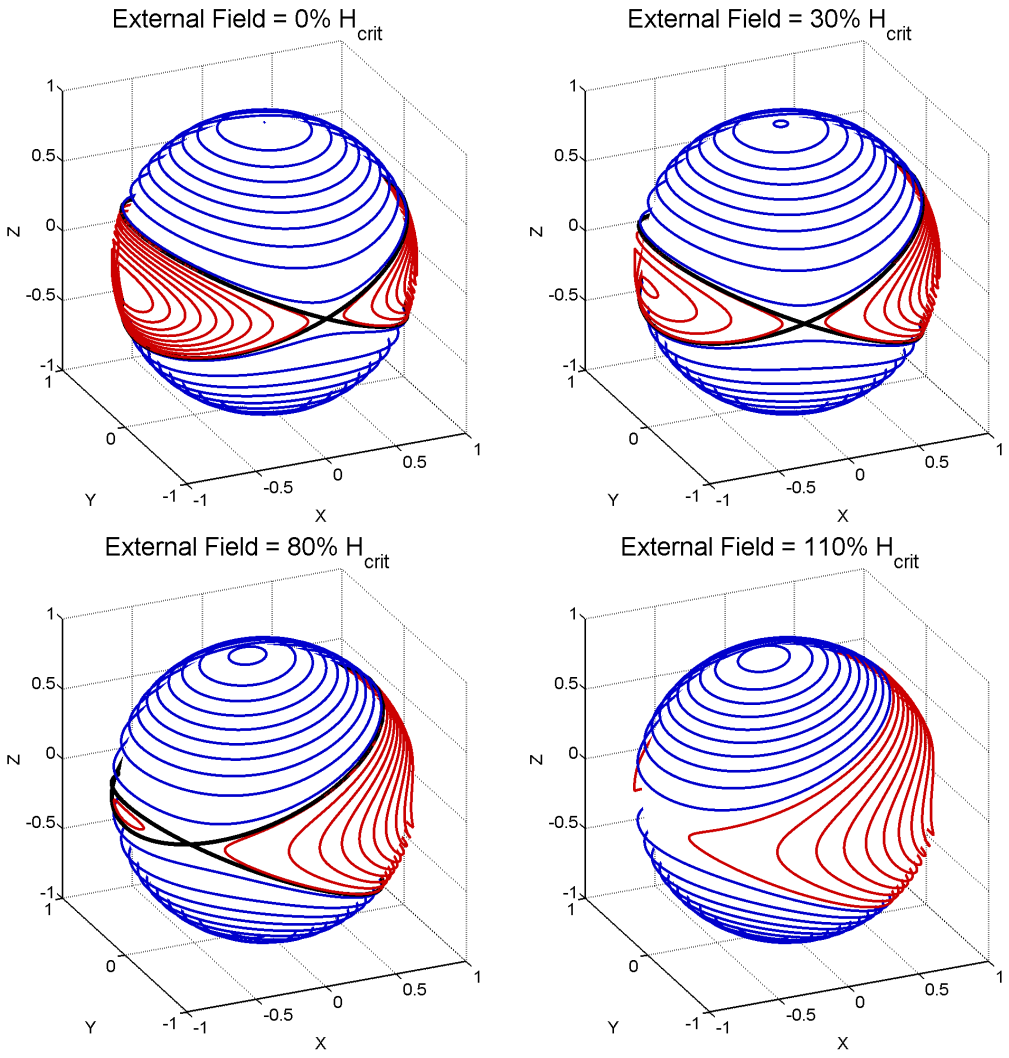


Figure 5.1: Subplots show precessional trajectories of a $60nm \times 45nm \times 2nm$ nanomagnet with a $K_u = 10^5 \frac{A}{m}$ and $M_s = 10^6 \frac{A}{m}$ under the influence of various magnitudes of constant longitudinal external fields. These plots demonstrate that as the external field is increased, one of the basins becomes more "weighted" over the other until $H_{crit}$ is exceeded in which case only one energy basin exists.

## 5.2 Sub-critical Longitudinal Field Relaxation

When the magnetic body is under the influence of an above-critical longitudinal field, the magnetization will reliably reverse given enough time. However, if the magnitude of the external field does not exceed this critical value, the situation is more complex. To escape this critical-excitation limitation, engineers have proposed new types of spintronic devices where the magnetization is initially forced into a high-energy state through the use of mag-

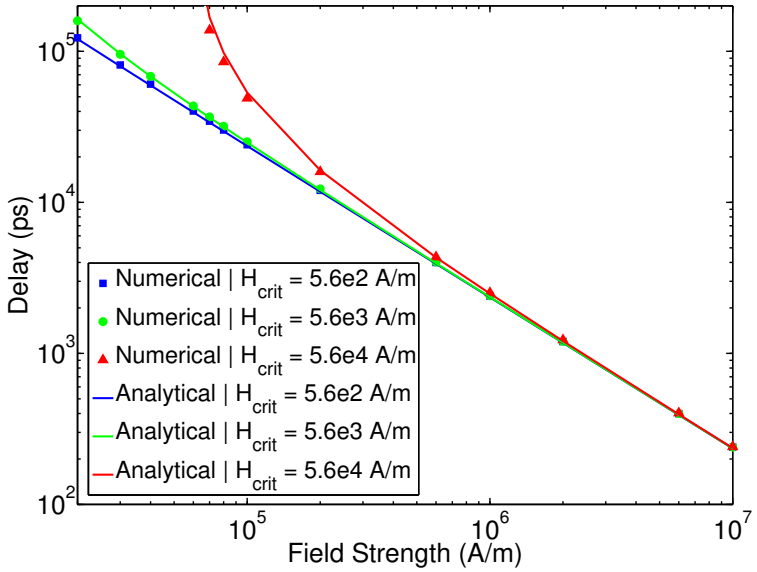


Figure 5.2: Delay of switching a magnet through an external field. Markers denotes point obtained from numerical simulations. Curves are obtained using analytic expression with $S = 2.34 \times 10^9$. Material and geometric parameters are adjusted such that critical field values shown in legend are achieved.

netostriction [135, 136]. After the nanomagnet is initialized to this state, it is then released under the influence of a sub-critical excitation and relaxes to what several engineers have argued is the correct, reversed state [27].

However, nanomagnet relaxation under the influence of sub-critical field is far from deterministic [137]. Even a magnet at rest along one of its poles has a non-zero probability of reversal due to thermal noise [109]. It follows then, that a nanomagnet reversing from a high energy state to a low energy state would have a non-zero probability of relaxing to any of the energy basins.

A sub-critical longitudinal field effectively "weights" one energy basin over the other. But while a sub-critical excitation can make it more probable that the nanomagnet will relax to one energy basin over the other, unless this excitation exceeds a critical value, there is still some non-zero probability that the nanomagnet will relax to either energy basin [138, 139, 140]. This section investigates the probability that a nanomagnet will correctly relax to a position parallel to a sub-critical critical excitation. These results can be used in analyzing

the reliability of various proposed spintronic devices such as Nanomagnetic Logic (NML) and Spin-Wave-Buses [141, 142]. Nanomagnet relaxations from the out-of-plane axis and hard axis are considered and analyzed.

### 5.2.1 Out-of-plane Initialization

Firstly, reversal from the out-of-plane ($\hat{z}$) axis is considered. Such a relaxation can be applied to certain proposed strain-induced logic devices [143]. In this situation, the nanomagnet is initialized into the high-energy region ($\Omega_{H+/-}$). While the nanomagnet is in $\Omega_{H+/-}$ it will precess around and fall away from the $\hat{z}$ axis. Eventually, the nanomagnet dissipates enough energy and falls into one of the energy basins. Figure 5.3 demonstrates sample relaxation trajectories under the influence of a sub-critical external field.

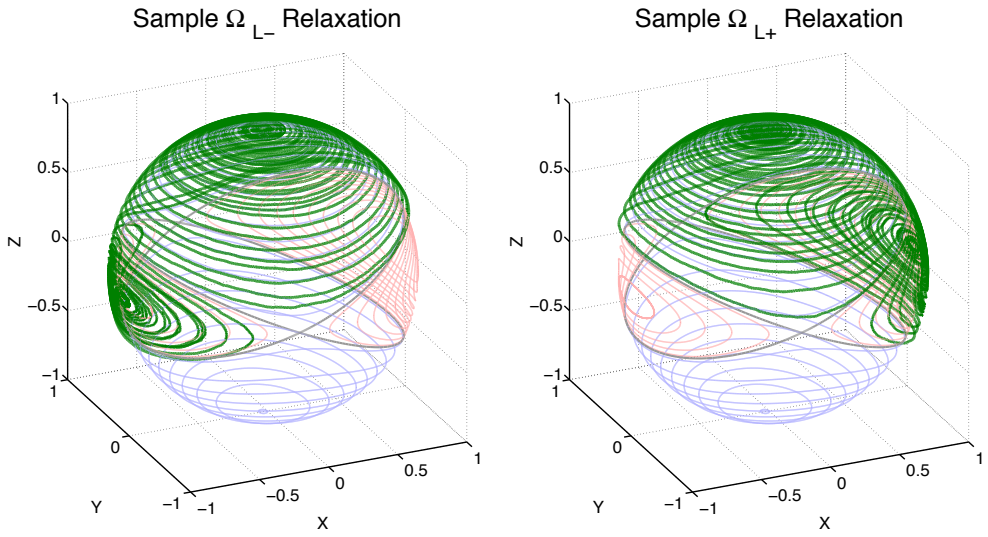


Figure 5.3: Subplots shows sample relaxations of a $60nm \times 45nm \times 2nm$ nanomagnet with a $K_u = 10^5 \frac{A}{m}$ and $M_s = 10^6 \frac{A}{m}$ under the influence of a longitudinal field with a magnitude of $20\%$ of $H_{crit}$. Thermal noise is included. The light-colored lines show the precessional trajectories of the nanomagnet under the influence of this field. These plots demonstrate that while the external field can bias the nanomagnet to relax towards one pole over another, it is still possible for the magnetization to fall in either basin.

*Analytic Expression for Relaxation Probability*

Figure 5.1 shows the precessional trajectories of the nanomagnet assuming no damping component ($\alpha = 0$). A non-zero damping simply forces the nanomagnet drop between trajectories and towards a pole. The damping component is proportional to effective field of the nanomagnet. In Figure 5.1, consider the precessional trajectory ($t_i$) just above the separatrix. As the nanomagnet precesses about $t_i$ it feels the damping torque pushing it towards the energy basins. Under a sub-critical field, $t_i$ becomes asymmetric with respect to $\hat{x}$. Therefore, the damping force along $t_i$ also becomes asymmetric with respect to $\hat{x}$; hence, the damping while the magnetization is above $\Omega_{L+}$ is different than when it is above $\Omega_{L-}$. Thus, assuming a longitudinal field, the probability the nanomagnet will settle into $\Omega_{L+}$ is different than the probability it will settle in $\Omega_{L-}$.

This observation is made by Serpico et al. in [138]. Assuming a random initial magnetization in $\Omega_{H+}$, the probability that a nanomagnet will relax to a parallel energy basin is proportional to the comparison of energy dissipated in each energy basin at the separation energy. The energy change of a nanomagnet over one precessional cycle can be found using Melnikov functions ($M_k(g)$). The probability can then be estimated to be:

$$P_{L+} = \frac{M_{L+}(g_d)}{M_{L+}(g_d) + M_{L-}(g_d)}, \tag{5.6}$$

where $g_d$ denotes the separation energy. More information on the derivation of this equation can be found in [138]. It should be noted that under most common physical parameters, this probability curve changes very little as shown in the inset plots of Figure 5.4.

*Thermal Noise Treatment*

One thing to note is that the expression shown previously has been derived using the assumption that the initial magnetization is a random variable and there is no thermal noise. However consider the following: ignoring the effect of thermal noise, it can be argued

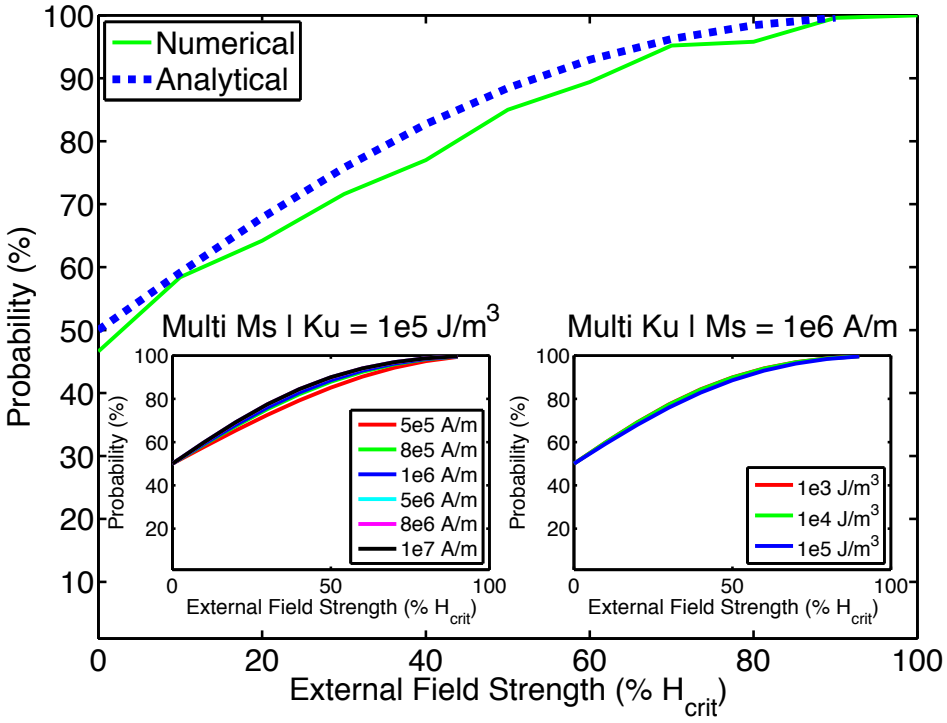


Figure 5.4: Shows the probability that the magnetization will relax to the positive energy basin. Results are shown using both numerical and analytic methods. Demonstrates analytic expression is valid for relaxations under the influence of thermal noise. Numerical results obtained using Monte-Carlo simulation of 1000 runs. Inset plots show probability curve for different $M_s$ and $K_u$ values. Hence, regardless of the material properties of the nanomagnet, the probability curves remain rather consistent.

that there is a set of relaxation paths which begin in the high energy region, and end in a particular energy basin. Because of thermal noise, regardless of the initial angle of the system, while the magnetization precesses around $\Omega_{H+}$, it will also jump between the paths and may land in either energy basin. The thermal noise effectively randomizes the trajectory the magnetization follows. These numerical tests have shown that the randomization, caused by the thermal noise, is equivalent to the initial angle approximation assumed in [138]; the expression obtained is a reasonable approximation for determining what pole the nanomagnet will relax towards as shown in Figure 5.4.

### 5.2.2 Hard-Axis Initialization

Another method strain-based devices use is initializing the nanomagnet along the hard-axis [135]. Unlike in the previous relaxation case, in the case of a hard-axis initialization, the nanomagnet will be initialized inside $\Omega_{L+}$. Hence, assuming no thermal noise, the nanomagnet will certainly relax to the $+\hat{x}$ pole. However with thermal noise, even though the magnetization might begin in $\Omega_{L+}$, the noise may knock the magnetization into $\Omega_{H-}$ where it can precess around $\hat{z}$ and into $\Omega_{L-}$. The two possible relaxation cases for a hard-axis initialization are shown in Figure 5.5. Where the magnetization relaxes depends greatly on whether or not the thermal noise is able to knock the magnetization across the barrier between the high and low energy regions (separatrix).

*Relaxation Probability*

Because nanomagnet is initialized in $\Omega_{L+}$, the nanomagnet much more reliably settles to the $+\hat{x}$ using smaller longitudinal excitations. The relaxation probability can be observed using a Monte-Carlo numerical analysis as shown in Figure 5.6. Comparing Figure 5.3 and Figure 5.5, it is clear that initializing the nanomagnet along the hard axis is much more reliable.

Unfortunately, no analytic model is currently available to determine the reliability of the hard-axis initialization relaxation. However, there are a few insights which can be obtained from the results. As mentioned above, the reliability of the y-initialization is dependent on the ability for the thermal noise to knock the magnetization across the separatrix and into the high-energy regions.

The nanomagnet can be evaluated in terms of energy. The separatrix exists at a certain energy and assuming a longitudinal field, the hard-axis also has an associated energy. The energy difference between the separatrix and hard-axis energies is evaluated in the inset plot of Figure 5.6. This energy gap is dependent on the magnitude of the external field and as it grows the thermal noise becomes less likely to add an energy greater than this gap to

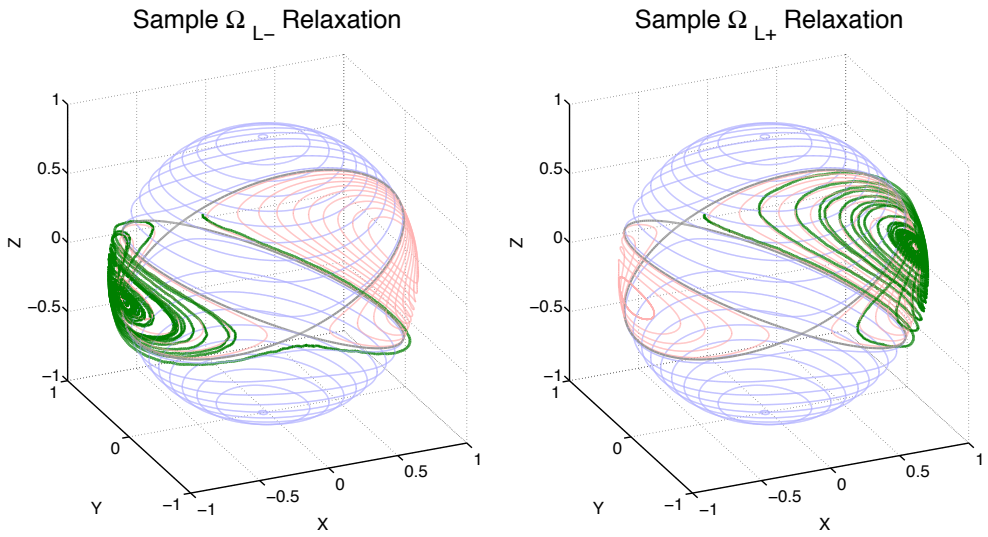


Figure 5.5: Subplots shows sample relaxation of a $60nm \times 45nm \times 2nm$ nanomagnet with a $K_u = 10^5 \frac{A}{m}$ and $M_s = 10^6 \frac{A}{m}$ under the influence of a longitudinal field with a magnitude of $20\%$ of $H_{crit}$ and an hard-axis initialization. Thermal noise is included. The light-colored lines show the precessional trajectories of the nanomagnet under the influence of this field. These plots demonstrate that while the magnetization starts in one energy basin, the thermal noise may knock the magnetization into a high energy region and allow it to precess and relax in the anti-parallel basin.

the nanomagnet.

Figure 5.5 also demonstrates that if able, the thermal noise will typically coax the nanomagnet into $\Omega_{H-}$ within the nanomagnet's first half precession in $\Omega_{L+}$. This is because given time, the damping factor will increase the energy gap between the nanomagnet and separatrix and hence, it is most probable that the thermal noise will knock the magnetization into $\Omega_{L+}$ very quickly, or not at all.

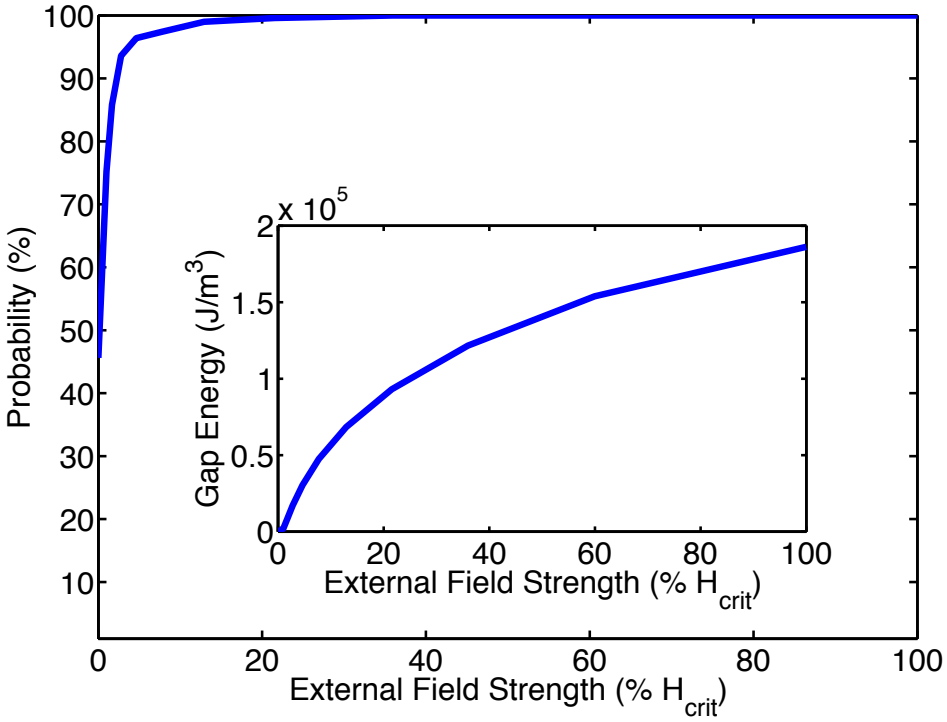


Figure 5.6: Shows the probability that the magnetization will relax to the parallel energy basin assuming a hard-axis initialization. Numerical results obtained using Monte-Carlo simulation of 1000 runs. Inset plot shows the difference in energy between the separatrix and initial $\hat{y}$ position for a given longitudinal field.

# CHAPTER 6

# DIPOLAR COUPLING I: QUALITATIVE ANALYSIS OF TWO-MAGNET SYSTEM

We now begin the bulk of the research in this thesis which is the characterization of nanomagnet reversal dipolar field interactions with neighboring magnetic bodies. The dipolar field-based switching of nanomagnets benefits from low energy dissipation when compared with STT-based nanomagnet switching [144]. In addition, transferring bit-information between nanomagnets through dipolar interaction is an effective way to provide input-output isolation in certain proposed logic devices [4]. Furthermore, this method of input-output isolation is an improvement over other methods such as straintronics which require precise clocking and may not be feasible in the presence of thermal noise [135, 38, 137]. Two magnet systems have also been used to create other spintronic devices such as oscillators [145].

Simple models for magnet reversal through an external magnetic field have been extensively studied in literature [44, 80, 146, 147, 148, 149, 150, 151]. External fields are commonly categorized into two categories: (a) a longitudinal field pulse which we studied in Chapter 5 and (b) a perpendicular external field where the external field is oriented perpendicularly to the free-axis of the nanomagnet [130]. These two applications of external field yield very different magnetization reversal behaviors [152].

As shown in Chapter 5, reversal through the application of a longitudinal field is very slow [129]. Since the dynamics in this switching are mainly governed by the damping parameter, this type of reversal is referred to as damping switching [3]. On the other hand, applying a perpendicular field imposes a very large field torque on the resting position of the nanomagnet. This large torque encourages a large and rapid shift in the magnetization of the nanomagnet [153, 154]. This shift in magnetization depends mostly on the preces-

sional component of the Landau-Lifshitz-Gilbert (LLG) equation; hence, magnet reversal in this manner is referred to as precessional switching [134, 155, 156]. Depending on the orientation of the external field with respect to the free-axis of the nanomagnet, the critical field strength and switching delay can vary greatly. In addition, because precessional switching happens on such a fast time-scale, it needs to be precisely clocked [157].

The dipolar field generated by a nanomagnet can be considered to be a mixture of both longitudinal and perpendicular field components. As the orientation of a nanomagnet changes, its dipolar field may also change in both magnitude and direction. There are a few examples in literature of nanomagnet dynamics under the influence time-variant external fields [158, 159, 160]. Most of these works have focused on time-harmonic excitations which allow for the use of chaos theory and Poincare-Index-theorem to analyze phase portraits of the magnetization dynamics [161, 162]. However, a time- and strength-variant excitation like the dipolar field considered here has never been substantially analyzed. This chapter is the first of three where we dissect the properties of reversal through dipolar interaction. In this chapter we simply conduct exhaustive numerical tests to provide qualitative insights into the nature of the coupled nanomagnets.

## 6.1 Simulation Parameters

To accurately model and capture the dipolar-coupling-induced magnet switching, the test bench shown in Figure 6.1 is considered. While this test-bench considers only two interacting magnets, it is nonetheless sufficient to capture most physical details of the dipolar-coupling.

### 6.1.1 Test Bench

Consider a system of two nanomagnets, which are stacked along the $\hat{z}$ direction as seen in Figure 6.1. Assume Magnet 1 (M1) is being driven by a another effect such as spin-transfer-torque (STT), which changes the orientation of M1. Magnet 2 (M2) needs to be

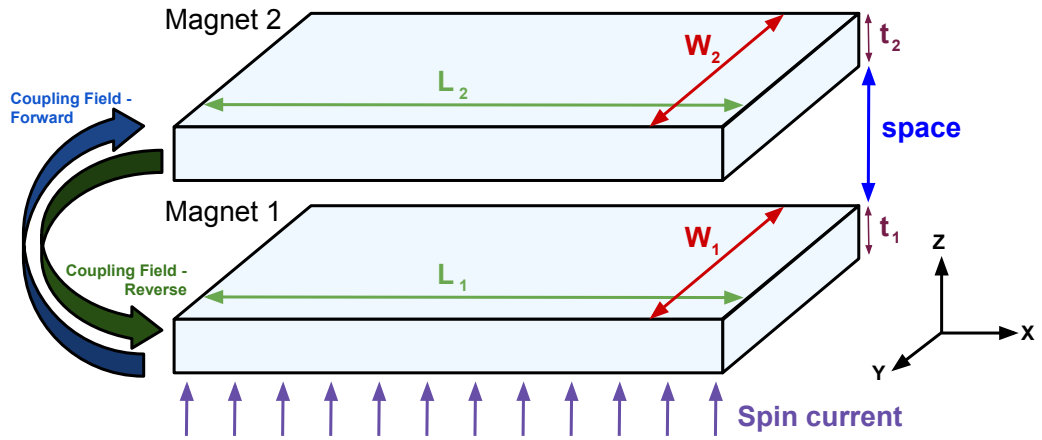


Figure 6.1: Test setup for a two-magnet system. Magnet 1 is driven through STT. Magnet 2 is driven through dipolar coupling field generated by Magnet 1. The SFM and DTM models consider only the coupling field generated by Magnet 1. The 2WDTM model considers the coupling field felt by both nanomagnets. Reversal through STT is typically stronger than reversal through an external field and thus, the precession of Magnet 1 is considered to be the "input" of the system.

reversed through the dipolar field of M1. Assuming the magnetization of M1 is at rest, M2 would mainly feel a constant longitudinal external field and switch through a damping reversal.

Next consider M1 and M2 oriented anti-parallel, and the spin-current into M1 causes a reversal in M1. It is known that the dipolar field is oriented along the same direction as the magnetization of M1 and, hence, during the reversal of M1, the dipolar field will behave as a time-variant external field on M2, which at a given instant can impose a mixture of longitudinal and perpendicular fields onto M2. Please note that a complex demagnetization field model (CHd) is used in this chapter. Because this is a qualitative description, the complexity introduced by the CHd model is minimal. In Chapters 7 and 8, other demagnetization field models are used, revealing the nuances of the dipolar interaction.

### 6.1.2 Dipolar Field Calculation

The magnetic field generated by a rectangular nanomagnet is given by (6.1-6.3) [163]. In Figure 6.2, it is seen that the strength of the magnetic field along the $\hat{x} - \hat{y}$ plane above M1

$$H_{XX}(x,y,z) = \frac{M_0}{4\pi}\sum_{k,l,m=1}^{2}(-1)^{k+l+m}\frac{\left[x+(-1)^k x_b\right]\left[y+(-1)^l y_b\right]}{\left|x+(-1)^k x_b\right|\left|y+(-1)^l y_b\right|} \times \arctan\left(\frac{\left|y+(-1)^l y_b\right|\cdot[z+(-1)^m z_b]}{\left|x+(-1)^k x_b\right|\cdot\sqrt{\left[x+(-1)^k x_b\right]^2+\left[y+(-1)^l y_b\right]^2+[z+(-1)^m z_b]^2}}\right) \quad (6.1)$$

$$H_{XY}(x,y,z) = \frac{M_0}{4\pi}\sum_{k,l,m=1}^{2}(-1)^{k+l+m}\ln\left(z+(-1)^m z_b+\sqrt{\left[x+(-1)^k x_b\right]^2+\left[y+(-1)^l y_b\right]^2+[z+(-1)^m z_b]^2}\right) \quad (6.2)$$

$$H_{XZ}(x,y,z) = \frac{M_0}{4\pi}\sum_{k,l,m=1}^{2}(-1)^{k+l+m}\ln\left(y+(-1)^l y_b+\sqrt{\left[x+(-1)^k x_b\right]^2+\left[y+(-1)^l y_b\right]^2+[z+(-1)^m z_b]^2}\right) \quad (6.3)$$

---

is non-uniform (as also noted in the governing equations). This implies that the offset in the $\hat{x}$ and $\hat{y}$ directions can be just as important as the $\hat{z}$ displacement of the nanomagnets. Interestingly, the shape of the curve of the coupling field strength changes as the distance between the two nanomagnets is increased. When the separation between the magnets is small, the coupling field is the strongest above the two poles of M1, but the location of the maximum coupling field moves to the center as the separation between the magnets increases.

In this chapter, two identically sized magnets which are centered along $\hat{z}$ are assumed. Because single-domain magnets are assumed, the strength of each component of the magnetic field is averaged over the entirety of the volume of M2. This method is very similar to numerically solving for the magnetization tensor presented in [164, 165]. $H_y$ and $H_z$ field components are reduced to zero assuming an $\hat{x}$ easy axis simplifying the analysis.

Equations (6.1-6.3) are derived under the assumption that the magnetization vector of a thin-film nanomagnet is aligned along $\hat{x}$. When the orientation of the driving magnet reverses, it exhibits a coupling field in the same direction as its precession. The coupling field felt by M2 precesses according to M1. At any given instant during the reversal of M1, the dipolar field can have both perpendicular and parallel field components. In order to account for the complexity of switching a nanomagnet by a coupling field, a tensor model is used to represent the strength of the dipolar field [166, 167]. Mathematically, external

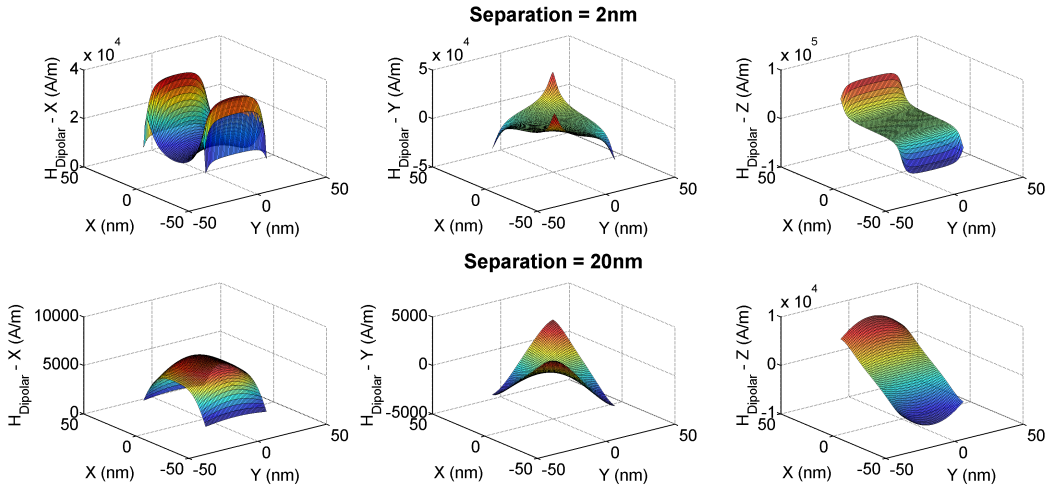


Figure 6.2: The magnitudes of the $\hat{x}$, $\hat{y}$, and $\hat{z}$ components of the dipolar field affecting the top magnet in the $\hat{x} - \hat{y}$ plane (averaged along $\hat{z}$). $\hat{z}$-centered 60 nm $\times$ 45 nm $\times$ 2 nm magnets are assumed with a separation of 2 nm and 20 nm. The separations between the magnets changes the shape of the dipolar field strength felt by the top magnet. Since only small, single-domain magnets are considered in this research, the strength of the dipolar field is considered to be the average field strength across the entire volume of the affected magnet. Due to the symmetrical nature of the $\hat{y}$ and $\hat{z}$ components around the center of the nanomagnet (where strength field strength is equal to zero), $DIP_{xy}$ and $DIP_{xz}$ can be assumed to be zero.

field imposed on M2 at any given magnetic moment is equal to

$$\mathbf{DIP} = \begin{bmatrix} DIP_{xx} & DIP_{yx} & DIP_{zx} \\ DIP_{xy} & DIP_{yy} & DIP_{zy} \\ DIP_{xz} & DIP_{yz} & DIP_{zz} \end{bmatrix}, \tag{6.4}$$

where $H_{\Xi\Delta}$ denotes the strength of the $\Xi$ component of the dipolar field assuming $\hat{m}_1$ oriented along $\Delta$. The external field on M2 becomes

$$\vec{H}_{EXT2} = \mathbf{DIP}\hat{m}_1. \tag{6.5}$$

Note that there are two dipolar fields involved in this two-magnet system: (a) the forward dipolar field generated by M1 encouraging the reversal of M2, and (b) the reverse field generated by M2 having a less pronounced, but still very significant effect on M1.

## 6.2 Delay Analysis

First, the delay of the top nanomagnet being reversed through the dipolar field is studied. In this section, a set of 60 nm $\times$ 45 nm $\times$ 2 nm permalloy-type ($K_u = 0, M_s = 8.6 \times 10^5 \frac{A}{m}$) nanomagnets with a 2 nm separation are considered. As shown in the following sections, this geometry ensures that the nanomagnets are perfectly coupled. As such the system will always come to rest in an anti-parallel configuration.

Consider the case where M1 and M2 are oriented in the $+\hat{x}$ and $-\hat{x}$ direction, respectively. Assuming a large enough spin current is applied to M1, M1 will reverse to $-\hat{x}$ and impose a time-variant external field on M2 during this reversal. Since we have chosen parameters which we know yield a reliably coupled system, one can assume that M2 will eventually come to rest at $+\hat{x}$. Two types of measurements for the delay of M2 are defined. The zero-delay of M2 is the time from when $\hat{m}_1$ crosses the $\hat{x} = 0$ equatorial plane to the time $\hat{m}_2$ last crosses the $\hat{x} = 0$ equatorial plane. Similarly, the ninety-delay of M2 is the time from when $\hat{m}_1$ crosses the $\hat{x} = -0.9$ equatorial plane to the time $\hat{m}_2$ last crosses the $\hat{x} = 0.9$ equatorial plane. This second delay measurement is useful because the relaxation time of a nanomagnet from a certain threshold to its resting position can often be far greater than the time it takes for the nanomagnet to cross that threshold from the beginning of its precession [3]. In addition to these delays, the zero- and ninety-delay of the entire system are calculated as the time from when the spin current begins the reversal of M1 to the time M2 last crosses the $\hat{x} = 0.0$ or $\hat{x} = 0.9$ equatorial plane, respectively.

To begin with, we simulate the system in the absence of thermal noise to provide an intuitive insight into the complex coupled dynamics of the system. In order to accurately measure the delay of M2, the reversal of M2 must be analyzed in the context of a variety of time-variant dipolar fields generated by the precession of M1. To generate this variety of magnetization trajectories, the spin current into M1 is altered. This does not change any of the strength components of the dipolar field imposes on M2 but it does alter the timing and

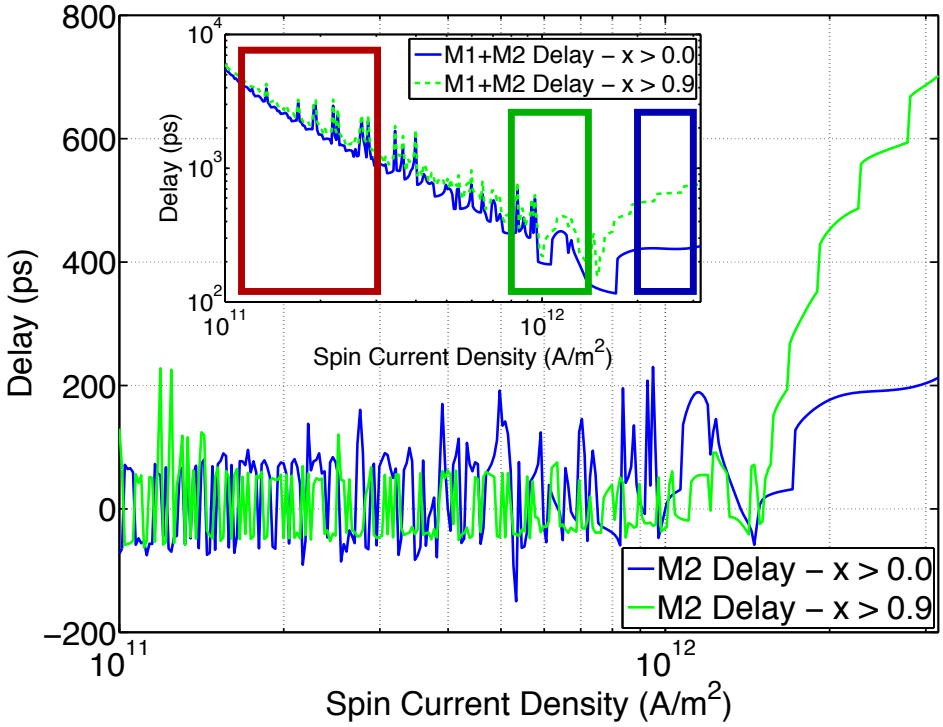


Figure 6.3: Switching delay for M2 versus the spin current density into M1. Spin current changes the precessional curve of the field imposed on M2. Zero-delay is defined as the time when M2 last crosses the $\hat{x} = 0$ equatorial plane less the time when M1 last crosses this plane. Ninety-delay is defined as the time when M2 lasts crosses the $\hat{x} = 0.9$ point less the time when M1 lasts crosses the $\hat{x} = -0.9$ point. In the inset plot, the delays are measured the same way except that the reversal time of M1 is included giving total system delay. Red, green and blue boxes represent slow/optimal/fast M1 precessions. Jumps in delay are explained in text.

the direction of this field. The delay of M2 and the delay of the magnet system compared against the spin current into M1 is shown Figure 6.3.

We note the key features in Figure 6.3. First, there are jumps in the measured delay of the system. As noted earlier, the dipolar field contains both longitudinal and perpendicular field components resulting from the precession of M1. During the reversal of M1, M2 is affected largely by a perpendicular dipolar field and feels a strong torque greatly altering $\hat{m}_2$. During this time, M2 is knocked into a high-energy state. Once the reversal of the magnetization of M2 concludes, M2 experiences a damping relaxation toward the anti-parallel dipole. This relaxation time from a high-energy state to a dipole is effectively

the delay of M2. This relaxation time is heavily dependent on both the energy state and position of M2 at the instant when M1 relaxes [139]. However, the state of M2 at this instant is largely a quasi-random variable as shown in Figure 6.5. The distribution of energy states M2 is left in is reflected in its delay and thus, causes some delay "randomness" in Figure 6.3.

This is not the first time quasi-random behavior has been noted in nanomagnet systems excluding thermal noise [138, 139, 140]. Hence, these delay jumps are also present in other literature which considers magnet reversal through a mixture of precessional and damping effects [109]. In addition, due to the way the delay is measured, M2 may have a negative delay if magnetization of M2 crosses the $\hat{x} = 0$ plane before M1 crosses that threshold. This is also explained by the variation in the magnetization states of M2 following the reversal of M1.

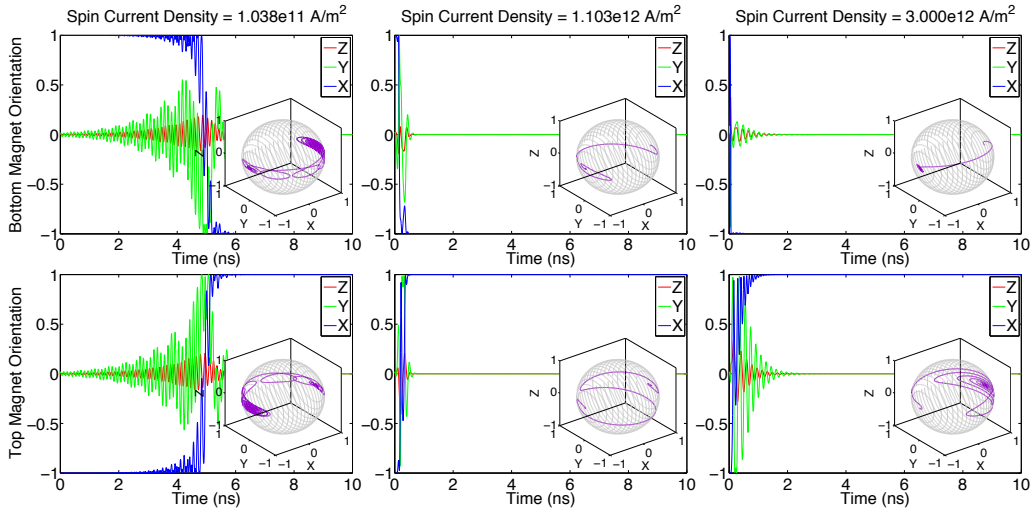


Figure 6.4: The $\hat{x}$, $\hat{y}$, and $\hat{z}$ components of the two magnets versus time calculated by the three different coupling models. Row 1 shows M1 (STT-driven) precession and row 2 shows M2 (field-driven) precession. Each column corresponds to a different spin current density. Inset plots show 3D precessional path. The figure highlights the differences in M2 precession for different M1 reversal trajectories.

Interestingly, there appear to be three reversal regions in the delay graph marked by three boxes in the inset plot of Figure 6.3. The red box marks a region where the precession of M1 is gradual. An example of this precession is shown in the left two subplots of Figure

6.4. It is clear that the large number of oscillations M1 experiences during reversal also affects M2 in a similar manner creating a complex magnetization trajectory. The green box denotes an optimized M1 precession which is shown in the middle two subplots of Figure 6.4. This precession oscillates only a few times before relaxing to a certain dipole. Even with the small number of oscillations, the dipolar field of M1 is still able to generate sufficient torque on the magnetization of M2, exciting $\hat{m}_2$ away from its initial dipole and towards the opposite pole. Finally the blue box denotes a very fast precession of M1 where the perpendicular components of the dipolar field are brief. As can be expected, because the field is perpendicular to the magnetization of M2 for such little time, $\hat{m}_2$ is barely affected during the magnetization reversal of M1 as shown in the right two subplots of Figure 6.4. Instead, M2 mainly feels a longitudinal dipolar field once M2 comes to rest along the easy axis. Because of this, in the fast M1 precession region, the reversal of M2 mimics the relaxation of a nanomagnet under a constant longitudinal field. In fact, as the spin current into M1 is increased, the delay of M2 will further increase until it becomes equivalent to the reversal delay of a nanomagnet under a longitudinal field with field strength equal to $DIP_{xx}$.

Figure 6.3 demonstrates that there is an optimal M1 precession that minimizes the delay of the two-magnet system. From this figure, it is evident that having a very rapid precession of M1 barely affects the magnetization of M2; hence, the reversal of M2 becomes equivalent to the reversal of a nanomagnet under a constant longitudinal field. Alternatively, the impact of M1 precession on M2 can be explained through an analysis of the position of $\hat{m}_2$ when $\hat{m}_1$ crosses a certain threshold. These values are recorded for each of the precessions in the three regions as shown in Figure 6.5. Starting with the blue (fast M1 precession) region, it becomes evident why the reversal of M2 is slow. During a fast M1 precession, $\hat{m}_2$ barely deviates from its resting position and hence would have a very long reversal time.

It is seen in Figure 6.5, that the delay for both the slow (red) and optimal (green) precessions is effectively random centered around zero. Due to the nature of the precession of

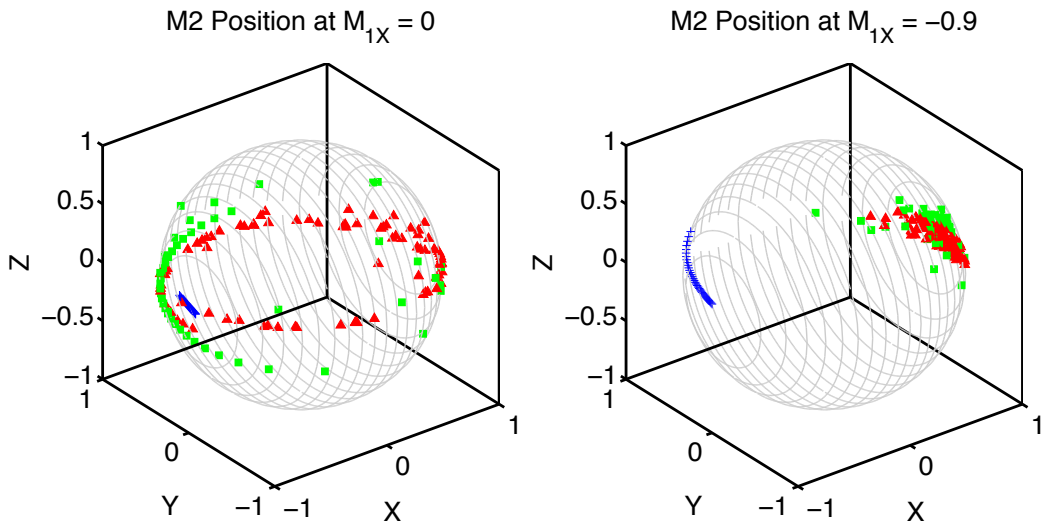


Figure 6.5: Shows position of $\hat{m}_2$ when $\hat{m}_1$ last crosses the $\hat{x} = 0$ (left) or $\hat{x} = -0.9$ (right) equatorial plane. Red triangles correspond to slow M1 precessions contained in red box in Figure 6.3. Green squares and blue crosses correspond to green and blue (optimal and fast M1 precessions) boxed regions found in Figure 6.3.

M1 in these regions, $\hat{m}_2$ can result in either side of the $\hat{x} = 0$ equatorial plane when $\hat{m}_1$ crosses $\hat{x} = 0$. The negative delay is simply a mathematical artifact of the delay definition.

### 6.3 Coupling Strength as a Function of Geometry

To find the operating conditions which guarantee error-free coupling, an analysis of dipolar field strength is useful. As shown in Figure 6.6, the coupling field strength of the dipolar field changes as the distance between the two nanomagnets is increased. Hence, one can change the dipolar field strength without changing the critical field of M1 or M2 by altering the separation between the nanomagnets.

It is useful to consider the case of a longitudinal field being exerted on a nanomagnet. We know that the critical field amplitude required for magnet reversal through a longitudinal field can be written as [129, 149]

$$H_{crit} = \frac{2K_u}{\mu_0 M_s} + M_s \left(N_y - N_x\right). \tag{6.6}$$

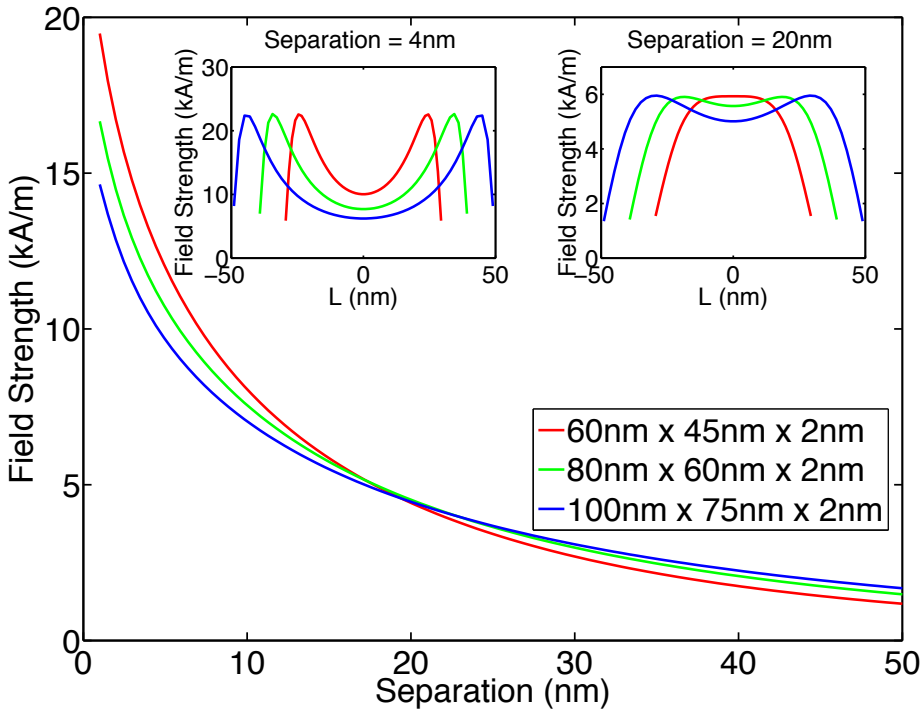


Figure 6.6: The averaged $\hat{x}$ field strength for equally sized, $\hat{z}$-centered magnets versus separation between the two magnets. Magnets are equally sized according to the legend. $M_s$ is assumed to be $8.6 \times 10^5 \frac{A}{m}$. All magnets have a length to width aspect ratio of $\frac{4}{3}$. Inset plots show average $\hat{x}$ field strength along length of M2 for two specific separation cases. The dipolar field shape is different for every magnet size and thus, the average field strength decreases at different rates.

The critical field is smallest when $K_u = 0$ such as in the case of a permalloy [168, 106]. According to (6.6) and (6.1-6.3), the critical field and field strength components are linearly proportional to $M_s$. Whether or not $H_{EXT}$ is greater than $H_{crit}$ depends only on the geometry of the magnets. If $L_2 = W_2$, the critical field of the magnet is zero since $N_y$ and $N_x$ cancel each other out. As the aspect ratio $\frac{L}{W}$ of the magnet increases, the critical field becomes larger and the longitudinal component of the dipolar field is reduced as shown in Figure 6.7. This critical field does not account for the mutual coupling between the two nanomagnets, which greatly lowers the requirements for a perfectly coupled nanomagnet system. However, this concept of a perfectly coupled nanomagnet system being primarily a function of geometry is necessary for understanding the tests being performed in later

sections.

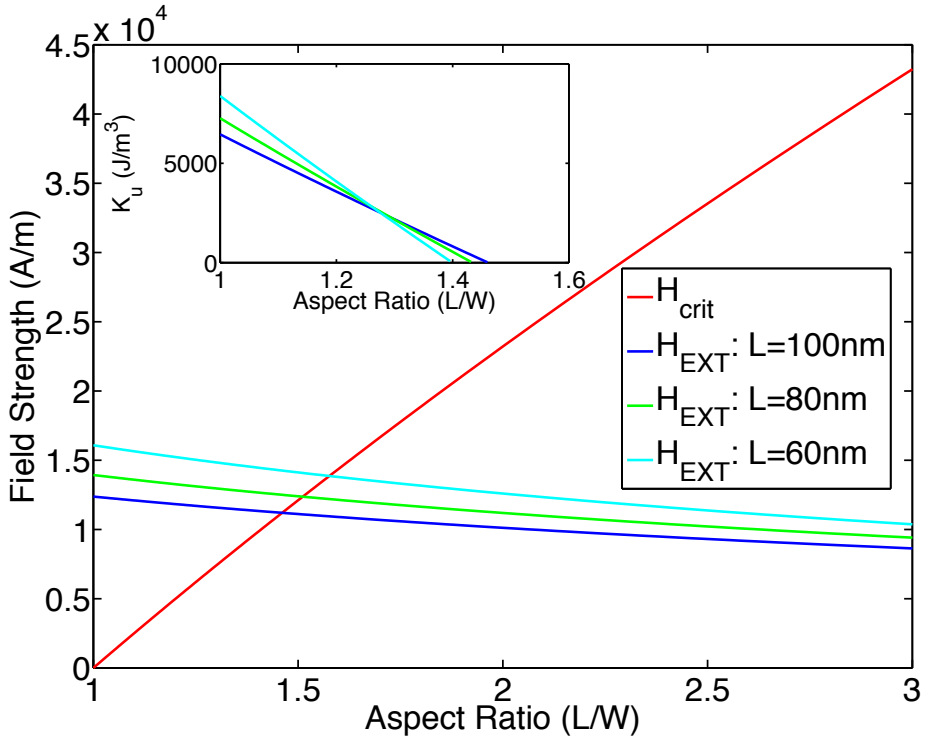


Figure 6.7: The $\hat{x}$-component average coupling field strength and the critical field (assuming $K_u = 0$) versus the length to width aspect ratio of the magnets. Assuming a constant thickness of $t = 2nm$, the geometry of the nanomagnet system is described in terms of aspect ratio. According to the SFM model, the left area where the coupling field is larger than the critical field suggests perfect coupling. Because $K_u$ only increases the critical field, the inset plot shows the maximum $K_u > 0$ for which the system can still be perfectly coupled (assuming it exists). $M_s$ of $8.6 \times 10^5 \frac{A}{m}$, and a separation of 3 nm are assumed.

## 6.4 Concept of Switching Glitch

Even if the magnetization crosses the $\hat{x} = 0$ threshold, it may still cross this threshold again and settle back on the original incorrect position as can be seen in Figure 6.8. As long as the critical field is below a certain threshold, there exist two stable poles where the magnet can settle [3, 138]. We can classify three types of magneto-switching. A successful switch occurs when the orientation of the magnetization vector is reversed from its original state as intended. An unsuccessful switch occurs when the magnetization vector stays at rest in its

original state. A glitch occurs when the magnetization vector crosses the $\hat{x} = 0$ equatorial plane, but precesses back to its original state. One can consider the glitch case a subset of incorrect switching events.

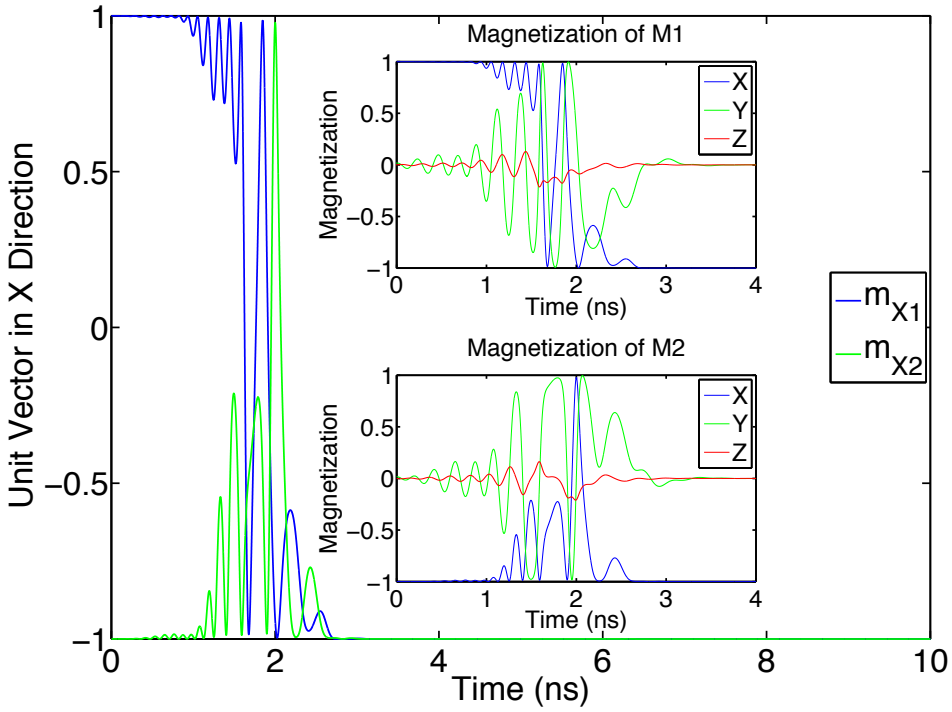


Figure 6.8: The $\hat{x}$-component of the magnetization for M1 and M2 versus time when a glitch happens and the M2 relaxes to the wrong pole. As long as the dipolar field is below the critical field, M2 may relax to either dipole. 60 nm $\times$ 45 nm $\times$ 2 nm magnets with a 20 nm spacing are assumed. A $2 \times 10^{11} \frac{A}{m^2}$ spin current density was used to reverse M1. Inset plots show all magnetization components for M1 and M2 during glitch.

Glitches do not occur when a nanomagnet reverses through the use of a longitudinal field because only one dipole exists if the field strength exceeds the critical value. However, in precessional switching, glitches are very possible which is why fields are often precisely clocked [169, 170]. The complex switching being investigated here is thus susceptible to glitches because of its perpendicular field component. As long as the $DIP_{xx}$ component of the dipolar field is below the critical field defined by (6.6), there exist two dipoles, either of which M2 may relax to. This is an especially important concept since several spin-based devices have been proposed which apply an excitation to set the magnet into a high

energy state and (in principle) allow the magnet to relax down to the correct dipole [141]. While there exists the possibility of the magnetization of M2 settling back to the initial, "incorrect", dipole, the system cannot be said to be perfectly coupled. Several simulations are required to make certain that even if a nanomagnet is knocked into a high-energy state, it will relax down to the anti-parallel position. The critical field of a magneto-system would be a value (or a set of values) such that M2 has no possibility of settling back into an incorrect position.

## 6.5 Numerical Estimation of Critical Field

Finding this critical field analytically is difficult since the tensor defining the dipolar field has multiple values and is dependent on the precession of M1. Depending on the speed and trajectory of the M1 reversal, M2 can be in any number of positions when M1 comes to a rest at its stable state. In order to accurately model this condition and to find the region of operation for the magneto-system, the following test was performed. For Figures 6.9-6.11, a pair of 60 nm $\times$ 45 nm $\times$ 2 nm permalloy magnets are assumed. M1 was set to the $\hat{x} = -1$ steady-state position while the initial position of $\hat{m}_2$ was varied over all possible values. If $m_{x2}$ came to a rest on the $\hat{x} = 1$, it was counted as a switch success. Otherwise $m_{x2}$ would come to rest on $\hat{x} = -1$ and be counted as a glitch or unsuccessful switch based on if its processional trajectory crossed $\hat{x} = 0$. This models all possibilities of the two-magnet coupled systems at the moment when M1 reverses to its stable-state.

If, for a certain set of parameters, the system is shown to not be perfectly coupled, the separation between the nanomagnets is reduced, increasing the coupling strength of the system, and the test is performed again.

### 6.5.1 Initial Angle Sweep Test

Figure 6.9 shows the results for all the initial angles tested. At large separations, the system is unable to provide fully correct operation. The separation between the nanomagnets

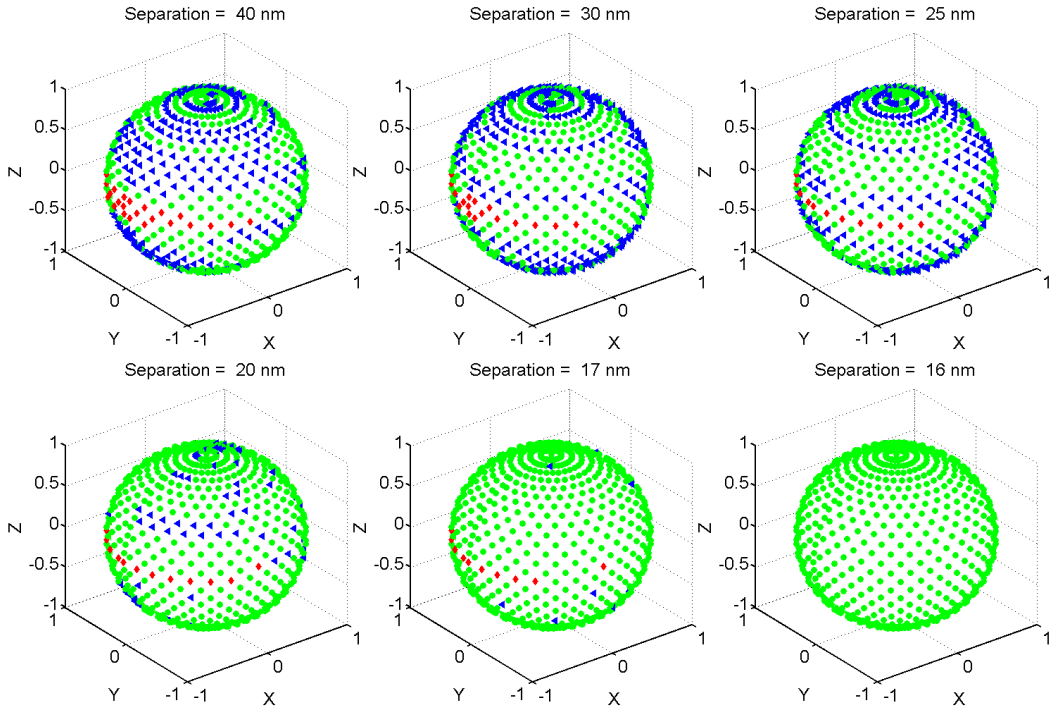


Figure 6.9: A color coded map of initial states for M2 based on the three possible switching outcomes for M2 assuming M1 has completed its reversal but is still under the influence of spin current density of $1 \times 10^{11} \frac{A}{m^2}$: Red diamonds = unsuccessful switches, blue triangles = glitch, green circle = successful switches. As the strength of the coupling is increased by reducing the separation between the two nanomagnets, the population of the initial angles resulting in glitched or unsuccessful outcomes goes to zero. A pair of $60nm \times 45nm \times 2nm$ permalloy magnets are assumed. Assuming the longitudinal field equal to $DIP_{XX}$, $H_{crit} = 1.24 \times 10^4 \frac{A}{m}$. $DIP_{XX}$ exceeds $H_{crit}$ when the separation between the two nanomagnets is under $4.5nm$ as can be seen in Figure 6.6. From the subplots above, it is evident that perfect coupling can be achieved at much higher separations. The mutual coupling between the two nanomagnets alters their energy space in such a way as to allow stronger coupling with weaker fields.

is reduced until all M2 positions result in correct final resting positions. The system is then tested again in an attempt to establish a region of operation for error-free coupling. Assuming a very large separation of 40 nm at the $\hat{x} = -1$ pole, there is a region where the vector will simply fall back down to the initial dipole and not switch at all. If M2 is initially in a high energy state, it has a chance of relaxing to either dipole.

As the coupling field is strengthened by reducing the separation between the nanomagnets, the unsuccessful switch region becomes smaller and the number of glitches is reduced. Eventually, a separation of 16 nm is achieved which guarantees correct coupling operation.

It is useful to compare this separation value to other critical field values derived in literature. One can hypothesize that the critical field of the nanomagnet is mainly dependent on longitudinal component of the dipolar field. As discussed earlier the critical field of a magnet under a longitudinal field can be found according to (6.6). In the case of a 60 nm $\times$ 45 nm $\times$ 2 nm permalloy-type nanomagnet, $H_{crit} = 1.24 \times 10^4 \frac{A}{m}$. $DIP_{XX}$ exceeds $H_{crit}$ when the separation between the two nanomagnets is under 4.5 nm as can be seen in Figure 6.6. However, in Figure 6.9, perfect coupling is guaranteed much before this limit. The strength of the coupling between the nanomagnets depends on more than the longitudinal component of the dipolar field.

### 6.5.2 Perpendicular Field Effects vs. Mutual Coupling

Other than the longitudinal field component of the dipolar field, there are two more effects which may hypothetically contribute to this increase in coupling strength. Firstly, it has been noted that the perpendicular field component during the reversal of M1 knocks the magnetization into a high energy state at which point M2 relaxes back down to a dipole. It is possible that this perpendicular field knocks $\hat{m}_2$ into a favorable state altering its precession and critical field value.

Another effect to consider is mutual coupling. M1 imposes a dipolar field onto M2 which cause its magnetization to precess. However, as the magnetization of M2 changes, it imposes a time-variant reverse field onto M1. This reverse field causes perturbations in the precession of M1 which, of course, cause the dipolar field generated by M1 and imposed on M2 to be altered.

In order to test which of the above-mentioned effects causes an increase in coupling strength, another initial angle sweep test is performed. As shown in Figure 6.10, in the absence of the reverse field, perfect coupling occurs only when the separation of the nanomagnet is 4 nm. This means that without the mutual coupling between the nanomagnets, the critical field of the system is equivalent to the critical field of a nanomagnet under a lon-

gitudinal field. Hence, the mutual coupling between the nanomagnets greatly strengthens nanomagnet coupling.

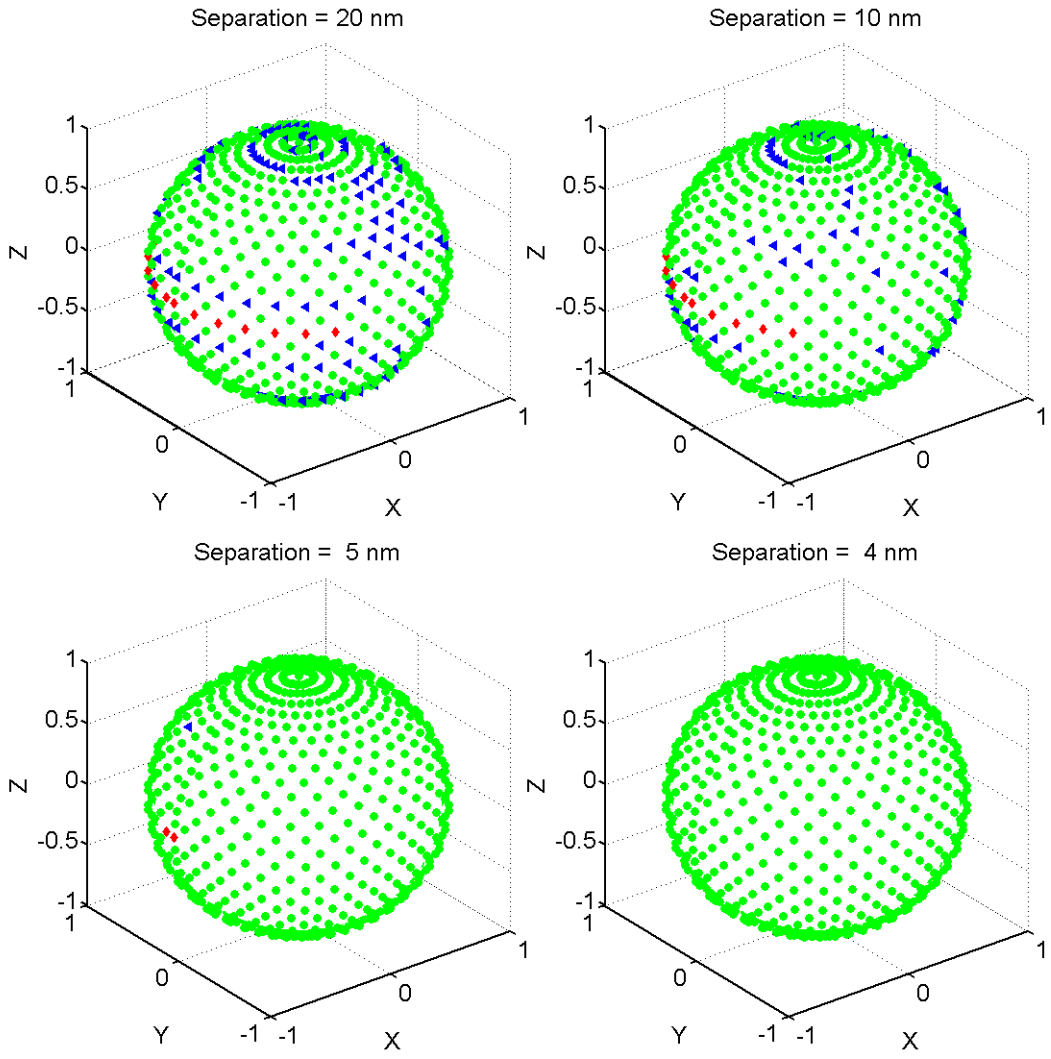


Figure 6.10: A color coded map of initial states for M2 based on the three possible switching outcomes for M2 assuming M1 has completed its reversal but is still under the influence of spin current density of $1 \times 10^{11} \frac{A}{m^2}$: Red diamonds = unsuccessful switches, blue triangles = glitch, green circle = successful switches. In this case, the reverse field of the dipolar coupling is removed and as such, M2 can no longer disturb the magnetization of M1. This removes the mutual coupling between the nanomagnets during $\hat{m}_2$ relaxation. Same system conditions are assumed as in Figure 6.9. From the subplots above, it is evident that without the mutual coupling between the two nanomagnets, perfect coupling is only achieved when the longitudinal component of the dipolar field of M1 exceeds $H_{crit}$. Hence, the perpendicular components of the dipolar field do not alter the critical requirements necessary for perfect coupling.

## 6.6 Dipolar Coupling with Thermal Noise

Until this point, thermal noise was omitted from our simulations. However, any analysis of magnetization dynamics is incomplete without the inclusion of thermal noise; hence, in this section, a series of simulations are performed in the presence of thermal noise.

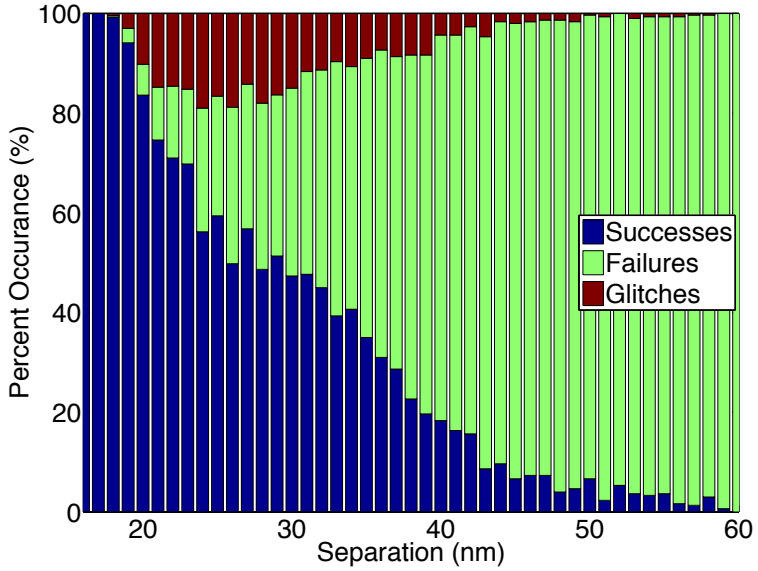


Figure 6.11: A Monte-Carlo simulation where the reversal of M1 encourages the reversal of M2 while including thermal noise. The percent (1000 runs) of successful, unsuccessful and glitched switchings versus the separation is measured. A pair of 60 nm $\times$ 45 nm $\times$ 2 nm magnets. M1 is reverse using a spin current density of $1 \times 10^{11} \frac{A}{m^2}$. Results are similar to those found in Figure 6.9. This suggests that the tests performed in Figure 6.9 can estimate magneto-reversal of the system in the context of thermal noise.

### 6.6.1 Critical Field Measurement with Thermal Noise

In Figure 6.11, the number of successful, unsuccessful, and glitched M2 switches are measured once a complete system reversal comes to rest. The thermal simulation was performed using the same geometric and physical parameters assumed in Figure 6.9. This is slightly different than the simulation preformed in Figure 6.9. In this case, the reversal of M1 randomizes the orientation of M2 magnetization. Instead of the uniform random distribution assumed in the previous section, $\hat{m}_2$ will have a distribution of probable positions

based on the precession of $\hat{m}_1$ as seen in Figure 6.5.

Interestingly, the thermal test performed in Figure 6.11 predicts perfect coupling is achieved when the separation is less than 17.5 nm. This is slightly more than the maximum separation of 16.5 nm predicted in Figure 6.9. This discrepancy is easily explained when considering the energy space of a nanomagnet under a external longitudinal field as shown in Figure 5.1. As a longitudinal field is applied to a nanomagnet, one dipole becomes "weighted" and the dipole which is anti-parallel to the external field becomes smaller. In Figure 5.1, the black orbit is often referred to as a "separatrix", denoting the energy that separates the high and low energy regions [3]. Assuming the nanomagnet is initially at rest in the smaller dipole, the thermal noise may add enough energy to the nanomagnet which would allow its magnetization to cross this separatrix and precess to the other dipole. As the longitudinal field grows stronger, the energy between the dipole and separatrix is reduced. The lesser this difference, the larger the probability that the thermal noise may knock the magnetization out of this small dipole and towards the larger dipole [109, 112, 171].

Perfect coupling is defined as occurring when during the simulation time interval, the magnetization will relax to the correct, larger dipole. An unsuccessful switch occurs when the magnetization cannot escape its initial low energy "well". When there is no thermal noise, this can only occur when the coupling grows strong enough that the smaller dipole ceases to exist and the magnetization must relax towards the only dipole left in the system. However, in the presence of thermal noise, even if this smaller dipole exists, it may be so small such that the thermal noise has a high probability of knocking the magnetization across the separatrix where it will precess and most likely settle towards the correct position. A similar argument can be made for the case of a switching glitch.

Analytically, the critical field is defined as the field which changes the energy space of the magnet such that there is only one dipole. However, one can argue that there is an "effective" critical field where, even though there are two existing dipoles, one may be so small that, for a nanomagnet under the influence of thermal noise, the probability that a

nanomagnet will stay at rest in the smaller dipole for a given time interval is nearly 0.

However, also consider that this probability only approaches unity but is never equal to it. In this and the next section, large Monte-Carlo simulations are used to estimate whether or not a system is perfectly coupled.

## 6.7 Regions of Operation

In the previous sections, a pair of weakly coupled magnets separated by a large gap were considered. This was mainly to determine the primary influences on the coupling strength between the nanomagnets. Now it is possible to apply the conclusions gained from the previous sections to more realistic magneto-systems.

### 6.7.1 Length and Width Operating Regions

As shown in Section IV, the coupling strength between the two nanomagnets is largely a function of geometry. Hence, it is possible, given a certain separation, to determine which nanomagnet geometries exhibit error-free coupling. In Figure 6.12, the geometries which secure perfect-coupling are mapped. The red and blue regions together map the coupled region assuming the full dipolar coupling model where the both the forward and reverse dipolar fields are considered.

The red region alone considers the case where the reverse dipolar field does not exist. Comparing this partial model to the full model is useful when trying to map the geometric regions which ensure perfect coupling primarily because of the mutual coupling between the nanomagnets. Interestingly, as the separation between the nanomagnets grows, the coupling regions of both models begin to converge. This is likely due to the weakening of the $DIP_{yy}$ and $DIP_{zz}$ tensor components resulting in weaker feedback at larger magnet sizes but more work is required in understanding the mutual coupling of the nanomagnet system.

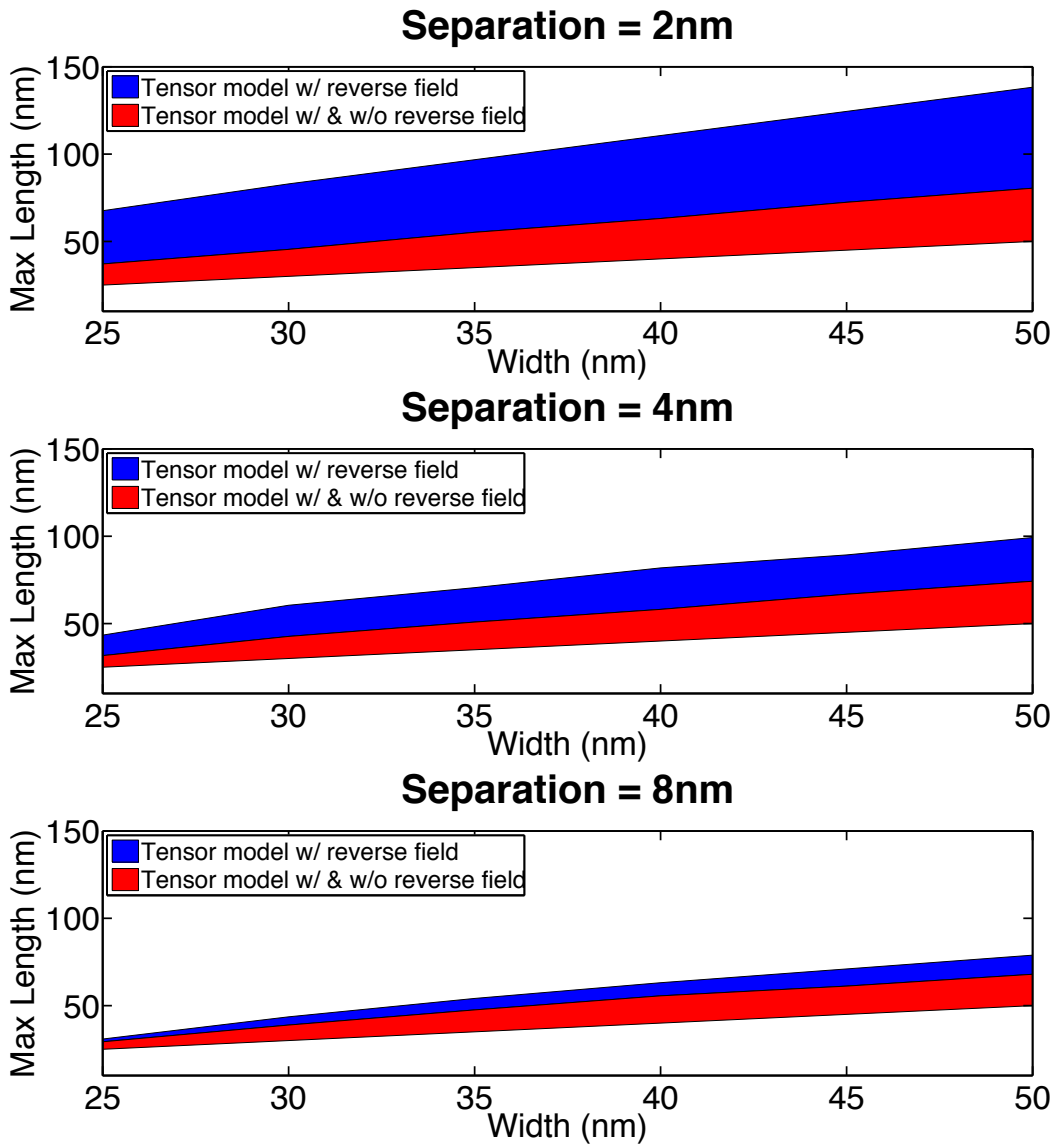


Figure 6.12: Maximum magnet length versus width for perfect coupling for three different separations (2nm, 4nm, and 8nm) determined using thermal test shown in Figure 6.11. Permalloy magneto-system with 2 nm thick magnets and a 2/4/8 nm separation are assumed. Red area denotes dimensions where default system with both forward and reverse components of the dipolar field perfect coupling. Blue area represents dimensions system with reverse component of dipolar field predicts perfect coupling. As the separation between the nanomagnets becomes greater, the strength of the dipolar coupling field is reduced. As the coupling strength is reduced, the mutual coupling strength is also reduced and the two models converge. For both models, minimum length is equal to width of nanomagnet to ensure free-axis in $\hat{x}$ direction.

### 6.7.2 Maximum Separation as a Function of Current

It has been proven that the mutual coupling plays a crucial role in the coupling strength between the two nanomagnets. However, the mutual coupling is dependent on the ability of M2, through its reverse dipolar field, to influence slight variations in the magnetization of M1 which would in turn create slight variations in the forward field affecting M2. However, most of the simulations done thus far have assumed lower current densities for the reversal of M1. If the current density of M1 is raised, this would more effectively pin $\hat{m}_1$ against the free-axis and make inducing variations by the reverse field more difficult. This effect can be seen in Figure 6.13. As the current density into M1 is increased, the maximum separation between the nanomagnets which predicts perfect coupling is lowered.

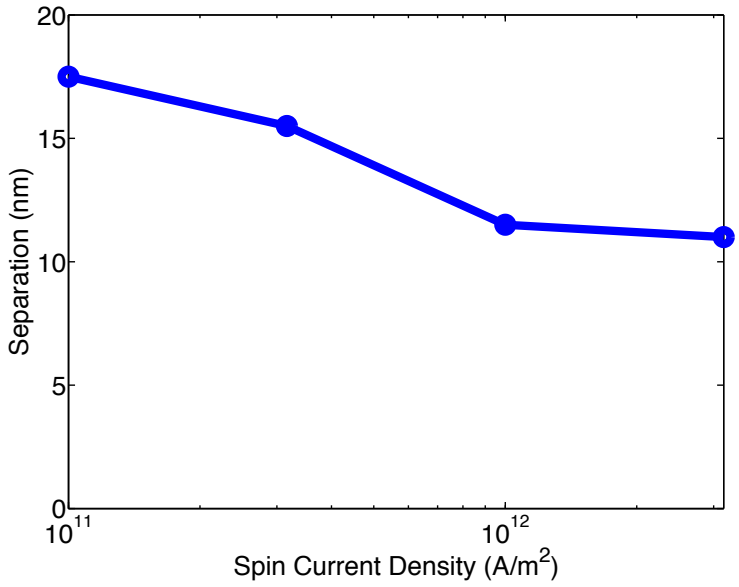


Figure 6.13: Maximum separation is measured according to a thermal test shown in Figure 6.11 for various spin current density. It was shown that the coupling strength of the system was largely due to the mutual coupling between the two nanomagnets. This mutual coupling allowed M2 to cause slight perturbation in $\hat{m}_1$ which in turn would cause variations in the dipolar field acting on M2. However, a larger spin current into M1 would better pin the magnetization to the free-axis and weaken the mutual coupling between the two nanomagnets reducing the coupling strength.

# CHAPTER 7

# DIPOLAR COUPLING II: ANALYTIC EXPRESSIONS FOR IDENTICAL MONO-DOMAIN BIAXIAL AND UNIAXIAL TWO-MAGNET SYSTEMS

Chapter 6 showed that the longitudinal field approximation is pessimistic. It is possible to achieve perfect coupling while failing to meet the limits imposed by the longitudinal field approximation [172, 173]. We refer to this increase in coupling strength due to complex interaction between magnetic bodies as the mutual-coupling effect (MCE). Our goal is to now develop analytic expressions which correctly categorize this increase in coupling strength through the MCE. In this chapter, we expand our understanding of this effect in two-magnet systems and construct new models for the critical conditions required for reliable coupling. The proposed analytic models are valid when the nanomagnet(s) undergoes slow, nanosecond reversals. This is not a problem considering most nanomagnet devices operate close to their critical currents. Two categories of nanomagnets are considered: uniaxial and biaxial [120, 109]. Both types of nanomagnets have a negative anisotropy energy along the free-axis creating an energy barrier between the two stable magnetization states [119]. However, biaxial nanomagnets also contain a positive anisotropy energy oriented perpendicular to the free-axis significantly altering the precessional dynamics of the nanomagnet system [156]. As a result, slightly different reliability models are needed for each of these cases [174].

### 7.0.1 Model Definition

Here too, we consider systems with identical nanomagnet bodies. Two examples of such a system are shown in Figure 7.1. Initially, the nanomagnets are oriented in an anti-parallel fashion. We can then reverse the bottom nanomagnet (M1) through STT. During the reversal, M1 generates a time-variant dipolar field which will encourage the top nanomagnet

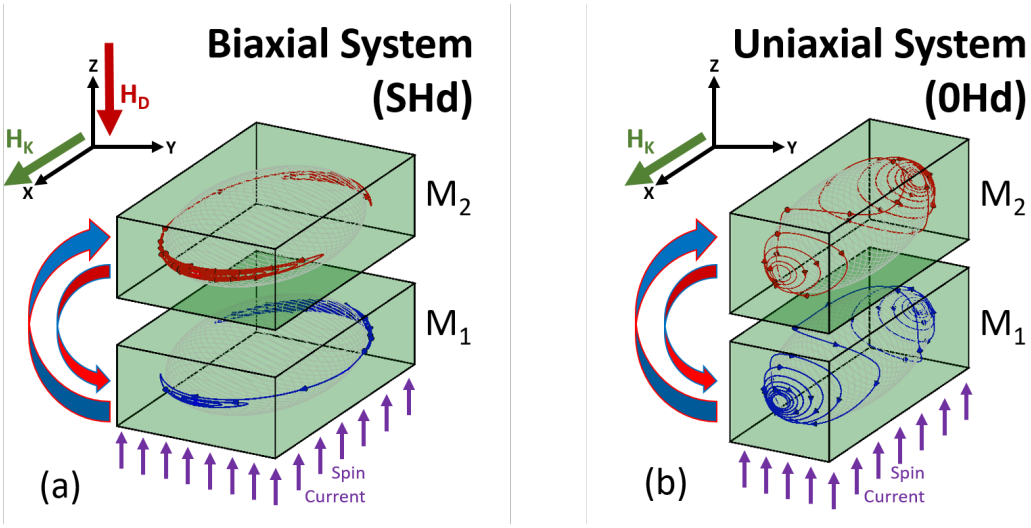


Figure 7.1: Test setup for a two-magnet system(s). Magnet 1 (M1) is driven through STT and Magnet 2 (M2) is driven through dipolar coupling field generated by Magnet 1. Two types of nanomagnet systems (biaxial (a) and uniaxial (b)) are considered in this chapter. As shown in the figure, the presence of a large demagnetization field fundamentally alters the precession of magnetization. The difference in trajectories alters coupling strength between nanomagnets even if both systems have equivalent field magnitudes. Sample magnetizations are shown in the nanomagnet bodies and correspond to Figure 7.4. Magnetization spheres are normalized against material geometry.

(M2) to also reverse. Note that the dipolar tensor was defined in Section 6.1.2.

The precessional dynamics of the nanomagnet is strongly influenced by the energy landscape [3]. It is prudent to categorize the magnetic coupling analysis according to the different types of energy landscapes[116]. Two types of energy landscapes are considered in this chapter: uniaxial and biaxial, which account for most nanomagnetic systems currently being researched. The uniaxial systems are analyzed using the 0Hd approximation while the biaxial case is analyzed using the SHd approximation. These approximations are defined in Section 2.1.2.

## 7.1 Impact of Separation on Coupling Reliability for SHd and 0Hd Cases

Nanomagnet systems may have equivalent dipolar field magnitudes and energy barriers, but significantly different precessional dynamics if a perpendicular anisotropy is present. Previous works have shown that a perpendicular anisotropy can significantly alter the dy-

namics and reliability of magnetic bodies [108]. In this section, it is shown that these altered precessional dynamics also alter the reliability of reversal in two-magnet systems.

Figure 7.2 measures the coupling reliability of the two-magnet system at different separations for both the SHd and 0Hd cases.

For the SHd case, the system stays perfectly coupled for a separation of up to $7.5\mathrm{nm}$. This is greater than the maximum separation of $0.38\mathrm{nm}$ predicted by the longitudinal field model. For larger separations, the reliability of reversal is reduced; unsuccessful and glitched reversals begin to be more prominent. Although the nanomagnets are not perfectly coupled, the mutual interactions lower their energy barrier increasing the likelihood of unstable system behavior.

Figure 7.2 also demonstrates the difference in coupling strength between the uniaxial and biaxial cases. Despite both these cases have the equal dipolar tensors and energy barriers, the uniaxial case can tolerate a significantly larger separation and, by extension, a weaker dipolar field magnitude. As shown in Figure 6.1, this is because the reversal dynamics are fundamentally different in the two cases. In the uniaxial case, the magnets precess close to the $\hat{x}-\hat{y}$ plane suggesting that only the $DIP_{xx}$ and $DIP_{yy}$ are acting upon $\hat{m}_2$. On the other hand, in the uniaxial case, $\hat{m}_2$ precesses throughout the unit sphere more fully utilizing both dimensions of the dipolar field. Hence, two models for reliable dipolar coupling will be developed corresponding to each energy landscape.

## 7.2 Effect of Reversal Speed on Coupling

Previous results have demonstrated that during a slow, nanosecond reversal of the bottom nanomagnet, the delay of the top nanomagnet is on the order of $\mathrm{ps}$ when compared to the delay of the bottom nanomagnet, assuming a strong enough tensor [173]. However, it is also known that an instantaneous reversal of the bottom nanomagnet would mean that the dipolar tensor would reduce to a simple longitudinal field. In this instantaneous case, reliable coupling is guaranteed if the longitudinal component of dipolar field exceeds

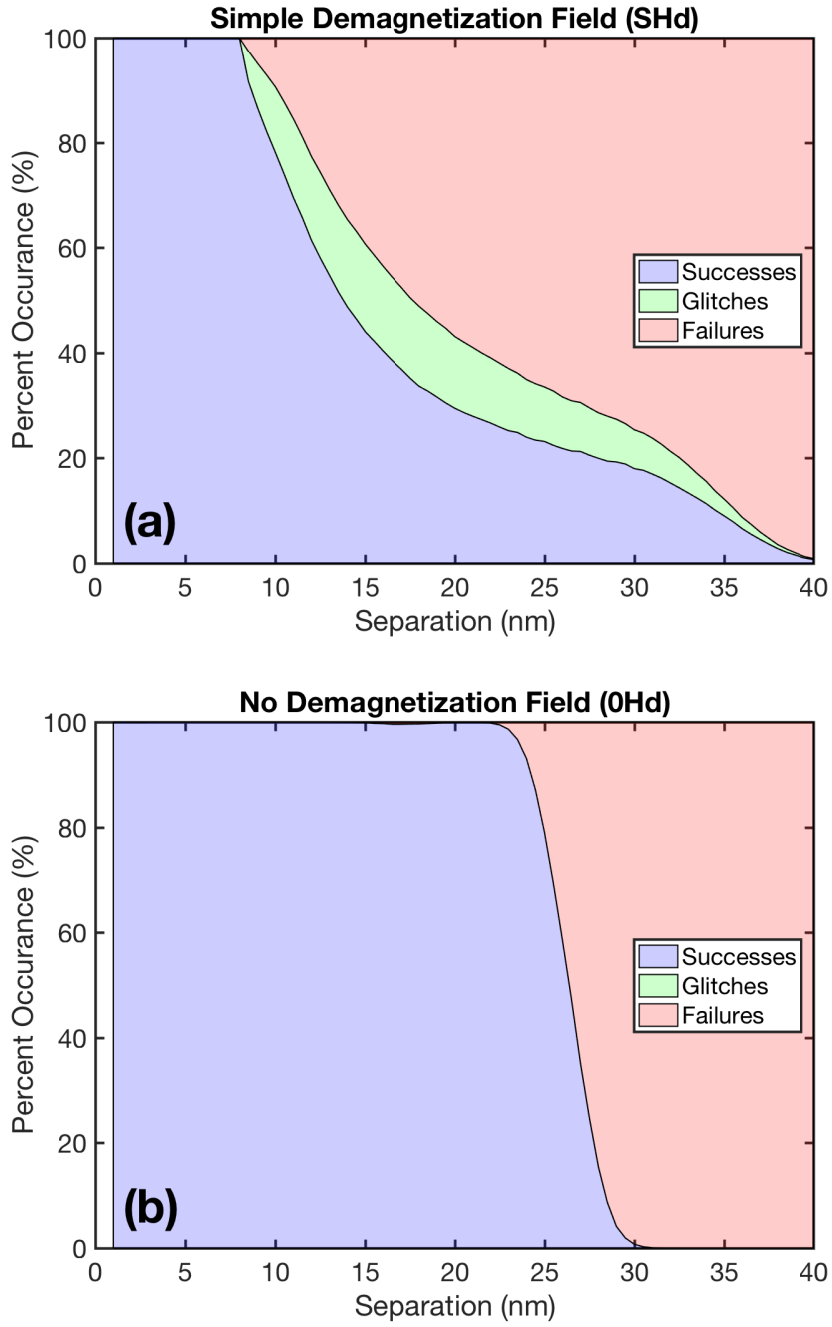


Figure 7.2: Probability of top magnet reversal in $\hat{z}$ - stacked and centered two-magnet system. Assuming two $60\text{nm} \times 45\text{nm} \times 2\text{nm}$ iron magnets. As the separation between the nanomagnets is increased, the magnitude of the tensor components of the dipolar field decreases. If the dipolar coupling consisted of only the longitudinal component, a reliable system would have a maximum separation of $0.38\text{nm}$. (a) Biaxial, SHd system whose nanomagnets have a large negative perpendicular anisotropy field oriented along the out-of-plane ($\hat{z}$) axis. (b) Uniaxial 0Hd case where this perpendicular anisotropy is not present. This comparison shows that given the same energy-barriers and dipolar-field magnitudes, coupling between uniaxial nanomagnets is actually stronger than coupling between their biaxial equivalent.

critical field value [152]:

$$DIP_{xx} > H_{crit}. \tag{7.1}$$

Conceptually, this critical field magnitude is the Zeeman energy magnitude required to turn the anti-parallel minima into a saddle-point and/or pole and is given as [149]:

$$H_{crit} = H_k + (N_{yy} - N_{xx})\, M_s. \tag{7.2}$$

In both the SHd and 0Hd cases, we assume there is no positive perpendicular anisotropy along the easy or hard axes; there is no demagnetization contribution to the critical field value. Assuming a SHd or 0Hd demagnetization field means that the critical field magnitude is equal to the anisotropy field. In the case of the $60\mathrm{nm} \times 45\mathrm{nm} \times 2\mathrm{nm}$ SHd iron ($M_s = 1.7\frac{\mathrm{MA}}{\mathrm{m}} | K_u = 48\frac{\mathrm{kA}}{\mathrm{m}^3}$) magnets considered in this chapter, $H_{crit} = H_k = 45\frac{\mathrm{kA}}{\mathrm{m}}$.

Figure 7.3 measure the delay and coupling reliability of an iron two-magnet system for various current inputs. The reduction of coupling strength is demonstrated in the background of Figure 7.3. By increasing the spin current into the bottom nanomagnet, M1's reversal delay is decreased and the dipolar coupling between the nanomagnets is weakened because the perpendicular components of the dipolar field have less time to apply a torque upon the magnetization of the top nanomagnet.

However, the spin current required for fast, picosecond reversals is very large and the current density required to produce spin currents of such magnitude would most likely cause other problems in a real-world systems [175, 176]. There is also substantial experimental evidence of large spin currents lowering the reliability of nanomagnet reversal because of the back-hopping effect [79, 177]. In addition, large spin currents encourage domain nucleation which would likely break the mutual coupling effect [172, 178]. For these reasons, spin-based devices are generally designed for delays in the nanosecond region where dipolar coupling is stronger than realized by the simple longitudinal case.

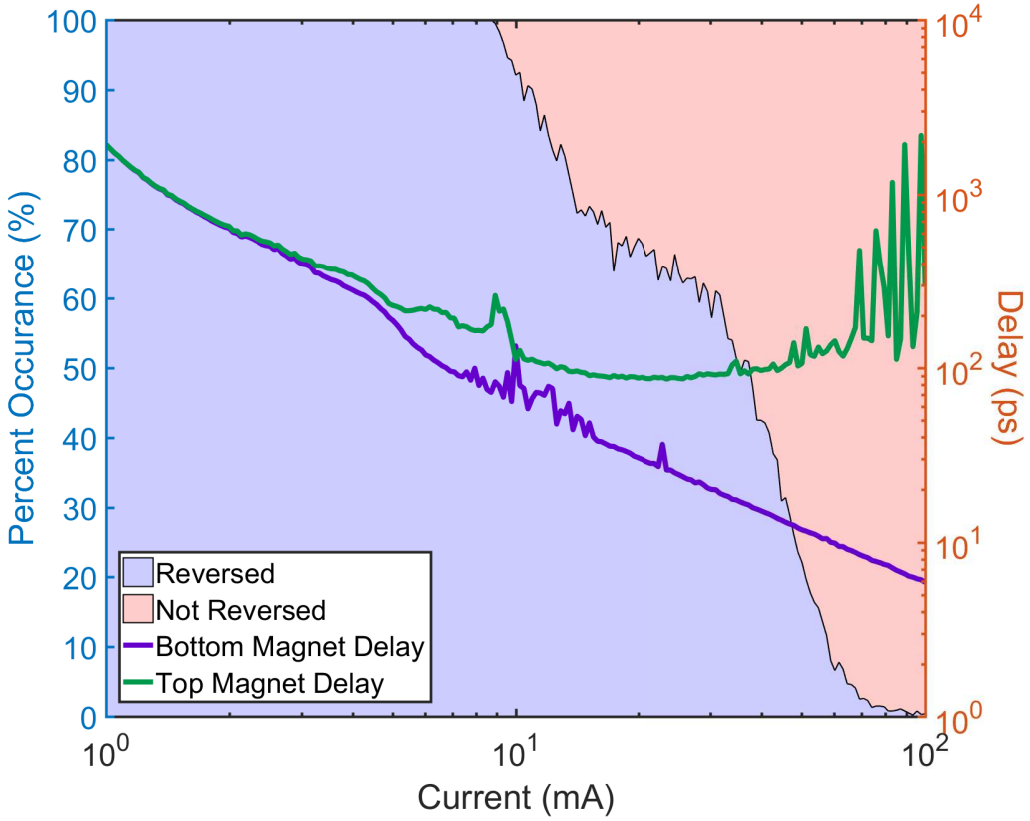


Figure 7.3: Delay of top and bottom nanomagnets in $\hat{z}$ - stacked and centered two magnet system. Assuming two $60\text{nm} \times 45\text{nm} \times 2\text{nm}$ iron magnets with a separation of $5nm$. In this case $DIP_{xx} = -24.54\frac{\text{kA}}{\text{m}}$ which is significantly less than $H_{crit} = 44.94\frac{\text{kA}}{\text{m}}$. Assuming SHd. Left axis corresponds to area plot in background and right axis corresponds to line graphs. Only successful reversals considered in the delay average. Hence, the delay average becomes volatile in the fast reversal case because fewer successful reversal cases can be averaged together. Figure demonstrates that if the reversal of the bottom nanomagnet is too small, the dipolar coupling between the magnets in the system weakens and thus the top nanomagnet reversal becomes very slow.

## 7.3 Coupling in Biaxial Nanomagnet Systems

Firstly, in this section, a SHd, biaxial nanomagnet-system is considered. The coupling strength between the nanomagnets depends on the three diagonal components of the dipolar tensor. Usually these three parameters are material and geometry dependent. To better understand the role of the individual field magnitudes when reversing a nanomagnet through dipolar coupling, we will assign dipolar tensor values independent of other system

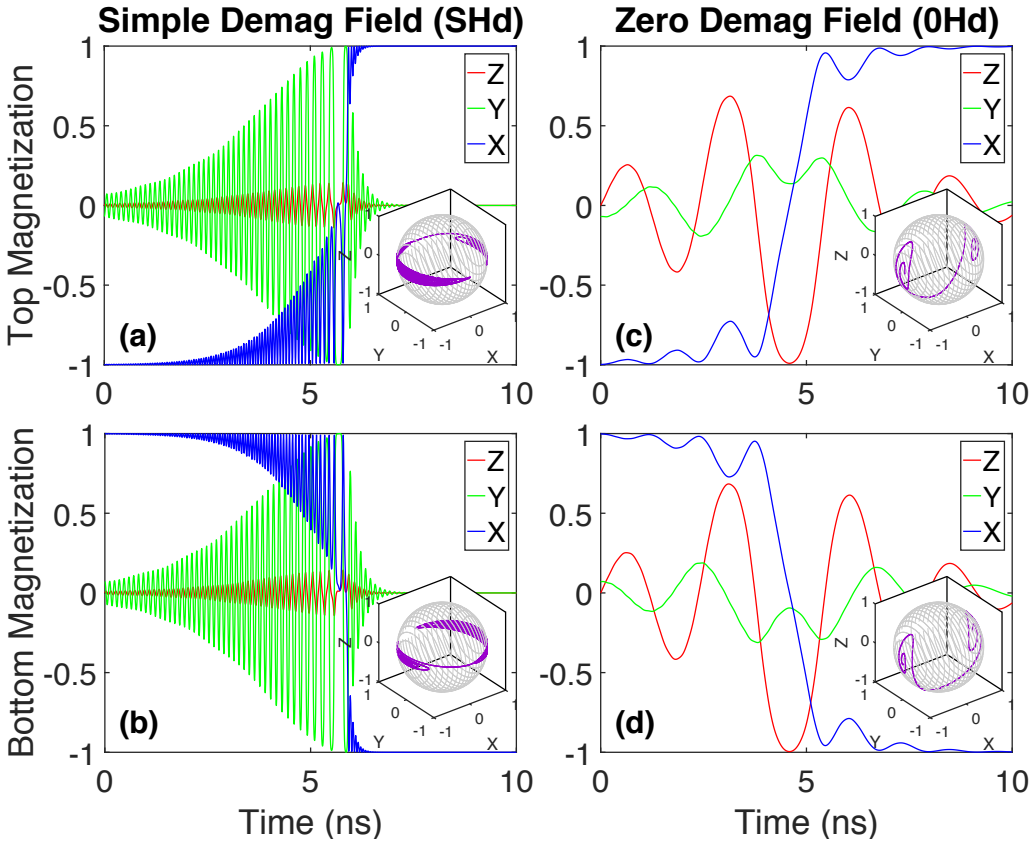


Figure 7.4: Sample reversals for nanomagnet systems for SHd (a,b) and 0Hd (c,d) cases. Assuming two $60\text{nm} \times 45\text{nm} \times 2\text{nm}$ iron magnets. In the SHd case, the bottom nanomagnet is driven by a $0.8mA$ spin current. In the 0Hd case, the bottom nanomagnet is driven by a $0.15\text{mA}$ spin current. The dipolar coupling of the nanomagnets is determined by their geometry. Figures demonstrate the different dynamics of both cases. Subplots show magnetization dynamics on unit sphere.

parameters. Note that because the dipolar field magnitude is being artificially assigned, the separation between nanomagnets does not impact the system. The models and conclusions proposed in this section are valid for biaxial systems whose demagnetization fields significantly larger than the dipolar field components. Figure 7.5 measures the reliability of a two-magnet iron system with a sub-critical longitudinal tensor component and varied perpendicular tensor components.

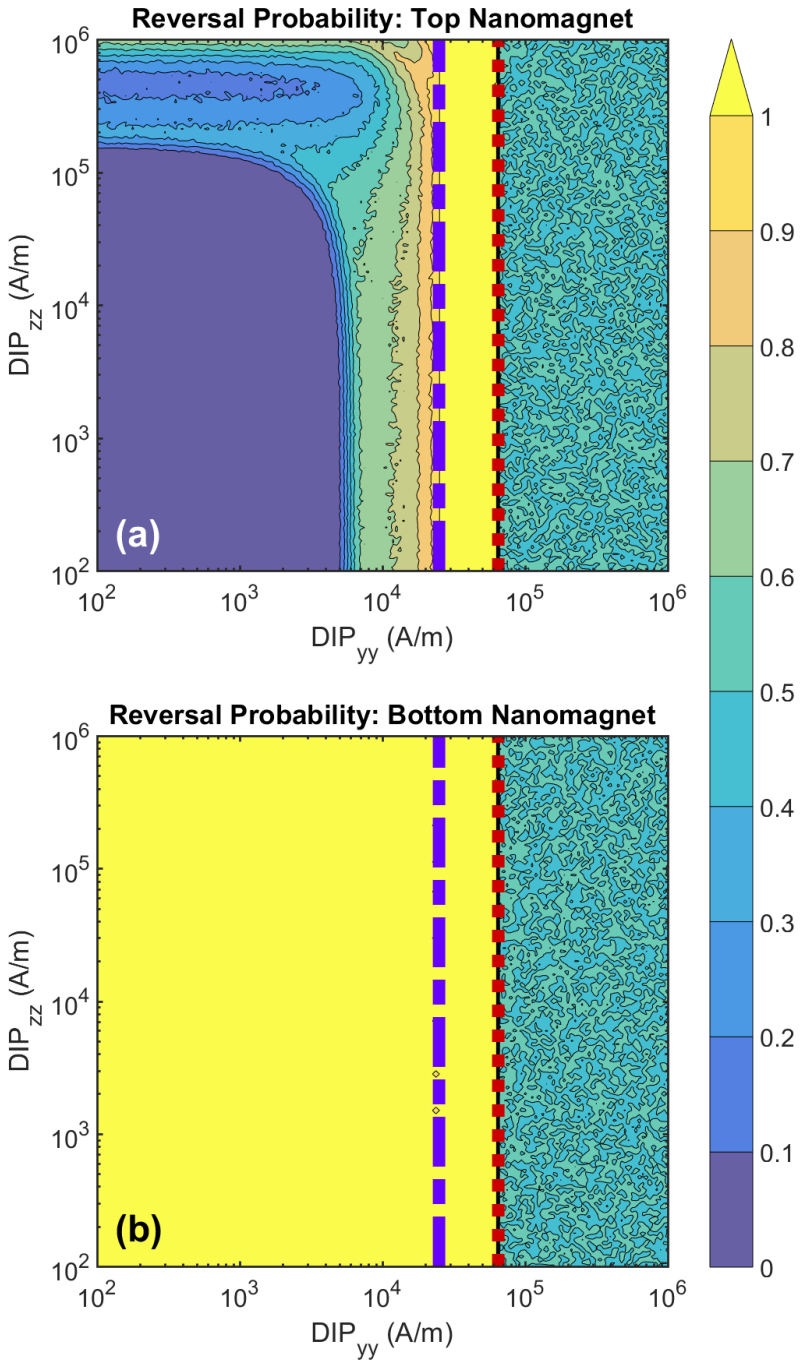


Figure 7.5: Probability of each of the nanomagnets reversing in a $\hat{z}$ - stacked and centered two-magnet biaxial system. Assuming two $60\text{nm} \times 45\text{nm} \times 2\text{nm}$ iron magnets. Bottom nanomagnet is driven by a $1.0\text{mA}$ spin current. The dipolar coupling between the nanomagnets is altered by manually changing the magnitudes of the dipolar tensor components. $DIP_{xx} = 2 \times 10^4 \frac{\text{A}}{\text{m}}$ while the $DIP_{yy}$ and $DIP_{zz}$ components of the tensor model correspond to the values marked by the x and y axes of the graph respectively. Colors of the shaded region correspond to the probability of reversal for the top and bottom magnets. Area to the right of the purple dash-dot line corresponds to values adhering to (7.6). Area to left of red dotted line corresponds to values adhering to (7.7).

### 7.3.1 Model for Reliable Coupling in Biaxial Systems

Figure 7.4 shows the trajectory of a coupled SHd system. It is shown that the large demagnetization field limits the precession of M1 to being contained mainly in the $\hat{x}$-$\hat{y}$ plane. The trajectory of the reversal implies only the $\hat{x}$ and $\hat{y}$ portions of the dipolar field are relevant during biaxial reversal. This is further reinforced by Figure 7.5 where the out-of-plane portion of the dipolar tensor ($DIP_{zz}$) does not contribute to the region of reliable M2 reversal.

In addition, Figure 7.4 demonstrates that, in a coupled two-magnet system, the magnetizations of the top and bottom nanomagnets precess approximately in an anti-parallel fashion. More specifically, referring to the magnetizations for each of the nanomagnets in the system, the $m_x$ and $m_y$ components precess with equal magnitude and opposing polarity (due to the negative $DIP_{xx}$ and $DIP_{yy}$ tensor components) and the $m_z$ components remain approximately equal. Knowing this, we can make the following approximation:

$$\hat{m}_2 = [-1, -1, 1] \cdot \hat{m}_1 \equiv \kappa \hat{m}_1. \tag{7.3}$$

This is significant when considering the two-magnet SHd system. The LLG equation states that the magnetization of each nanomagnet is a two-dimensional variable. Each of the magnetization vectors are also linked to each other because the external field imposed on M2 is controlled by $\hat{m}_1$ through the dipolar field and vice-versa. Consequently, the two-magnet system is governed by a four-dimensional system of differential equations. However, during slow nanomagnet reversals, we can make the approximation shown in (7.3); hence, the external field can be rewritten as:

$$\vec{H}_{DIP1} = \mathbf{DIP}\hat{m}_1 \approx \mathbf{DIP}\kappa\hat{m}_2. \tag{7.4}$$

Returning to our formulation of the dipolar Zeeman energy, the following approxima-

tion can be made using (7.4):

$$\begin{aligned}\epsilon_{DIP1}(\hat{m}_1) &= -\mu_0 M_s(\mathbf{DIP}\hat{m}_2)\hat{m}_1 \\ &= -\mu_0 M_s(\mathbf{DIP}\kappa\hat{m}_1)\hat{m}_1 \\ &= -\kappa\mu_0 M_s\mathbf{DIP}\hat{m}_1^2.\end{aligned} \tag{7.5}$$

The double $\hat{m}$ dependence suggests that the dipolar field, which is technically a Zeeman energy, can be approximated as an anisotropy energy where each of the tensor components is an anisotropy energy added to the magnetic body. More importantly, (7.5) demonstrates that the energy landscapes of the two magnetic bodies can be separated.

However, the polarization of the anisotropy energy is not as clear cut. A negative anisotropy energy encourages the magnetization toward a particular axis while a positive anisotropy energy encourages the magnetization to fall away from an axis. By contrast, regardless of polarity, Zeeman energies always apply a torque towards the axis of the external field, the perpendicular components can be considered to be negative anisotropy energies. Therefore, the perpendicular tensor components are each negative anisotropy energies.

The polarization of the longitudinal anisotropy energy is somewhat more complex. It is known that the steady state configuration of the two-magnet system is when the magnetizations are anti-parallel to one another. This is because the dipolar field reduces the magnetization energy at the free-axis. When the nanomagnets are resting along their steady-states, the longitudinal component of the anisotropy field is effectively a negative anisotropy energy. During reversal, the longitudinal component of the dipolar field reverses, making the free-axis magnetization position less stable. Here, the longitudinal component of the dipolar field behaves as a positive anisotropy energy.

Knowing this, an analytic expression for reliable coupling can be formulated. The critical field value ($H_k$) is the derivative of the energy barrier with respect to the magnetization. This can also be approximated by the magnitude of effective field along the free-axis less

the effective field at the hard-axis. Adding the dipolar anisotropies to effective field, we can formulate the following model to define the region of reliable M2 reversal:

$$DIP_{xx} + DIP_{yy} > H_{crit}. \tag{7.6}$$

The boundary of this inequality is shown in the purple dash dash-dotted line shown in Figure 7.5 and 7.6. This model perfectly matches the numerical results.

### 7.3.2 Field Requirements for Unstable System Behavior

Figure 7.5 also reveals that if $DIP_{yy}$ becomes too large, the probability that the top nanomagnet will end up left of the $\hat{x} = 0$ (thus signaling a successful reversal) at the end of the transient simulation is close to 50%. This is because a very large $DIP_{yy}$ component will create a stable, low-energy state, along $\hat{y}$.

We previously mentioned that the longitudinal component of the dipolar field behaves as a negative anisotropy energy while the nanomagnet system is resting in a stable magnetization state along the free-axis. The free-axis is defined as the lowest-energy axis in the magnetization landscape. The meta-stable state can only occur when the energy while the anti-parallel magnetizations oriented along $\hat{y}$ is lower than the energy when the magnetizations are anti-parallel along $\hat{x}$. Therefore the meta-stable state occurs when the perpendicular anisotropy field exceeds the longitudinal steady-state, anisotropy and zeeman fields:

$$DIP_{yy} > DIP_{xx} + H_{crit}. \tag{7.7}$$

The boundary of this region is shown in a red dotted line in Figure 7.5 and 7.6 and matches the numerical results.

It is important to note that this meta-stable state only exists because the driving current of the bottom nanomagnet is low to maximize the coupling strength in the system. It is

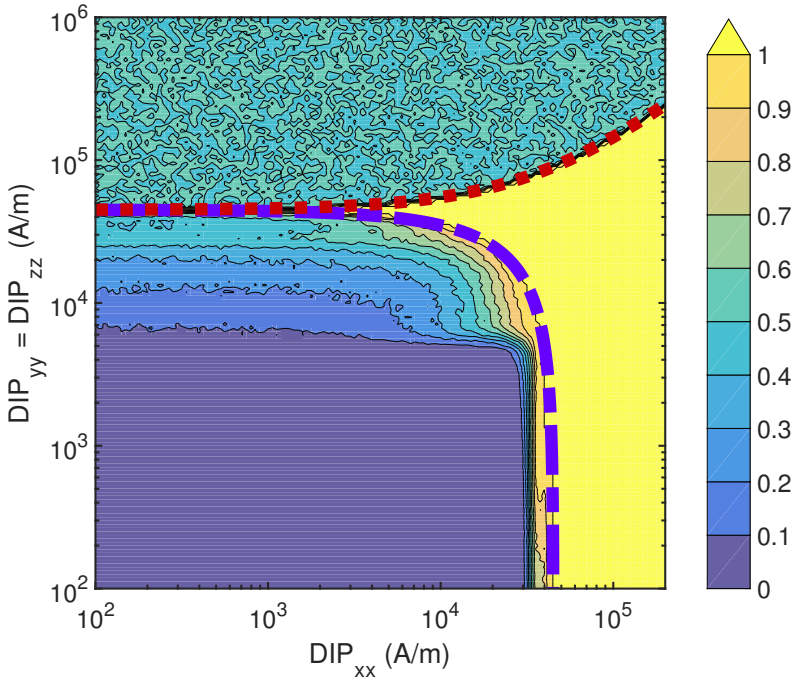


Figure 7.6: Probability of top nanomagnet reversing in a $\hat{z}$ - stacked and centered two-magnet biaxial system. Assuming two $60\text{nm} \times 45\text{nm} \times 2\text{nm}$ iron magnets. Bottom nanomagnet is driven by a $1.0\text{mA}$ spin current. The the dipolar coupling between the nanomagnets is altered by manually changing the magnitudes of the dipolar tensor components. $DIP_{yy}$ and $DIP_{zz}$ are set to be equal. Colors of the shaded region correspond to the probability of reversal for the top and bottom magnets. Area to the right of the purple dash-dot line corresponds to values adhering to (7.6). Area to left of red dotted line corresponds to values adhering to (7.7). Each axis consists of 40 logarithmically spaced data points per decade.

possible to eliminate this meta-stable state by increasing the spin current into the bottom nanomagnet, forcing its magnetization to be parallel with the free-axis. Doing so would weaken the coupling strength between the nanomagnets. Not only would it break the mutual coupling effect, but high-bias reversals are also likely to produce other undesirable physical effects in real-world systems as discussed in Section 7.2.

### 7.3.3 Effect of Damping on Coupling Strength

While the damping coefficient in a bulk iron nanomagnet is known to be low, in many other materials the damping torque can be quite larger [91]. Because $\alpha$ significantly impacts the dynamics of the nanomagnet system, the relation of $\alpha$ to the coupling strength must also

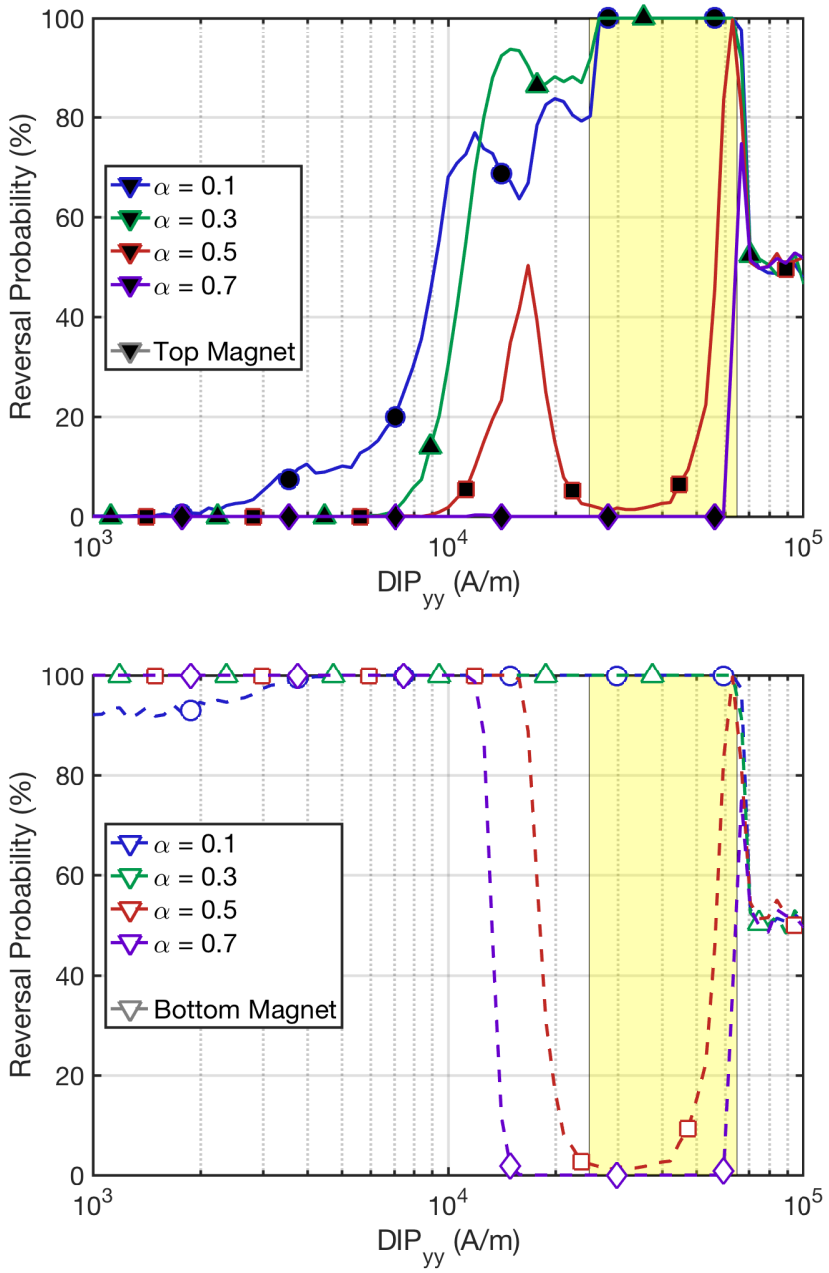


Figure 7.7: A one-dimensional version of the analysis conducted in Figure 7.5 looking at the reliability of coupling as a function of the $DIP_{yy}$ component magnitude. Assuming two $60\text{nm} \times 45\text{nm} \times 2\text{nm}$ iron magnets and $DIP_{xx} = 2 \times 10^4 \frac{\text{A}}{\text{m}}$. Bottom nanomagnet is driven by a $3.0\text{mA}$ spin current. Yellow shaded region corresponds to region of perfect coupling predicted by (7.6) and (7.7). Line colors and marker style corresponds to a particular $\alpha$ value. Line style and marker face color correspond to top or bottom nanomagnet reversal reliability. Figure demonstrates $\alpha$ does not alter the coupling strength of the system, but may alter the critical current required to reverse the bottom nanomagnet.

be addressed.

Knowing that the $DIP_{zz}$ component does not affect the coupling reliability of biaxial systems, Figure 7.7 performs a one-dimensional version of the tensor shape analysis conducted in Figure 7.5 for different $\alpha$ values. First notice that in this figure we have increased the driving current to 3 mA compared to the 1 mA current used in Figure 5. This is to ensure the driving current is larger than the critical current of the nanomagnet with the largest alpha value. Figure 7.7 demonstrates that for small values of $\alpha$, the coupling strength remains largely unchanged and matches the analytic expressions well.

However, for larger values of $\alpha$, the reversal of the top magnet is largely eliminated. The coupling strength of the system is not reduced, but rather the probability that the bottom nanomagnet will reverse goes to zero as the $DIP_{yy}$ value nears the region required for reliable coupling. This suggests that the critical current required to reverse the bottom nanomagnet is altered if the requirements for mutual coupling are met.

It can also be concluded that $\alpha$ does not alter the coupling strength between nanomagnets. It does however, alter the critical requirement for reversing one of the nanomagnet bodies. This can be more directly observed in Figure 7.8. This figure demonstrates the maximum current before the mutual coupling effect breaks remains the same regardless of $\alpha$. However, as $\alpha$ is increased, the minimum current required to reverse the system is also increased. For very large values of alpha, the minimum current exceeds the current cap for the mutual coupling effect. This is because the reversal time of a nanomagnet is proportional to $I_s - I_c$. Hence, for very-large $\alpha$ systems, a spin current even slightly larger than $I_c$ may cause very rapid reversals which harms the mutual coupling effect as noted in Section 7.2.

## 7.4 Coupling in Uniaxial Nanomagnets

As mentioned in Section IV, the energy landscape greatly alters magnetization trajectories during reversal. Having derived analytic predictive models for reliable coupling in biaxial

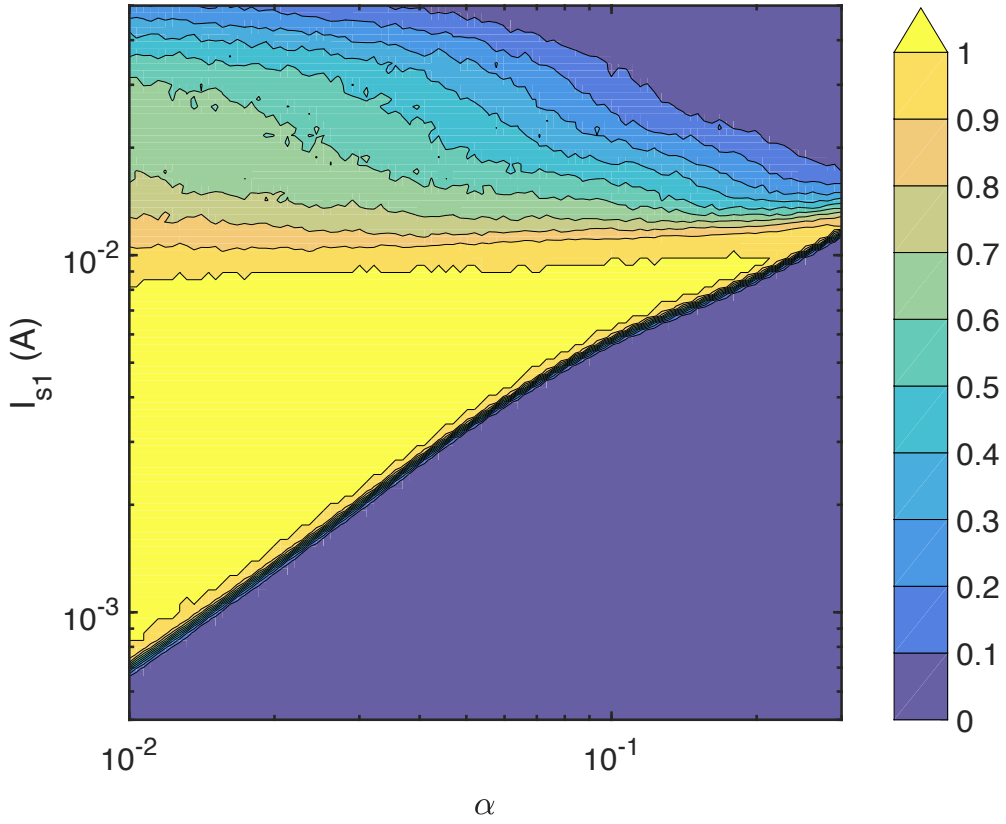


Figure 7.8: Analyzing the reversal probability of the top nanomagnet for a $60\text{nm} \times 45\text{nm} \times 2\text{nm}$ Fe Nanomagnet system with a separation of $5nm$ as a function of $\alpha$ and $I_s$. $I_s$ needs to be large enough to reverse the bottom nanomagnet, but if it is too large, the mutual coupling between the nanomagnets is broken and the coupling strength is reduced. This follows results obtained in Section 7.2. $\alpha$ does not alter the coupling strength, but it does increase the critical current required to reverse the bottom nanomagnet. This increase in $I_c$ means that if $\alpha$ is large enough, any $I_s > I_c$ will break the mutual coupling condition and reduce the coupling strength to the fats reversal case.

nanomagnet systems, we can do the same for uniaxial systems. For the uniaxial case, slightly modified models are needed to encapsulate the increase in coupling strength seen in Figure 7.2.

### 7.4.1 Model for Reliable Coupling in Uniaxial Systems

An analysis of sample reversal precessions (shown in Figure 7.4) demonstrates a key difference between the SHd and 0Hd cases. In the 0Hd case, during the reversal of the bottom nanomagnet, the magnetization deviates further away from the $\hat{x}$-$\hat{y}$ plane. This pushes the

magnetization of the top nanomagnet further away from the $\hat{x}$-$\hat{y}$ plane because of the larger $\hat{z}$ field component generated by the bottom nanomagnet. Unlike the SHd case, the $\hat{z}$ component of the dipolar tensor will have a significant contribution to the coupling strength of the overall system.

This can be more clearly seen in Figure 7.9. Similar to the test performed in Figure 7.5, the longitudinal component of the dipolar tensor is held constant while the perpendicular components are varied. The only difference is that in Figure 7.9, the demagnetization field is eliminated.

Figure 7.9 demonstrates that when $DIP_{zz}$ is very small, the probability of coupling while altering the magnitude of $DIP_{yy}$ follows the trend demonstrated in the biaxial case. There is a minimum value which ensures perfect coupling. The same can be seen when $DIP_{yy}$ is small and the magnitude of $DIP_{zz}$ is varied. This is because when these two perpendicular components are mismatched, the reversal trajectory will favor either the $\hat{x}$-$\hat{y}$ or $\hat{x}$-$\hat{z}$ plane during reversal. As a result, the system will reduce to the biaxial coupling case. We can assume at minimum, the model proposed for the biaxial case, (7.6), is applicable to each of the perpendicular components individually and so, perfect coupling is guaranteed if:

$$\begin{cases} DIP_{xx} + DIP_{yy} > H_{crit}, & \text{(7.8a)} \\ DIP_{xx} + DIP_{zz} > H_{crit}. & \text{(7.8b)} \end{cases}$$

where "{" denotes the union of the system of inequalities. The boundaries of this model are shown in the purple dash-dot line in Figure 7.9 and strongly match the numerical results when the magnitudes of $DIP_{yy}$ and $DIP_{zz}$ are significantly different. This is further proof that the dipolar field can be approximated as an internal anisotropy field since the addition of the dipolar anisotropies creates biaxial behavior from uniaxial magnetic bodies.

However, it is evident that this model alone is incomplete. The case where $DIP_{yy} \approx DIP_{zz}$ is of particular interest because two-magnet, stacked uniaxial systems typically have square-shaped geometries and hence, should have equal perpendicular components in their

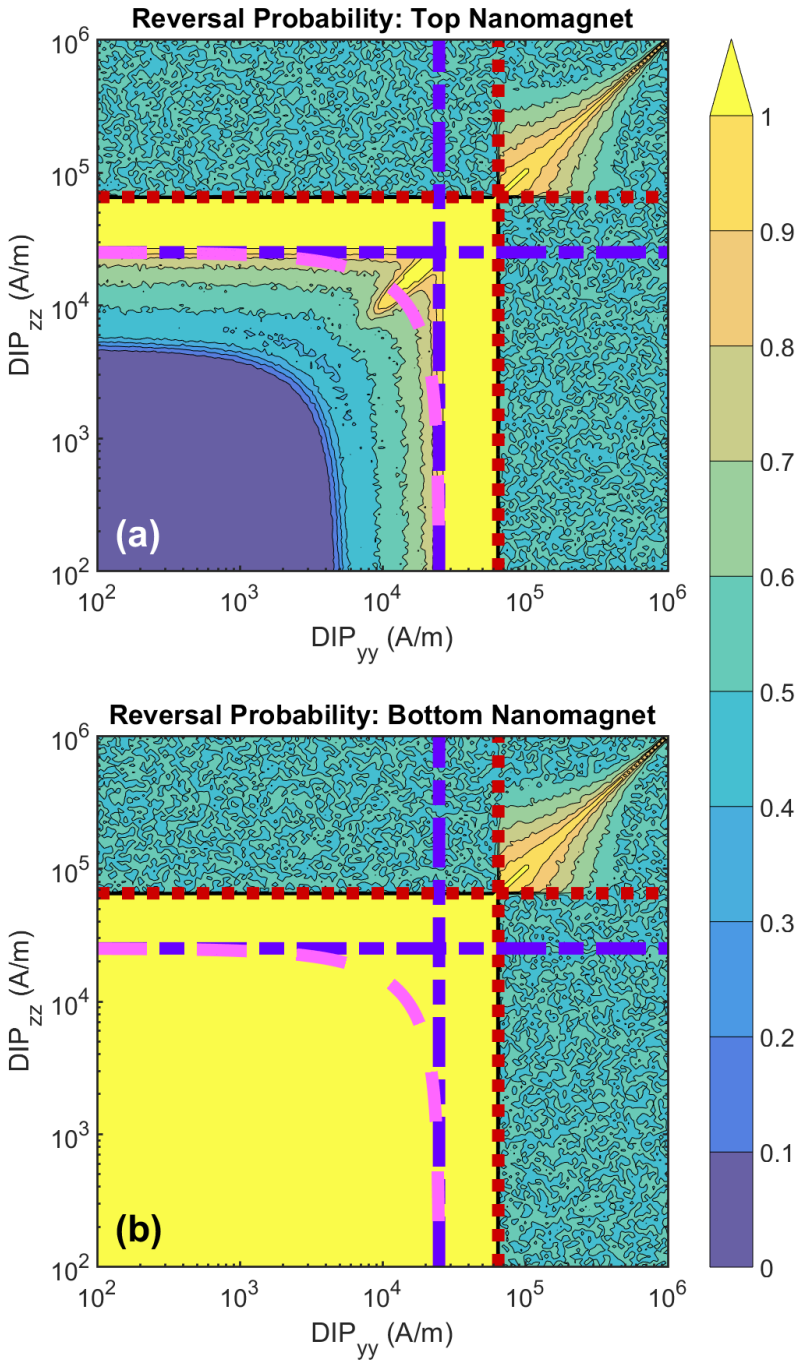


Figure 7.9: Probability of each nanomagnet reversing in a $\hat{z}$ - stacked and centered two-magnet uniaxial system. Assuming two $60\text{nm} \times 45\text{nm} \times 2\text{nm}$ iron magnets. Bottom nanomagnet is driven by a $0.15\text{mA}$ spin current. The the dipolar coupling between the nanomagnets is altered by manually changing the magnitudes of the dipolar tensor components. $DIP_{xx} = 2 \times 10^4 \frac{\text{A}}{\text{m}}$ while the $DIP_{yy}$ and $DIP_{zz}$ components of the tensor model correspond to the values marked by the x and y axes of the graph respectively. Colors of the shaded region correspond to the probability of reversal for the top (a) and bottom (b) magnets. Area to the right of the purple dash-dot line corresponds to values adhering to (7.8). Area to left of red dotted line corresponds to values adhering to (7.10). Area to right of pink dashed line corresponds to (7.9).

dipolar tensor [73, 85]. When the perpendicular components are approximately equal, the boundaries suggested by (7.8) are clearly pessimistic. This is because when $DIP_{yy}$ and $DIP_{zz}$ are both large and within the same order of magnitude, both tensor components significantly contribute to the reversal of M2 doubling the impact of the perpendicular field components.

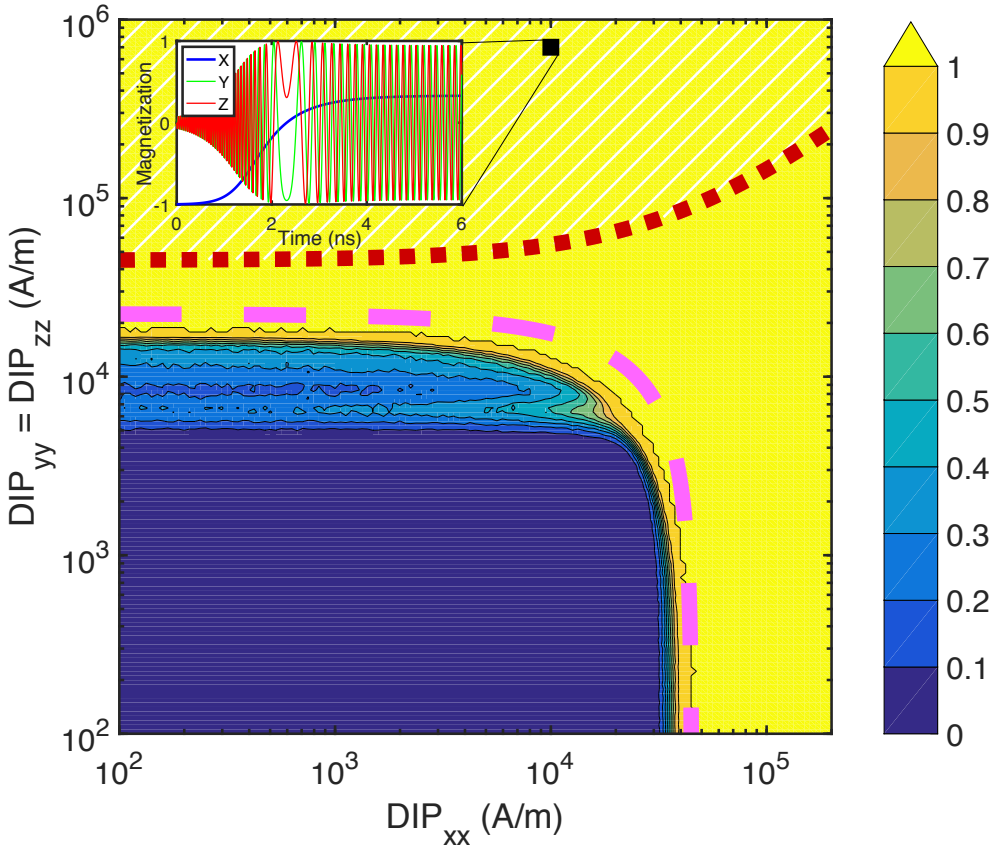


Figure 7.10: Probability of top nanomagnet reversing in a $\hat{z}$ - stacked and centered two-magnet uniaxial system. Assuming two $60\text{nm} \times 45\text{nm} \times 2\text{nm}$ iron magnets. Bottom nanomagnet is driven by a $0.15\text{mA}$ spin current. The dipolar coupling between the nanomagnets is altered by manually changing the magnitudes of the dipolar tensor components. $DIP_{yy}$ and $DIP_{zz}$ are set to be equal. Colors of the shaded region correspond to the probability of reversal for the top and bottom magnets. Area to the right of the purple dash-dot line corresponds to values adhering to (7.9). Each point on the plot is calculated with 1000 transient simulations and each axis consists of 40 logarithmically spaced data points per decade. The perpendicular components create a net easy plane anisotropy. If this easy plane anisotropy is too large, the magnetization will favor a oscillatory state denoted by the hatched region. However, the spin current can still nudge the oscillating magnetization towards the correct free axis.

Figure 7.9 shows that the lower limit for reliable coupling can be approximated by:

$$DIP_{xx} + DIP_{yy} + DIP_{zz} > H_{crit}. \tag{7.9}$$

The boundary of this model is shown in the pink dashed line in Figures 7.9 and 7.10. While (7.9) slightly overestimates the critical parameters required for perfect coupling, it is a fairly accurate approximation. Interestingly this approximation only holds true if the two precessional components are very similar in magnitude. If $DIP_{yy}$ and $DIP_{zz}$ differ by a factor of 2 or greater, the coupling can no longer be considered reliable outside of the region denoted by (7.8).

### 7.4.2 Field Requirements for Unstable System Behavior

If the perpendicular components of the dipolar field are too large, the system may find a steady state away from the free-axis. This alternate steady-state is again shown in the camouflage pattern regions in Figure 7.9. For systems with mismatched perpendicular components, it is possible to expand the models from the in-plane case to determine the areas where the system will find alternate steady states:

$$\begin{cases} DIP_{yy} > DIP_{xx} + H_{crit}. & \text{(7.10a)} \\ DIP_{zz} > DIP_{xx} + H_{crit}. & \text{(7.10b)} \end{cases}$$

The boundaries of (7.10) are shown as red dotted lines in Figure 7.9. Interestingly, if there is a large mismatch between the perpendicular components of the $DIP$ tensor, the field requirements for a meta-stable steady-state are equivalent to the biaxial case and agree well with the numerical results. This is because if one perpendicular field component is significantly larger than the other, the nanomagnet precessions will favor one magnetization dimension over the other. This follows previous experimental works which noted biaxial behavior in coupled uniaxial systems [179].

It is clear from the figure that this model is accurate while the inequalities in (7.10) are mutually exclusive. However, the case where $DIP_{yy} = DIP_{zz}$ is special. If the two perpendicular components of the dipolar tensor are equal and the inequalities in (7.10) are both true, it means that the system will have a low-energy oscillatory state around the $\hat{x}$ axis. With the application of spin current, the bottom nanomagnet will trend towards the free axis. The top nanomagnet is driven towards the anti-parallel free-axis. Figure 7.10 shows that if the perpendicular components of the tensor are exactly equal, the reversal is perfectly reliable. This is due to the fact that the simulation measures a successful reversal as anytime the top nanomagnet ends the transient simulation on the correct side of the energy barrier. As seen in the inset of Figure 7.10, the equal, large perpendicular components of the field create an oscillatory state which the spin current nudges towards the free-axis. Even though the simulation can be technically categorized as a successful reversal, the magnetization is still in a oscillatory state which will fall back to the $\hat{x} = 0$ plane when the spin current is turned off.

### 7.4.3 Effects of Perpendicular Component Polarity

Recall that $\kappa$ parameter in (7.3) indicates the polarity of the diagonal tensor components and is solely dependent on the geometric arrangement of the two magnetic bodies. Up until this point, a $\kappa = [-1, -1, 1]$ has been used that would correspond to two nanomagnets with a free-axis along $\hat{x}$ and physically stacked along the $\hat{z}$ axis. However there are other possibilities for the polarity of the dipolar components. If the free-axis of the magnetic bodies are along $\hat{z}$-axis, perpendicular components of the dipolar field would have equal polarity.

An evaluation for a 0Hd system with equal-polarity perpendicular DIP components is shown in Figure 7.11. Comparing Figures 7.9 and 7.11, we see significantly different coupling reliabilities when the perpendicular tensor components are roughly equal. When the polarity of the perpendicular components are different, as in Figure 7.9, the coupling is en-

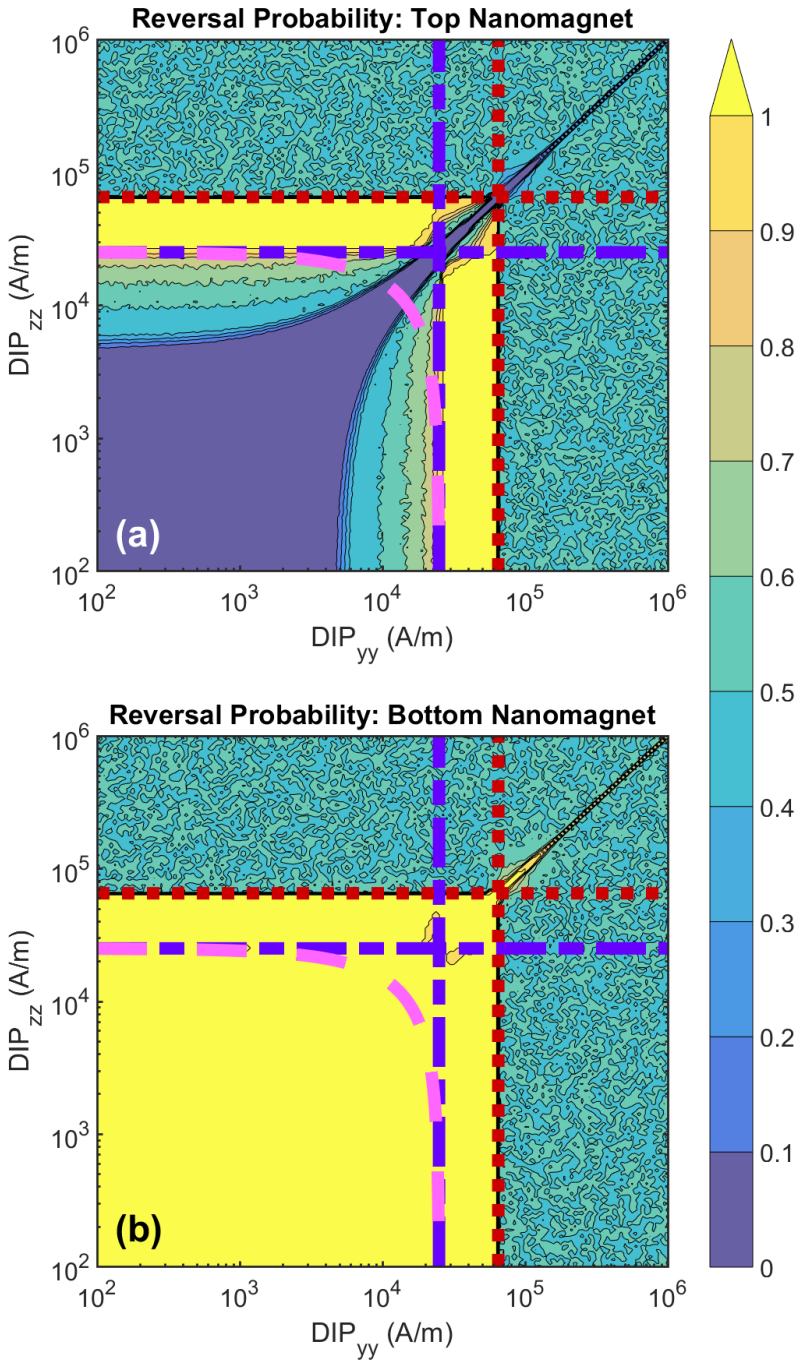


Figure 7.11: Identical test performed as in Figure 7.9 except the polarity of the dipolar tensor is changed so that $\kappa = [-1, -1, -1]$. Hence, in this case, the perpendicular components of the dipolar tensor have equivalent polarity. It is evident that have perpendicular dipolar components of equal magnitude and polarity negates the mutual coupling effect.

hanced with equal perpendicular components. In contrast, the coupling is nearly eliminated when the polarity of equal perpendicular components are the same.

This is because the mutual coupling effect relies on complex interaction between magnetic bodies. If both perpendicular components have an equal polarity and magnitude, it is effectively the same as having an equal anisotropy energy along both perpendicular axes. In such a case, the energy gradient becomes normalized so that the perpendicular components combine. They get added to the free-axis energy and are effectively negated. This is not a problem for biaxial systems since the demagnetization field negates one of the perpendicular components.

We can summarize the $\kappa$'s effect on the MCE in uniaxial systems as follows: the polarity of the longitudinal component of the dipolar tensor determines if the system has a parallel (+) or anti-parallel (-) stable state configuration. Assuming the perpendicular components differ by a factor $> 2$, you can use the larger perpendicular to determine if a two-magnet system is reliably coupled according to (7.10). If the perpendicular components are of equal magnitude, the MCE is enhanced if the the perpendicular components have opposing polarities and negated if they have equal polarities.

## 7.5 Material Parameter Requirements for Reliable Coupling

The analytic models presented allow for the determination of the material parameters required for reliably coupled systems. Referring back to Figure 2.1, in-plane and PMA nanomagnet bodies are both subsets of biaxial and uniaxial systems, respectively. Magnets with uniaxial energy landscapes can also be fabricated using bulk material shaped into a rectangular prism as shown Figure 6.1. By making the nanomagnet width and thickness equal, the shape anisotropies along the two longest axes have no net effect on the precessional dynamics of the system. Similarly, a biaxial system can be created from two-uniaxial magnets if the perpendicular components of the dipolar tensor are severely unbalanced as mentioned Section 7.4. This is why the coupling analysis was performed using the abstracted biaxial and uniaxial landscapes. Now having completed those analyses, the models derived can be applied to more realistic in-plane and PMA nanomagnets assuming a CHd fields.

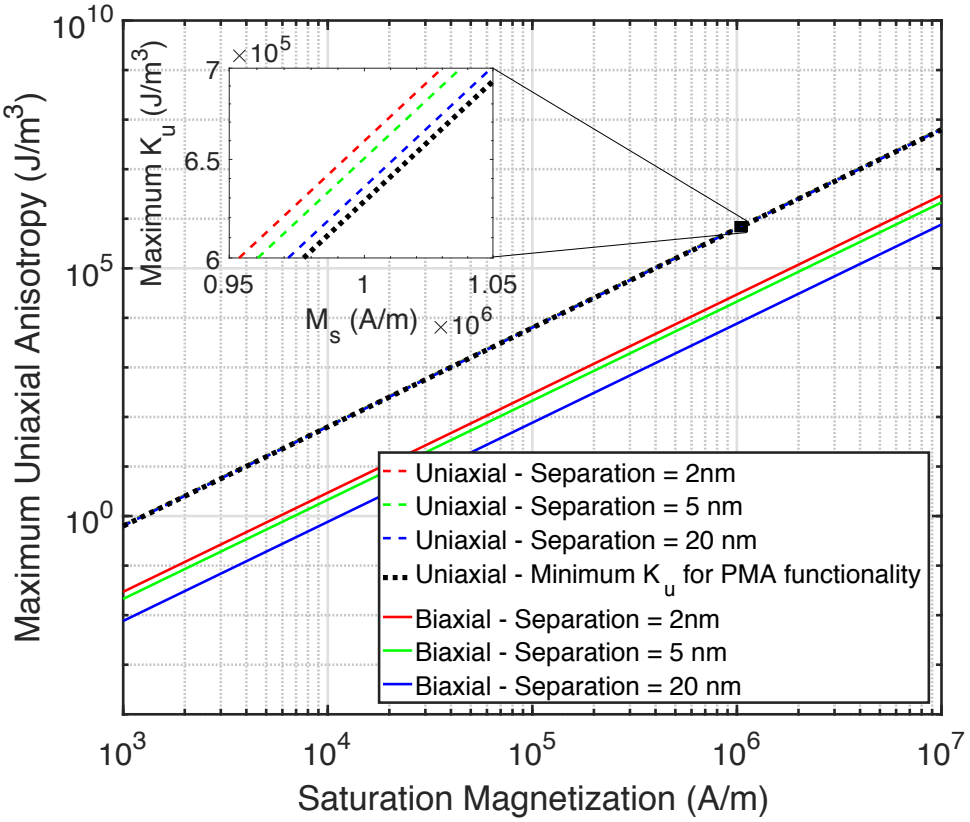


Figure 7.12: *Solid lines*: Maximum $K_u$ per $M_s$ value for a in-plane, $60\text{nm} \times 45\text{nm} \times 2\text{nm}$, two-magnet systems with a separation of $2\text{nm}$. Free-axis along $\hat{x}$. Various separations are considered and SHd is assumed. *Dashed colored lines*: maximum $K_u$ parameters for PMA, $45\text{nm} \times 45\text{nm} \times 2\text{nm}$, two-magnet system whose uniaxial anisotropy energy and free-axis oriented along $\hat{z}$. *Dashed black line*: For uniaxial nanomagnets, uniaxial anisotropy field must be greater than the demagnetization field creating a minimum required anisotropy energy. This figure demonstrates that uniaxial nanomagnet systems have strict material requirements for reliable reversal.

### 7.5.1 Parameter Requirements for In-plane Nanomagnet Systems

The in-plane case corresponds to a SHd energy space. Typically, the free-axis for in-plane nanomagnets is oriented along the physically longest geometric dimension and is assumed to be along $\hat{x}$ for a $60\text{nm} \times 45\text{nm} \times 2\text{nm}$ thin-film nanomagnet. Figure 7.12 shows the maximum $K_u$ given an $M_s$, which still allows for reliable coupling. $K_u$ values which exceed this maximum make the energy barrier too large for the dipolar field to consistently overcome. While iron nanomagnets fall just below this limit, materials with larger energy

barriers, such as cobalt, exceed this limit and will not be reliably coupled at any separation. Other materials with small crystalline anisotropies such as Nickel and Terfenol-D would be useful for creating coupled in-plane magnetic systems as well.

### 7.5.2 Parameter Requirements for PMA nanomagnet Systems

PMA nanomagnet systems have both their uniaxial-anisotropy and demagnetization fields oriented along $\hat{z}$ [82]. This matches the uniaxial case considered here. Assuming a pair of $45\text{nm} \times 45\text{nm} \times 2\text{nm}$ PMA nanomagnets making the perpendicular components of the dipolar tensor in this system equal. Note that since the PMA magnets are stacked and have a free-axis along the $\hat{z}$ axis, they will have perpendicular components with the same polarity. As noted in Section 7.4.3, the mutual coupling effect is effectively negated if the perpendicular dipolar components have equal polarity and magnitudes. The reliability of coupling then reduces to the simple longitudinal model. You can arrange the PMA bodies side-by-side along $\hat{x}$ instead of stacking them vertically. In this case, $\kappa = [1, -1, -1]$, meaning that the perpendicular components are opposing polarities with respect to the free-axis. In this case, the distance between the centers of the magnetic bodies would be significantly larger, significantly reducing the dipolar field magnitude. The $\hat{z}$-stacked system is optimal even though the strength of the dipolar field is reduced to the longitudinal field model.

The dashed lines in Figure 7.12 shows the maximum $K_u$ for a PMA nanomagnet system. Unlike the in-plane case, there is also a minimum $K_u$ because $H_K$ must be greater than $H_D$ in order to create two stable minimas. There is a very small range of material values which allow for a coupled PMA nanomagnet system.

# CHAPTER 8
# DIPOLAR COUPLING III: ANALYTIC EXPRESSIONS FOR NON-IDENTICAL BIAXIAL TWO-MAGNET SYSTEMS

## 8.1 Introduction

In the previous chapter, analytic models of reliable magnetization reversal driven by dipolar coupling in an identical two-magnet system were developed [174, 180]. Since the magnetization of identical nanomagnets precess in-step, it becomes possible to decouple the magnetic bodies. In this case, dipolar fields behave as magnetic anisotropy altering the energy space of the nanomagnets. In this chapter, we extend our prior analysis to consider dipolar coupling in non-identical two-magnet systems. This is a more general case applicable to a broad range of coupled nanomagnetic devices and circuits. We formulate new models that accurately predict conditions under which deterministic stable coupling between the magnets is established. New reversal dynamics that emerge due to the increased complexity and lack of symmetry in the setup are carefully analyzed in this chapter. We consider two categories of reversals, namely deterministic- and pseudo-reversals. The latter reversals are stochastic in nature and require complex Fokker-Plank analysis. While we discuss the pseudo-reversal regime, analytic models for this region are outside the scope of this thesis.

In the non-identical two-magnet system, there exists a robust or deterministic stable-reversal regime in which the two non-identical magnets remain in their parallel or anti-parallel configurations along their free-axes regardless of stochastic effects [180]. There also exists a deterministic meta-stable regime in which the nanomagnets reverse toward the perpendicular axes within the plane, a 90-degree rotation). We identified a new oscillatory state in which the nanomagnet being driven oscillates in-plane around its out-of-plane ($\hat{z}$) axis. We also note that large perpendicular dipolar field components may cause some instability in systems in the presence of thermal noise.

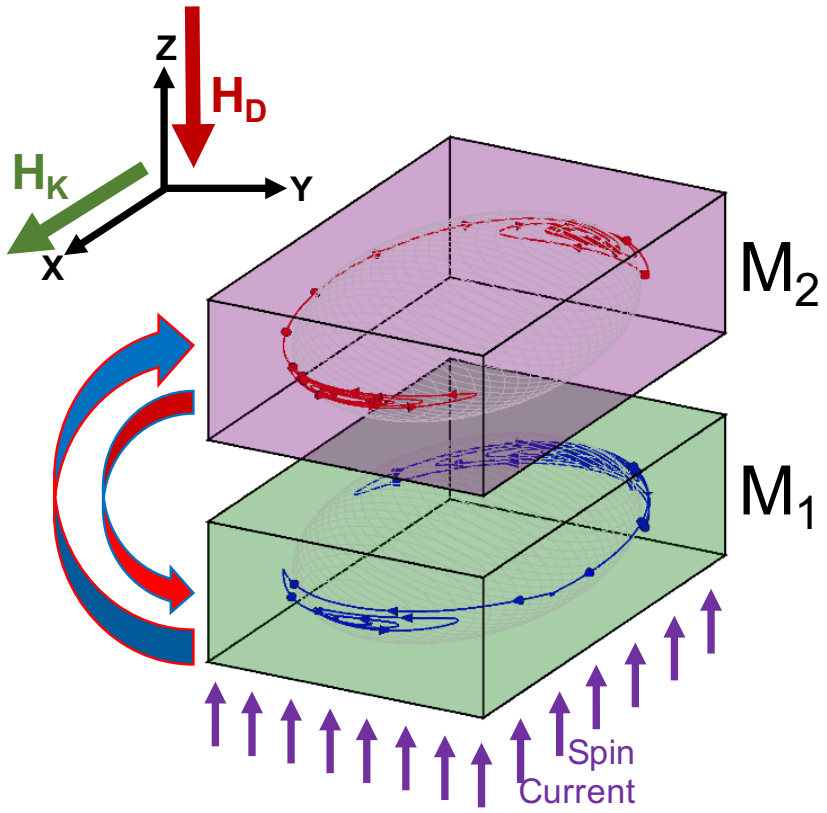


Figure 8.1: Illustration of two-magnet system considered in this study. Bottom magnet (M1) is driven through spin-transfer torque, while the top magnet (M2) is driven through the dipolar coupling field generated by the bottom magnet M1. Note that the magnetic bodies are shaded in different colors to represent their different material parameters. $H_K$ denotes the uniaxial field along the free-axis of the magnets, while $H_D$ is the demagnetization field oriented perpendicular to the plane of the magnets.

## 8.2 General Formalism

The non-identical two-magnet system under study is illustrated in Figure 8.1. Both magnets are assumed to be mono-domain bodies, labeled as M1 and M2, with biaxial magnetic anisotropy. The magnet denoted as M1 is subject to a spin current imparting a finite spin torque to it. As M1 reverses, it interacts with the magnet denoted as M2 through a time-dependent dipolar field encouraging M2 to reverse its orientation. Because we are analyzing non-identical magnets in this chapter, we have two sets of material parameters, $M_{s1}|M_{s2}$ and $K_{u1}|K_{u2}$ where the subscript indicate which nanomagnet the parameters corresponds to. We're keeping the geometry of the magnetic bodies equivalent ($60\text{nm} \times 45\text{nm} \times 2\text{nm}$)

because we are artificially assigning values to the dipolar tensor components. The exact geometry is largely irrelevant when determining coupling strength. The magnetic moments of M1 and M2 are specified as $\vec{M}_1 = M_{s1}\hat{m}_1$ and $\vec{M}_2 = M_{s2}\hat{m}_2$, where $\hat{m}_1$ and $\hat{m}_2$ are the corresponding unit vectors. The magnetization energies of the mono-domains are

$$\epsilon_1(\hat{m}_1) = \epsilon_{K1}(\hat{m}_1) + \epsilon_{D1}(\hat{m}_1) + \epsilon_{DIP1}(\hat{m}_2, \hat{m}_1), \tag{8.1a}$$

$$\epsilon_2(\hat{m}_2) = \epsilon_{K2}(\hat{m}_2) + \epsilon_{D2}(\hat{m}_2) + \epsilon_{DIP2}(\hat{m}_1, \hat{m}_2), \tag{8.1b}$$

Unlike before, we are assuming non-equivalent dipolar tensors denoted by $\mathbf{DIP_1}$ and $\mathbf{DIP_2}$ corresponding to the stray field emitted by M1 and M2 respectively. In this chapter, we are only assuming a biaxial, SHd mono-domain, the effect of shape anisotropy is captured through demagnetizing coefficients, $N_{xx}$ = $N_{yy}$ = 0, $N_{zz}$ = 1.

For the majority of this chapter, we assume that spin current is injected only into M1 to drive the reversal of the coupled system. In Section 8.8.1, spin current injection into M2 is also considered. This setup allows us to study magnetization dynamics that emerge due to the interaction of opposing non-conservative forces in dipolarly coupled magnets. Values of $M_s$ and $K_u$, uniaxial energy density, of both nanomagnets are varied for the results reported in this chapter.

## 8.3 Regions of Reversal

The key differences in a coupled system with non-identical magnets compared to identical magnets are:

- Unequal energy barriers ($\epsilon_{K1} \neq \epsilon_{K2}$)
- Unequal dipolar fields ($\mathbf{DIP_1} \neq \mathbf{DIP_2}$)

To understand the coupling strength of the two-magnet system, we consider different material parameters of the two nanomagnets, while also varying the magnitudes of the tensor

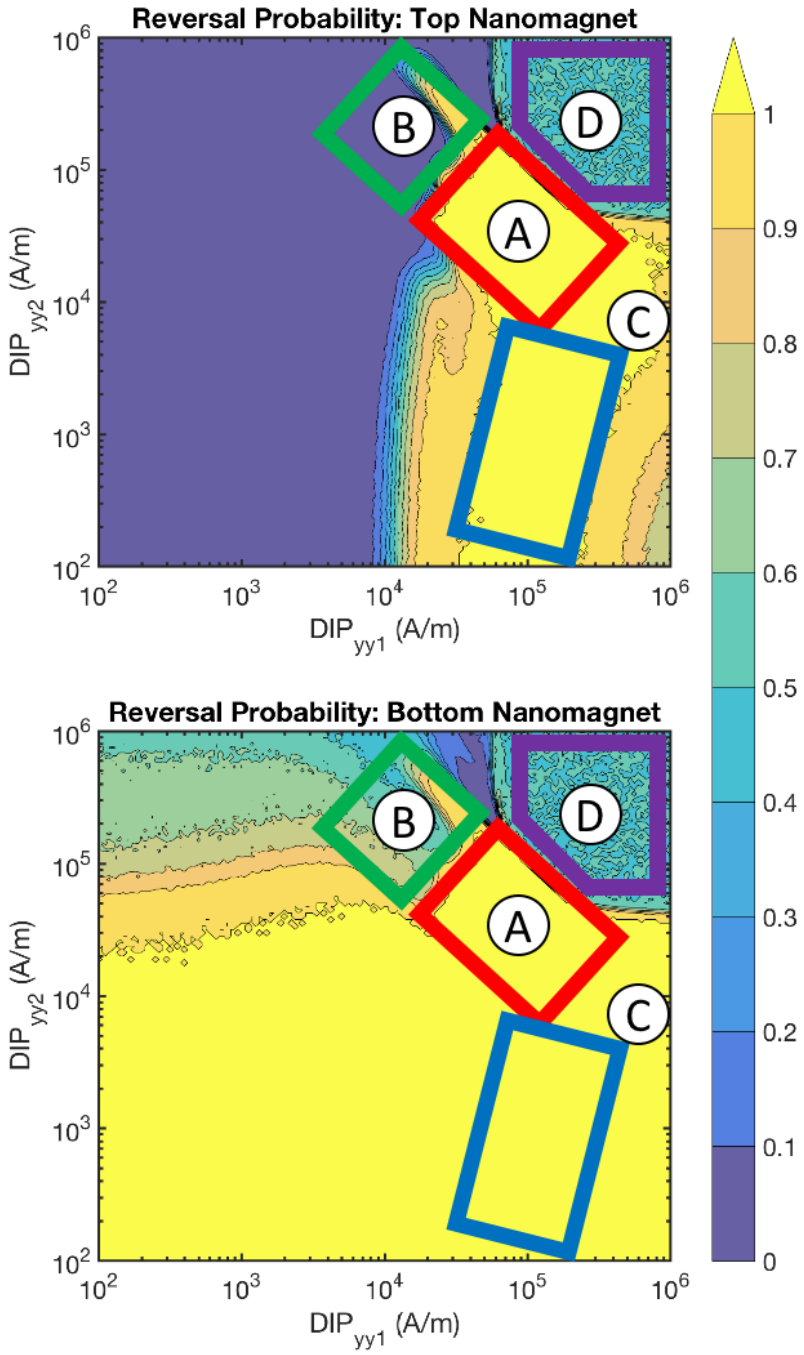


Figure 8.2: Probability of magnetization reversal obtained under TOTTHERM setup. The bottom magnet is M1 (under spin torque), while the top magnet is M2 as illustrated in Figure 8.1. Rectangular outlines bound regions that display distinct magnetization dynamics for which analytic models are developed. The area bounded by the red rectangle corresponds to the deterministic stable reversal region. The area within the green rectangle is the M1 oscillatory region. The blue rectangle outlines the pseudo reversal region, while the purple rectangle outlines the meta-stable reversal region. The circled letters correspond to sample reversals shown in Figure 8.3.

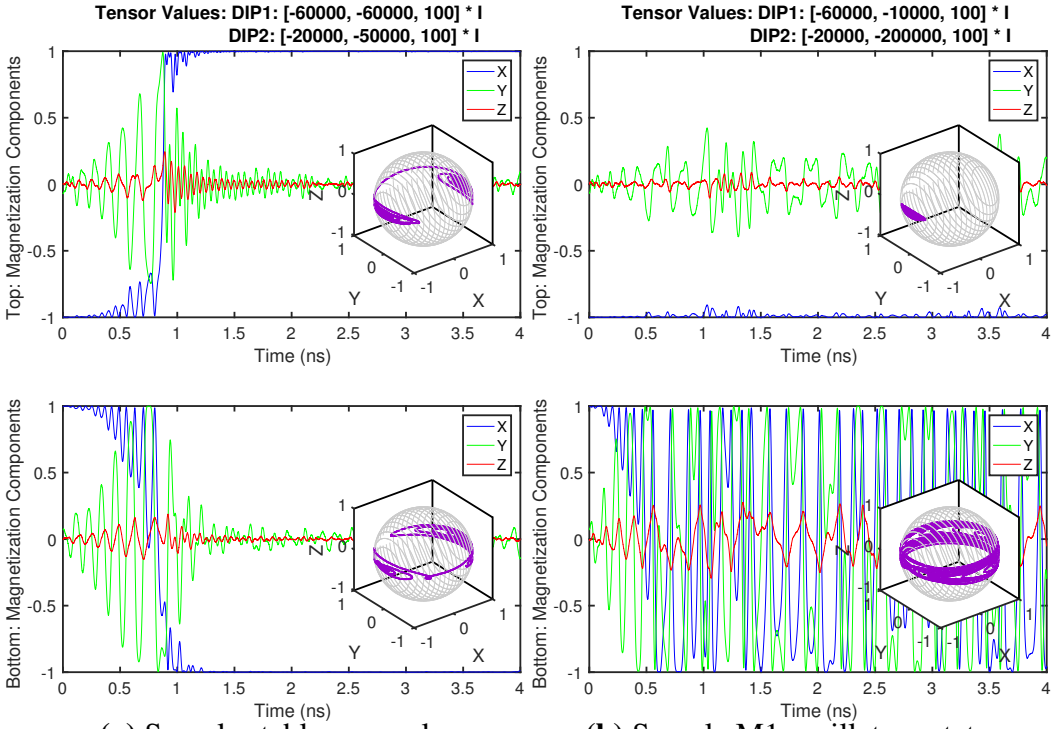


**(a)** Sample stable reversal **(b)** Sample M1 oscillatory state

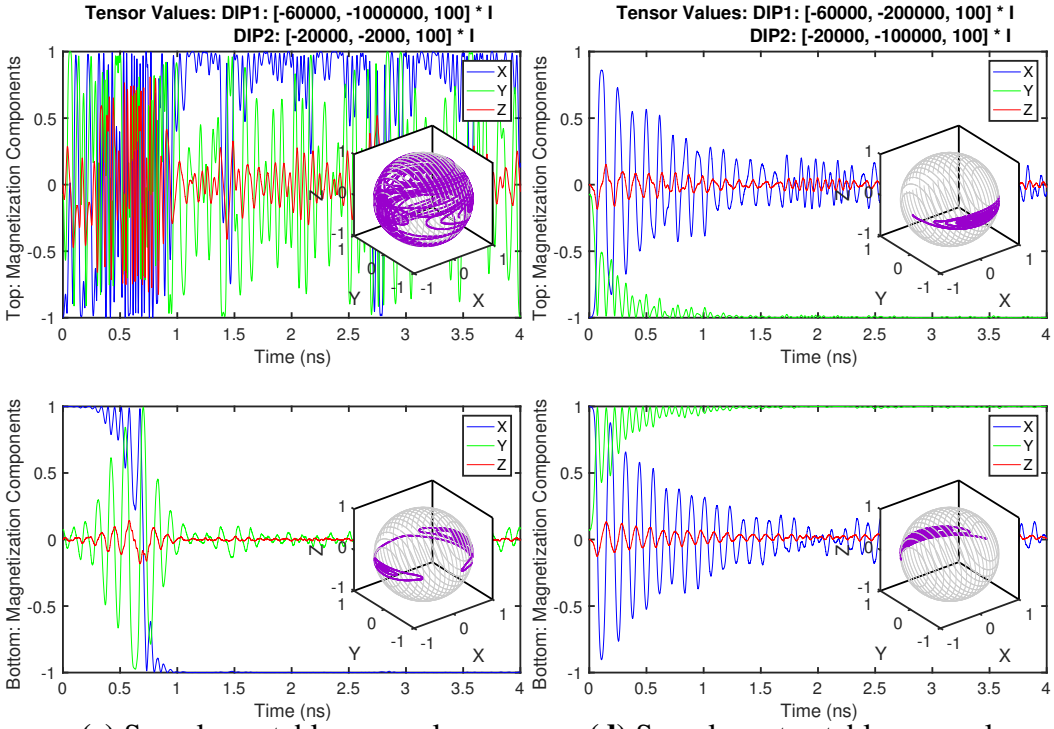


**(c)** Sample unstable reversal **(d)** Sample meta-stable reversal

Figure 8.3: Sample trajectories of each reversal region corresponding to the markers seen in Figure 8.2. Assuming TOTTHERM conditions. Non-identical magnetic bodies considered with material parameters $M_{s1} = 1.7\frac{MA}{m}|M_{s2} = 1.4\frac{MA}{m}$ and $K_{u1} = 48\frac{kJ}{m^3}|K_{u2} = 80\frac{kJ}{m^3}$ and longitudinal tensor components $D_{xx1} = -60\frac{kA}{m}$ and $D_{xx2} = -20\frac{kA}{m}$. We vary the perpendicular components displaying the trajectory characteristics of each of the reversal regimes.

components in the simulation setup. In the previous chapter, the analysis of dipolar coupling in a two-magnet system was focused solely on identical nanomagnets. This simplification allowed us to more easily interpret the results due to the inherent symmetry in the setup. However, in the case of non-identical nanomagnets, the number of system variables is doubled, increasing the system complexity. To address this, we construct the two-magnet system to possess a common geometric axis. The mono-domains are centered with respect to each other and the off-diagonal dipolar tensor components will be averaged out and set equal to zero. The only relevant parameters of the system are the material parameters of the magnetic bodies and the three diagonal tensor components of the dipolar field. To constrain the complexity of the system further, a system of biaxial mono-domains is analyzed. A large positive perpendicular anisotropy restricts the magnetization to precess largely in-plane minimizing the effect of dipolar field along the perpendicular orientation. Given the nature of the precession, it is reasonable to ignore one of the perpendicular tensor components in a biaxial system. This reduces the rank of the dipolar tensor such that only the longitudinal and one of the perpendicular field components suffice to describe the effects of the dipolar field.

To analyze the field requirement for robust coupling, Monte-Carlo tests on the sLLG of the coupled system are performed by varying uniaxial energy density, $K_u$, and saturation magnetization, $M_s$. Effects of magnet geometry and Gilbert damping are considered in Sec. 8.7 as these parameters affect coupling only under thermal activation or slow dynamics.

The longitudinal field magnitude required for reversing a M2 is given as

$$H_{crit2_X} = H_{k2} + (N_{yy} - N_{xx})\, M_{s2}. \tag{8.2}$$

If the longitudinal component of the dipolar field of M1, $DIP_{xx1}$, is greater than the critical field magnitude of M2, $H_{crit}$, M2 will be reliably coupled to M1 regardless of the preces-

sion of M1. If the longitudinal component of the dipolar field of M2, $DIP_{xx2}$, is larger than $H_{crit1_X}$ then the dynamics of the system become unstable. In this case, the coupling of the system depends critically on the relative magnitudes of $DIP_{xx1}$ and $H_{crit2_X}$ during the reversal of M1. For certain cases, it is likely that the system will be oscillatory, particularly if the strength of the STT is weak. However, a large perpendicular component of the dipolar tensor can enhance the coupling between M1 and M2. To study the regime of robust coupling, specific values of $K_u$, $M_s$, $DIP_{xx}$ are chosen for M1 and M2 and the reliability of reversal of M2 is measured for a range of perpendicular tensor components $DIP_{yy1}$ and $DIP_{yy2}$.

Thermal noise is included in two ways: (i) TOTTHERM models thermal noise to be present during the entirety of the transient simulation and (ii) INITTHERM considers thermal noise to act only during the first nanosecond of simulation to achieve a random thermal distribution of initial magnetization states of M1 and M2. In both cases, spin current is injected into M1 to achieve STT-driven reversal. In both tests, spin current is injected only after the first nanosecond randomization phase. The purpose of these two tests is to highlight the deterministic and stochastic effects impacting the two-magnet system. In the TOTTHERM test, reversal is achieved through both deterministic field switching and noise drift. However, the INITTHERM case eliminates noise drift by turning off thermal noise during the system reversal. The TOTTHERM test highlights unstable system configurations that cannot be modeled using only the INITTHERM test.

A sample of the TOTTHERM test is shown in Figure 8.2. Regions denoting the four major types of reversals are outlined. The top-right of this figure within the purple enclosed boundary represents the deterministic meta-stable region (DMSR). In this case, the perpendicular tensor components grow large enough that the lowest energy state of the system is driven away from the free-axis. The green outlined region in Figure 8.2, is the M1-oscillatory region. In this case, the dipolar field of M1 acting on M2 is too weak to reverse M2, but the perpendicular component of the dipolar field of M2 interacts with M1

to create oscillations in M1 dynamics. The pseudo reversal region is marked by the blue outline in Figure 8.2. In this region, the perpendicular components of $\mathbf{DIP2}$ are weak to ensure reliable coupling of M1 and M2. Instead, the stray field created by M1 is sufficient to reverse M2 depending on the trajectory of the magnetization vectors. This region is created by thermal perturbations in M1 magnetization trajectory and can be qualified as a thermal drift effect. Finally, the red outlined region in Figure 8.2 marks the deterministic reversal region. In this region, the two magnetic bodies are strongly coupled. Each region noted in Figure 8.2 is analyzed in detail in Sections 8.4–8.7. The analysis in these sections follows the coupling tests shown in Figure 8.4. Tests are conducted for three sets of material parameters establishing the validity of analytic models developed in this chapter.

## 8.4 Deterministic Coupled Region I

Our analysis is first centered on the semi-balanced tensor components (SBTC) region of Figure 8.2, which is the stable reversal region. In this region, the four dipolar tensor components, $DIP_{xx1}, DIP_{yy1}, DIP_{xx2}$,and$DIP_{yy2}$, do not differ from each other by more than an order of magnitude. For an identical biaxial two-magnet system, the requirement for a coupled tensor system is specified as,

$$DIP_{xx} + DIP_{yy} > H_{crit}, \tag{8.3}$$

where $H_{crit}$ is given in equation (8.2). Due to the mutual coupling effect (MCE), the $\hat{x} - \hat{y}$ components of the dipolar field have identical contribution to the stability of the two-magnet system. Equation (8.3) is derived under the assumption that the nanomagnets mirror each other during reversal, and dipolar fields behave as anisotropy fields. While this model was derived through the mirrored-domain observation, the magnetic moments do not necessarily have to maintain anti-parallel orientation during reversal for the MCE to exist. In fact, it is seen that any type of slow relaxation from an unstable to a stable orientation displays the MCE [173].

$H_{k1} > H_{k2}$

| | M1 | M2 |
|---|---|---|
| $M_s$ | $1.0\frac{MA}{m}$ | $1.7\frac{MA}{m}$ |
| $K_u$ | $60\frac{kJ}{m^3}$ | $48\frac{kJ}{m^3}$ |
| $DIP_{xx}$ | $10\frac{kA}{m}$ | $20\frac{kA}{m}$ |

$H_{k1} = H_{k2}$

| | M1 | M2 |
|---|---|---|
| $M_s$ | $1.7\frac{MA}{m}$ | $1.7\frac{MA}{m}$ |
| $K_u$ | $48\frac{kJ}{m^3}$ | $48\frac{kJ}{m^3}$ |
| $DIP_{xx}$ | $20\frac{kA}{m}$ | $30\frac{kA}{m}$ |

$H_{k1} < H_{k2}$

| | M1 | M2 |
|---|---|---|
| $M_s$ | $1.7\frac{MA}{m}$ | $1.4\frac{MA}{m}$ |
| $K_u$ | $48\frac{kJ}{m^3}$ | $80\frac{kJ}{m^3}$ |
| $DIP_{xx}$ | $60\frac{kA}{m}$ | $20\frac{kA}{m}$ |

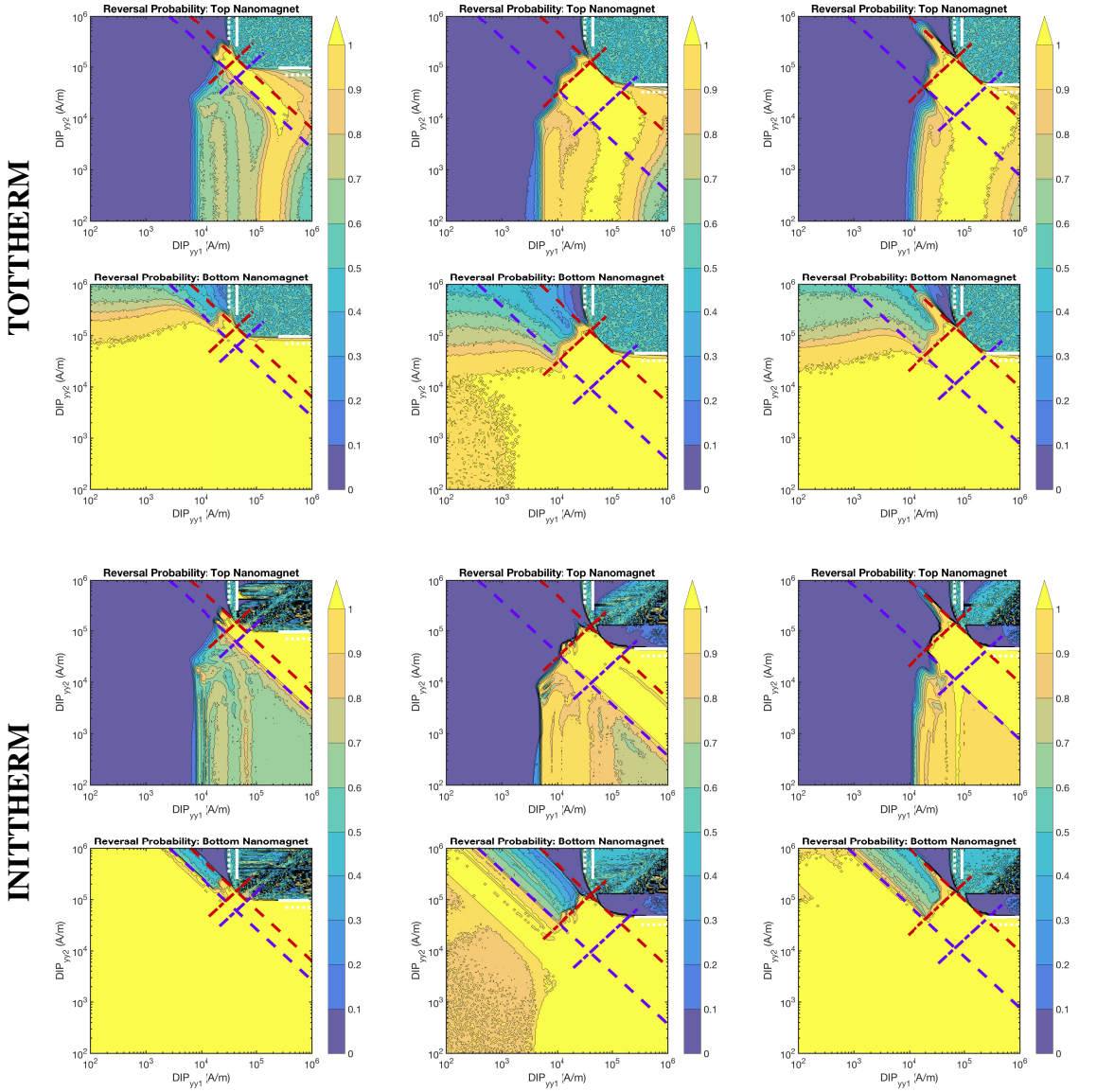


Figure 8.4: Numerical results analyzing the probability of nanomagnet reversal given a set of system parameters. Biaxial systems are considered; hence, $DIP_{zz1}$/$DIP_{zz2}$ values are irrelevant and set to 0. Three different systems with distinct $M_s$ and $K_u$ parameters are considered. Both TOTTHERM and INITTHERM tests are considered. Limits of analytic models are plotted demonstrating strong agreement with numerical results. Purple and red dashed lines correspond to boundaries of equations (8.6) and (8.10), respectively. Purple and red dash-dot lines correspond to boundaries of equations (8.16) and (8.13), respectively. The white lines correspond to limits of meta-stable region. Dotted and solid white lines correspond to limits of equations (8.19) and (8.18), respectively.

In the case of non-identical nanomagnets, we can form two independent requirements for the reversal of each nanomagnet. Mathematically, these criteria are specified as,

$$DIP_{xx1} + DIP_{yy1} > H_{crit2}, \tag{8.4}$$

$$DIP_{xx2} + DIP_{yy2} > H_{crit1}, \tag{8.5}$$

where $H_{crit1}$ and $H_{crit2}$ are obtained using equation (8.2). It is known that the stray field from one magnetic body is insufficient to reliably reverse the neighboring magnetic body on its own. However, MCE comes into play when the nanomagnets have a dynamic interaction with each other through their dipolar fields. Figure 8.4 highlights that simple lower bounds on the perpendicular components are not sufficient to define the deterministic reversal boundaries. In fact, the two perpendicular components have a multiplicative relationship on coupling such that the conditions in equations (8.4) must be combined leading to the following relationship for robust coupling:

$$DIP_{yy1}DIP_{yy2} > (H_{crit1} - DIP_{xx2})(H_{crit2} - DIP_{xx1}). \tag{8.6}$$

The lower limit of this equality is shown by the dashed line in Figure 8.4. There is a strong agreement of the analytic model, (8.6), and numerical simulation results. This confirms that the MCE exists even when the nanomagnet system is not perfectly symmetrical. We can further confirm the validity of multiplicative behavior of perpendicular dipolar field components on the coupling requirement by examining their maximum values for robust coupling during the two-magnet reversal. In the case of identical nanomagnets, the two-magnet system was found to relax to a meta-stable orientation when the Zeeman energy due to the perpendicular dipolar field undercut the free-axis energy. The analytic expression of the meta-stable state in an identical two-magnet system is given as

$$DIP_{yy} > H_{crit} + DIP_{xx}. \tag{8.7}$$

By applying the above condition to each magnetic domain in the case of non-identical magnets, we obtain

$$DIP_{yy1} > H_{crit2} + DIP_{xx1}, \tag{8.8}$$

$$DIP_{yy2} > H_{crit1} + DIP_{xx2}. \tag{8.9}$$

Knowing that the effect of dipolar fields on robustness of coupling is multiplicative in nature, we obtain the following inequality that must be satisfied for deterministic stable-reversal region in Figure 8.2:

$$DIP_{yy1}DIP_{yy2} < (H_{crit1} + DIP_{xx2})(H_{crit2} + DIP_{xx1}). \tag{8.10}$$

The upper bound of equation (8.10) is plotted in Figure 8.4 and shows very strong agreement with the numerical results. However, if the perpendicular components of the dipolar field of the two magnets are significantly unbalanced, the minimum $DIP_{yy1/2}$ requirements diverge from equation (8.10) and must be analyzed separately.

## 8.5 Deterministic Coupled Region II

In the case of unbalanced perpendicular components of the dipolar field, non-ideal reversal dynamics emerge as highlighted in Figure 8.2. We refer to this region as the unbalanced tensor region (UTR). In this work, we consider two specific UTR regions that are distinguished based on the values of $DIP_{yy1}$ and $DIP_{yy2}$.

### 8.5.1 Oscillatory M1 State

The first UTR occurs when $DIP_{yy2} \to \infty$ when both equations (8.6) and (8.10) are satisfied. Once the ratio $\frac{DIP_{yy2}}{DIP_{yy1}}$ exceeds a certain value, the system becomes unstable, and the reversal probability approaches 50%. A transient sample of this type of reversal is shown in Figure 8.38.2b. This is an oscillatory state where M1 oscillates close to the $\hat{x} - \hat{y}$ plane,

and M2 stays near the free-axis. This state is a result of the competition between the STT acting on M1 and the dipolar field of M2 driving M1 in opposite directions. When $DIP_{yy1}$ decreases beyond a certain point, the strength of the dipolar field of M1 is insufficient to reverse M2, and $\hat{m}_2$ remains in its initial energy basin. The condition that the perpendicular component of the dipolar field of M1 satisfies in this region is given as

$$DIP_{yy1} < H_{crit2} - DIP_{xx1}. \tag{8.11}$$

At the same time, the dipolar field of M2 acting on M1 could be strong enough to reverse the state of M1 if

$$DIP_{yy2} > H_{crit1} + DIP_{xx2}. \tag{8.12}$$

For low spin currents in M1, an oscillatory behavior of the magnetization of M1 emerges when equations (8.11) and (8.12) are simultaneously satisfied.

It is clear from Figure 8.4 that the boundary of the oscillatory region depends on the tensor components of both magnetic bodies. Considering that the effects of dipolar fields of the two magnets are multiplicative in nature, the following relationship is obtained for the oscillatory state of M1

$$\frac{DIP_{yy2}}{DIP_{yy1}} < \frac{H_{crit1} + DIP_{xx2}}{H_{crit2} - DIP_{xx1}}. \tag{8.13}$$

The above expression also gives an upper limit on the dipolar fields of M1 and M2 for stable reversal regime, which is bounded by the red dash-dot line in Figure 8.4.

### 8.5.2 Noise-induced M2 instability

Next, we analyze the case when $DIP_{yy1} \to \infty$. From the tests reported in Figure 8.4, we see that if the $DIP_{yy1}$ becomes too large and significantly exceeds the values required for stable magnetization reversal, the probability of M2 reversal decreases for TOTTHERM

case but not for INITTHERM case. These results clarify that thermal effects are important to consider during the entirety of magnetization dynamics. A sample transient simulation to elucidate this is shown in Figure 8.38.2c.

The cause of this instability is due to the stochastic perturbations in $\hat{m}_1$ after reversal. During M1 reversal, M2 will also reverse similar to reversals in the deterministic stable region. However, once the reversal is complete, M1 continues to exhibit Brownian motion around the free-axis and imposes a stochastic dipolar field on M2. If the perpendicular component of the dipolar field of M1 ($DIP_{yy1}$) is significantly larger than $DIP_{xx1} + H_{k2}$, M1 has the potential to knock the magnetization of M2 into a high-energy region and away from its free-axis. Clearly, the boundaries of this region depend on several factors including the maximum value of $\vec{m}_{y1}$ component during the evolution time of the system. However, precise modeling of the dipolar field requirement for coupling M1-M2 under stochastic thermal effects is outside the scope of this work as it entails Fokker-Planck analysis. As a useful metric, we determine the boundaries for deterministic reversal. This boundary can be determined using principles similar to those applied during the analysis of the oscillatory two-magnet system in Sec. 8.4. Under thermal effects, the condition that must be satisfied to ensure the reversal of M2 due to M1 is expressed as

$$DIP_{yy1} > H_{crit2} + DIP_{xx1}. \tag{8.14}$$

It can be reasoned that if M2 was able to reverse M1, then the spin current has the potential to reverse the system again. However, in the case of unstable system, M2 is unable to fully reverse M1 even when the magnets are in the weak parallel orientation. Therefore, the following bound must also be satisfied in this regime:

$$DIP_{xx2} + DIP_{yy2} < H_{crit1}. \tag{8.15}$$

Combining equations (8.14) and (8.15), we obtain

$$\frac{DIP_{yy2}}{DIP_{yy1}} > \frac{H_{crit1} - DIP_{xx2}}{H_{crit2} + DIP_{xx1}}. \tag{8.16}$$

The boundary of the above inequality is shown by the purple, dash-dot line in Figure 8.4. While this boundary represents a conservative estimate of the reliable reversal region, it successfully separates out deterministic reversals from thermally induced reversals. Like the oscillatory region, the limits of this region can be expanded by increasing the spin-current. However, doing so will likely hamper the mutual coupling effects in the two-magnet system.

### 8.5.3 Complete Stable reversal Model

Equations (8.6), (8.10), (8.13), and (8.16) provide the conditions imposed on the dipolar field components of the magnets M1 and M2 to ensure deterministic reversal of the non-identical two-magnet system. Deterministic coupling region is distinguished from other dynamical regions of operation since in the deterministic case the reversal of one magnet guarantees the reversal of the other even under thermal noise. Strong agreement of analytic models against numerical data can be seen in Figure 8.4.

## 8.6 Deterministic Meta-stable States

The camouflaged upper-right region in Figure 8.2 represents magnetic systems with meta-stable resting states. In the camouflaged regions, the perpendicular tensor components of the dipolar field overwhelm the natural free-axis anisotropies of the magnetic bodies resulting in their magnetizations to rest along the $\hat{y}$-axis.

For balanced tensor components, we derive the limit of this meta-stable region as in equation (8.10). However, when the dipolar field components of the magnetic bodies are severely unbalanced, an asymptotic boundary distinguishing this region is obtained. Consider the case where $DIP_{yy1} \to \infty$. In this case, the condition that the dipolar field com-

ponents must meet to obtain deterministic meta-stable state in the magnetization dynamics is specified as

$$DIP_{yy1} \rightarrow \infty, DIP_{yy2} > H_{crit1}. \tag{8.17}$$

This boundary is indicated by the solid white line in Figure 8.4. Excellent agreement with numerical results can be seen. Notice that in the asymptotic case the longitudinal tensor components are not considered. This is because the energy of the total system is always minimized if the magnetizations of M1 and M2 are oriented along the perpendicular axis ($\hat{y}$). This is significantly different than the balanced dipolar field case where the energy of the system is minimized through both longitudinal and perpendicular components of the dipolar field.

While equation (8.17) shows strong numerical agreement, the condition

$$DIP_{yy2} \rightarrow \infty, DIP_{yy1} > H_{crit2}. \tag{8.18}$$

overestimates the $DIP_{yy1}$ magnitude required for reliable reversal. To understand this, we must refer to the precessional dynamics of a magnet under the influence of perpendicular fields. When a transverse field is introduced to a biaxial energy space, an intermediate energy region is introduced whose trajectories encircle the axis parallel to the applied transverse field. Similar to a basin or pole, if the magnetization falls within this region, it will oscillate around the $\pm\hat{y}$ axis.

Assuming the magnetization is initially at rest along the free-axis, the transverse field acting upon the magnetic body can be large enough to encourage the magnetization to escape the initial energy basin. For this to happen, the magnitude of the transverse field must be greater than $0.77H_{crit}$ [3]. Hence, we propose a new limit such that $\hat{m}_2$ is able to relax toward the meta-stable position after escaping its initial energy basin. This condition is expressed as

$$DIP_{yy2} \rightarrow \infty, DIP_{yy1} > 0.77H_{crit2}. \tag{8.19}$$

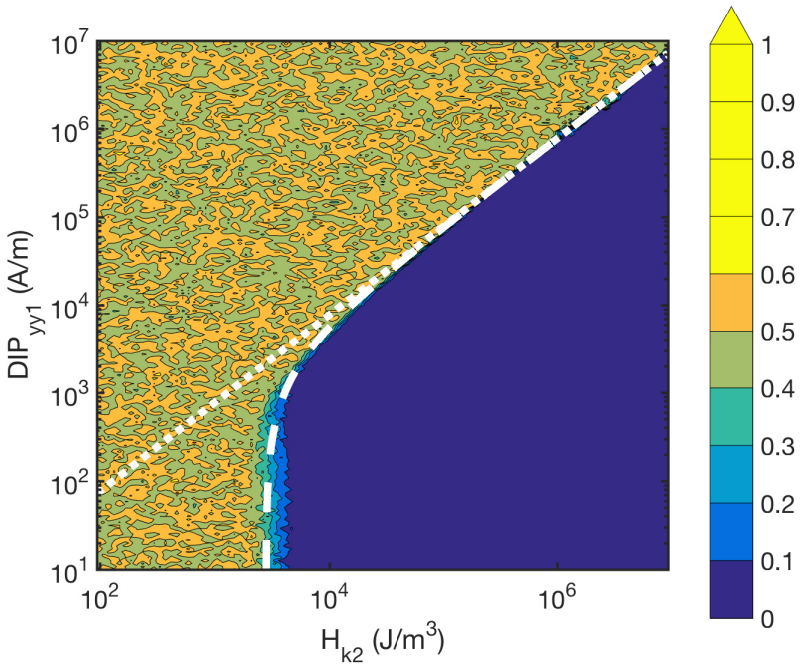


Figure 8.5: Probability of M2 magnetization reversal obtained under TOTTHERM setup for various $K_{u1}$ and $DIP_{yy1}$ values. Material parameters of M1 and M2 are $M_{s1} = M_{s2} = 1.7\frac{MA}{m}$ and $K_{u1} = 48\frac{kJ}{m_3}$. $DIP_1 = [10, Y, 0] \cdot I\frac{kA}{m}$ and $DIP_2 = [10, 1000, 0] \cdot I\frac{kA}{m}$. Dotted line maps the boundary predicted by equation (8.19). Dashed line corresponds to the boundary noted by (8.20). Note that the dashed line simply includes a fitting parameter to account for stochastic magnet reversal under thermal noise. As the energy barrier of M2 increases, the thermal field is less likely to reverse its magnetization and hence, the reversal characteristics are given by equation (8.19).

This boundary is shown by the dotted white line in Figure 8.4 and is a accurate estimation of the boundary of the meta-stable region. Note that the difference in equations (8.17) and (8.19) is due to the fact that $\hat{m}_1$ is being driven by an above-critical STT, while $\hat{m}_2$ is guided by precessional dynamics.

To further demonstrate that equation (8.19) accurately predicts the limits of the meta-stable system, we perform TOTTHERM simulations while varying $K_{u1}$ and $DIP_{yy1}$. Simulation results are shown in Figure 8.5. As the energy barrier increases, the boundary of the region defined by equation (8.19) matches numerical results. It can also be seen that an asymptotic limit appears as $K_{u2}$ is decreased. This is due to thermal noise knocking the magnetization out of its initial basin for systems with low energy barriers. To account for

this thermal effect, equation (8.19) can be modified to

$$DIP_{yy2} \rightarrow \infty, DIP_{yy1} > 0.77H_{crit2} - \xi \frac{k_B T}{\mu_0 M_{s2} V_2}, \tag{8.20}$$

where $\xi$ is a fitting parameter dependent on the observation time of the system.

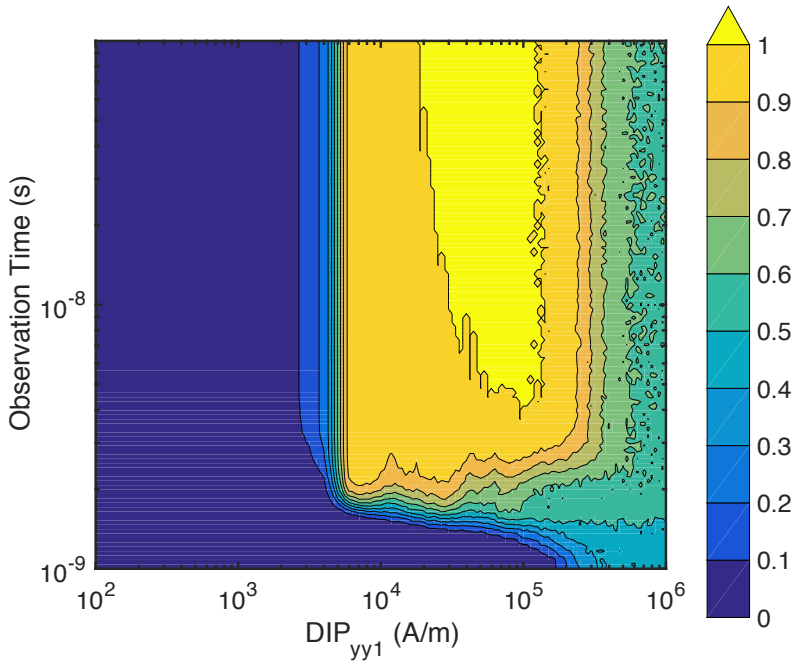


Figure 8.6: Probability of reversal of M2 magnetization obtained under TOTTHERM setup by varying the observation time and $DIP_{yy1}$ values. Material parameters of M1 and M2 are $M_{s1} = M_{s2} = 1.7\frac{MA}{m}$ and $K_{u1} = 48\frac{kJ}{m_3}$. $DIP_1 = [20, Y, 0] \cdot I\frac{kA}{m}$ and $DIP_2 = [30, 0, 0] \cdot I\frac{kA}{m}$. This figure highlights the drift effect due to thermal noise that governs the pseudo reversal region.

## 8.7 Pseudo-reversal Region

The pseudo-reversal region is denoted by the blue rectangle in Figure 8.2. In the pseudo-reversal regime, the dipolar field components are large enough such that the precession of M1 results in the probabilistic reversal of M2 into its anti-parallel state. This is similar to the probabilistic relaxation of a nanomagnet to the energy basin under the influence of a constant longitudinal field [139, 140]. In such a case, one direction along the free-axis has

$H_{k1} > H_{k2}$

| | M1 | M2 |
|---|---|---|
| $M_s$ | $1.0\frac{MA}{m}$ | $1.7\frac{MA}{m}$ |
| $K_u$ | $60\frac{kJ}{m^3}$ | $48\frac{kJ}{m^3}$ |
| $DIP_{xx}$ | $10\frac{kA}{m}$ | $20\frac{kA}{m}$ |

$H_{k1} = H_{k2}$

| | M1 | M2 |
|---|---|---|
| $M_s$ | $1.7\frac{MA}{m}$ | $1.7\frac{MA}{m}$ |
| $K_u$ | $48\frac{kJ}{m^3}$ | $48\frac{kJ}{m^3}$ |
| $DIP_{xx}$ | $20\frac{kA}{m}$ | $30\frac{kA}{m}$ |

$H_{k1} < H_{k2}$

| | M1 | M2 |
|---|---|---|
| $M_s$ | $1.7\frac{MA}{m}$ | $1.4\frac{MA}{m}$ |
| $K_u$ | $48\frac{kJ}{m^3}$ | $80\frac{kJ}{m^3}$ |
| $DIP_{xx}$ | $60\frac{kA}{m}$ | $20\frac{kA}{m}$ |

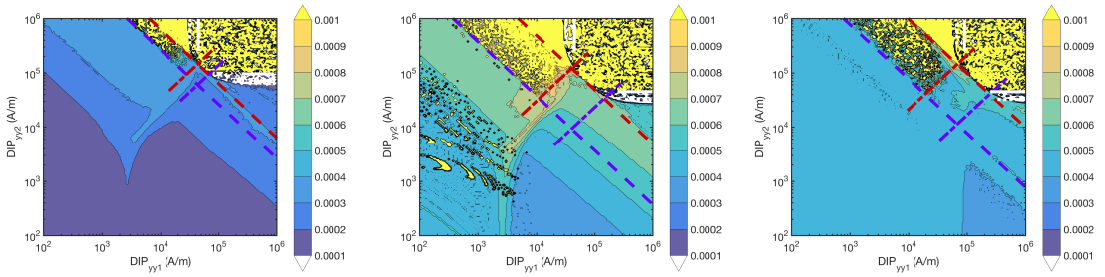


Figure 8.7: Numerical results analyzing the minimum spin current to be injected into M1 to ensure reversal. The critical current is numerically calculated by setting the system to an anti-parallel state and the initial angle of $\hat{m}_1$ to $\langle \theta, \phi \rangle = \langle 0.01°, 90° \rangle$. Biaxial systems are considered; hence, $DIP_{zz1}/DIP_{zz2}$ values are irrelevant and set to 0. Results of analytic models are plotted demonstrating a change in critical current required for system reversal. In this case, there is no spin current injection into M2.

a smaller magnetization energy weighting the probability that the magnetization falls in the parallel energy basin larger greater than 50%.

We note that the pseudo-reversal region exists only when the nanomagnets are under the effects of thermal noise. Figure 8.4 demonstrates this by comparing the results of TOTTHERM and INITTHERM cases. To further emphasize this point, we perform the TOTTHERM test while setting the perpendicular components of $DIP_2$ to zero. Results are reported in Figure 8.6. The probability of reversal of M2 magnetization is analyzed as a function of $DIP_{yy1}$ and observation time. As the observation time increases, the range of $DIP_{yy1}$ values that ensure the reliable reversal of M2 magnetization also increases. Hence, the reliability of pseudo reversal is a stochastic function of observation time and its analysis is outside the scope of this research. However, the existence of this region indicates that there is a range of $DIP_1$ tensor values that alone encourage reversal of neighboring magnetic bodies and when the system is in the presence of thermal noise, the dipolar field of M1 is sufficient to reverse M2 assuming a long enough observation time.

## 8.8 Minimum current required for system reversal

Thus far, the M1 nanomagnet is subject to STT, while the M2 nanomagnet is coupled to M1 through dipolar fields. This setup is specifically important for a variety of spin-based devices [4]. We analyze the critical spin current required for deterministic reversal of the two-magnet system with spin current injection into M1 referred to as the driving nanomagnet. Results are reported in Figure 8.7. Several observations can be made from this figure. First, the critical current mirrors the reversal regions of the INITTHERM test shown in Figure 8.4. This further validates the fact that the region identified as the pseudo-reversal region is a thermally induced effect and not a deterministic one. The critical current analysis also clearly shows the meta-stable and oscillatory regions, which require a significantly large spin current to break free from the perpendicular low energy states.

We note that that there are two critical spin currents defined for a biaxial magnetic body in STT-induced magnetization reversal. $I_c^1$ refers to the critical current required to shift the magnetization away from the free-axis, while $I_c^0$ indicates the critical current required to force the magnetization over the energy barrier [74, 110]. For an individual magnetic body, the critical current for full reversal is simply $I_c = max(I_c^1, I_c^0)$. However, in the case of the complex reversal discussed in this chapter, the magnetizations of M1 and M2 enter an intermediate energy region during reversal and cross their energy barriers using precessional mechanics. Therefore, the STT is only relevant when forcing the magnetizations away from the free-axis stable state.

However, there does not appear to be a clear boundary between the deterministic reversal region and the regions were one or both nanomagnets do not reverse. Instead, the critical current increases gradually as the perpendicular tensor components are increased. This is likely because the critical current magnitude is highly sensitive to the type of precession the system undergoes which, in turn, depends on the tensor values. Despite this sensitivity, we can approximate the maximum critical current magnitude in the deterministic reversal

region. In this region, we see that the critical current increases because the STT is reversing both magnetic bodies instead of just M1. Hence, is it reasonable to conclude that the critical current of the system is simply the sum of the critical currents of each magnetic body. That is,

$$I_{ctot} = I_{c1}^{1} + I_{c2}^{1}, \tag{8.21}$$

where $I_{ctot}$ is the current required to deterministically reverse a coupled system, and $I_{c1}^{0}/I_{c2}^{0}$ are the free-axis critical currents of each magnetic body in isolation.

### 8.8.1 Effects of spin current injection into M2

In this section, we analyze the interaction of bias currents injected into both M1 and M2, while forming a coupled system. We refer to the spin current injected into M2 as the bias current ($I_{s2}$). We also assume that $I_{s2}$ has the same negative polarity as $I_{s1}$. In this case, $I_{s1}$ encourages system reversal by attempting to reverse M1 while $I_{s2}$ discourages the system reversal by forcing M2 to remain in its original energy basin. In this case, there exist two non-conservative torques interacting with each other through dipolar fields.

To analyze the relationship between the spin currents acting on M1 and M2, we consider the system with a particular set of material and dipolar tensor parameters. Driving and bias current magnitudes are swept while measuring the reversal probability of M1 and M2. Results are reported in Figure 8.8. Notice that there appear to be two limits that determine the system behavior. If the driving current into M1 ($I_{s1}$) is close to, but larger than $I_{ctot}$, then a sufficiently large $I_{s2}$ can stop the reversal of both nanomagnets. A linear relationship emerges between these two current in the weak driving case. In this case, the driving current dominates the system dynamics, deciding whether or not the two-magnet system reverses.

As the current into M1 increases, a different scaling trend emerges referred to as the large-current magnitude region. While M1 may reverse in this regime, M2 reversal is not guaranteed, indicating that the dipolar coupling between the magnets is either broken or that the system enters into unstable dynamics. Another linear trend appears in the bound-

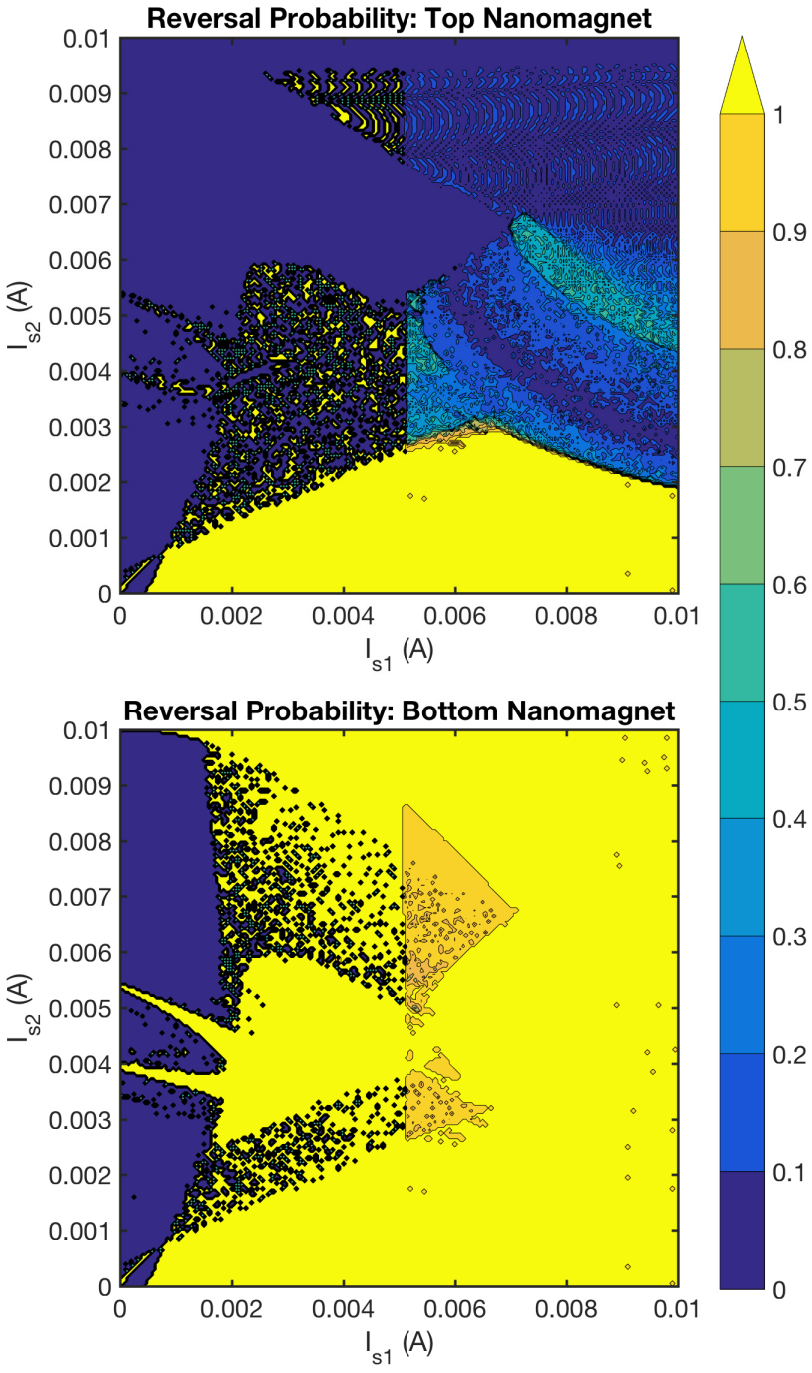


Figure 8.8: Probability of magnetization reversal of M1 and M2 using INITTHERM setup. Spin currents injected into M1 is denotes as $I_{s1}$ and the spin current injected into M2 is denoted as $I_{s2}$. Material parameters of M1 and M2 are $M_{s1} = 1.7\frac{MA}{m}, M_{s2} = 1.4\frac{MA}{m}$ and $K_{u1} = 48\frac{kJ}{m_3}, K_{u2} = 80\frac{kJ}{m_3}$. $DIP_1 = [60, 70, 0] \cdot I\frac{kA}{m}$ and $DIP_2 = [20, 50, 0] \cdot I\frac{kA}{m}$. Figure demonstrates the relationship between non-conservative spin-torque forces when interacting through dipolar fields.

ary of reliable M2 reversal suggesting that an increase in the driving current overwhelms the effects of the biasing current. Unlike the near-critical case, the slope of the linear separation in the large-current magnitude region is less than unity. This suggests that the biasing current becomes dominant when establishing the system reliability. Interestingly, the boundary of the reliable reversal region has a positive slope when $I_{s1} < 6$ mA and negative slope when $I_{s1} > 6$ mA. This is due to the MCE which exists only for slow reversals. Once the driving current exceeds a certain threshold, the reversal of M1 becomes too rapid and breaks the MCE.

# CHAPTER 9

# DIPOLAR COUPLING IV: COUPLING IN MULTI-DOMAIN MAGNETIC BODIES

Chapters 6-8 have exhaustively analyzed the coupling between two mono-domain magnetic bodies. However, we must also ask if this effect exists in larger multi-domain magnetic systems. While it is expected that very small magnets can be treated as single-domain objects, it is not quite clear how small is small enough. Second, it is not clear whether using a single-domain analysis underestimates or overestimates the coupling. In this chapter, we quantify the coupling between nanomagnets while considering their multi-domain behavior.

To analyze the coupling strength between a pair of nanomagnets, we can again refer to the the complex nanomagnet system shown in Figure 6.1 is considered. For this case, let's analyze a system consisting of two thin-film, same-sized, permalloy-type (anisotropy energy density ($K_u$) = 0), saturation magnetization ($M_s = 8e5\frac{A}{m}$), exchange stiffness ($A$ = $13\frac{pJ}{m}$) nanomagnets stacked along the z-axis with a free-axis along the x-axis. The bottom nanomagnet is switched via a spin-transfer-torque current which, in turn, flips the top nanomagnet through dipolar coupling. For only this chapter, this setup was modeled using multi-domain numerical simulations in OOMMF, assuming $2 \times 2 \times 2nm^3$ unit sizes [106].

Assuming the bottom magnetization is completely along the free-axis, the strength of the magnetic field imposed on the top magnet by the bottom magnet is spatially non-uniform across domains according to (6.1-6.3). This is shown in Figure 6.2. Up until this point, because we have been assuming a single domain model, this field is averaged over the entirety of the top magnet [173]. In a multi-domain model, this non-uniformity suggests that certain domains feel different coupling field magnitudes and directions than their neighboring domains. Here, edge domains feel different exchange and demagnetization

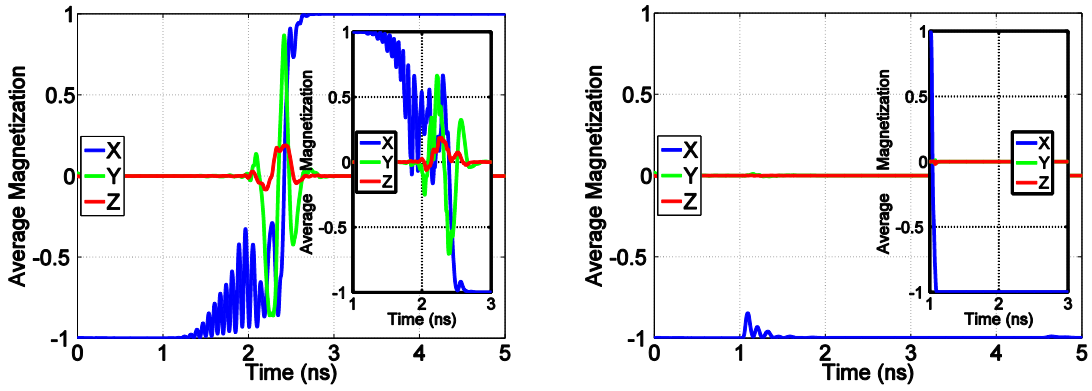


(a) $I_s = 1.6mA$ (b) $I_s = 9.6mA$

Figure 9.1: *Left*: Successful switching of $80 \times 40 \times 2nm^3$ bottom (Main plot) and top (subplot) magnets using multi-domain model. Note average magnetization magnitude isnt constant. *Right*: Unsuccessful reversal due to increased current in bottom nanomagnet resulting in rapid reversals with increased domain nucleation.

energies compared to their center counterparts; the magnet switches in a non-uniform fashion [6]. Edge domains typically switch first and the change in magnetization spreads to the center domains. Because of this, the average magnetization across the entirety of the magnet is not constant as shown in Figure 9.1.

While this insight appears to suggest multi-domain magnets are easier to switch through dipolar fields, the following results show that this is not the case for large nanomagnets due to two important multi-domain effects which become especially present for larger nanomagnets. First, in this complex magneto-system scheme, coupling is achieved through dampening and precessional field effects. While the dipolar-field components parallel to the easy-axis serve to align the magnets in anti-parallel orientations, the perpendicular field components induce a large torque on the top magnet making it easier to switch during reversal and also establish a feedback loop between the magnets strengthening the coupling. However, assuming a fast reversal in the multi-domain case, the bottom magnet has no net perpendicular field components because the different domains of the bottom nanomagnet align themselves in opposite directions. They precess with different phase such that the net energy is minimized as shown in Figure 9.2, yielding a net-zero Y/Z dipolar field compo-

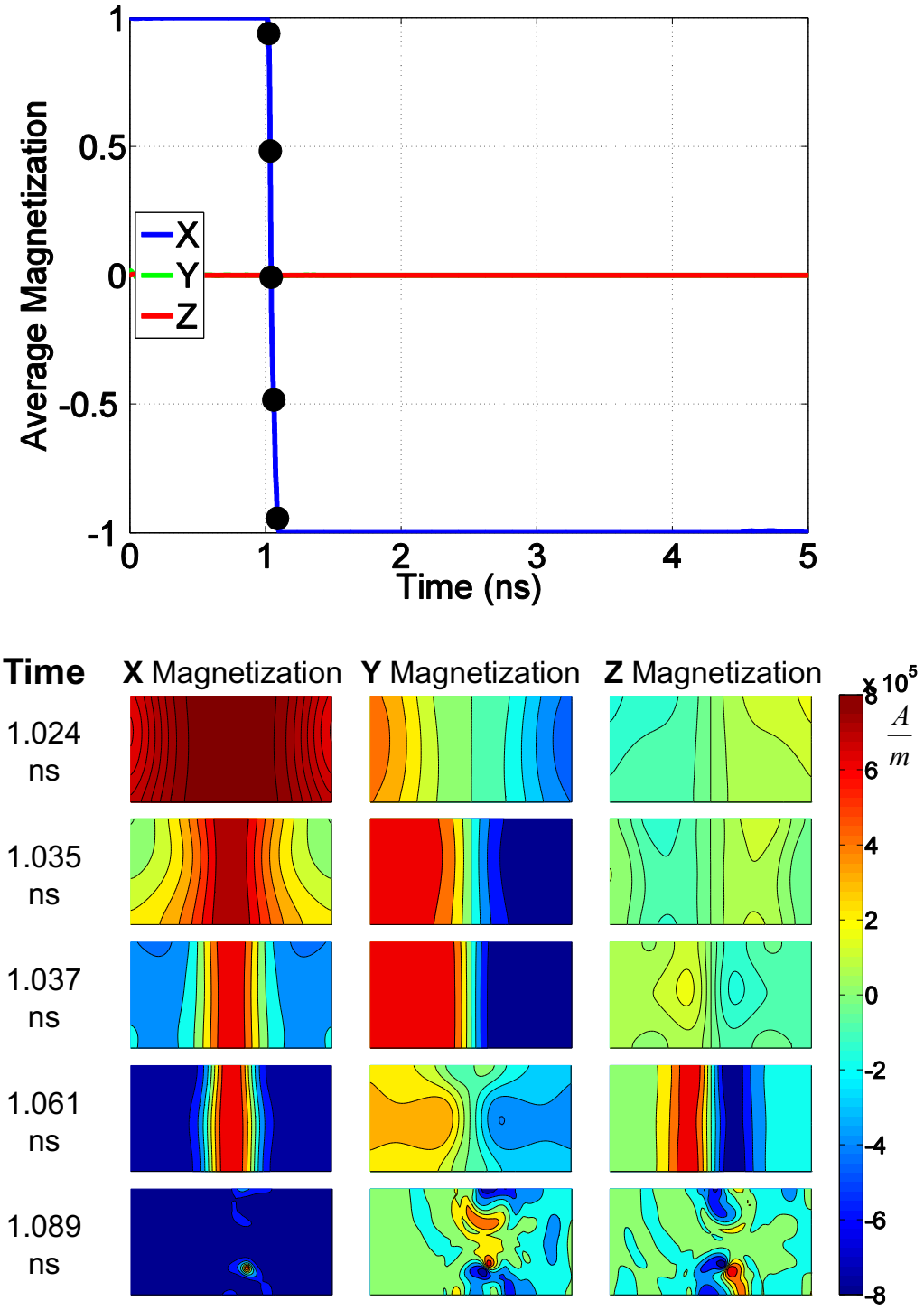


Figure 9.2: Switching of the bottom magnet through spin-transfer-torque at a high current density. Subplots show magnetization across domains at marked times during magnet reversal.

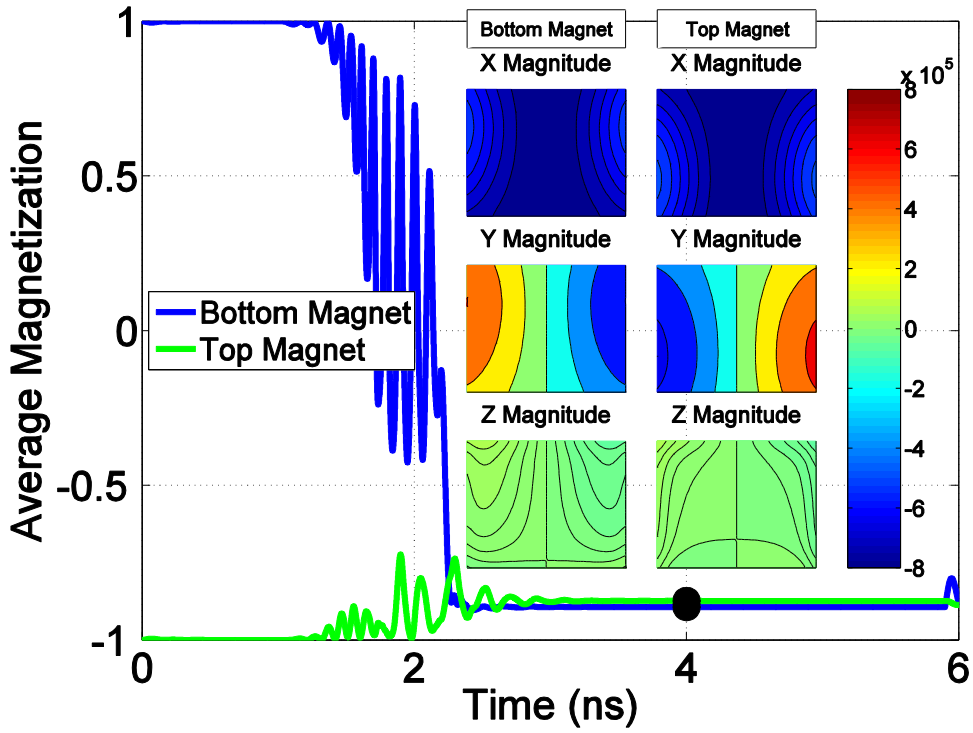


Figure 9.3: Main plot shows average x component of magnetization of each magnet. The magnets settle away from the easy axis because of the low current density. Subplots show magnetization across domains at settled positions (t = 4.0ns).

nent. This breaks the feedback loop and consequently weakens the magnetic coupling. It is important to consider the non-uniformity of the dipolar field shown in Figure 9.3. This again complicates reversal through coupling field by shifting the critical field values needed to switch each domain.

Most importantly, it is critical to determine when this nanomagnet system is perfectly coupled. Since both the critical field and the coupling field strengths are linearly proportional to the saturation magnetization, the overall coupling between the nanomagnets becomes a function of the nanomagnet geometrical parameters. Assuming a constant width, longer nanomagnets would have a larger critical field and weaker coupling field. There exists a length above which the system will not be perfectly coupled. To accurately quantify the impact of multiple domains on dipolar coupling, numerical simulations are performed to find the maximum length given a fixed width for the magneto-system assuming both

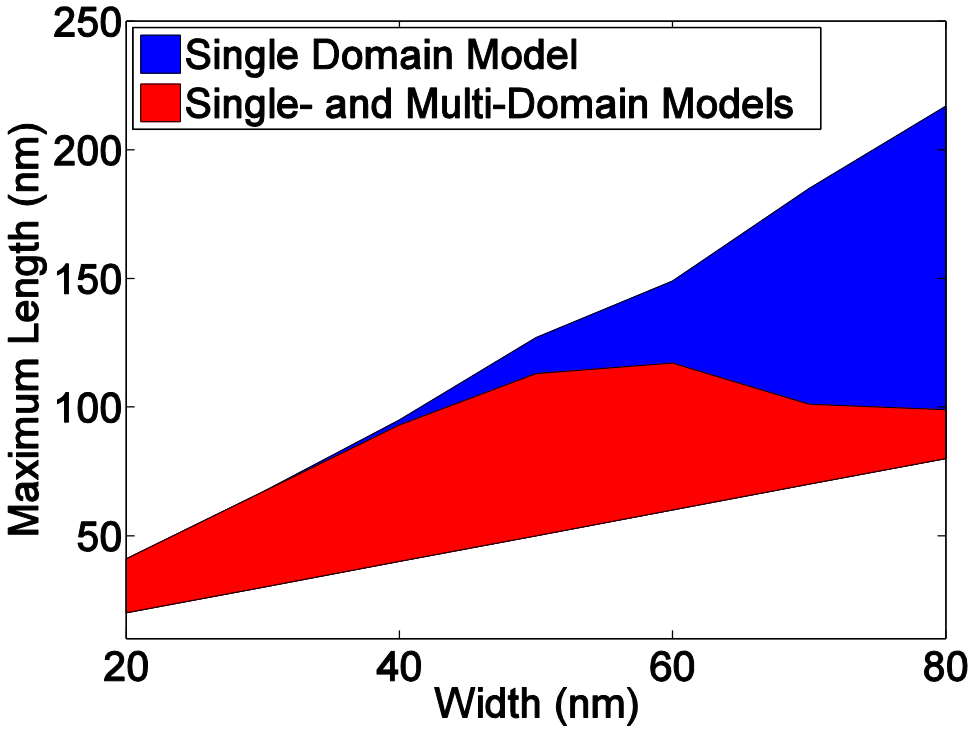


Figure 9.4: Red region denotes magnet geometries where both multi- and single-domain models predict perfect coupling assuming 2 nm thick magnets with a 2nm separation. Blue region is where only single-domain model predicts perfect coupling.

single- and multi-domain magnets. For every magnet width and length, 30 simulations were performed with different current densities into the bottom magnet. This variation is essential to see if the magnets are truly coupled or if only for a particular set of values. The precessional components of the coupling knock the magnets into a high energy state which then relax into the expected orientations. It is shown in Figure 9.4 that for smaller magnets, the single-domain approximation is reasonable for modeling a coupled nanomagnet system. However, assuming thin-film nanomagnets, if the area of the nanomagnets is larger than $1\mu m^2$, the single-domain assumption overestimates the overall coupling strength between the nanomagnets and is inaccurate for modeling real devices. Note that the $60 \times 45 \times 2nm^3$ magnetic bodies commonly used in this research fall well within the range where single domain models can accurately represent multi-domain magnetic bodies [172].

# CHAPTER 10

# COMPLETE DEVICE EVALUATION

From the onset of this work, we noted that the goal of this research was to find analytic expressions for the fast evaluation of spin-based devices. We noted that there are four prominent effects contributing to the operation of the Spin-Switch device: GSHE, STT, dipolar coupling, and the MTJ effect. The GSHE and MTJ effects are heavily dependent on fabrication and material parameters. They are only describable via the simple analytic models covered previously. Chapter 4 formulated new models for reversal through STT. Chapters 5-9 exhaustively analyzed coupling between magnetic bodies through dipolar interaction.

Using these models we can accurately map out the set of values for which the Spin-Switch device will operate as intended given a set of constraints. We design two Spin-Switch devices based on layout constraints and reliability constraints. These two constraints yield very different device designs and performance metrics yielding significant insight to the feasibility of Spin-Switch device technology.

## 10.1 Model Derivation and Definition

Recall from Figure 1.9 that the operation of the Spin-Switch device is dependent on four main effects:

**GSHE** Electrical current goes into the device input and is converted to a spin current.

**STT Reversal** The spin current generated by the GSHE effect reverses the input magnet.

**Dipolar Coupling** Communicates information between input/output stages.

**MTJ Effects** The output current polarity determined by dual-MTJ subsystem.

We can combine the analytic models developed in this thesis to form a complete evaluation of the Spin-Switch device. In this section we review and define the models describing these four effects before conducting a complete Spin-Switch device evaluation in Sections 10.2–10.4[1].

### 10.1.1 Model: Giant Spin-Hall Effect

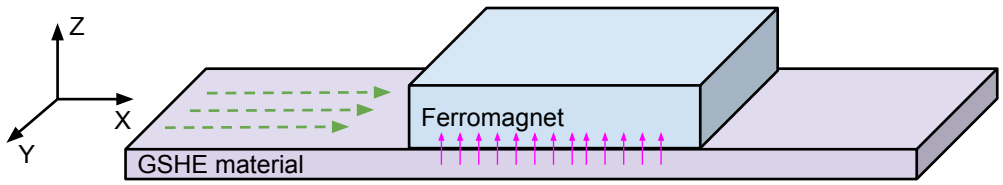


Figure 10.1: Diagram of standard setup to drive a nanomagnet through the use of the GSHE. Electrical current is oriented along $\hat{x}$ and is represented by green-dashed arrows. Spin current represented by pink arrows which flows along the $\hat{z}$. This means that the spin current is polarized along the $\hat{y}$.

While this effect has been observed at length experimentally, it unfortunately does not have a strong theoretical foundation. Every variation in a bulk material's crystalline structure and geometry can greatly impact the magnitude of the GSHE. For this reason, analytic expressions with strong physical foundation are difficult. Beyond bulk materials, interface effects between the GSHE layer and bottom free-magnet greatly impact spin current generated by the electrical current flowing through the GSHE material. Regardless, certain experimental works have suggested that the conversion of electrical to spin current through the GSHE can be approximated by [70, 71]:

$$\frac{J_s}{J_e} = \theta_{SH}\frac{L}{t}\left(1 - sech\left(\frac{t}{\lambda_s}\right)\right) = \beta. \tag{10.1}$$

We often refer to the amplification of electrical to spin current densities as the parameter $\beta$. Note that the polarization of the spin current must be perpendicular to the flow of

[1]For the complete device evaluation, we omit stochastic effects thereby simplifying analysis. The inclusion of thermal noise would obfuscate the effects limiting device operation.

spin and electrical current. According to Figure 11.3, this means that the length ($L$) used in (10.1) is the width of the free magnet. $t$ is the thickness of the giant spin hall effect material. Making the GSHE material too thick means you'll eliminate the amplification factor. However, making the GSHE material too thin is also problematic for two reasons. First, it would make the resistence into the input port of the device larger which will reduce the magnitude of the electrical current outputted by two-MTJ output stack in this system and will be discussed later in this section. Second, it is important to emphasize that the last "$\left(1 - sech\left(\frac{t}{\lambda_s}\right)\right)$" term is a recent addition to our understanding of the GSHE [70]. Up until recently, it was believed that the expression is simply $\frac{J_s}{J_e} = \theta_{SH}\frac{L}{t}$. This has led to a generation of spin devices to be modeled using this unrealistically optimistic optimistic expression as can be seen in Figure 10.2.

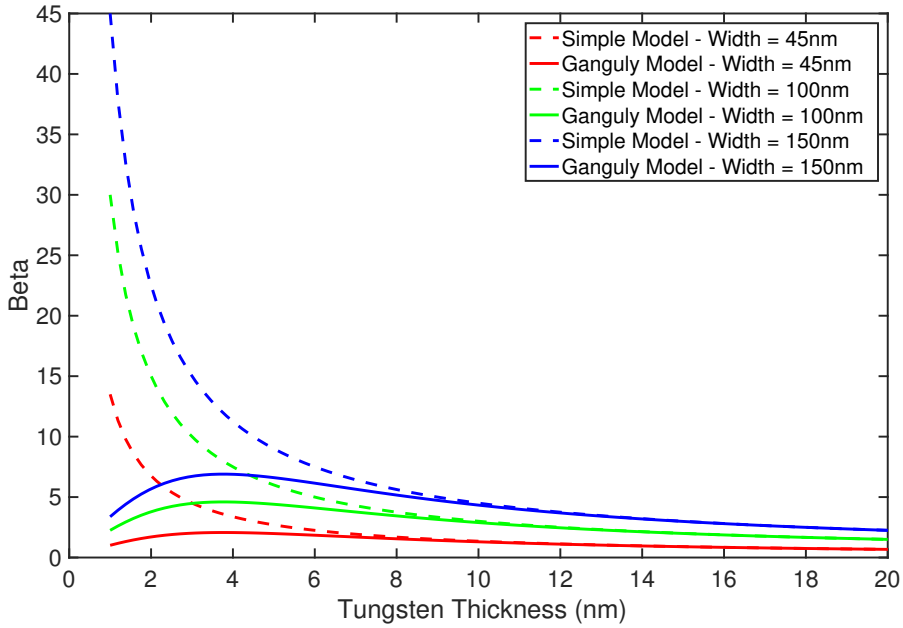


Figure 10.2: Calculates the amplification ($\beta$) of electrical to spin current assuming a nano-magnet of multiple sizes. The Gangulay model refers to (10.1) while the ideal case corresponds to the GSHE expression without the $\left(1 - sech\left(\frac{t}{\lambda_s}\right)\right)$ term. Assumes a $\theta_{SH} = 0.3$ and $\lambda_s = 2.5nm$ which corresponds to a tungsten material.

Without the $sech$ term, as the thickness approaches 0, the amplification would go to infinity. This is clearly incorrect and thus the $sech$ term is necessary for describing the

GSHE at thin films. Several materials have been shown spin hall conductivities as seen in Table 10.1. To my knowledge, tungsten has the largest spin-hall angle of any known bulk material. Therefore we note that for a tungsten material, the $\beta$ is optimized when the thickness of the tungsten film $t_W \approx 4nm$.

Table 10.1: Selection of experimental literature which measure the spin-hall angle for various metals. Further review can be found in [56]. Tungsten is found to have the largest GSHE amplification factor.

| **Material** | $\theta_{SH}$ (%) | **Ref.** |
|---|---|---|
| Au | 11 | [181] |
| Pd | 1.2 | [182, 183] |
| Pt | 6.8 | [184, 185] |
| Ta | 12 | [66] |
| W | 30 | [68] |

### 10.1.2 Model: Dipolar Coupling

The most crucial component of this device are the dipolar interactions between the free magnets which control the input and output stages of the device. Having established that PMA (uniaxial) magnetic bodies are unsuitable for dipolar interaction, only bulk in-plane magnetic bodies are considered for the Spin-Switch design. Additionally, Chapter 7 proves only the $DIP_{xx}$ and $DIP_{yy}$ tensor components are relevant when considering biaxial magnetic bodies with a free-axis along $\hat{x}$ and positive perpendicular anisotropy along $\hat{z}$.

As the input and output stages of the Spin-Switch device have distinct requirements, the magnetic bodies for both stages will need to be different. As such the expressions derived in Chapter 8 are particularly useful. For reliable reversal in biaxial systems with balanced tensor components, the following models:

$$DIP_{yy1}DIP_{yy2} > (H_{crit1} - DIP_{xx2})(H_{crit2} - DIP_{xx1}), \tag{10.2}$$

$$DIP_{yy1}DIP_{yy2} < (H_{crit1} + DIP_{xx2})(H_{crit2} + DIP_{xx1}), \tag{10.3}$$

must be satisfied. To avoid unstable system behaviors such as oscillatory and thermally-

reactive states, the following two conditions must be satisfied:

$$\frac{DIP_{yy2}}{DIP_{yy1}} < \frac{H_{crit1} + DIP_{xx2}}{H_{crit2} - DIP_{xx1}}, \tag{10.4}$$

$$\frac{DIP_{yy2}}{DIP_{yy1}} > \frac{H_{crit1} - DIP_{xx2}}{H_{crit2} + DIP_{xx1}}. \tag{10.5}$$

For the evaluation of the Spin-Switch device, tensor component values are determined by nanomagnet geometry according to (6.1-6.3). This system of equations allows us to determine if two magnetic bodies are reliably coupled.

### 10.1.3 Model: Two-MTJ Output Stack System

The two-MTJ output stack can be modeled as a resistor network shown Figure 10.3:

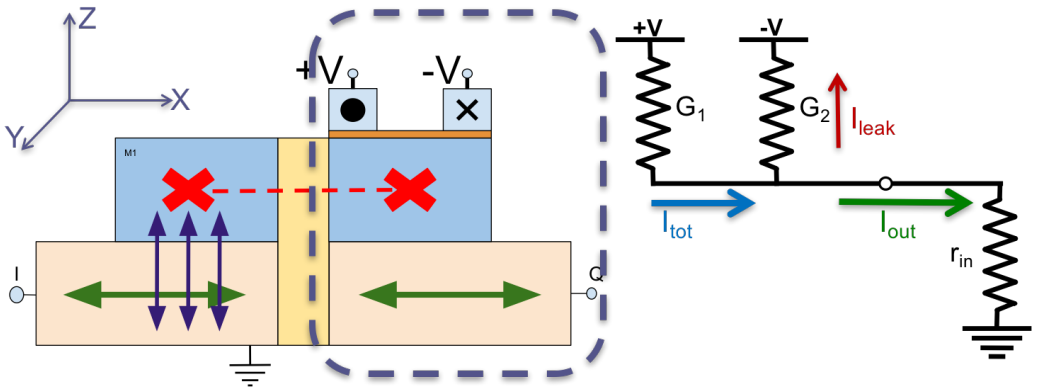


Figure 10.3: Diagram of two-MTJ resistor network equivalent used in this analysis.

where $G_1$ and $G_2$ are the resistance of the two-MTJ stacks, V is the supply amplitude and $r_{in}$ is the output resistance. Notice that both MTJ stacks share a free-magnet body but have opposing fixed layers. This means that one MTJ stack will always be in the low-resistance, parallel configuration while the other stack will be in high-resistance anti-parallel configuration. The change in resistance is typically modeled as:

$$\frac{\Delta G}{G} = \frac{TMR}{TMR + 2}, \tag{10.6}$$

where $TMR$ is the tunnel magnetoresistance factor and is typically treated as a fitting parameter to experimental results. $G$ is the average resistance of the stack while $\Delta G$ is the change in resistance. Using this dual-MTJ structure, the polarity of the free-magnet will control the polarity of the output electrical current. For the purposes of device characterization analysis, we assume the MTJ stack connected to the positive supply is in the low-resistance parallel state. The conductances of the stacks can be written as:

$$G_1 = \frac{G}{2} + \frac{\Delta G}{2}, \tag{10.7}$$

$$G_2 = \frac{G}{2} - \frac{\Delta G}{2}. \tag{10.8}$$

and therefore, the resistance of the two stacks would be $R_1 = G_1^{-1}$ and $R_2 = G_2^{-1}$. According to Figure 10.3, there are three key currents to be aware of. $I_{tot}$ is simply the amount of current leaving the low-resistance supply. $I_{leak}$ and $I_{out}$ are the electrical currents flowing into the high-resistance supply and output respectively. After some circuit analysis, $I_{out}$ can be calculated as:

$$I_{out} = \frac{R_2 - R_1}{R_1 R_2 + R_1 r_{in} + R_2 r_{in}} V. \tag{10.9}$$

Knowing the output current also allows us to know the total current traveling through the nanomagnet:

$$I_{tot} = \frac{V - I_{out} r_{in}}{R_1}. \tag{10.10}$$

$I_{out}$ is the total electrical current flowing through the output free magnet. Given that this current is passing through an MTJ system, it will also be significantly polarized. Therefore the spin current following through the top nanomagnet can be modeled as:

$$I_{s2} = P I_{tot}. \tag{10.11}$$

where $P$ is the polarization of the current exiting the MTJ stack. This polarization factor

can be any value between 0 and 1 but is typically assumed $P = 0.5$ for modeling purposes.

Note that the output resistance in the circuit model ($r_{in}$) is considered to be the input of the next magnet stage. If this resistance becomes too large, the leakage current becomes larger while the the output current shrinks which is problematic for device operation; $r_{in}$ should be as small as possible. However, the input of the device is controlled by the resistance of the GSHE material which needs to be thin to maximize the the amplification of the electrical current to spin current.

If the input resistance is large, one way to avoid leakage current is through making the MTJ stack resistance larger. However, this would greatly increase the power consumption of the total device and is generally not beneficial to the performance metrics of the device. However, it may help increase the range of supply magnitudes for which the device is operable.

### 10.1.4 Model: Spin-transfer Torque

We note that we primarily use biaxial mono-domain magnetic bodies where we do not have exact expressions for reversal delay through STT. We did manage to obtain an analytic model (4.6):

$$\tau^{bi} = (\frac{I_C}{I_s - I_C})^X \cdot \tau^{uni}, \tag{10.12}$$

where $X$ is a fitting parameter. However, as demonstrated in Figure 4.5, we can approximate $X \approx 0.75$ for materials with a very large perpendicular anisotropy. This delay model promises lower energy costs for STT reversal as the $M_s$, $K_u$ and volume of the bottom nanomagnet is minimized. This is in contrast to the dipolar coupling which requires a minimum $M_s$ and geometry for reliable coupling. In addition, the $M_s$ and volume of the top nanomagnet should be maximized to prevent the output/leakage current from impairing device operation. However, again the dipolar coupling models assert that if the dipolar field emitted by the top nanomagnet is too strong, the system will trend towards an oscillatory state. While we use (10.12) to guide our design process, the performance metrics of a par-

ticular Spin-Switch design are calculated using transient numerical simulations to ensure the correctness of our performance metrics.

### 10.1.5 Demagnetization Field Model

In other chapters, either SHd or 0Hd demagnetization field models were utilized to more easily analyze biaxial and uniaxial systems respectively. However, the shape anisotropy of a magnetic body may significantly alter the magnetic body's energy barrier and precessional dynamics. For the Spin-Switch device designs in this chapter, we will use the complex demagnetization fields which will more accurately represent a real-world nanomagnetic system.

## 10.2 Layout-Constrained Device Characterization

From the previous chapters, it is clear that the Spin-Switch device is an amalgam of interacting magnetic effects with contradictory ideal material parameters. It is most prudent to begin this evaluation of the layout-constrained device by first determining the size of the bulk materials involved in devices operation. Realistic floorplanning rules were followed according [27]. While this work offers a number of layout rules and regulations the ones relevant to our purposes are as follows:

- Length and width of bulk material bodies must be a multiple of the feature size ($F$).
- Supply contacts consume a $F \times F$ area and must be four feature lengths away from other contacts.
- Material parameters limited to those of common bulk materials listed in Table 10.2.

### 10.2.1 Layout of Iterative Device Design

In our case, we assumed a feature size $F = 15\mathrm{nm}$. The thickness of bulk materials has no specific design rule associated with it but we attempted to keep the thickness in multiples

Table 10.2: Material parameters of common bulk material used spintronic research and modeling [106, 91].

| Material | $M_s \left(\frac{MA}{m}\right)$ | $K_u \left(\frac{kJ}{m^3}\right)$ |
|---|---|---|
| Co | 1.4 | 520 |
| Fe | 1.7 | 48 |
| Ni | 0.49 | -5.7 |
| Permalloy | 0.86 | 0 |

of 0.5 nm which should be achievable with modern fabrication technology. Using the rules described, we obtained the following device layout shown in Figure 10.4. To understand

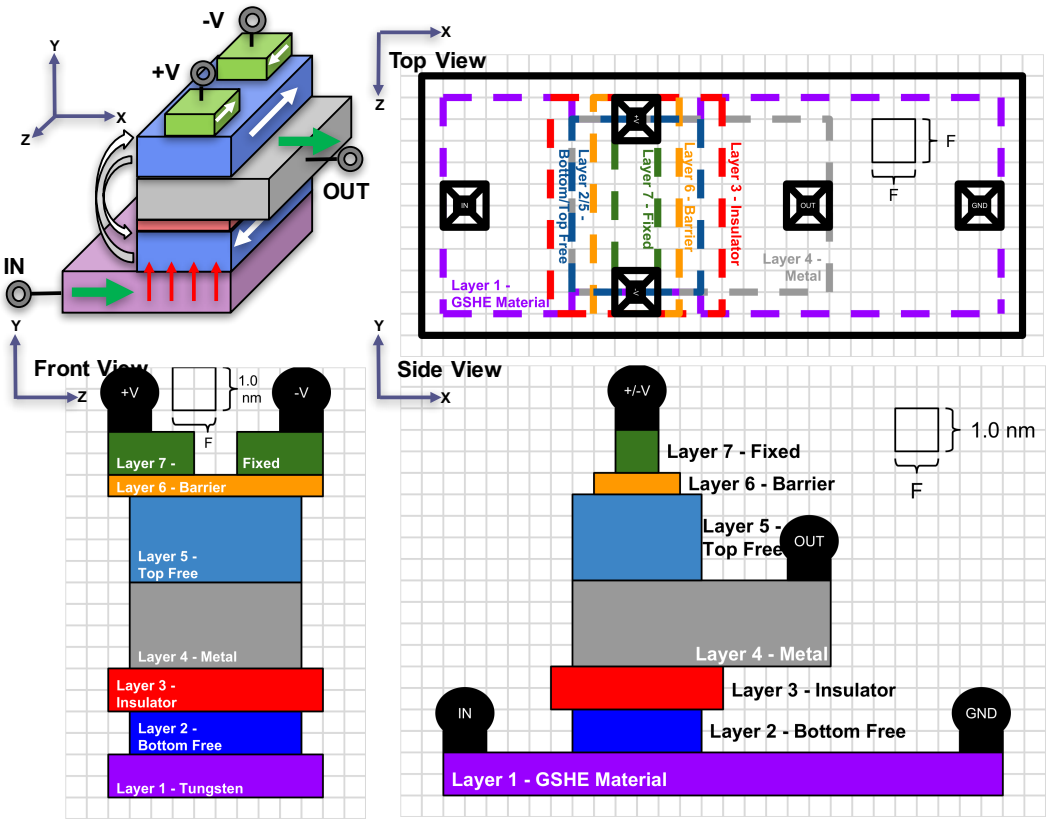


Figure 10.4: Classic device layout using layout rules outlined in [27].

this layout it is simpler to begin from the top layer down (opposite to the flow of information). First we begin by placing the supply contacts. The spacing between these contacts is determined by the next layer, the fixed magnet. Because these magnets are in-plane fixed magnets, an L/W aspect ratio of 2 was chosen to increase the contribution to the energy barrier by the shape anisotropy and help preserve their magnetization states. Next the tun-

neling barrier is made slightly larger than the fixed magnets to ensure full contact between the top free- and fixed-nanomagnets.

The top free magnet is laid next and we decide to make this magnet a $60nm \times 45nm \times 2nm$ magnet because we found that making the aspect ratio any larger would increase the current to a level which would make dipolar coupling impossible. The geometries and material parameters for the system will be further discussed in the next section. The metal layer and GSHE material are extended to account for the space requirements between the contacts.

The bottom nanomagnet and top free magnet have the same lengths and widths. This is because it can be shown that the averaged dipolar tensor is maximized for systems whose interacting areas are equal. The nanomagnet bosies are also centered with respect to one another along the $\hat{z}$-axis. This ensure that the non-diagonal components of the dipolar tensor average to zero maintaining ensuring a free-axis along $\hat{x}$.

### 10.2.2 Material Parameters

Tungsten, having the largest known spin hall angle, was the natural choice for the GSHE material layer. This gives a $\theta_{SH} = 0.3$ and $\lambda_s = 2.5nm$. The GSHE material also determines the input resistance of the device. Figure 10.2 shows that the amplification of the GSHE material is optimized at 4nm thickness. The bulk resistivity of tungsten is $5.60 \times 10^{-8}\Omega \cdot m$ [186]. Using these values we get a resistance a resistance $R_W = 42\Omega$. In most digital circuits, the output of one gate must be connected to the input of multiple others. This is referred to as "fan-out" where a value of 1 would indicate a repeater circuit, and $> 1$ would suggest a logic circuit. We must multiply $r_{in}$ by the fan-out value of 4 normally used to characterizes devices to obtain: $r_{in} = 168\Omega$.

Next the parameter values for the MTJ stacks need to be assigned. We need to minimize the proportion of current being leaked between supplies. This leakage is solely achieved by increasing $TMR$. A large amount of experimental research has been dedicated to the

Table 10.3: Free magnet material parameters for layout-constrained device design.

| | M1 (Bottom) | M2 (Top) |
|---|---|---|
| $M_s(\frac{MA}{m})$ | 1.7 | 0.86 |
| $K_u(\frac{kJ}{m^3})$ | 48 | 0 |
| Geometry $(nm^3)$ | $60 \times 45 \times 1$ | $60 \times 45 \times 2$ |

analysis of MTJ structures. Currently, MTJ's with MgO tunneling barriers appear to offer the largest TMR values [20, 187, 83, 188]. A $TMR = 8$ falls within range of such devices. The resistivity of the MTJ stacks needs to be as low as possible to minimize the power consumption of the device. After a review of various experimental research, the lowest resistance MTJ values seen are $2\Omega\mu m^2$ [189, 190, 191].

Most important are the material parameters composing the two-magnet system. Note that the bottom nanomagnet should emit a strong dipolar field making the reversal of the top nanomagnet reliable. The strength of the dipolar field is proportional to the $M_s$ of the magnetic material. Of the common bulk magnetic materials normally considered, iron (Fe) has the largest $M_s$ with material parameters: $M_s = 1.7\frac{MA}{m}$ and $K_u = 48\frac{kJ}{m^3}$. However, a large $M_s$ increases the critical current required for STT reversal. We mitigate this issue by making the bottom magnet as thin as possible reducing its volume.

The top nanomagnet should have a fairly large $M_s$, but should also have a small energy barrier such that the dipolar field emitted from the bottom nanomagnet is strong enough to reverse the top. A permalloy has theoretically no uniaxial anisotropy energy making the energy barrier determined solely by the shape anisotropy of the magnetic body. In this evaluation we are using the complex (CHd) demagnetization field. Therefore, we assume a permalloy material for the top nanomagnet with material parameters $M_s = 0.86\frac{MA}{m}$ and $K_u = 0\frac{kJ}{m^3}$. Because we lowered the energy barrier of the top nanomagnet, M2 is susceptible to the bias current flowing through the top magnet. To counteract this bias current, we increase the thickness of the top magnet to 2 nm.

Therefore, for the layout constrained device design, we use the device parameters listed in Tables 10.3–10.5.

Table 10.4: MTJ material parameters for layout-constrained device design. Values correspond to MgO based MTJ device.

| TMR | 8 |
|---|---|
| $R_{MTJ}$ | $1.475k\Omega$ |
| $Areanm^2$ | $30 \times 15$ |

Table 10.5: GSHE material parameters for iterative design device. Values correspond to Tungsten material which has been shown to have the largest amplification factor of any known GSHE material to date [56].

| $\theta_{SH}$ | 0.3 |
|---|---|
| $R_W$ | $42\Omega$ |
| $t_W$ | $4nm$ |

### 10.2.3 Performance of Layout-Constrained Device Design

We first verify the operation of the layout-constrained design by analyzing sample device reversals for a multitude of supply amplitudes as shown in Figure 10.5. Figure 10.5 demonstrates that the device has a limited range of operation. If the voltage is too small, there is insufficient current to reverse the two-magnet system. However, if the spin current is large, the dual free-magnet system enters into an oscillatory state. This is different than the oscillatory states observed in Section 8.5 as those oscillatory states occured with a single spin current driving the bottom nanomagnet. Sweeping across a range of voltage values, we can obtain an approximate performance values for the device:

Figure 10.6 shows the results of the voltage sweep. We have chosen to initially omit stochastic effects from the performance metrics during this stage of our analysis. In such a complex system, stochastic perturbations would needlessly complicate the analysis. The delay variation observed in Figure 10.6 is an example of deterministic noise caused by the precessional effects of magnetization and it has very similar characteristics to the stochastic noise. Note that the variation is on the order of the period of a precessional orbit of the magnetization near the separation energy. The delay variation increases as the voltage approaches the maximum limit for nominal operation. This is due to the nanomagnet undergoing many oscillations before relaxing to the free-axis.

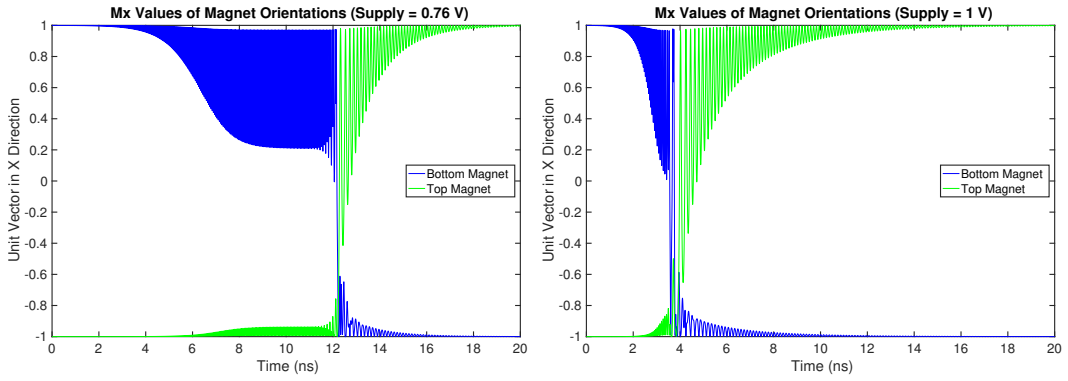


(a) 0.76 V (b) 1.00 V

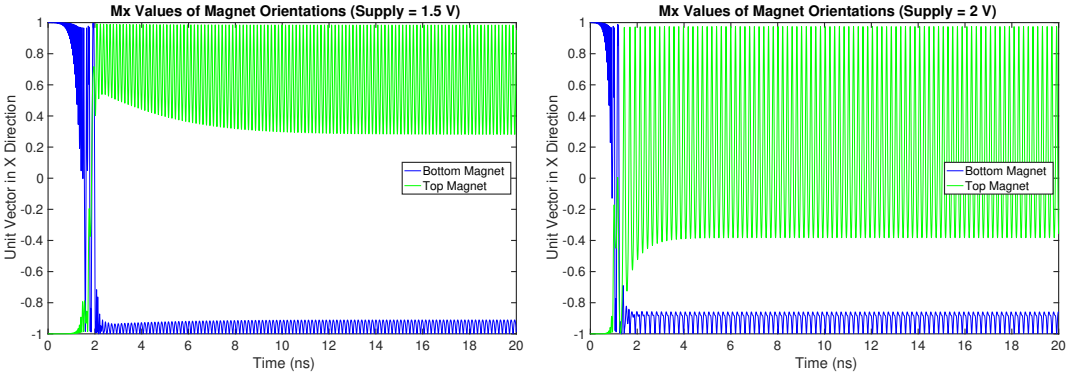


(c) 1.50 V (d) 2.00 V

Figure 10.5: Sample reversals for layout-constrained Spin-Switch device. $\vec{m}_x$ component of magnetizations shown for top and bottom free magnets.

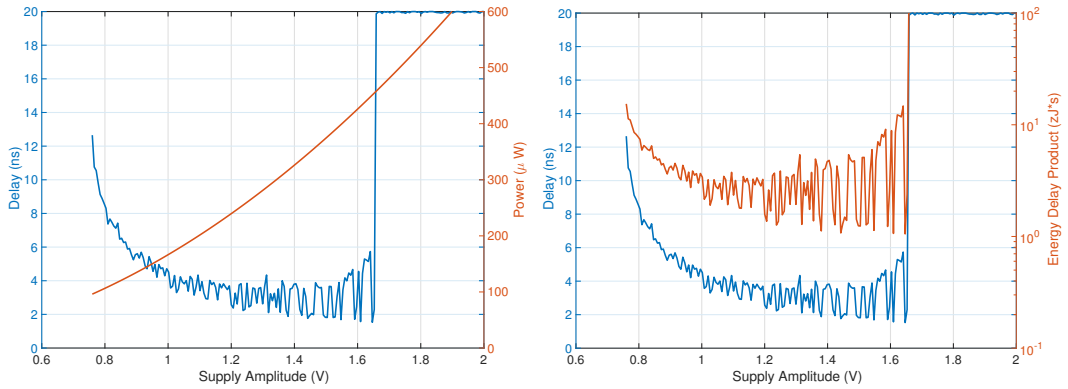


(a) Delay and Power (b) Delay and EDP

Figure 10.6: Voltage amplitude sweep for layout constrained Spin-Switch device.

It is useful to look at the energy-delay-product (EDP) because it gives useful, albeit simplified, metric for the device performance. Looking at the average trends in Figure 10.6, once the voltage amplitude is sufficiently larger than some critical current, the EDP remains

roughly constant. This average EDP value is $2.5\times10^{-21}\mathrm{J}\cdot\mathrm{s}$. For the sake of comparison, the approximate EDP for current CMOS technology can be found in the International Technology Roadmap for Semiconductors (ITRS) [192]. Assuming a feature size of 15nm, high performance CMOS has an EDP of approximately $0.21\times10^{-24}\mathrm{J}\cdot\mathrm{s}$. This is approximately four orders-of-magnitude less than the EDP of our layout-constrained device design.

### 10.3 Enhanced Layout-Constrained Spin-Switch Layout

One criticism of this device concerns the fabrication of the fixed magnets. Fixed nanomagnets are typically composed of multiple magnetic layers resulting in a ferromagnetic body layered next to a pinning layer. The interaction between the magnetic body and pinning layer results in a very large net anisotropy energy along the free-axis making the reversal of such a magnet, be it through STT, thermal effect or otherwise, unlikely. The fixed magnet is then set to a particular direction by applying a very large magnetic field across the chip. However, the device in Figure 10.4 has two fixed magnets in the opposite direction. This is problematic since applying a large field to one small portion of a chip is extremely difficult from a fabrication standpoint.

To simplify the fabrication of the Spin-Switch device, we can split the ferromagnet bodies in two, complementary devices. By routing the electrical current in opposing directions for each M1 portion, we can orient the fixed magnetizations in a parallel fashion, greatly decreasing the complexity of fabrication. This enhanced layout-constrained design is shown in Figure 10.7. The primary benefit of this design is that the fixed magnetizations are oriented in the same direction allowing easier device fabrication. We can do this because of the new free magnet structure. Notice that the GSHE material is bent into a "U" shape running under each free magnet. Assuming a positive current into the input, the electrical current flows in the positive $+\hat{x}$ direction under one of the lower free magnets and in the $-\hat{x}$ direction under the other lower free magnet. This means that the GSHE material applies opposing spin torques to the two lower free magnets and hence, the split, lower free

magnets reverse to anti-parallel directions

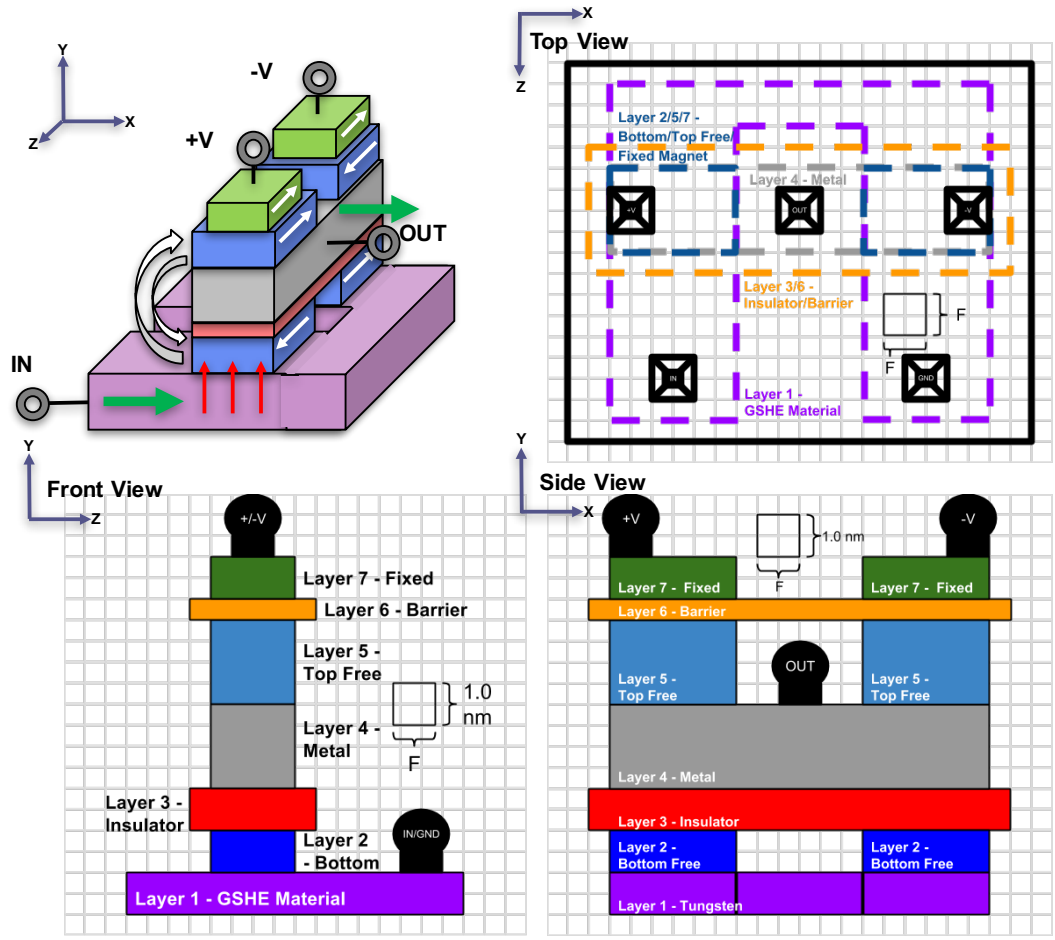


Figure 10.7: Enhanced device layout where the free magnets are separated into two stacks. This modification allows the simpler fabrication of dual fixed magnets whose magnetizations are oriented in the same direction. This design also makes the free magnets smaller theoretically improving device performance.

There is a secondary benefit to this enhanced layout. Making the free magnet bodies smaller will require less energy for reversal. But there is a problem with simply making the free-magnet bodies smaller. If there was no cost to do so, one can simply scale the device down infinitely and argue that the energy costs of this device trend towards zero. But spin-based technologies and charge-based technologies share the same weakness as the feature size is scale down, *reliability*. This is especially true in spin-base devices since reducing the volume of a magnetic body makes its magnetization state less stable and prone to thermal effects. Reliability gates the full potential of the device.

## 10.4 Reliability-Constrained Spin-Switch Device Design

The limiting factor for the layout-constrained device were the benchmarking rules. These rules were developed in an effort to compare different logic technologies assuming current device technology. However, one can argue that as fabrication technology improves and the devices are scaled down, spin-based technology will become more viable, if not superior to current CMOS technology. But the limiting factor to this argument is that the magnetic systems must be reliable above all else. Reliability becomes an issue for smaller devices because the magnitude of the thermal field is inversely proportional to the volume, $M_s$ and $K_u$. Therefore, we can approach the design of the Spin-Switch in an alternate manner. We will attempt to design the best Spin-Switch device possible while making sure the magnetization states are robust and meet a certain reliability criteria. We can simply ask what the best performance parameters for this device are given theoretically, a set of favorable input conditions, and ignoring the feasibility of fabrication. The material and geometric parameters are largely unbounded. Because physical layout is not a concern for the theoretical case, let's return to the classic device design shown in Figure 1.9.

### 10.4.1 Model Definition: Thermal Reversal Probability

In Chapter 3, we discussed the probability of reversal for biaxial magnetic body and concluded that given a long observation time, the probability of reversal for biaxial and uniaxial systems are equivalent. Therefore, it is possible to use thermal reversal probability equation (3.2) repeated here for ease of reference

$$P_{SW} = 1 - exp[t f_0 e^{-\frac{E_b}{k_b T}}], \tag{10.13}$$

where

$$f_0 = \frac{\gamma\alpha}{1+\alpha^2}\sqrt{\frac{H_K^3 M_s V}{2\pi k_B T}}. \tag{10.14}$$

We can reformulate (10.13) to become a function of material parameters and desired stability

$$f_0 = \frac{-ln(1 - P_{SW})}{texp(\frac{-K_u V}{k_B T})}. \tag{10.15}$$

Setting $P_{SW}$ and $t$ to the desired values allows us to solve for material parameters $M_s$, $H_k$, and $V$. We can assume an observation time $t = 100ns$ and $P_{SW} = 10^{-6}$. While this set of reliability metrics are far below what current CMOS technology offers, it is difficult to increase the reliability metrics further while also designing a device using a reasonable set of material parameters.

### 10.4.2 Initial Approximations

We need to consider the number of variables in the two-magnet system and attempt to reduce the number of variables making the complexity of the analysis more manageable. We begin by noting that $\alpha$ should be as small as possible. Not only would a large $\alpha$ increase the critical current of the two-magnet system, it also inhibits the coupling between the nanomagnets as noted in Section 7.3.3. Therefore, a small $\alpha = 0.01$ is considered. Next, for each free magnet, $L, W, t$ define the length, width and thickness of the ferromagnetic body and $M_s/K_u$ describe the material parameters of the magnetic body. For the GSHE effect to be maximized, the width of the magnetic body should be as large as possible. However, the width of an in-plane nanomagnet should not exceed its length because its shape anisotropy would end up working against it's uniaxial anisotropy and unstable behavior may occur. In addition, from (6.1)-(6.3), the tensor components are maximized when the length of the magnetic body is equal to the width. Hence, it is most beneficial to assume that $L_1 = W_1$ and $L_2 = W_2$. Furthermore, in a $\hat{z}$-centered two-magnet system, the magnitudes of the dipolar components are maximized when the areas of the two magnet system are approximately equal. Therefore we expand our geometric approximation such that $L_1 = W_1 = L_2 = W_2 = Lm$ where $Lm$ is simply an abstraction of the value assigned to those four geometric parameters. Lastly, we want to bottom nanomagnet to be as spread

out as possible to ensure it receives the maximum benefit from the GSHE. Therefore, we can make $t_1 = 1$ nm. Six unknowns in the two-magnet system need to be solved for: $Lm$, $t_2$, $M_{s1}$, $K_{u1}$, $M_{s2}$ and $K_{u2}$.

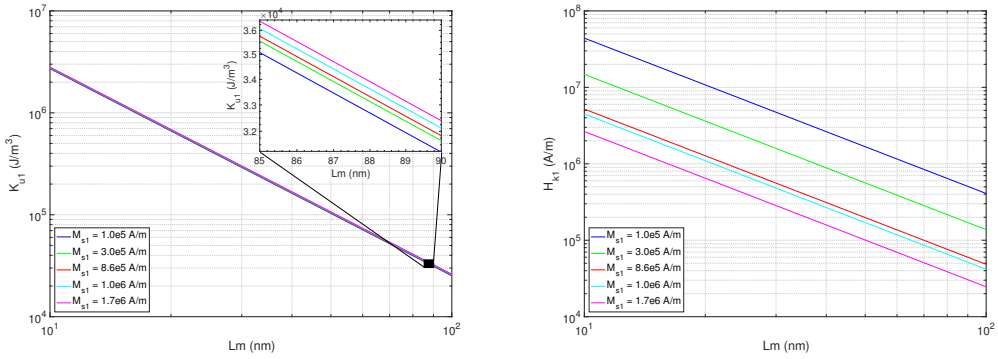


Figure 10.8: Minimum $K_u$ (*Left*) and $H_k$ (*Right*) required for a $Lm \times Lm \times 1$nm magnetic body while maintaining reliability metrics $P_{SW} = 10^{-6}$ and $t = 100ns$.

### 10.4.3 Minimum Free-Magnet Size

Our minimum reliability metrics allow us to determine the material parameters necessary for a robust magnetic body. In Figure 10.8, we find the minimum $K_u$ which establishes a reliable magnetic body for a given set of $M_s$ and $Lm$ values. The minimum $K_u$ value is roughly constant regardless of $M_s$. When calculating the $H_k$ value, we notice that the magnitude of the uniaxial field varies greatly with both $Lm$ and $M_s$. Looking at the actual $H_k$ values, we begin to see a problem. From (6.1), we know that the components of the dipolar tensor are linearly proportional to $M_s$ such that $DIP_{xyz} = M_s\iota$ where $\iota$ is some complex calculation dependent on the geometry of the two magnet system. From our previous calculations we also know that for the two-magnet systems we are considering $\iota$ is on the order of 0.01. Using common $M_s$ values such as the ones found in Table 10.2, $DIP_{xyz}$ is on the order of $10^4 \frac{A}{m}$ which is less than many of the minimum $H_k$ values calculated in Figure 10.8.

Assuming $Lm, t_1$, and $t_2$ are known, the $M_s$ and $K_u$ of each magnetic body needs to be determined. For a given $M_{s1}$, the minimum $K_{u1}$ can be calculated using (10.13). In

addition, the geometry and $M_{s1}$ determine the magnitude of the tensor components emitted by M1. If $M_{s2}$ is small, $H_{k2}$ will be large. The dipolar field emitted by M2 will be too small to establish coupling between the magnetic bodies according to 10.2. As $M_{s2}$ increases, $DIP_2$ becomes larger and $H_{k2}$ shrinks strengthening coupling. Using this principle, Figure 10.9 calculates the minimum $M_{s2}$ given $M_{s1}$ for a variety of geometric parameters. Notice that the minimum $M_s$ values for a operational two-magnet system are large given that iron has a $M_s = 1.7\frac{MA}{m}$, the largest saturation magnetization of all known materials. Because

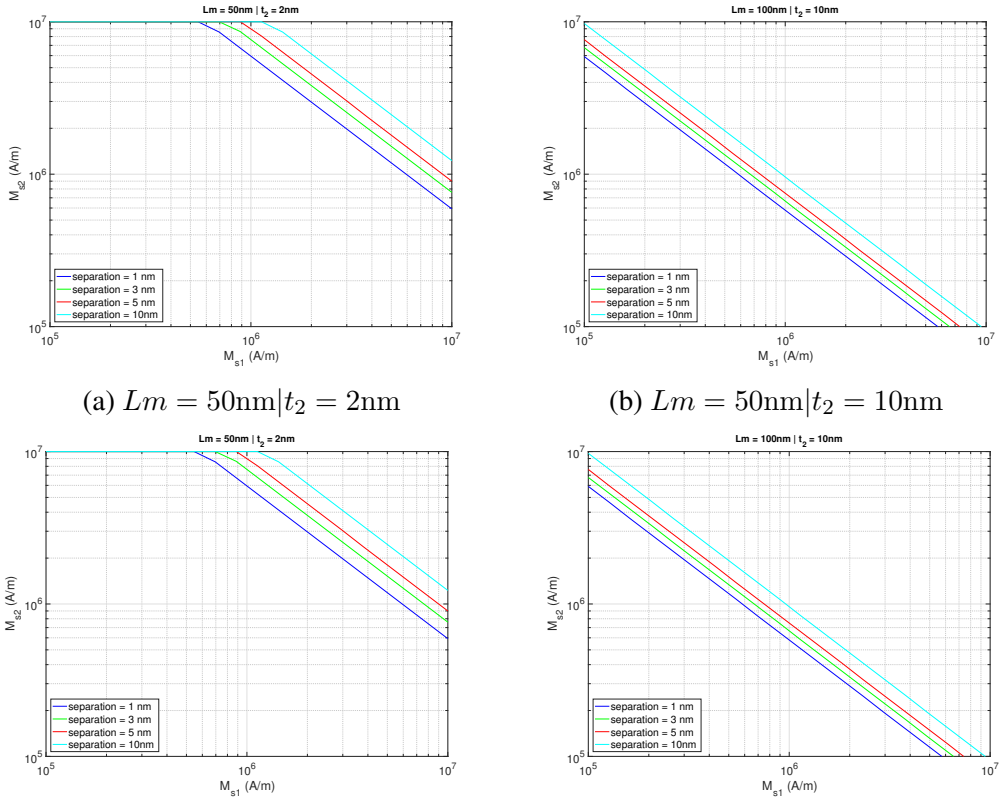


(a) $Lm = 50\text{nm}|t_2 = 2\text{nm}$ (b) $Lm = 50\text{nm}|t_2 = 10\text{nm}$

(c) $Lm = 100\text{nm}|t_2 = 2\text{nm}$ (d) $Lm = 100\text{nm}|t_2 = 10\text{nm}$

Figure 10.9: Minimum $M_{s2}$ values for nanomagnet system given $M_{s1}$. Assuming $t_1 = 1nm$ and $L_1 = L_2 = W_1 = W_2 = Lm$. $K_{u1}$ is determined by $M_{s1}$ according to the reliability constraints. Therefore, there is a minimum $M_{s2}$ which will allow a $DIP_2$ large enough to satisfy the dipolar coupling model given by (10.2).

$t_1 = 1\text{ns}$ has been fixed to ensure the bottom nanomagnet is as spread out as possible, ensuring maximum amplification from the GSHE effect, there are two geometric unknowns in the system, $Lm$ and $t_2$. Thermal reliability is inversely proportional to nanomagnet vol-

ume. A larger M1 volume permits a smaller $H_{k1}$ field. This means $M_{s1}$ and $M_{s2}$ values can be reduced while still ensuring ideal coupling. Figure 10.10 maps the minimum geometric requirements for an operational Spin-Switch device.

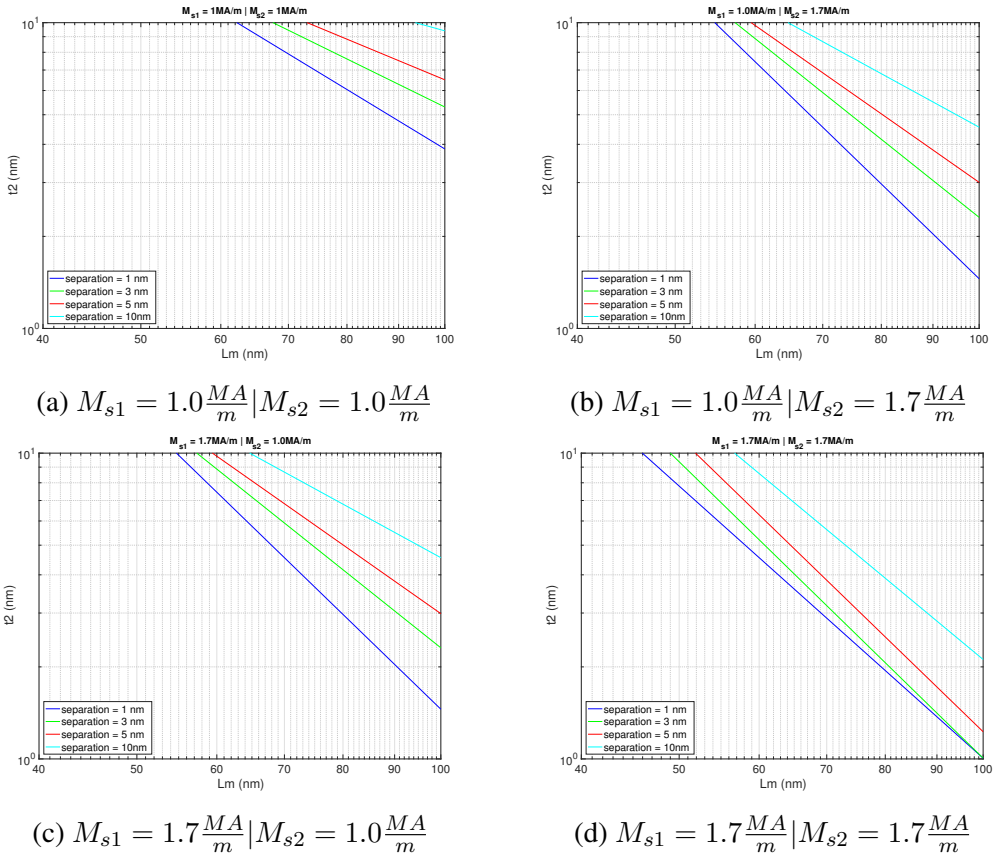


(a) $M_{s1} = 1.0\frac{MA}{m} | M_{s2} = 1.0\frac{MA}{m}$

(b) $M_{s1} = 1.0\frac{MA}{m} | M_{s2} = 1.7\frac{MA}{m}$

(c) $M_{s1} = 1.7\frac{MA}{m} | M_{s2} = 1.0\frac{MA}{m}$

(d) $M_{s1} = 1.7\frac{MA}{m} | M_{s2} = 1.7\frac{MA}{m}$

Figure 10.10: Minimum $t_2$ values for nanomagnet system given $Lm$. Assuming $t_1 = 1nm$ to maximize the amplification for the GSHE. As the volume of a nanomagnet increases, the thickness of the top nanomagnet may be reduced will maintaining equivalent reliability metrics.

### 10.4.4 Performance of Reliability-Constrained Device Design

Using extensive numerical calculations, we determine the lowest energy nanomagnet configuration which satisfies the reliability parameters defined as:

Note that the nanomagnets considered here are actually larger than those of the layout-constrained design. Ensuring reliability of a nanomagnet system is very difficult because the thermal field has such a large effect on magnetization state. Because the nanomagnet's

Table 10.6: Free magnet material parameters for reliability-constrained device design.

| | M1 (Bottom) | M2 (Top) |
|---|---|---|
| $M_s(\frac{MA}{m})$ | 1.7 | 1.7 |
| $K_u(\frac{kJ}{m^3})$ | 40 | 40 |
| Geometry $(nm^3)$ | $83 \times 83 \times 1$ | $83 \times 83 \times 2$ |

are larger, they can support the MTJs as they were sized in the layout-constrained design. Hence, GSHE (Table 10.5) and MTJ (Table 10.4), parameters kept were same.

Figure 10.11 measures the device performance over a variety of voltage magnitudes. In this device design, there are a few oscillatory states at certain voltage supply currents indicated by the EDP spikes. This is significantly different than the layout-constrained case where there was an oscillatory state once the voltage magnitude exceeds a certain threshold. The reliability-constrained case designs the top nanomagnet to be as stable as the bottom, reducing the likelihood of oscillatory states.

Like the layout-constrained case, we see a constant EDP once the voltage magnitude is beyond a critical threshold. The average of this value is approximately $5\times10^{-21}\mathrm{J}\cdot\mathrm{s}$. This EDP value is roughly 25$\times$ the EDP of the layout constrained case because the larger nanomagnets have greater $M_s$ and $K_u$ values. This shows that the EDP of Spin-Switch device technology is roughly five orders-of-magnitude greater than the EDP of modern CMOS technology. Significant performance improvements need to be made that improve the delay and power consumption of spin-based technologies.

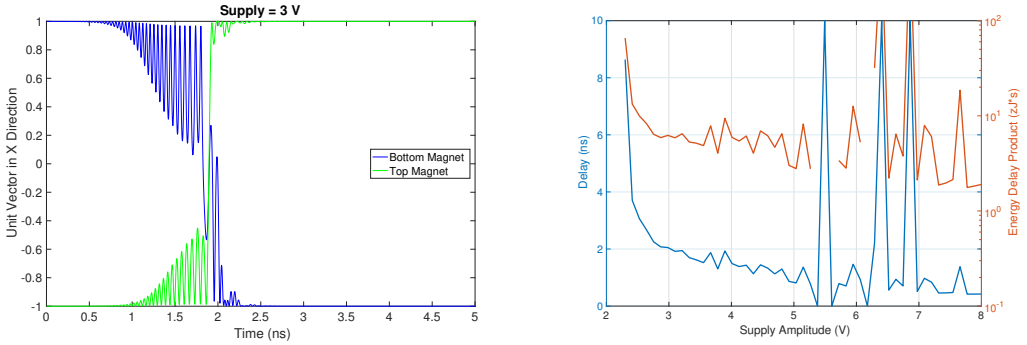


Figure 10.11: Performance metrics of reliability constrained device design. Free magnet parameters listed in Table 10.6 which were optimized while maintaining reliability metrics $P_{SW} = 10^{-6}$ and $t = 100\text{ns}$. (*Left*) Sample of device functionality assuming a 1 V supply magnitude. (*Right*) Voltage sweep of reliability constrained device design measuring delay and EDP metrics.

# CHAPTER 11

# POSSIBLE IMPROVEMENTS I: GENERAL

Having proven that Spin-Switch devices in their proposed configuration yield poor performance metrics, we aim to consider whether spin-based devices have any advantages which would bring their performance metrics closer to or even exceed current CMOS standards. As such, Chapters 11 are dedicated to finding possible benefits of spintronic devices which may not be evident when conducting a simple energy-delay analysis. In addition, Chapters 11–12 propose possible augmentations applicable to a variety of spin-based devices which theoretically promise to improve the performance of these technologies.

## 11.1 Latch-less Pipelining in Spin-Based Circuits

In CMOS pipelines, dynamic flip-flops (DFFs) are placed at the either end of pipeline stages. Spin devices are non-volatile since the magnets maintain their orientation even when not being driven by a spin current. Instead of the stage input needing to be held for the entirety of the clock period, the stage input of a spintronic pipeline only needs to be held long enough to switch the next device. By carefully manipulating the supply voltages of the logical device at the beginning and end of a pipeline stage, the use of latches may be avoided when building a pipelined circuit [54].

Figure 11.1 demonstrates an example of latch-less pipelining using the Spin-Switch devices. This technique uses no extraneous switches. The Spin-Switch logic devices shown at the end of stage N and beginning of stage N+1 can be used as logic gates that are part of a more complex circuit. Their supplies must be clocked and never on at the same time. All other switches may use static supplies, which is important because of the delay variation issues in spintronic devices. In Figure 11.1, the switch in the $N^{th}$ stage is on during the negative portion of the clock and off otherwise. Conversely, the switch in the $(N+1)^{th}$ stage

is powered during the positive portion of the clock.

To gain a full understanding of the pipeline, it is useful to step through it. In Figure 11.1, the supplies of Switch 1 (S1) are turned off and the supplies of Switch 2 (S2) are turned on. The input signal is stopped at S1 and cannot propagate to the next stage while the input for Stage N+1 is held by S2. When the clock falls, the supplies of S2 are turned off and the supplies of S1 are turned on. S2 no longer outputs the input for the previous stage. This is okay as long as there is enough delay to flip the magnets of the next switch. S1 now can propagate the input to S2 which will then block the input from proceeding into Stage N+1. The clock now goes high and S1 is turned off again. S2 then outputs the signal it read from Stage N at the positive edge of the clock.

The input signal only passes to the next stage at the positive edge of the clock and is blocked otherwise. This fulfills the requirements needed for pipelining. There are a few caveats needed to be considered. The on-time of the switch does not need to be half the clock period. It needs to be long enough such that the switch can flip the magnetization of the next switch. The last switch of the $N^{th}$ pipeline stage and the first switch of Stage N+1 cannot be on at the same time. This ensures that a signal is blocked until the pipeline is ready to proceed. The only drawback of this method is that the supplies must be clocked, which can make system architecture design challenging. Clocking in spintronic devices is preferred to reduce their power dissipation [2].

## 11.2 Benefit of Majority Gate Logic Functionality

An interesting aspect of current based logic devices is that they are functionally majority gates. They can only perform Boolean operations when their inputs are weighted. Adding a new Boolean operation can reduce the number of devices required in certain circuits. For instance, a full adder requires five NOT/AND/OR gates, but only three majority gates as seen in Figure 11.2 [193]. It has been theoretically evaluated that majority gate functionality can reduce the nominal gate count by roughly 20-25% [194, 195].

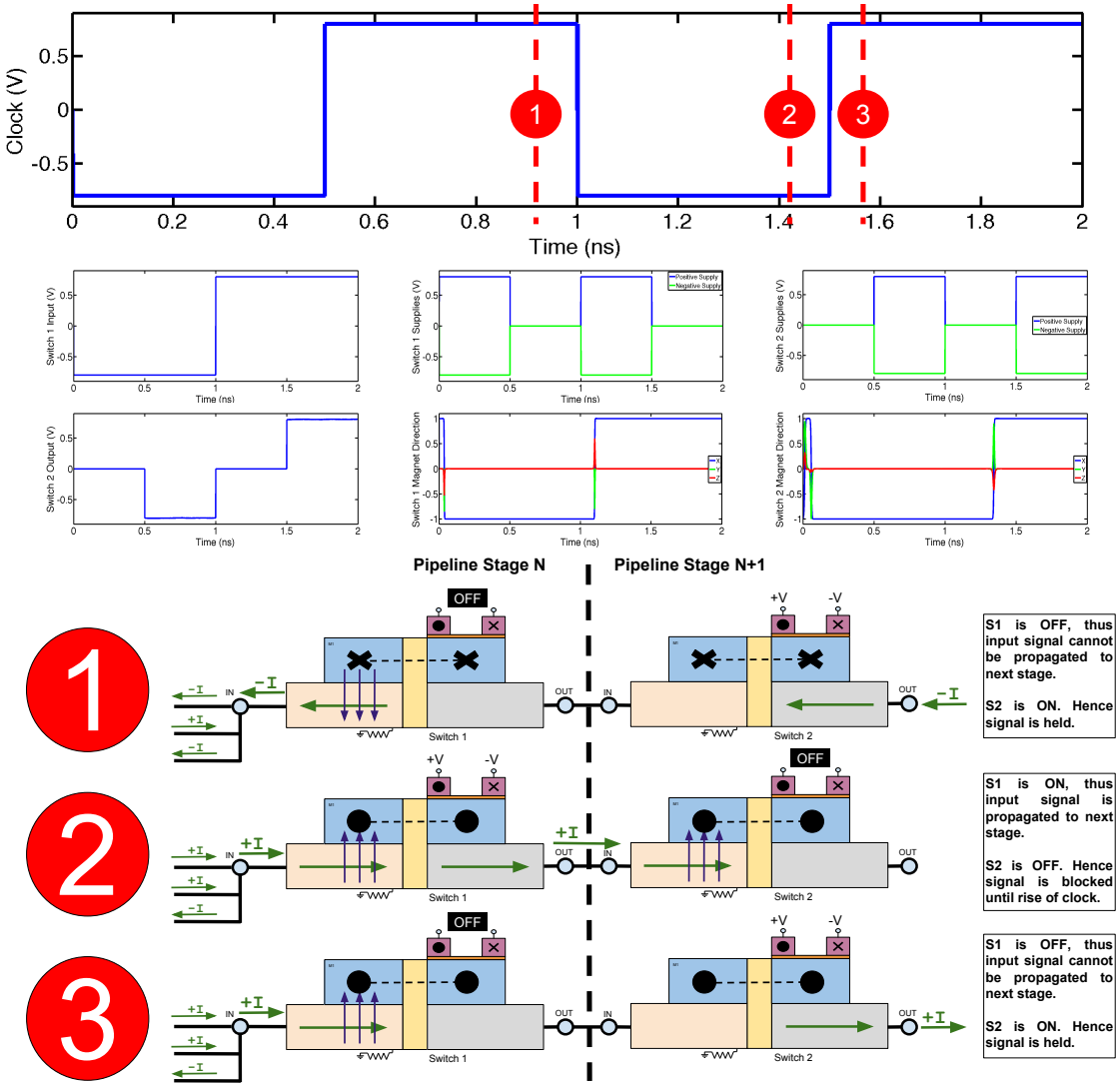


Figure 11.1: Figure demonstrates latch-less pipeline design. The waveforms are obtained using SPICE simulations of the Spin-Switch device. Free and fixed magnets are in blue and magenta, respectively. Arrows represent direction of current flow, not signal propagation.

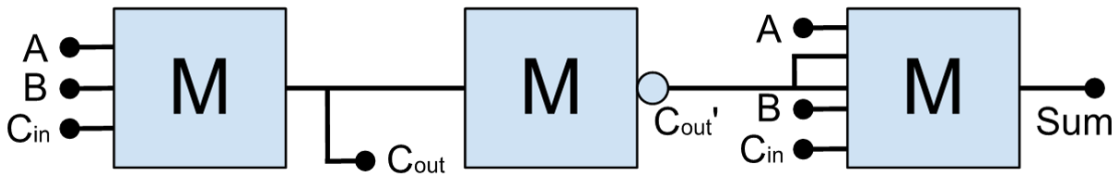


Figure 11.2: Logic diagram of a 1 bit full adder system

## 11.3 Copper Collector

Consider Figure 10.1. Due to the nature of the GSHE material, the spin current must be orthogonal to the electrical current. In a similar fashion, the polarization of the spin current must be orthogonal to the spin current itself. In Figure 10.1, the polarization of the spin current is in the $\hat{y}$ direction. If it is desired the nanomagnet be reversed through a damping reversal, its easy-axis must also be in the $\hat{y}$.

This becomes problematic because the free-axis direction should the the longest direction for in-plane nanomagnets. As seen in Figure 10.1, it would be preferable to make the $\hat{x}$ axis, the hard-axis, as long as possible. The width of the nanomagnet should be as long as possible, not its length. The contribution of the GSHE is given in (1.3) and repeated here:

$$I_s = I_e \theta_{SH} \frac{W_{NM}}{t_{GSHE\_M}} \left(1 - sech\left(\frac{t_{GSHE\_M}}{\lambda_s}\right)\right), \tag{11.1}$$

where $I_s$ and $I_e$ represent the spin and electrical currents respectively. $\theta_{SH}$ is the spin hall angle and is specific to the material being assumed. $W_{NM}$ and $t_{GSHE\_M}$ are the width of the nanomagnet and thickness of the spin-hall material respectively.

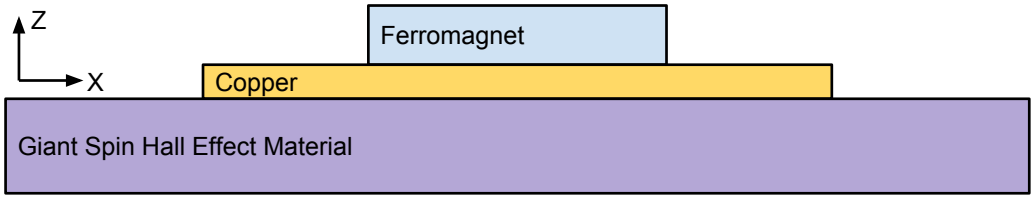


Figure 11.3: Diagram of spin collector setup to drive a ferromagnet through the use of the GSHE. this is similar to the standard setup but includes a copper collector between the ferromagnet and GSHE material. Ideally the copper plate will collect the spin current from the GSHE material and diffuse it to the ferromagnet.

### 11.3.1 Spin Collector Setup

It has been suggested that the addition of copper plate in between the GSHE material and ferromagnet (as shown in Figure 11.3) can amplify the conversion from electrical to spin

current [196]. The addition of the copper plate in Figure 11.3 aims to extend the width of the ferromagnet from the GSHE material's perspective, but keep the magnet properties the same from the ferromagnet perspective. In theory, the GSHE will inject a spin current into the the copper plate. This spin current will diffuse through the copper material and into the ferromagnet which functionally behaves as a spin sink. Because the copper plate has a larger area than the ferromagnet, it collects a larger spin current from the GSHE material which is delivered to the ferromagnet. Because the ferromagnet size is unaltered, it is easier to reverse with this larger spin current.

Several things were missing from the analysis provided in [196]. Most notably, the spin diffusion through the copper collector was completely omitted from this analysis. The spin current attenuates as it passes through a metal because of electron scattering events with the crystal structure [197, 198]. This analysis will attempt to measure the efficacy of the spin collector idea assuming the following:

1. Time Independence - Only the DC case of the circuit will be evaluated

2. No Interface Effects - Interface scattering and edge effects are neglected. Assumes perfect material matching.

It is important to emphasize that this analysis focuses on the maximum possible benefit of the copper collector, assuming no interface contribution. We know experimentally that the interface between the metallic layers critically alters the dynamics of the system. There are a few benchmarking works which assume the existence of an ideal copper collector in their calculations.

### 11.3.2 Circuit Model

There are three distinct spin injection regions which are shown in Figure 11.4.

In Zone 1, assuming no interface effects, the copper plate can be ignored and the spin injection is simply that of a standard ferromagnet on top of a GSHE material. The spin

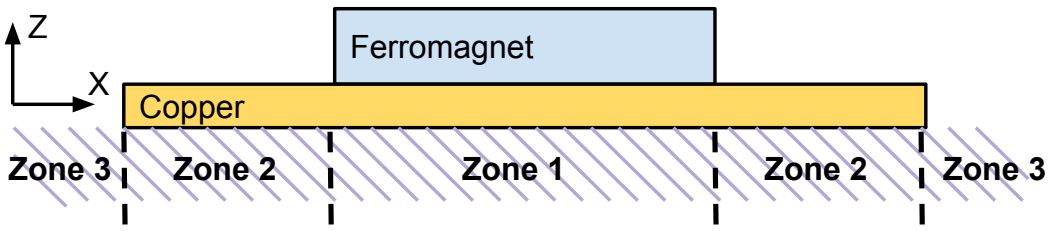


Figure 11.4: 3 distinct spin injection regions exist. In Zone 1, assuming no interface effects, the copper plate can be ignored and the spin injection that of a standard ferromagnet on top of a GSHE material. In Zone 2, spin current accumulates in the copper and diffuse toward the ferromagnet. In Zone 3, there is no spin contribution towards the ferromagnet.

current contribution from this region can be modeled as (11.58). This assumes that the interface effects have no significant impact on the spin current delivered to the magnetic body. There is no spin current injection from Zone 3.

Zone 2 is the basis of the spin amplification. This region theoretically collects extra spin current from the GSHE material and delivers it to the magnetic body. We focus on the spin current contribution by this region.

*Circuit Model of Diffusion Channel*

According to [199], the spin channel can be modeled as a complex RC circuit as shown in Figure 11.5.

The objective of this work is to find the additional spin-injection the copper plate allows over a long period of time meaning that the capacitors can be ignored. The resulting circuit per unit length is shown in Figure 11.6.

In the circuit model given in Figure 11.6, the resistances and current sources are defined using the following reasoning. The spin current generated by the GSHE material is given by (11.2):

$$I_T \Delta x = I_e \theta_{SH} \frac{\Delta x}{t_{GSHE\_M}}, \tag{11.2}$$

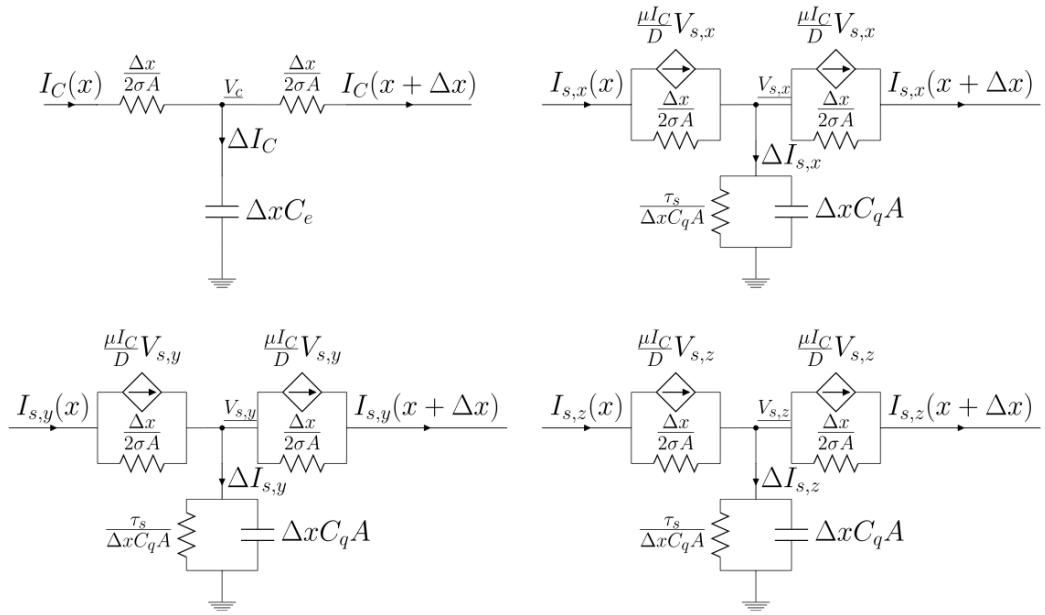


Figure 11.5: Circuit model for spin channel diffusion. Taken from [199].

the resistances are given in the following manner:

$$R_\perp = \frac{D\tau_S}{\sigma A}, R_{||} = \frac{1}{2\sigma A}, \tag{11.3}$$

where $C_q$ is the quantum capacitance per unit volume, A is the area of the diffusion channel, and $\tau_S$ is the spin relaxation time in the non-magnetic material. $D$ is the spin diffusion coefficient of the electrons in the channel. $\sigma$ is the conductivity of the non-magnetic conductor. In our model, we include size effects and thus, as the copper collector is made thinner, the resistivity is increased. The total channel circuit can be modeled as in Figure 11.7.

*Generalized Differential Equation for Channel Cell*

We define the current going through the circuit cell according to Figure 11.6. Using KCL we can derive the differential equation describing the cell's center node voltage.

$$I_{||2} + I_{\perp 2} = I_{||1} + I_{\perp 1} \tag{11.4}$$

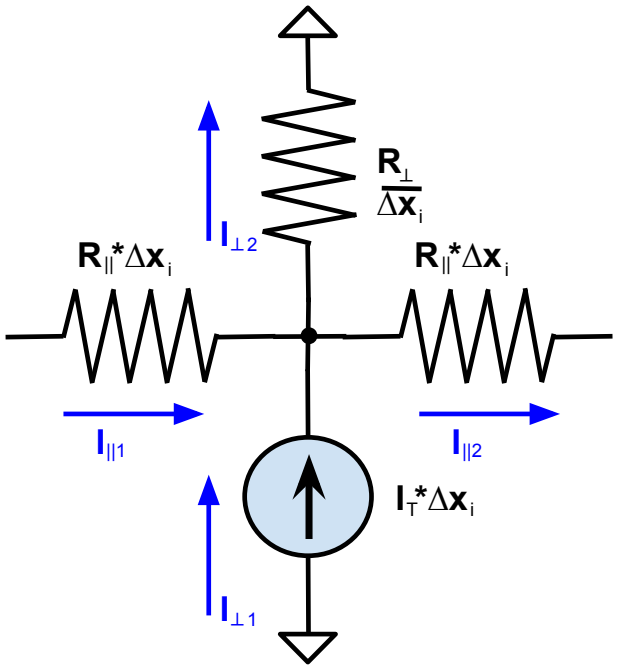


Figure 11.6: The steady state circuit cell model of the copper diffusion channel and spin injection from the GSHE. This circuit gives us the total possible spin injection of the copper plate model.

$$\frac{V(x)-V(x+\Delta x)}{R_{||}\Delta x}+\frac{V(x)\Delta x}{R_{\perp}}=\frac{V(x-\Delta x)-V(x)}{R_{||}\Delta x}+I_T\Delta x \tag{11.5}$$

$$\frac{V(x)-V(x+\Delta x)}{R_{||}\Delta x}-\frac{V(x-\Delta x)-V(x)}{R_{||}\Delta x}+\frac{V(x)\Delta x}{R_{\perp}}=I_T\Delta x \tag{11.6}$$

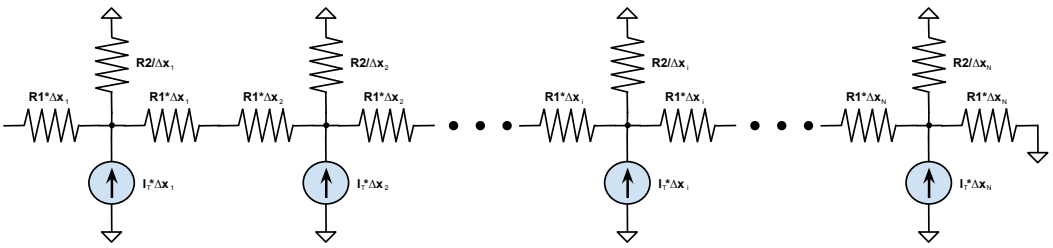

Figure 11.7: Circuit model of the copper diffusion channel and spin injection from the GSHE. The total circuit is simply a series of the cells shown in Figure 11.6.

$$\frac{2V(x) - V(x+\Delta x) - V(x-\Delta x)}{R_{||}\Delta x^2} + \frac{V(x)}{R_\perp} = I_T \tag{11.7}$$

$$\frac{V(x)}{R_\perp} - I_T = \frac{(V(x+\Delta x) - V(x)) - (V(x) - V(x-\Delta x))}{R_{||}\Delta x^2} \tag{11.8}$$

$$\frac{V(x)}{R_\perp} - I_T = \frac{1}{R_{||}}\frac{d^2V}{dx^2} \tag{11.9}$$

### 11.3.3 Solution 1 to Differential Equation

The generalized differential equation takes the form:

$$\frac{1}{R_{||}}\frac{d^2V}{dx^2} = \frac{V(x)}{R_\perp} - I_T \tag{11.10}$$

or

$$\frac{d^2V}{dx^2} = \frac{R_{||}}{R_\perp}V(x) - I_T R_{||} \tag{11.11}$$

we know that the solution to this differential equation must take the form:

$$V(x) = (V_0 - V_\infty)\, e^{-\alpha x} + V_\infty. \tag{11.12}$$

We define the voltages as shown in Figure 11.8

Plugging (11.12) into (11.11) we get:

$$\alpha^2 (V_0 - V_\infty)\, e^{-\alpha x} = \frac{R_{||}}{R_\perp}\left((V_0 - V_\infty)\, e^{-\alpha x} + V_\infty\right) - I_T R_{||} \tag{11.13}$$

There are 2 parts to this exponential equation. First, we solve for the constants in the equation:

$$0 = \frac{R_{||}}{R_\perp}V_\infty - I_T R_{||} \tag{11.14}$$

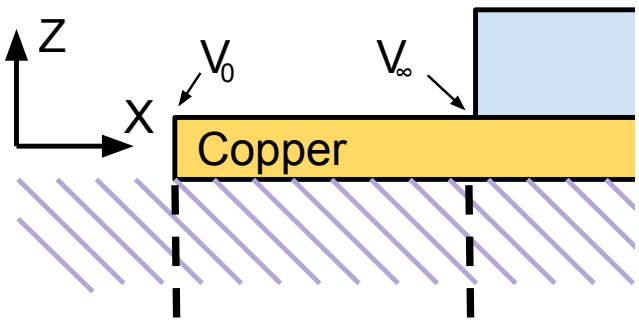


Figure 11.8: Labeling of voltages along the spin copper channel.

$$V_\infty = I_T R_\perp \tag{11.15}$$

Next, we solve for the exponentials in the equation:

$$\alpha^2 \left(V_0 - V_\infty\right) e^{-\alpha x} = \frac{R_{||}}{R_\perp} \left(\left(V_0 - V_\infty\right) e^{-\alpha x}\right) \tag{11.16}$$

$$\alpha = \sqrt{\frac{R_{||}}{R_\perp}} \tag{11.17}$$

All the constants in (11.12) have been solved for except $V_0$. We can say $V_0 = 0$ since it is assumed, at the very beginning of the copper channel, very little current is shunted. The solution for the voltage along the copper channel can be written as:

$$V\left(x\right) = I_T R_\perp \left(1 - e^{-\sqrt{\frac{R_{||}}{R_\perp}} x}\right) \tag{11.18}$$

*Current injected to Magnet from Copper Channel*

Looking at Figure 11.6 it is straightforward to obtain the current through each of the resistors at a certain distance. They would be:

$$I_{||}(x) = -\frac{1}{R_{||}\Delta x}\Delta V = -\frac{1}{R_{||}}\frac{dV}{dx} = I_T\frac{R_\perp}{R_{||}}\sqrt{\frac{R_{||}}{R_\perp}}e^{-\sqrt{\frac{R_{||}}{R_\perp}}x} = I_T\sqrt{\frac{R_\perp}{R_{||}}}e^{-\sqrt{\frac{R_{||}}{R_\perp}}x} \quad (11.19)$$

*Copper Channel Diffusion Results*

This section analyzes the improvement in spin injection from Zone 2. It is important to realize the relationship between the length of the Zone 2 copper, the overhang length and the spin current injected into the nanomagnet.

The equation for the spin current injected into the nanomagnet is given by (11.19). Let's assume a $60nm \times 45nm \times 2nm$ ferromagnet. The resistivity, diffusion coefficient, etc. of the copper channel can be calculated according to [52].The spin current injection into the nanomagnet for various copper overhangs and thicknesses follows in Figure 11.9.

Figure 11.9 reveals a problem with this model. (11.19) is monotonically decreasing. The maximum spin injection occurs when the copper channel is 0 nm long. This is evident from (11.19). None of the variables in the equation are dependent on $x$ according to (11.2-11.3). (11.19) is monotonically decreasing. An error in either the model or one of the assumptions exists because this result means no copper channel has more spin current injection one exactly the length of the nanomagnet body.

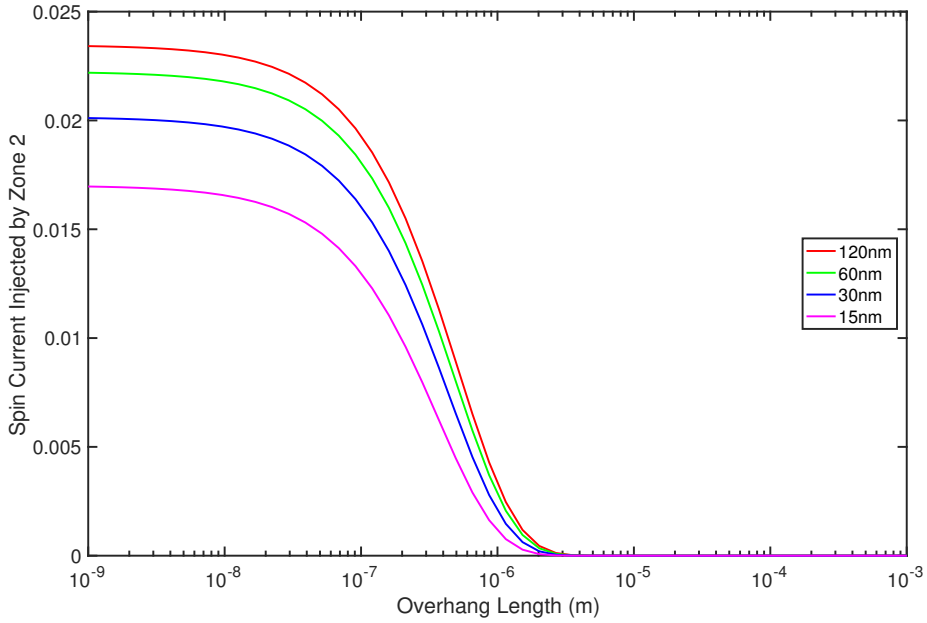


Figure 11.9: Current injected to ferromagnet vs. various copper lengths using Solution 1. Legend denotes various copper plate thicknesses (Z dimension). Assuming a 1mA electrical current passing through the GSHE material.

### 11.3.4 Solution 2 to Differential Equation

The boundary conditions used in Section 11.3.3 are the likely cause of error. The most likely conclusion is that:

$$V_\infty \neq I_T R_\perp \tag{11.20}$$

At $L = \infty$, the copper and the nanomagnet meet. It is believed that the nanomagnet behaves as a spin sink and as a ground at the point shunting the current. If the solution to (11.9) is of the form (11.12), (11.20) must be true. Therefore, (11.12) is not the solution to the system.

(11.12) assumes $\frac{dV}{dx} = 0$. This is not necessarily true. If you attempt to solve the equation numerically with $V(\infty) = \frac{dV(\infty)}{dx} = 0$ a nonsensical equation results in a similar fashion to the analytic case. Solutions to these differential equations need to be bounded.

*Generalized Solution using Laplace Transform*

Using another approach, we can solve the differential equation in the Laplace form using the coordinates shown in Figure 11.10:

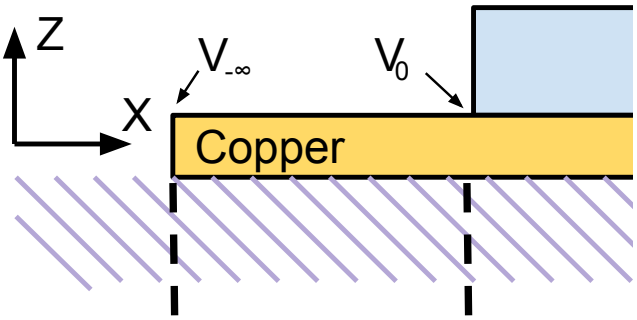


Figure 11.10: Alternate labeling of voltages along the spin copper channel.

Assuming the following initial conditions,

$$V(0) = 0 \tag{11.21}$$

$$\frac{dV(0)}{dx} = a \tag{11.22}$$

The characteristic equation is of the form:

$$\frac{d^2V(x)}{dx^2} - \frac{V(x)}{\lambda^2} + C = 0 \tag{11.23}$$

where:

$$\lambda = \sqrt{\frac{R_\perp}{R_{||}}} \tag{11.24}$$

$$C = I_T R_{||} \tag{11.25}$$

The terms in (11.23) can be written in Laplacian form as follows:

$$\mathcal{L}\left[\frac{d^2V(x)}{dx^2}\right] = s^2V(s) - sV(0) - \frac{dV(x)}{dx} \tag{11.26}$$

$$\mathcal{L}\left[\frac{V(x)}{\lambda^2}\right] = \frac{V(s)}{\lambda^2} \tag{11.27}$$

$$\mathcal{L}[C] = \frac{C}{s} \tag{11.28}$$

Hence, the Laplacian of (11.23) would be:

$$\left(s^2V(s) - a\right) - \frac{V(s)}{\lambda^2} + \frac{C}{s} = 0 \tag{11.29}$$

Grouping the $V(s)$ terms together:

$$V(s)\left[s^2 - \frac{1}{\lambda^2}\right] = a - \frac{C}{s} \tag{11.30}$$

$$V(s) = \frac{as - C}{s\left(s^2 - \frac{1}{\lambda^2}\right)} = \frac{as - C}{s\left(s + \frac{1}{\lambda}\right)\left(s - \frac{1}{\lambda}\right)} \tag{11.31}$$

We can use the method of partial fractions to rewrite that equation as:

$$\frac{as - C}{s\left(s + \frac{1}{\lambda}\right)\left(s - \frac{1}{\lambda}\right)} = \frac{u}{s} + \frac{v}{\left(s + \frac{1}{\lambda}\right)} + \frac{w}{\left(s - \frac{1}{\lambda}\right)} \tag{11.32}$$

We find:

$$u = c\lambda^2 \tag{11.33}$$

$$v = -\frac{(a\lambda - c\lambda^2)}{2} \tag{11.34}$$

$$w = \frac{a\lambda - c\lambda^2}{2} \tag{11.35}$$

The Laplacian equation becomes:

$$V(s) = \frac{c\lambda^2}{s} - \frac{(a\lambda + c\lambda^2)}{2\left(s + \frac{1}{\lambda}\right)} + \frac{(a\lambda - c\lambda^2)}{2\left(s - \frac{1}{\lambda}\right)} \tag{11.36}$$

We can take the inverse Laplace transform and find the solution of $V(s)$ as:

$$V(x) = c\lambda^2 - \frac{(a\lambda + c\lambda^2)}{2} e^{-\frac{x}{\lambda}} + \frac{(a\lambda - c\lambda^2)}{2} e^{\frac{x}{\lambda}} \tag{11.37}$$

*Solution with Boundary Condition*

In the solution above, we have assumed two boundary conditions according to (11.21-11.22). $a$ must be found. The other boundary condition can be that the parallel current at the negative infinity point is 0. The characteristic equation cannot be evaluated at $\infty$. Another boundary condition is needed.

Assume a finite magnet geometry where the overhang of the copper is $L$. In Figure 11.10, the copper overhang would extend from $-L$ to 0. We know that the equation of the parallel current at any point on $x$ is given as:

$$I_{||}(x) = -\frac{1}{R_{||} dx} dV(x) = -\frac{1}{R_{||}} \frac{dV(x)}{dx} \tag{11.38}$$

We can argue that at the $-L$ boundary:

$$I_{||}(x = -L) = 0 \tag{11.39}$$

At this boundary, there is no parallel current component coming from the copper to the left. If the collector is infinitely long, the spin voltage would converge to a constant value. Therefore, the derivative of the voltage would converge to 0. Knowing (11.39) and (11.37)

we can find $a$:

$$\frac{dV(-L)}{dx} = \frac{(a+c\lambda)}{2}e^{\frac{L}{\lambda}} + \frac{(a-c\lambda)}{2}e^{\frac{-L}{\lambda}} = 0 \tag{11.40}$$

$$a\left[e^{\frac{L}{\lambda}} + e^{\frac{-L}{\lambda}}\right] = c\lambda\left[e^{\frac{-L}{\lambda}} - e^{\frac{L}{\lambda}}\right] \tag{11.41}$$

$$a = c\lambda\frac{\left[e^{\frac{-L}{\lambda}} - e^{\frac{L}{\lambda}}\right]}{\left[e^{\frac{L}{\lambda}} + e^{\frac{-L}{\lambda}}\right]} = -c\lambda\frac{\left[e^{\frac{L}{\lambda}} - e^{\frac{-L}{\lambda}}\right]}{\left[e^{\frac{L}{\lambda}} + e^{\frac{-L}{\lambda}}\right]} = -c\lambda\tanh\left(\frac{L}{\lambda}\right) \tag{11.42}$$

knowing $a$, we can further solve (11.37):

$$V(x) = c\lambda^2 - \frac{(a\lambda + c\lambda^2)}{2}e^{-\frac{x}{\lambda}} + \frac{(a\lambda - c\lambda^2)}{2}e^{\frac{x}{\lambda}} \tag{11.43}$$

$$V(x) = c\lambda^2 - \frac{1}{2}\left(c\lambda^2 - c\lambda^2\tanh\left(\frac{L}{\lambda}\right)\right)e^{-\frac{x}{\lambda}} - \frac{1}{2}\left(c\lambda^2 + c\lambda^2\tanh\left(\frac{L}{\lambda}\right)\right)e^{\frac{x}{\lambda}} \tag{11.44}$$

$$V(x) = c\lambda^2 - \frac{c\lambda^2}{2}\left(1 - \tanh\left(\frac{L}{\lambda}\right)\right)e^{-\frac{x}{\lambda}} - \frac{c\lambda^2}{2}\left(1 + \tanh\left(\frac{L}{\lambda}\right)\right)e^{\frac{x}{\lambda}} \tag{11.45}$$

$$V(x) = c\lambda^2\left[1 - \frac{1}{2}\left(1 - \tanh\left(\frac{L}{\lambda}\right)\right)e^{-\frac{x}{\lambda}} - \frac{1}{2}\left(1 + \tanh\left(\frac{L}{\lambda}\right)\right)e^{\frac{x}{\lambda}}\right] \tag{11.46}$$

(11.46) is the solution to the system that will be used in the analysis.

*Re-derivation Copper Channel Diffusion Results*

From (11.42) and (11.38) we can write the current contribution of the copper overhang as:

$$I_{||}(x) = -\frac{1}{R_{||}}\frac{dV(x)}{dx} = \frac{c\lambda}{R_{||}}\tanh\left(\frac{L}{\lambda}\right) \tag{11.47}$$

This equation is plotted in Figure 11.11 for various overhang lengths and copper thicknesses.

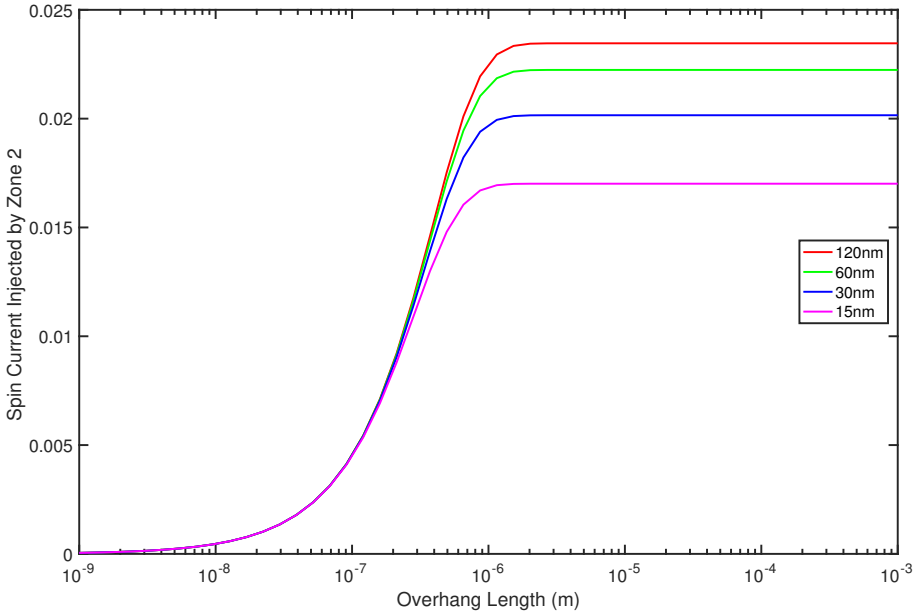


Figure 11.11: Current injected to ferromagnet vs. various copper overhang lengths using the re-derived current equations (Solution 2). Legend denotes various copper plate thicknesses (Z dimension). Assuming a 1 mA electrical current passing through the GSHE material.

The results in Figure 11.11 appear to make more sense than the results shown in the previous section. For the no overhang case, the current contribution is close to zero.If the overhang grows too large, the current contribution levels out. Overall, this equation seems to adhere to the general principles of spin transport.

### 11.3.5 Comparison of Solutions 1 and 2

We need to consider the differences between the two solutions since both are solutions to the characteristic equation. Regardless of the direction of the coordinate system, the characteristic equation remains the same.

Solution 1 is of the form:

$$V(x) = I_T R_\perp \left(1 - e^{-\sqrt{\frac{R_{||}}{R_\perp}}x}\right) \tag{11.48}$$

the current through the copper channel would then be:

$$I_{||1}(x) = -\frac{1}{R_{||}\Delta x}\Delta V = -\frac{1}{R_{||}}\frac{dV}{dx} = I_T\frac{R_\perp}{R_{||}}\sqrt{\frac{R_{||}}{R_\perp}}e^{-\sqrt{\frac{R_{||}}{R_\perp}}x} = I_T\sqrt{\frac{R_\perp}{R_{||}}}e^{-\sqrt{\frac{R_{||}}{R_\perp}}x} \tag{11.49}$$

the current going into the ferromagnet when $x = 0$ would be:

$$I_{||1}(x) = I_T\sqrt{\frac{R_\perp}{R_{||}}} \tag{11.50}$$

Consider Solution 2:

$$V(x) = c\lambda^2\left[1 - \frac{1}{2}\left(1 - \tanh\left(\frac{L}{\lambda}\right)\right)e^{-\frac{x}{\lambda}} - \frac{1}{2}\left(1 + \tanh\left(\frac{L}{\lambda}\right)\right)e^{\frac{x}{\lambda}}\right] \tag{11.51}$$

where

$$\lambda = \sqrt{\frac{R_\perp}{R_{||}}} \tag{11.52}$$

$$C = I_T R_{||} \tag{11.53}$$

$$I_{||2}(x) = -\frac{1}{R_{||}}\frac{dV}{dx} = -\frac{1}{R_{||}}a = \frac{1}{R_{||}}c\lambda\tanh\left(\frac{L}{\lambda}\right) = I_T\sqrt{\frac{R_\perp}{R_{||}}}\tanh\left(\frac{L}{\lambda}\right) \tag{11.54}$$

If the length of the channel is infinitely long, the current going into the ferromagnet becomes:

$$I_{||2}(x) = I_T\sqrt{\frac{R_\perp}{R_{||}}} \tag{11.55}$$

The two solutions match if the length of the copper channel is $L \to \infty$. Solution 1 is correct for an infinitely long copper channel while Solution 2 also considers a copper channel of finite length. The remainder of the chapter utilizes Solution 2.

### 11.3.6 Complete Solution to Spin Injection from Collector

We've spent the last two sections discussing the overhang components of the copper collector. However, as shown in Figure 11.4, there are three regions contributing to the total spin current delivered to the magnetic body. In this section, we will derive and analyze the complete expression for the spin current delivered to the magnetic body.

*Full System Analytic Models*

We know the current contribution from Zone 3 is:

$$I_{||3} = 0 \tag{11.56}$$

The current contribution from Zone 2 discussed in the previous section is:

$$I_{||2} = 2\frac{c\lambda}{R_{||}} \tanh\left(\frac{L_{overhang}}{\lambda}\right) \tag{11.57}$$

From Section 11.3 we know that the current contribution for Zone 1 is:

$$I_s = I_e \theta_{SH} \frac{W_{NM}}{t_{GSHE\_M}} \left(1 - sech\left(\frac{t_{GSHE\_M}}{\lambda_s}\right)\right), \tag{11.58}$$

Given a copper length $L_{Cu}$, the overhang length, relative to the total copper width and magnet width, is given by:

$$L_{overhang} = \frac{L_{Cu} - W_{FM}}{2} \tag{11.59}$$

The total current delivered to the nanomagnet from the copper collector becomes:

$$I_{tots} = I_e \theta_{SH} \frac{W_{NM}}{t_{GSHE}} \left(1 - sech\left(\frac{t_{GSHE\_M}}{\lambda_s}\right)\right) + 2\frac{c\lambda}{R_{||}} \tanh\left(\frac{L_{Cu} - W_{NM}}{2\lambda}\right) \quad (11.60)$$

The parameters assumed for Figure 11.12 are given by Table 11.1.

Table 11.1: Parameters used for Figure 11.12. Diffusion coefficients are derived from the models in [52].

| | |
|---|---|
| **General System** | |
| Injected Electrical Current | 1 mA |
| **Nanomagnet Dimensions** | |
| Length | 60 nm |
| Width | 45 nm |
| Thickness | 2nm |
| **GSHE Material (Tungsten)** | |
| thickness | 4 nm |
| spin hall angle | 0.3 |
| spin flip length | 2.5 nm |
| **Spin Collector Plate Dimensions** | |
| Width | 60 nm |
| **Copper Material Parameters** | |
| Specularity | 0.2 |
| Reflectivity | 0.2 |

*Electrical Current shunting through Copper Plate*

So far, we have assumed that the electrical current is limited to the GSHE material. However, because the copper plate is a conductive material, some of the electrical current may be shunted through the copper plate decreasing the spin current produced by the GSHE. Here, we will include that shunting effect and attempt to resolve whether this copper collector benefit is sustained. The resistance of the copper and tungsten heterostructure can be modeled as two parallel resistances. The current traveling through the GSHE material,

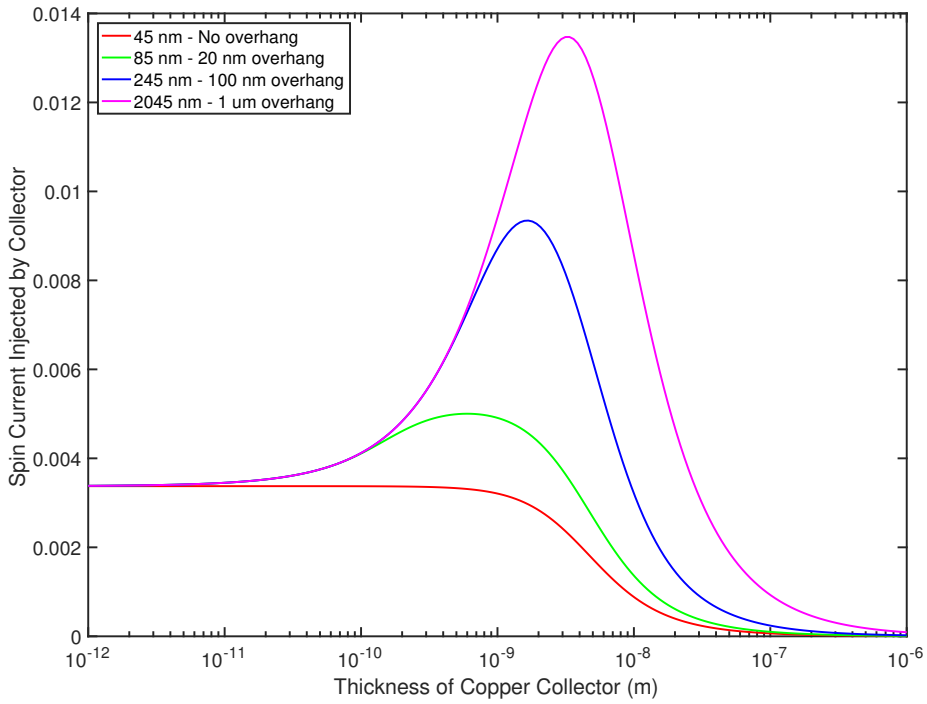


Figure 11.12: Total Current injected to nanomagnet vs. copper collector thicknesses using parameters from Table 11.1. Legend denotes various copper plate lengths in the $\hat{x}$ dimension. This assumes that a portion of the total current passes through the copper collector.

tungsten, is equal to:

$$I_W = I_{elec}\frac{\rho_{Cu}t_W}{\rho_W t_{Cu} + \rho_{Cu}t_W} \tag{11.61}$$

We are able to calculate the total spin current being delivered to the magnetic body using the models provided. Note that we assume size effects alter the resistivity of thin copper films [200]. However, for the tungsten GSHE material, we assume a bulk resistivity which is sufficient for the purposes of our analysis. As shown in Figure 11.12, this calculation is completed as a function of copper thickness and length. Very little electrical current gets shunted through the copper collector if the copper plate is too thin since size effects cause the resistivity of the thin to be very large. This causes the spin diffusion through the copper plate to limit; there is no amplification. If the copper collector is very thick, the spin current diffuses through the copper collector more easily. Little spin current is generated by the GSHE material because more electrical current is shunted through the copper. There

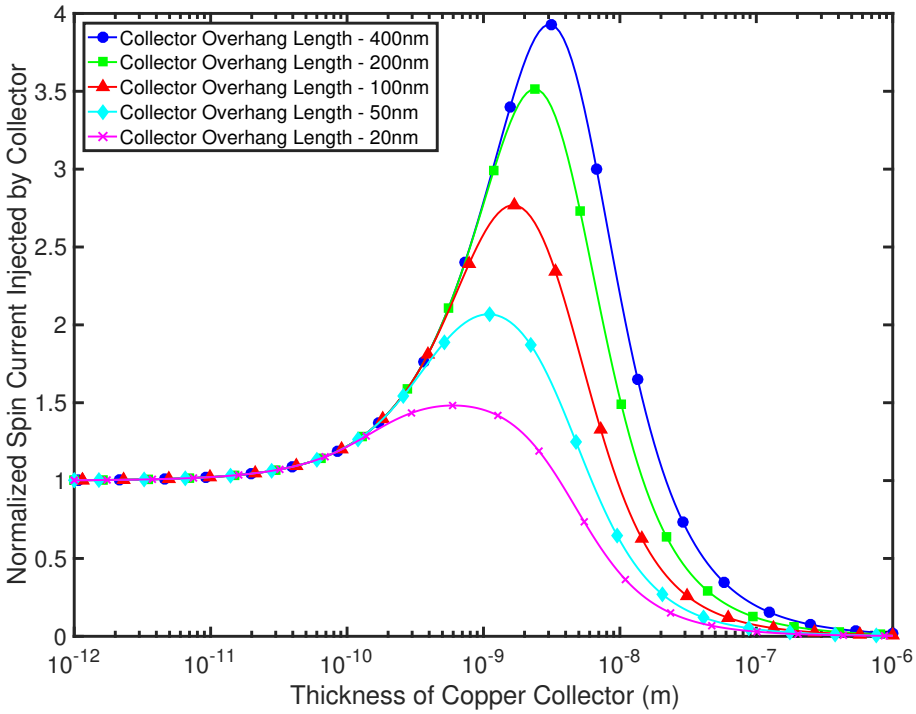


Figure 11.13: Total current injected to nanomagnet vs. copper collector thicknesses using parameters from Table 11.1. Spin current is normalized against the nominal case where the copper collector is not present. Legend denotes various copper plate lengths in the $\hat{x}$ dimension. This assumes that a portion of the total current passes through the copper collector.

is a range of collector thicknesses for which the spin current is amplified. This is seen in Figure 11.13 where the spin current is normalized against the no collector case. We observe a $4\times$ improvement over the nominal no collector case shown in Figure 10.1. Spin current is amplified when the copper collector is in the nm range, a relatively small value. A $4\times$ improvement is not especially significant and will likely be damped by the effect of adding another interface to the system. The electrical current being shunted through the copper collector is a significant problem. If there is a way to stop this current shunting, the amplification can be significantly increased as shown in Figure 11.14. Assuming no shunting, an amplification of $10\times$ is achievable. It is unclear if this amplification would result in a net positive amplification after negative interface effects are considered. The full benefit of the copper collector can only be realized by mitigating the electrical current

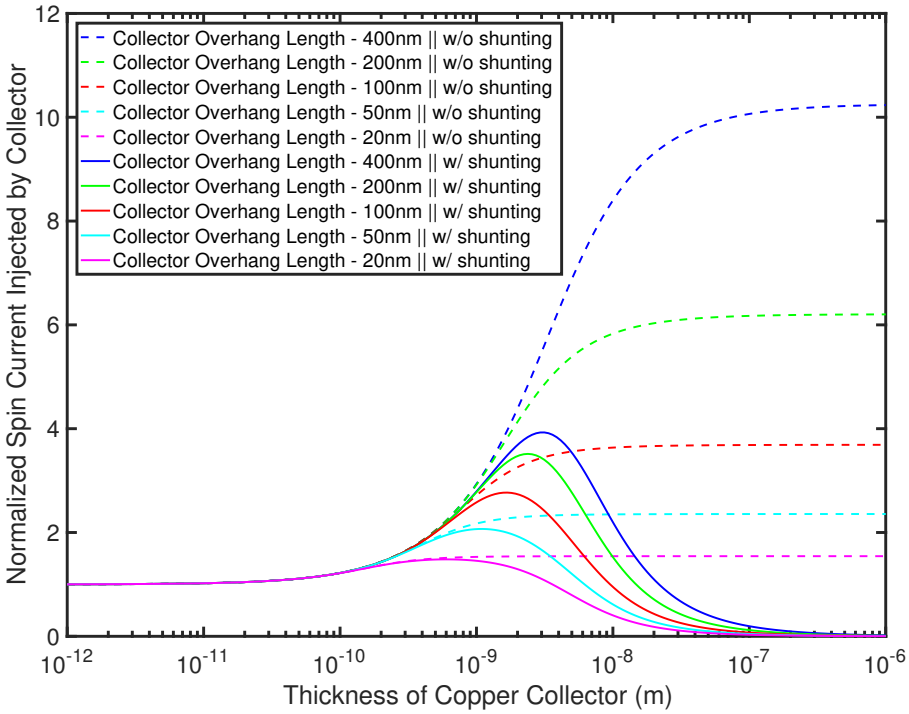


Figure 11.14: Normalized current injected into the magnetic body vs. copper collector lengths and thicknesses using parameters from Table 11.1. Legend denotes various copper plate lengths in the $\hat{x}$ dimension. This assumes that a portion of the total current passes through the copper collector.

being shunted away from the GSHE material. A barrier material which allows spin current through but blocks electrical current may be one solution. Such barriers have already been suggested for all-spin-logic [201]. It is unclear if such methods are suitable for GSHE-generated spin current amplification.

Even a small increase in the ”effective magnet width” can lead to a large increase in spin current for a small magnet. However, if the magnetic body was larger, the normalized amplification would be reduced.

# CHAPTER 12

# POSSIBLE IMPROVEMENTS II: STRAIN MEDIATED STT REVERSAL

Magnetostrictive thin-film hetero-structures have been found to be useful for a myriad of microelectronic applications [202, 203, 204, 205]. This technology presents an opportunity to augment proposed spin-based devices that rely on the manipulation of the magnetic moment for data storage and/or processing [2, 54, 206, 207].

We consider an improved version of nanomagnet reversal through spin-transfer torque (STT)[90, 208]. Nominally, the magnetization is initially at rest along the free-axis of the nanomagnet near its low-energy state. When the longitudinal spin current is applied, it imparts a torque on the magnetization and slowly fights the damping torque of the initial energy basin until it crosses the energy barrier and settles towards the opposing direction [209, 210]. This process is shown in the left subplot of Figure 12.1. The disadvantage of this type of reversal is that a large amount of energy is used to counteract damping and drive the magnetization from its initial energy basin across the energy barrier to the opposite

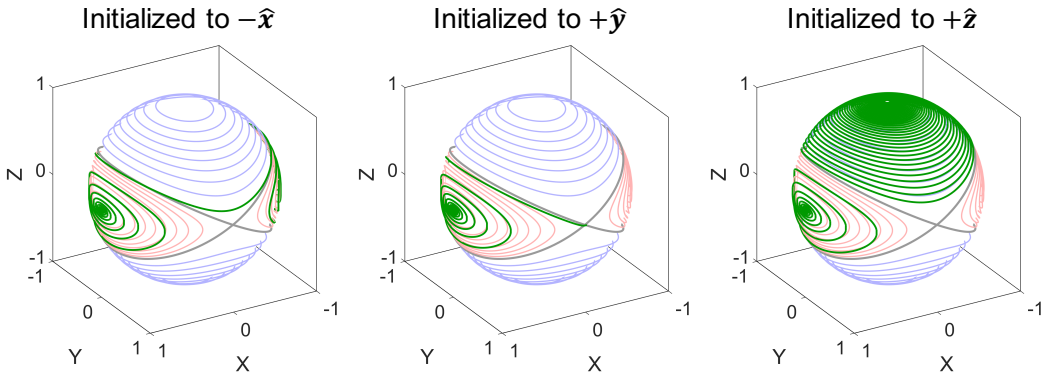


Figure 12.1: Sample nanomagnet reversals assuming various initial states. Left/Center/Right subplots correspond to initial position along $-\hat{x}$, $+\hat{y}$, and $+\hat{z}$ axes respectively. Background lines show precessional trajectories at particular magnetization energies. Red and blue trajectories denote precessional orbits in energy poles and basins, respectively [80]. Magnetization is under influence of above-critical $+\hat{x}$ longitudinal spin current.

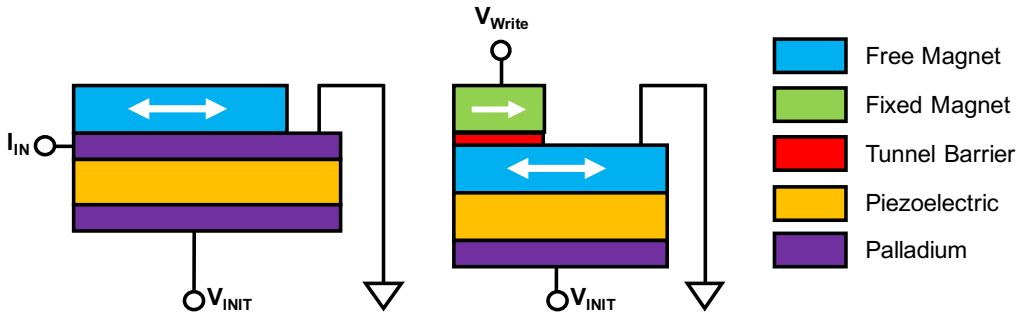


Figure 12.2: Schematic of two types of augmented nanomagnet reversal structures [212, 136]. While not directly analyzed, a rough approximation of the theoretical benefits of strain-mediated reversals can be applied when evaluating the efficacy of spin-based technologies.

orientation. Yet, a large energy barrier is necessary for nanomagnet stability [108, 211]. If the magnetization can be initialized outside of its initial energy basin, we can presumably save a great deal of energy reversing the magnetization. These types of reversals are shown in the center and right subplots of Figure 12.1.

This initialization can be accomplished through magnetostriction [207]. Recent works have shown that the energy landscape of a magnetic body can be altered by a voltage-induced strain in ferromagnet and piezoelectric hetero-structures [213, 214, 215, 216, 217, 218, 219]. By layering a ferromagnet on top of a piezoelectric material, a large anisotropy can be added to the energy landscape of magnetic body when a voltage is applied to the piezoelectric material [220, 213]. Figure 12.2 demonstrates two types of augmented reversal structures which can be utilized by several spin-based technologies [2]. Assuming this strain-induced anisotropy is large enough, the magnetization will be forced in a new low-energy state defined by the axis of strain. This effectively initializes the magnetization to a new energy state. Next, the voltage can be turned off and a spin current applied, pushing the magnetization into the preferred state. A sample of such a strain-mediated reversal is shown in Figure 12.3.

This chapter provides a theoretical framework for such strain-mediated reversals. We can represent the change in energy landscape caused by the voltage-controlled strain-

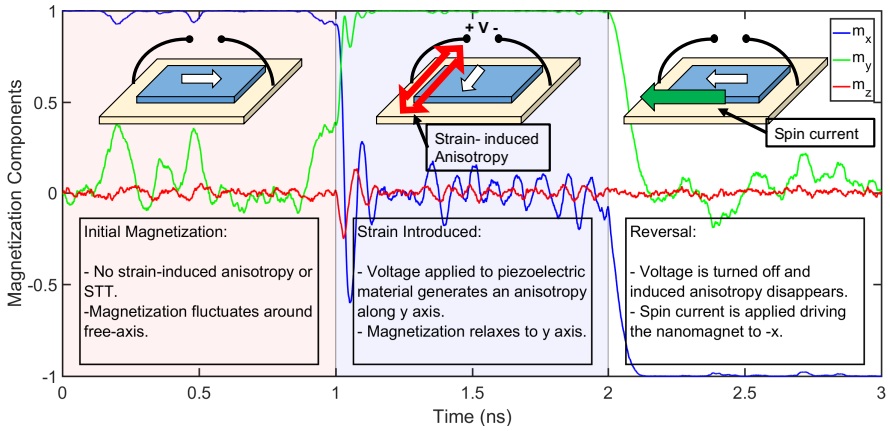


Figure 12.3: Sample strain-mediated reversal assuming a FeGaB nanomagnet and $K_{TY} = 10^5 \frac{J}{m^3}$. The nanomagnet is initially at rest along the free-axis. When the voltage is applied, a strain-induced anisotropy is introduced to the nanomagnet energy landscape. This anisotropy overpowers the free-axis anisotropy and shifts the low-energy position to $\hat{y}$ which the magnetization relaxes. Once this new initial state is achieved, the voltage is turned off. The induced anisotropy ceases and a spin current is applied to nudge the magnetization towards the appropriate final magnetization state.

interaction as a time-dependent temporary anisotropy ($K_T$). Using this model, we can assess the requirements for reliable reversal. It is shown that the principle advantage of strain-mediated reversal is achieved through the smaller pulse-widths (PWs), required for reliable reversal. The energy is minimized when using a current pulse whose magnitude is $50 - 100\%$ greater than the critical current value. We assume a finite strain-induced anisotropy magnitude and demonstrate that there is a critical anisotropy magnitude required for strain-mediated reversal. As the strain-induced anisotropy magnitude is increased beyond this critical value, the PW and equivalently energy requirements trend toward the ideal case, yielding a $10\times$ reduction.

## 12.1 Strain-mediated Nanomagnet Model

A single-domain thin-film in-plane nanomagnet under the influence of a longitudinal spin current is considered. Because this chapter conceptually analyzes an ideal nanomagnet system during near-critical reversals, the macrospin approximation is used [43, 73]. It is

assumed that the easy-axis is along the $\hat{x}$ axis while the hard and out-of-plane axes are oriented along the $\hat{y}$ and $\hat{z}$ directions, respectively.

### 12.1.1 Representation of Strain-Induced Anisotropy

Ample experimental work has been dedicated to the analysis of magnetostrictive thin-films and hetero-structures [221, 222, 223, 224]. A number of models can be used to describe these magnetostrictive effects [84, 225]. Because the goal of this chapter is a theoretical understanding of the strain-mediated STT reversal process in an idealized system, it is more prudent to abstract the strain-induced anisotropy so that the conclusions presented are clear.

We model the strain-induced anisotropy as a temporary anisotropy energy, $\epsilon_{KT}$, which is added to the energy landscape for a given period of time. This anisotropy can be generated in multiple given directions depending on the direction of the strain and/or electric-field [226, 227]. Two types of strain-induced anisotropies exist: $\epsilon_{TY} = -K_{TY}m_y^2$ and $\epsilon_{TZ} = -K_{TZ}m_z^2$. An analysis of these anisotropies will complete our understanding of strain-mediated reversal. Similar to $K_u$, $K_T$ is the magnitude of the strain-induced anisotropy energy.

### 12.1.2 Material Parameters

In this chapter, we consider two magnetostrictive materials: FeGaB ($M_s = 1.3\frac{MA}{m}$ — $K_u = 1.3\frac{kJ}{m^3}$) and Terfenol-D ($M_s = 0.8\frac{MA}{m}$ — $K_u = 320\frac{kJ}{m^3}$) [228, 229, 230, 231, 232]. Each has extensive experimental studies demonstrating strong magnetostrictive properties [233, 234]. The magnitude of the Gilbert damping is material and shape dependent [235, 236, 237]. Unless otherwise stated, $\alpha = 0.10$ [238]. Several other $\alpha$ values are considered to make the analysis applicable to a variety of magnetic materials. We assume a $60nm \times 45nm \times 2nm$ thin-film nanomagnet. The probability of reliable reversal is evaluated numerically and determined by a Monte-Carlo analysis of $10^4$ transient simulations [100]. Reversal probability is defined as the number of simulations where the magnetiza-

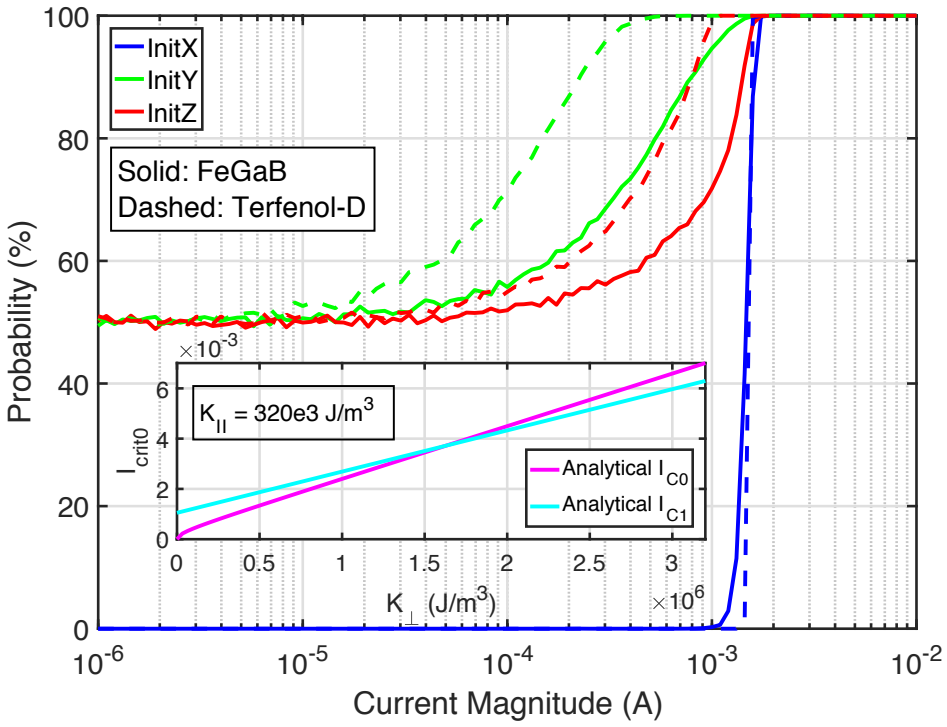


Figure 12.4: Assuming an ideal initial state along the $\hat{x}$, $\hat{y}$, and $\hat{z}$ axes, the reliability of reversal is measured for a nanomagnet under the influence of a longitudinal, infinite PW spin current. The InitY and InitZ cases correspond to an infinitely large $K_{TY}$ and $K_{TZ}$, respectively. This graph demonstrates that for $D > 5.09$ materials, such as FeGaB, the minimum current required for perfect reversal is the same regardless of its initialization case. It can be analytically determined as $I_c = 1.9mA$. For materials with $D < 5.09$, such as Terfenol-D, it is possible to achieve reliable reversal using current magnitude less than its full reversal critical current, $I_c = 1.6mA$, if it is initialized to a high-energy state. For $D > 5.09$ materials, the damping at the energy barrier is actually greater than the damping at the free-axis as shown in the inset plot. *Inset*: Critical current for a magnetic body with $K_{\parallel}$ and $K_{\perp}$ values shown.

tion ends the simulation with a positive $m_x$ component.

## 12.2 Ideal Current Magnitude Requirement

Consider the idealized case where the strain-induced anisotropy has an infinite magnitude. When a voltage is applied, the magnetization will become perfectly aligned with the strain-induced axis. Three initialization cases at the moment the strain is turned off and the spin current is applied are considered. InitX supposes no strain-induced anisotropy and the

magnetization begins reversal from its low-energy state along the free-axis. The InitY and InitZ cases correspond to an infinitely large $K_{TY}$ and $K_{TZ}$, respectively.

Assuming an infinitely long spin-current pulse-width (PW), we can measure the probability of successful reversal for a given current magnitude. From Figure 12.4, it is evident that there is a minimum critical current required for all three initialization cases.

### 12.2.1 Critical Current for Different Initialization Cases

These critical current expressions are important when considering the minimum current magnitude required for each initialization case. There are two materials considered in Figure 12.4, FeGaB and Terfenol-D, with $D$ and $I_C$ parameters shown in Table 12.1.

Table 12.1: Critical current values of the FeGaB and Terfenol-D thin-film nanomagnets considered in this chapter.

| | **D** | $I_{C1}$ **(mA)** | $I_{C0}$ **(mA)** |
|---|---|---|---|
| **FeGaB** | 53.52 | 1.5 | 1.9 |
| **Terfenol-D** | 1.04 | 1.6 | 0.99 |

For a material with a large perpendicular anisotropy such as FeGaB, the damping torque is maximized at the energy barrier and $I_{C0} > I_{C1}$. As shown in Figure 12.4, the current requirement for reliable nanomagnet reversal should be the same regardless of initialization.

For Terfenol-D, $I_{C1} > I_{C0}$ and the damping torque monotonically increases from the energy-barrier to the free-axis. For the InitX case, we can assume the current magnitude requirement is equal to $I_{C1}$ according to (4.3). The high-energy initialization cases are harder to predict. In these cases, the required current magnitude should be equal to the critical current at the energy barrier. The possibility of the magnetization getting knocked in the anti-parallel energy basin due to thermal noise must also be considered. In this case, the critical current value increases the closer the magnetization gets to the free-axis. If the spin current magnitude is equal to $I_{C0}$, the STT will not be able to overcome the damping torque in the energy basin.

Because reversal probability is measured by a finite number of simulations, Figure 12.4

clearly demonstrates a reduction in required current magnitude between the Terfenol-D initialization cases. As we increase the granularity of our probability measurement, the minimum reliable current magnitude will trend towards the INITX case. Now, we assume a critical current magnitude given by (4.3) for the Terfenol-D case as well.

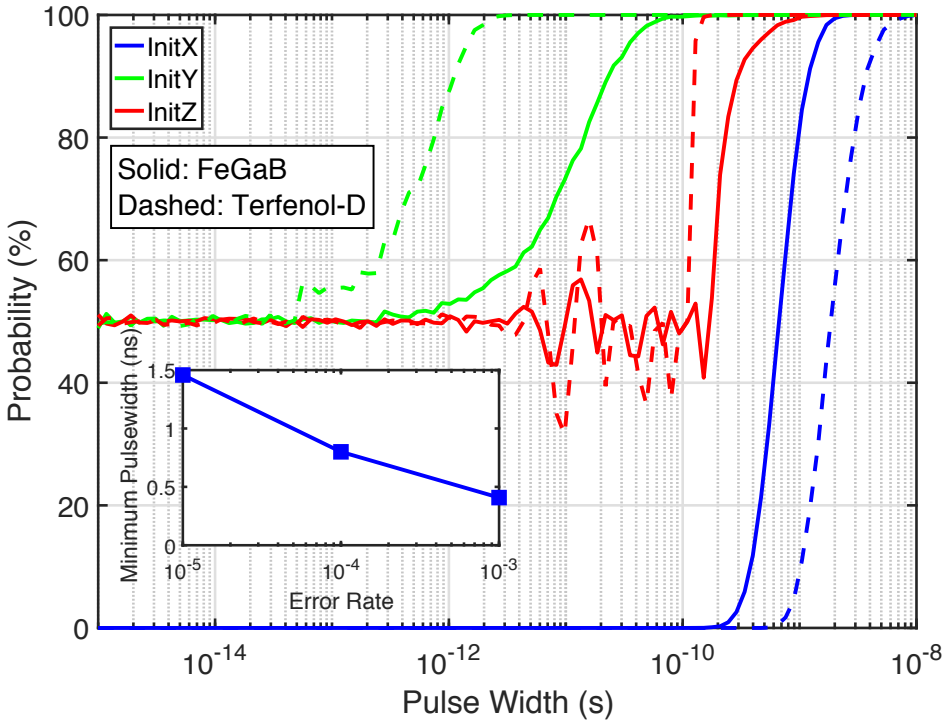


Figure 12.5: The probability of reversal versus the pulse width of a longitudinal spin current, assuming an ideal initialization and a current amplitude, given by (4.3). This graph demonstrates that significantly shorter current pulses can be used, if initializing the magnetization to one of the two high-energy states. When initializing the magnetization to these high energy states, the reversal process skips the time otherwise spent precessing in its initial energy basin as in the case of standard reversal. *Inset*: Minimum PW required for InitY case as a function of error rate.

## 12.3 Ideal Pulsewidth Requirement

Even though InitY and InitZ cases provide little benefit in terms of the current magnitude required for reliable reversal, such initializations are beneficial in shortening the spin-current pulse-width. By minimizing the PW, the energy required for reversal will also be

minimized.

### 12.3.1 Ideal Pulsewidth Analysis

Figure 12.5 shows the reliability of the FeGaB and Terfenol-D nanomagnet systems for various current PWs when the spin current magnitudes equal to the critical current defined by (4.3). The InitX case must spend time escaping the nanomagnet's initial energy basin fighting its natural damping torque. Therefore, both the InitY and InitZ cases are shown to require far smaller PWs than the nominal InitX case, unlike Figure 12.4.

Terfenol-D is shown to benefit far more from the high-energy initialization cases than the FeGaB material. In the FeGaB-InitY case, we observe a $\sim 10^{1.5}\times$ PW reduction over the standard (InitX) reversal. There is a $\sim 10^{3.5}\times$ PW reduction for the Terfenol-D case due to the energy landscape difference between the two types of materials. As the damping torque of Terfenol-D is minimized at the energy barrier, the InitY case is especially effective.

### 12.3.2 PW Requirement for +Z Initialization Case

The InitZ case offers a smaller PW benefit compared to the InitY case as shown in Figure 12.5. Observing a sample InitZ reversal shown in the right subplot of Figure 12.1 provides an explanation. In this type of reversal, a large amount of time is spent with the magnetization precessing in the high-energy region before crossing the energy barrier and coming to rest in the appropriate energy basin.

The spin current is only needed as the magnetization nears and crosses the energy-barrier. We can use a shorter current PW if we delay the application of the current by a set amount of time. The reliability of such a system is shown in Figure 12.6. Even with the delayed current pulse, the InitZ case is still inferior to the InitY case since the time spent relaxing from $+\hat{z}$ to the energy-barrier is variable due to thermal noise. The InitY case negates this variability by initializing the magnetization exactly on the energy barrier. A

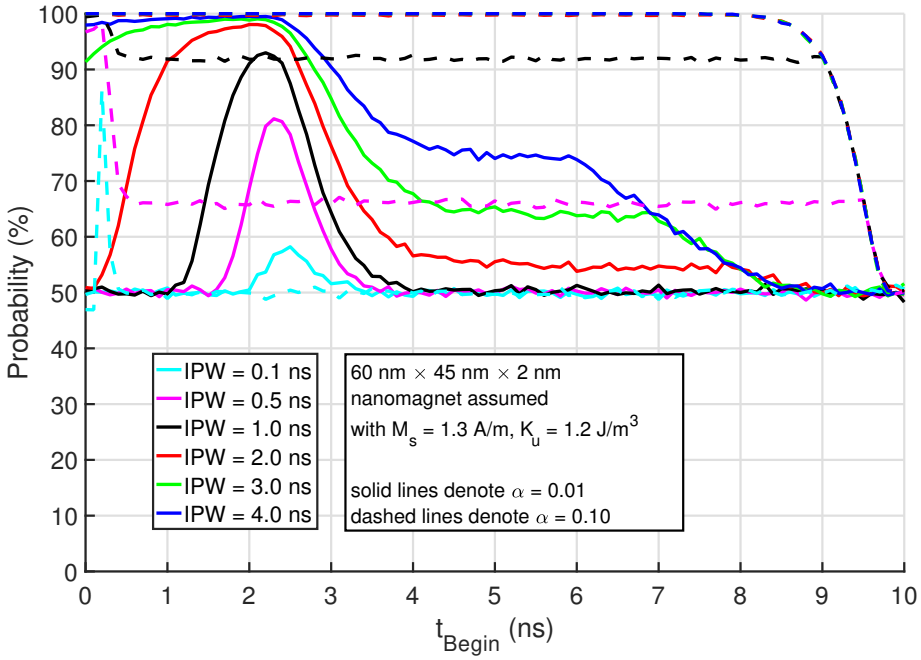


Figure 12.6: Assuming ideal initialization, the reliability of reversal is measured for a nanomagnet under the influence of a longitudinal spin current with magnitude determined by (4.3) and PW shown in legend. After the strain is turned off, the pulse is delayed by a certain amount of time. The reliability of reversal is measured for each of these delays. Solid and dashed lines denote a $\alpha$ value of $0.01$ and $0.10$, respectively. This figure demonstrates that the primary difference between the InitY and InitZ conditions is the time the InitZ has to spend recessing in the high-energy position. The current pulse is only required when the magnetization nears and crosses the energy barrier. Because of thermal noise, this initial time is variable.

smaller $\alpha$ is desirable in this case since more time is spent precessing in the high-energy position leading to less variation in the time it takes for the magnetization to cross the energy-barrier.

The non-monotonic behavior exhibited in Figure 12.5 is also noteworthy. Previous analyses have suggested that the relaxation process from the high-energy region can be conceptualized as a series of trajectories which end in one of two energy basins [138, 139, 140]. In a non-biased system, there is an equal number of these trajectories for each basin-destination. The thermal noise causes the magnetization to jump between these trajectories until it crosses the separatrix. In a biased system, the number of trajectories ending in one basin is greater. The probability of crossing the energy barrier into a particular energy basin

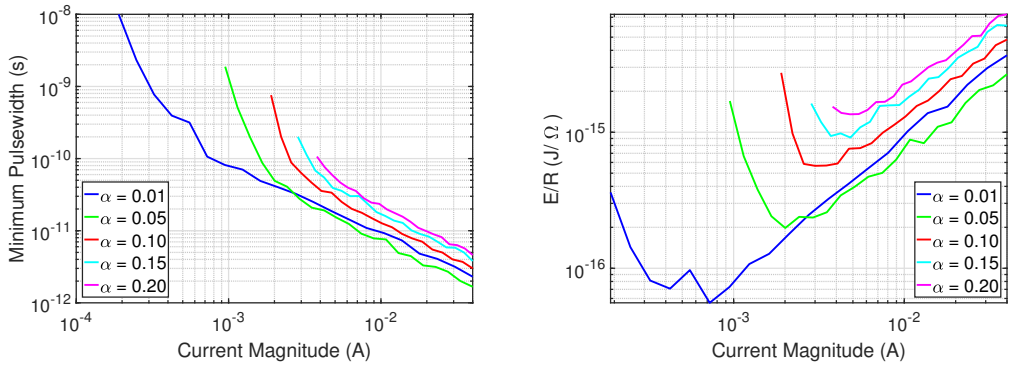


Figure 12.7: Assuming ideal InitY, the minimum PW required for reliable (error rate $< 10^{-4}$) reversal is measured for FeGaB thin films. This plot demonstrates that the required PW decays exponentially will the current magnitude. Different values of $\alpha$ are assumed showing that at any given magnitude, the required pulse-width decays exponentially with $\alpha$. However, if alpha is too small, the required PW actually increases due to the nanomagnet's stability being effected. *Inset*: Calculates energy dissipation per ohm per reversal as a function of current magnitude. Energy is normalized against the resistance since the nanomagnet hetero-structure can greatly alter the resistance value and such analysis is outside the scope of this research. Energy is minimized when operating at $50 - 100\%$ greater than $I_C$.

then increases [239]. In Figure 12.5, there is a non-monotonic trend if the bias lasts shy of the time it takes the magnetization to cross the energy barrier. The short current bias forces the magnetization into a set of trajectories determined by the nanomagnet's precessional dynamics and likely ending in one energy basin over another. This non-monotonic trend is mainly observable in systems with large damping; the rapid relaxations give the thermal noise less time to knock the magnetization across precessional trajectories.

### 12.3.3 Minimum Pulse-width Requirement

Using extensive numerical simulations we can estimate the minimum PW required for reliable reversal at a given current magnitude. It should be noted that this minimum current PW is a function of the desired error rate as can be seen in the inset of Fig. 12.5. For this chapter, we assume an error rate of $< 10^{-4}$. If we assume smaller error rates, then the thermal stability of the nanomagnet will become a significant factor in our analysis.

Fig. 12.7 measures the minimum PW required for a FeGaB nanomagnet with different

values of $\alpha$. This graph shows that the minimum PW varies linearly with the current magnitude and has a vertical asymptote at $I_C$. The analysis of FeGaB at different $\alpha$ values also demonstrates the damping parameter is linearly proportional to the minimum PW value. However, if $\alpha$ is too small, then the nanomagnet becomes unstable requiring a longer spin-current simply to ensure that the magnetization remains within the desired energy basin until the end of the simulation.

This minimum PW analysis allows one to estimate the energy requirement for this type of reversal. This is shown in the inset of Fig. 12.7. We calculate the energy value in terms of $\frac{J}{\Omega}$ because the actual resistance of the magnetic hetero-structure is unknown. However, this figure does demonstrate that the energy is minimized when the current magnitude is $50 - 100\%$ greater than $I_C$.

## 12.4 Non-ideal Current Pulse-width Requirement

Using the insight gained from the analysis of the ideal strain-mediated case, we can now analyze a more realistic situation with a finite strain-induced anisotropy. The primary difference between the ideal and realistic cases is that in the latter, because the strain induced anisotropy is finite, the magnetization will fluctuate around the strain axis. Hence, when the strain is turned off, the nanomagnet will be initialized *near* the hard-axis instead of exactly on it. A sample of this more realistic case is shown in Figure 12.3.

In the previous section, it was shown that the InitY case is superior to all other initialization cases. Therefore, we can perform the same PW analysis as in the previous section for various finite values of $K_{TY}$. The inset of Figure 12.8 demonstrates that as the magnitude of the strain anisotropy increases, the probability of reliable reversal reduces to the ideal case.

It is also possible to determine the minimum PW required for these finite $K_{TY}$ values using extensive numerical simulations. Figure 12.8 demonstrates that the strain anisotropy magnitude must exceed a critical value before any benefit is realized for this type of rever-

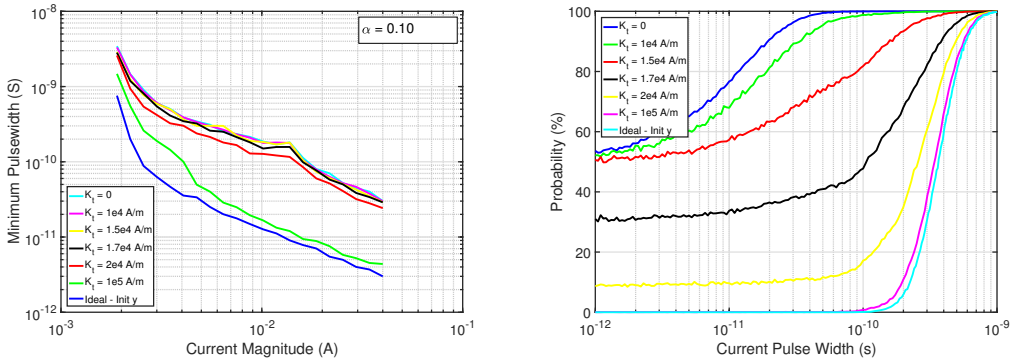


Figure 12.8: *Left*: Assuming a non-ideal reversal with a finite $K_{TY}$, we measure the minimum PW to reverse a FeGaB thin-film nanomagnet. Note that the nanomagnet is initially at rest for $1ns$, then the strain-induced anisotropy is applied for $1ns$. Afterwards the strain is turned off and a current pulse is delivered to the nanomagnet. Plot demonstrates that the strain-induced anisotropy must have a minimum magnitude to overpower the nanomagnet's natural anisotropy initializing its magnetization away from the free-axis. *Right*: Measure reliability for a non-ideal InitY reversal using a current pulse whose magnitude is equal to $I_C$. As the magnitude of the strain-induced anisotropy increases, the magnetization dynamics reduce to the ideal case.

sal. This is because $K_{TY}$ must be strong enough to overpower the nanomagnet's internal uniaxial anisotropy in order to drive the magnetization to the strain axis creating the high-energy initialized state. For the FeGaB system considered, this critical strain anisotropy value is $1.676 \times 10^4 \frac{J}{m^3}$ which corresponds well to Figure 12.8 and the strain values which provides smaller PW requirements.

Figure 12.8 also reveals the PW improvement for strain mediated reversals as compared to the nominal reversal case. We see a single order of magnitude reduction in required PW assuming $K_{TY} \gg K_{\parallel}$ ($> 10\times$). Given that we can formulate the energy as $E = I^2Rt$, this reduction in PW would correspond to a similar $10\times$ reduction in reversal energy over the InitX (no strain-anisotropy) case.

# CHAPTER 13

# CONCLUSIONS AND FUTURE OUTLOOK

During the course of this research, several types of magnetization dynamics were modeled and analyzed to quantify the performance of Spin-Switch Logic. In Chapter 3, we observed that the reversal probability of a biaxial nanomagnet for a fixed energy barrier is a non-monotonic function of the perpendicular magnetic anisotropy. We show that a large perpendicular anisotropy increases the frequency of the precessional orbits of the magnetization, which increases the likelihood for the magnetization to cross the $\hat{x}$ = 0 plane leading to reversal. On the other hand, a large anisotropy also shapes the precessional orbits by bringing the separatrix closer to the free-axis. As the thermal-field torque is enhanced closer to the free axis, the probability that the magnetization energy will exceed the energy barrier increases. We also show that such non-monotonic behavior is observed at short time-scales (sub-100 ns), while at longer time-scales the model presented in this chapter converges to the well-known random-walk model proposed by W. Brown. It is therefore sufficient to use the uniaxial reliability models for biaxial systems when observed at long time-scales.

After analyzing the reliability of the magnetization state, we turned our attention towards the mechanics STT reversal. In Chapter 4, we investigate deterministic magnetization reversal through spin-transfer torque for both uniaxial and biaxial magnetic bodies. While the exact solution to STT reversals in uniaxial landscapes had been found previously, we expanded this model to include biaxial cases as well. We then investigate the this type of reversal when the nanomagnet body is under the influence of thermal noise and propose new models to represent the reversal delay PDF. Knowing the delay of a single nanomagnet, it is possible to analyze nanomagnet circuits where nanomagnets are evaluated in either parallel or series configurations. It is shown that a circuit with nanomagnets evaluated in

parallel has a larger variation but a smaller average delay than a circuit with nanomagnets in series. Finally, these concepts are applied to the evaluation of a ASL-AND gate. It is shown that having more inputs to an AND circuit is beneficial since the fraction of the time the nanomagnet is operating under the minimum input spin current is reduced.

Chapters 6–9 are dedicated to the analysis of complex interaction between nanomagnetic bodies. We have developed comprehensive analytic models for the critical limits of reliable reversal in identical and non-identical two-magnet systems. We find that during slow reversals, the dipolar fields act as anisotropy energies instead of Zeeman energies. This results in the enhancement of coupling strength between magnetic bodies dubbed the "mutual coupling effect." Through extensive numerical tests we have provided a model of nanomagnet coupling reliability which includes the impact of the perpendicular field components in slow reversal cases. It is shown that the dynamics for uniaxial and biaxial systems are fundamentally different and thus require different models to capture their critical limits for reversal. These models do not contain any fitting parameters while accurately predicting the material and geometric requirements for a deterministically-coupled, two magnet system. It is shown that the range of materials which allow for coupling between PMA nanomagnets is extremely limited and hence, in-plane nanomagnets are a far more suitable choice when designing a coupled system.

In summary, we have developed models which accurately describe magnetization reversals through the use of spin-transfer torque and dipolar coupling. Additionally, we have quantified the impact of thermal noise on magnetization state reliability and STT reversal delay. Having developed new models, we are able to accurately assess the performance of Spin-Switch Logic and propose new augmentations to enhance the performance of this and other spin-based technologies.

## 13.1 Future of Spin-Switch Technology

Current CMOS technology offers a EDP of $0.21\times10^{-24}\mathrm{J}\cdot\mathrm{s}$. From Chapter 10 we established that the EDP of Spin-Switch is approximately $2.5\times10^{-21}\mathrm{J}\cdot\mathrm{s}$ assuming a layout constrained design where reliability is not a major concern. Clearly, by this metric alone, the future of Spin-Switch technology does not look too bright. Chapter 11 posited that a layer of copper under the ferromagnet can aid in the amplification of the GSHE device. The amplification of the spin current increase by a factor of four allowing for an EDP reduction of $16\times$. Furthermore, in Chapter 12 we proposed strain-mediated STT reversal where, through the use of magnetostrictive effects, the magnetization is initialized to high-energy position before being driven to the appropriate energy basin by a small spin current. Using this reversal method results in a factor of ten delay improvement for biaxial nanomagnet systems yielding a $100\times$ improvement in EDP. We can estimate that if these augmentations are included with the Spin-Switch, then we may be able to achieve a EDP of approximately $1\times10^{-24}\mathrm{J}\cdot\mathrm{s}$. Although this is still larger than the EDP of a CMOS device ($0.21\times10^{-24}\mathrm{J}\cdot\mathrm{s}$), the improved EDP does allow for some hope regarding the future of this technology.

In order to weigh fair judgment, one must also accept the possible problems with the device. In Chapter 4 we showed that the STT reversal delay is a stochastic function and hence, must be modeled using an exponential PDF. This means that the device and/or circuit must be clocked for much longer than its nominal delay to ensure reversal reliability. Second, the Spin-Switch is a current-based technology and is constantly using power. A potential remedy to this problem is proposed by utilizing a latch-less pipelining scheme and turning the supplies of the devices on/off when appropriate. While there is nothing theoretically wrong with this line of reasoning, clocking every gate is impractical. Even in current CMOS technology, ensuring synchronized clocked latches in between pipeline stages is a significant challenge.

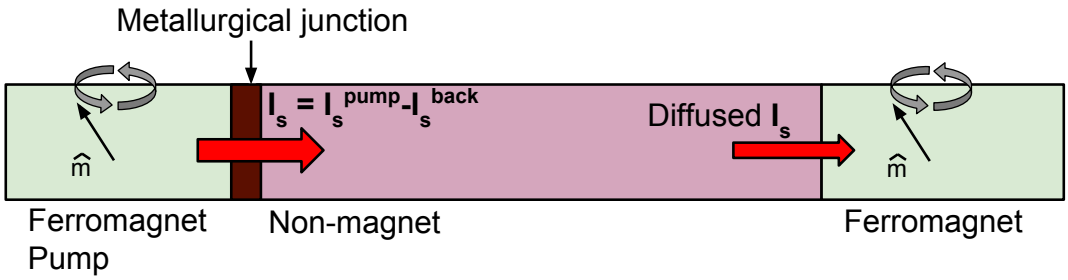


Figure 13.1: Illustration of Spin Pumping Oscillator Coupled logic device [240]. Initially, a spin current causes the input nanomagnet to oscillate. Using spin pumping, the oscillation of the nanomagnet generates a spin current that will diffuse through the metallic channel driving the moment of the output ferromagnet to oscillate.

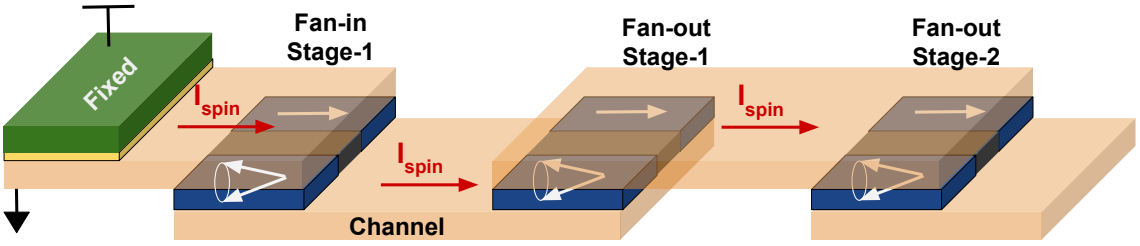


Figure 13.2: Using the principles described in Figure 13.1, we can transmit Boolean information as shown above. Logical operations can be performed by summing spin currents similar to how ASL circuits process information.

Finally, there is the central issue of reliability. There is no true analogue to thermal noise in CMOS technology. Nanomagnet's have an inherent weakness in that their magnetization state will always be a random variable and the randomness becomes greater as the nanomagnet is scaled down. In Section 10.4, we abandoned all layout constraints focusing solely on designing a Spin-Switch that met an already weak set of reliability standards and ultimately ended with worse performance characteristics than the layout-constrained design. Reliability is often omitted from technology analyses because it is mathematically difficult and computationally expensive to study. Yet, reliability is ultimately the foundation of computing. Every modern chip carries our implicit trust that it will produce a certain output given a certain set of inputs. It is highly doubtful that any technology will ever become popular if that trust is broken.

## 13.2 Future of Spin-based Devices

It is useful to note that from a macroscopic viewpoint, the Spin-Switch device is simply a current-in, current-out logic gate. All-spin logic (ASL) can also be abstracted in this manner. From this viewpoint, the Spin-Switch is functionally equivalent to a bipolar junction diode (BJT) except for the mechanics which translate the input current to an output electrical current. The Spin-Switch is not a spintronic device. It is a current-driven device which relies on spin phenomena for operation. Because the BJT has limited usefulness in logical circuits, we can logically conclude that any current-based technology will be unsuitable for modern Boolean circuit designs and architectures.

The promise of spintronics is that information may one day be communicated and processed using solely electron spin avoiding power-loss because no electrical current is theoretically required. The future of spintronics is in developing such spin devices. To our knowledge, there are currently two such devices proposed in literature. First is Nanomagnetic Logic which was introduced in Chapter 1, and operates through arrays of nanomagnets communicating using their stray fields [241]. Interest in this technology has waned due to bit-signal propagation issues. However, current research into the use of magnetostrictive hetero-structures means that these propagation issues may be rectified by initializing output stages in high-energy positions and allowing the input bit arrays to dictate the bit-value the output array relaxes to.

The second device technology, shown in Figure 13.1 has only recently been published in literature [240]. In a SPOC device, an oscillating ferromagnet creates a spin in a metallic channel through the use of spin pumping. The spin current then diffuses through the channel before being injected into the output ferromagnet which will then oscillate with a phase determined by the spin current. This technology is functionally similar to ASL in that logic is achieved by combing spin currents from multiple input ferromagnets as shown in Figure 13.2. The only difference is the way SPOC and ASL generate the spin current in

the metallic channel. The major weakness of SPOC logic is that the spin current must diffuse through the channel resulting in a negative gain between input and output. Its possible that this issue can be resolved through the use of spin current amplification techniques or special oscillators which are insensitive to input spin current magnitudes.

Ultimately, there is still potential in the field of spintronics but it can only be realized through the careful evaluation of spintronic devices and accurate modeling of magnetic phenomenon. This thesis was one more step towards finding a true spintronic device which consumes no electrical power. Good luck to those taking the next steps.

# Appendices

# APPENDIX A

# IMPORTANT PARAMETERS AND CONSTANTS

## A.1 Magnetization Dynamics

The nanomagnetic body can be represented by a single energy gradient which is the sum of the the nanomagnet's internal anisotropy energies and any external Zeeman energies applied to the magnetic body defined by Table A.1. These energies create a gradient system represented by the fields applied to the magnetic moment and is related to the magnetization energy by:

$$\vec{H}_{eff} = \frac{1}{\mu_0 M_s} \frac{\partial \epsilon}{\partial \hat{m}}, \tag{A.1}$$

where the magnetization energy $\hat{m}$ is the unit magnetization vector and $(\epsilon(\hat{m}))$ is the sum of the individual energy components in Table A.1. Table A.1 lists the energies contained in each of the magnetic bodies and their corresponding field formulations.

The dipolar energy is a Zeeman energy whose magnitude and direction is determined by the magnetization of the neighboring magnetic body. For this reason, the field representation of the dipolar energy is modeled using a tensor representation [166, 167]:

$$H_{DIP2} = \mathbf{DIP}\hat{m}_2 = \begin{bmatrix} DIP_{xx} & DIP_{yx} & DIP_{zx} \\ DIP_{xy} & DIP_{yy} & DIP_{zy} \\ DIP_{xz} & DIP_{yz} & DIP_{zz} \end{bmatrix} \hat{m}_2 \tag{A.2}$$

whose individual components, $DIP_{\Xi\Delta}$, denote the strength of the $\Xi$ component of the dipolar field assuming $\hat{m}_1$ oriented along $\Delta$. In this way, the dipolar field is a mixture of time-variant longitudinal and perpendicular components [80]. The strength of the stray field generated by a thin film nanomagnet to some point in space can be directly calculated [163]. The tensor values are found by averaging the dipolar field over the target body which

Table A.1: Energy/field components describing the energy space of each magnetic body. The magnetization energy is the summation of all the different energy components acting upon the nanomagnet [149]. $K_{u1}$ and $K_{u2}$ are the uniaxial energy densities, $M_{s1}$ and $M_{s2}$ are the saturation magnetizations of M1 and M2, respectively. $N_{xx}$, $N_{yy}$, and $N_{zz}$ denote the demagnetization coefficients of the nanomagnets and are assigned values of 0, 0, and 1, respectively. The unit vector $\hat{r}_{free}$ is along the direction of the free-axis of the system, while $\hat{m}_1$ and $\hat{m}_2$ are the unit vectors pointing along the magnetization of M1 and M2, respectively. Thermal noise field is modeled as a 3D Wiener process given as $H_T(t)dt = \nu$ d$\mathbf{W}$(t), where $\nu = \sqrt{2\alpha k_B T/(\mu_0 \gamma M_s V)}$. Note that $\mu_0$ is the free-space permeability, $\gamma$ is the gyromagnetic ratio, $V$ is the volume of the nanomagnet. Details of the dipolar field modeling are presented in the text.

| Energy | Energy Symbol | Energy Representation | Field Symbol | Field Representation |
|---|---|---|---|---|
| Stoner-Wahlforth | $\epsilon_{K1}(\hat{m}_1)$ | $-K_{u1}\hat{r}_{free}\hat{m}_1^2$ | $H_{K1}$ | $\left(\frac{2K_{u1}}{\mu_0 M_{s1}}\hat{r}_{free}\right)\hat{m}_1$ |
| | $\epsilon_{K2}(\hat{m}_2)$ | $-K_{u2}\hat{r}_{free}\hat{m}_2^2$ | $H_{K2}$ | $\left(\frac{2K_{u2}}{\mu_0 M_{s2}}\hat{r}_{free}\right)\hat{m}_2$ |
| Demagnetization | $\epsilon_{D1}(\hat{m}_1)$ | $\frac{1}{2}\mu_0 M_{s1}^2\left(N_{xx}m_{x1}^2 + N_{yy}m_{y1}^2 + N_{zz}m_{z1}^2\right)$ | $H_{D1}$ | $M_{s1}\langle N_{xx}, N_{yy}, N_{zz}\rangle \hat{m}_1$ |
| | $\epsilon_{D2}(\hat{m}_2)$ | $\frac{1}{2}\mu_0 M_{s2}^2\left(N_{xx}m_{x2}^2 + N_{yy}m_{y2}^2 + N_{zz}m_{z2}^2\right)$ | $H_{D2}$ | $M_{s2}\langle N_{xx}, N_{yy}, N_{zz}\rangle \hat{m}_2$ |
| Dipolar | $\epsilon_{DIP}(\hat{m})$ | $\epsilon_{DIP1}(\hat{m}_1) = -\mu_0 M_s(\mathbf{DIP_2}\hat{m}_2)\hat{m}_1$ | $H_{DIP1}$ | $\mathbf{DIP_2}\hat{m}_2$ |
| | | $\epsilon_{DIP2}(\hat{m}_2) = -\mu_0 M_s(\mathbf{DIP_1}\hat{m}_1)\hat{m}_2$ | $H_{DIP2}$ | $\mathbf{DIP_1}\hat{m}_1$ |
| Thermal | | | $H_T$ | $\sqrt{\frac{2\alpha k_B T}{\mu_0^2 \gamma M_s V}}\left(\frac{\partial W_X}{\partial t}\hat{x} + \frac{\partial W_Y}{\partial t}\hat{y} + \frac{\partial W_Z}{\partial t}\hat{z}\right)$ |

Table A.2: Relevant constants to calculation of magnetization dynamics.

| Symbol | Definition | Nominal Value |
|---|---|---|
| $\gamma$ | Gyromagnetic ratio | $17.6 \times 10^{10} \frac{1}{\mathrm{sT}}$ |
| $\mu_0$ | Free-space permeability | $4\pi \times 10^{-7}$ |
| $q$ | Free electron charge | $1.6 \times 10^{-19}\mathrm{C}$ |
| $\hbar$ | Reduced Plank constant | $1.054 \times 10^{-34}\mathrm{J} * \mathrm{sec}$ |

Table A.3: Relevant material constants to calculation of magnetization dynamics.

| Symbol | Definition |
|---|---|
| $L, W, t$ | Geometry |
| $V$ | Volume |
| $\alpha$ | Gilbert damping coefficient |
| $M_s$ | Saturation Magnetization |
| $K_u$ | Uniaxial Anisotropy |
| $T$ | Temperature |

is similar to previous approaches of calculating stray field over mono-domain bodies [166, 167].

The thermal field ($\vec{H}_T$) is included to account for the variations in the nanomagnets' anisotropy due to thermal effects [92, 113]. This field is modeled as a Gaussian white noise where $W_k$ represents a standard Wiener process [93, 116].

The traversal of the magnetic moment through the energy gradient is described by the Landau-Lifshitz-Gilbert equation [41, 75, 89, 90, 44]

$$\frac{d\hat{m}}{dt} = -\gamma\mu_0\left(\hat{m}\times\vec{H}_{eff}\right) + \alpha\left(\hat{m}\times\frac{d\hat{m}}{dt}\right) + \frac{\gamma\hbar\hat{m}\times(\hat{m}\times\vec{I}_s)}{2qM_sV}. \tag{A.3}$$

whose physical constants are described in Table A.2 [1]. $\vec{I}_s$ is the spin current into the bottom nanomagnet [242].

The physical equations are numerically are evaluated using a second-order Heun scheme which has been previously verified against known micromagnetic solvers and analytical expressions [100, 199, 106, 87]. The reversal probabilities were evaluated using Monte-Carlo analysis on a collection of 1000 transient simulations.

[1] In non-identical multi-magnet systems, a "1" or "2" is included in the subscript of the parameter to indicate which magnetic body is being referenced.

# APPENDIX B

# CHANNEL MODEL IN ASL DEVICE

The amount of electric current, $I_{elec}$, pumped into the transmitter that reaches the receiver is quantified through spin injection and transport efficiency (SITE). Here, we use the mathematical models for SITE derived in [52, 53] to obtain the amount of $I_{elec}$ required to achieve a specific amount of spin current at the receiver. The models take into account size effects in ultra-scaled metallic channels. As shown in Figure B.1, for a channel length of 500 nm and in the absence of grain-boundary ($R = 0$) and sidewall scatterings ($p = 1$), the amount of electrical current to obtain 1.5 mA of spin current at the receiver nanomagnet is 5.3 mA and 4.5 mA for copper and aluminum channels, respectively. The required electrical current increases in the presence of realistic size effects. The inset plot of Figure B.1 shows the electrical current density through the nanomagnet as a function of channel length for different values of channel width. While increasing the width of the channel reduces the electrical current density through the nanomagnet and improves reliability of the ASL device, it also increases the overall device footprint and will limit the device scalability.

The delay associated with spin diffusion through the channel is given as

$$t_{diff} = \frac{L_{int}^2}{2D_s}, \tag{B.1}$$

where $D_s$ is the diffusion coefficient of electrons in the channel. Using $D_s$ = 126 $cm^2/Vs$ and 80 $cm^2/Vs$ for Cu and Al, respectively, the diffusion delay through a 500-nm long spin channel is only about 20 ps [52]. This delay is more than an order of magnitude lower than the nanomagnet switching delay and will not be considered in this work.

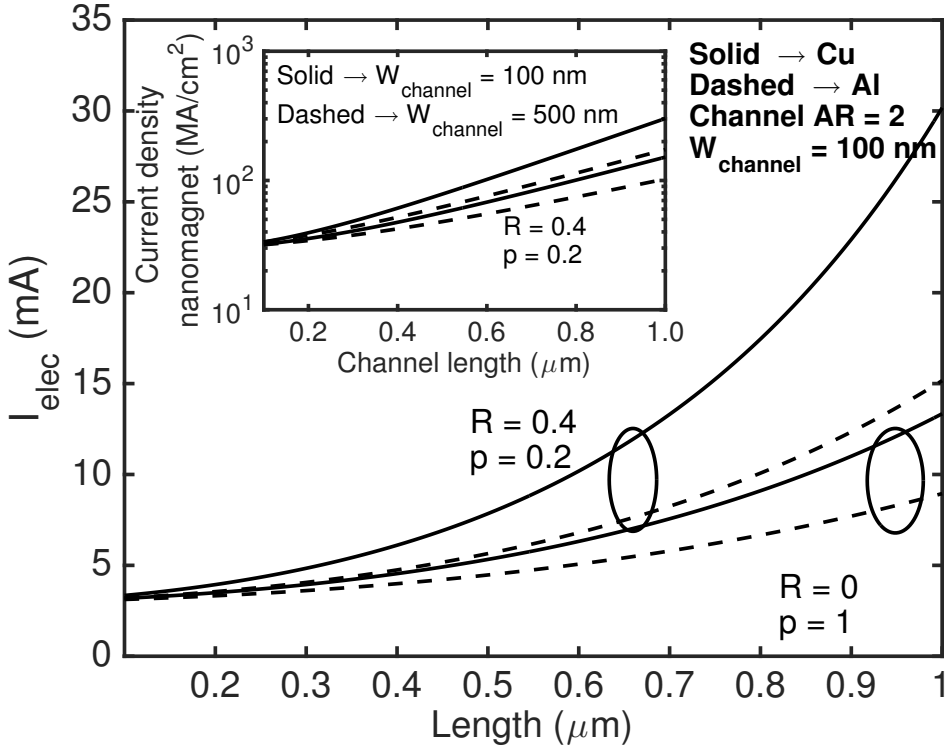


Figure B.1: Required electrical current in the ASL device to achieve 1.5 mA of spin current at the receiver as a function of the channel length. Different values of size-effect parameters are considered. The inset plot shows the corresponding electrical current density through the nanomagnet. The spin polarization of the nanomagnet is assumed to be 0.5. Other simulation parameters are noted in the figure.

# APPENDIX C

# STOCHASTIC INTEGRATION

The addition of stochastic effects in the LLG equation (referred to as the sLLG equation) necessities a formal review of the interpretation of stochastic processes. We begin this review with the classical definition of an integral:

$$\int_0^t f(t)dt = \lim_{n\to\infty} \sum_{j=1}^{n} f(\tau_j)(t_{j+1} - t_j) \tag{C.1}$$

where $\tau_j$ is on the interval $[t_j, t_{j+1}]$. This is identical to a Riemann-Stieltjes integral which takes the form:

$$\int_0^t f(t)dg(t) = \lim_{n\to\infty} \sum_{j=1}^{n} f(\tau_j)(g(t_{j+1}) - g(t_j)) \tag{C.2}$$

Consider a Weiner process ($W(t)$) which is a form of brownian motion. $W(t)$ is not a smooth process. In fact, $dW(t)$ is delta-autocorrelated with means that for any interval of time $[t_j, t_{j+1}]$, $dW(t)$ fluctuates an infinite number of times. Assuming $f(t)$ has a stochastic component, the choice of $\tau_j$ greatly alters the evaluation of the equation. If a $\tau_j = t_j$ is chosen, we obtain a Itô integral and must follow the rules of Itô calculus [243, 244, 245, 246]. If a $\tau_j = \frac{t_j + t_{j+1}}{2}$ is chosen, $f(t)$ becomes a Stratonovich integral and we must follow the rules of Stratonovich stochastic calculus [247, 248, 249].

The difference between these two classes of integrals is that Itô calculus does not follow the typical rules of integration due to the Itô isometry:

$$\mathbb{E}\left[\left(\int_0^T X_t dW_t\right)^2\right] = \mathbb{E}\left[\int_0^T X_t^2 dt\right] \tag{C.3}$$

This means that if $f(t) = g(t) = W(t)$, we get the following when evaluating (C.2):

$$(Itô) : \int_0^t W(t')dW(t') = \frac{1}{2}\left[W(t)^2 - W(0)^2 - t\right] \tag{C.4}$$

$$(Stratonovich) : \int_0^t W(t')dW(t') = \frac{1}{2}\left[W(t)^2 - W(0)^2\right] \tag{C.5}$$

To denote these two types of integrals we use the following notation to convey if a stochastic process should be evaluated in the Itô or Stratonovich sense:

$$(Itô) : \frac{dx}{dt} = A(x,t) + B(x,t)dW(t) \tag{C.6}$$

$$(Stratonovich) : \frac{dx}{dt} = A(x,t) + B(x,t) \circ dW(t) \tag{C.7}$$

From (C.4), it is evident that the difference between the two interpretations of the stochastic integral is a drift term occurring due to the differences between integration rules. Therefore it is possible to switch between interpretations of the using the following equality:

$$\frac{dx}{dt} = A(x,t) + B(x,t)dW(t) \equiv A(x,t) - \frac{1}{2}B(x,t)\partial_x B(x,t) + B(x,t) \circ dW(t). \tag{C.8}$$

The choice of stochastic calculus depends on application and the noise being considered. The white noise being considered in our research is an approximation to the continuously fluctuating thermal noise with little memory (no covariance between time-steps). According to the Wong-Zakai theorem, any noise which satisfies the zero correlation time limit becomes white noise and therefore, the Stratonovich interpretation of the differential equation is most appropriate and is preferred in the physics community [250]. However, Itô interpretations are still preferred in the mathematics community due to its conceptual simplicity arising form the fact that noise increments are statistically independent. The financial industry also prefers Itô models because evaluating the function at the beginning of the time interval better represents human behavior [251].

For this reason, Itô integrals are a natural starting point when defining a stochastic

integral before being converted to their Stratonovich to eb solved analytically. Consider the following stochastic differential equation:

$$dX_t = rX_t dt + \alpha X_t dW_t. \tag{C.9}$$

Using (C.8), (C.3) can be converted to it's Stratonovich form:

$$dX_t = rX_t dt - \frac{1}{2}\alpha^2 X_t dt + \alpha X_t \circ dW_t. \tag{C.10}$$

Because (C.11) is in its Stratonovich form, we can use normal rules of integration and obtain

$$X_t = X_0 exp\left[r - \frac{1}{2}\alpha^2 t + \alpha W_t\right]. \tag{C.11}$$

which is the analytic solution to (C.9).

However, many stochastic differential equations (including the sLLG) are too complex for analytic solutions making numerical integration schemes necessary. The selection of stochastic interpretation is crucial when choosing a numerical scheme to evaluate a stochastic differential equation [252, 100]. Most common numerical schemes can be categorized as resulting to one of these two interpretations of stochastic calculus and therefore, must be matched to the appropriate stochastic integral. For instance, consider Euler's method whose numerical procedure is defined as

$$y_{j+1} = y_j + hf(t_j, y_j), \tag{C.12}$$

where $t_{j+1} = t_j + h$. In Euler's method, the function is evaluated at the beginning of the time interval which means that the Euler method adheres to the Itô interpretation. In contrast, the midpoint method is defined as

$$y_{j+1} = y_j + hf(t_j + \frac{h}{2}), \frac{1}{2}(y_j + y_{j+1})), \tag{C.13}$$

and adheres to the Stratonovich interpretation because the function is evaluated at the middle of the time interval.

## REFERENCES


[1] S. Wolf, D. Awschalom, R. Buhrman, J. Daughton, S Von Molnar, M. Roukes, A. Y. Chtchelkanova, and D. Treger, "Spintronics: A spin-based electronics vision for the future," *Science*, vol. 294, no. 5546, pp. 1488–1495, 2001.

[2] D. E. Nikonov and I. A. Young, "Overview of beyond-cmos devices and a uniform methodology for their benchmarking," *Proceedings of the IEEE*, vol. 101, no. 12, pp. 2498–2533, 2013.

[3] I. D. Mayergoyz, G. Bertotti, and C. Serpico, *Nonlinear magnetization dynamics in nanosystems*. Elsevier, 2009.

[4] S. Datta, S. Salahuddin, and B. Behin-Aein, "Non-volatile spin switch for boolean and non-boolean logic," *Applied Physics Letters*, vol. 101, no. 25, p. 252 411, 2012.

[5] T. Miyazaki and N Tezuka, "Giant magnetic tunneling effect in Fe/$Al_2O_3$/Fe junction," *Journal of Magnetism and Magnetic Materials*, vol. 139, no. 3, pp. L231–L234, 1995.

[6] M. N. Baibich, J. M. Broto, A. Fert, F. N. Van Dau, F. Petroff, P Etienne, G Creuzet, A Friederich, and J Chazelas, "Giant magnetoresistance of (001) fe/(001) cr magnetic superlattices," *Physical review letters*, vol. 61, no. 21, p. 2472, 1988.

[7] G. Binasch, P. Grünberg, F Saurenbach, and W Zinn, "Enhanced magnetoresistance in layered magnetic structures with antiferromagnetic interlayer exchange," *Physical review B*, vol. 39, no. 7, p. 4828, 1989.

[8] S. Maekawa, *Concepts in spin electronics*. Oxford University Press on Demand, 2006, vol. 13.

[9] S. Ikeda, J. Hayakawa, Y. M. Lee, F. Matsukura, Y. Ohno, T. Hanyu, and H. Ohno, "Magnetic tunnel junctions for spintronic memories and beyond," *IEEE Transactions on Electron Devices*, vol. 54, no. 5, pp. 991–1002, 2007.

[10] J. C. Slonczewski, "Conductance and exchange coupling of two ferromagnets separated by a tunneling barrier," *Physical Review B*, vol. 39, no. 10, p. 6995, 1989.

[11] J. Slonczewski, "Currents and torques in metallic magnetic multilayers," *Journal of Magnetism and Magnetic Materials*, vol. 247, no. 3, pp. 324–338, 2002.

[12] J. S. Moodera and P. LeClair, "Spin electronics: A quantum leap," *Nature materials*, vol. 2, no. 11, pp. 707–708, 2003.

[13] J.-G. J. Zhu and C. Park, "Magnetic tunnel junctions," *Materials Today*, vol. 9, no. 11, pp. 36–45, 2006.

[14] J. P. Volkerts, *Magnetic thin films: Properties, performance and applications*. Nova Science Publ., 2011.

[15] J. Slonczewski, "Currents, torques, and polarization factors in magnetic tunnel junctions," *Physical Review B*, vol. 71, no. 2, p. 024 411, 2005.

[16] J. Katine and E. E. Fullerton, "Device implications of spin-transfer torques," *Journal of Magnetism and Magnetic Materials*, vol. 320, no. 7, pp. 1217–1226, 2008.

[17] E. Y. Tsymbal, O. N. Mryasov, and P. R. LeClair, "Spin-dependent tunnelling in magnetic tunnel junctions," *Journal of Physics: Condensed Matter*, vol. 15, no. 4, R109, 2003.

[18] M. Julliere, "Tunneling between ferromagnetic films," *Physics letters A*, vol. 54, no. 3, pp. 225–226, 1975.

[19] S. Tehrani, J. M. Slaughter, M. Deherrera, B. N. Engel, N. D. Rizzo, J. Salter, M. Durlam, R. W. Dave, J. Janesky, B. Butcher, *et al.*, "Magnetoresistive random access memory using magnetic tunnel junctions," *Proceedings of the IEEE*, vol. 91, no. 5, pp. 703–714, 2003.

[20] S Yuasa and D. Djayaprawira, "Giant tunnel magnetoresistance in magnetic tunnel junctions with a crystalline MgO (001) barrier," *Journal of Physics D: Applied Physics*, vol. 40, no. 21, R337, 2007.

[21] J. Atulasimha and S. Bandyopadhyay, *Nanomagnetic and spintronic devices for energy-efficient memory and computing*. John Wiley & Sons, 2016.

[22] S. Yamamoto and S. Sugahara, "Nonvolatile static random access memory using magnetic tunnel junctions with current-induced magnetization switching architecture," *Japanese Journal of Applied Physics*, vol. 48, no. 4R, p. 043 001, 2009.

[23] S Petit, C Baraduc, C Thirion, U Ebels, Y Liu, M. Li, P Wang, and B Dieny, "Spin-torque influence on the high-frequency magnetization fluctuations in magnetic tunnel junctions," *Physical review letters*, vol. 98, no. 7, p. 077 203, 2007.

[24] M. Durlam, P Naji, M DeHerrera, S Tehrani, G Kerszykowski, and K Kyler, "Non-volatile ram based on magnetic tunnel junction elements," in *Solid-State Circuits*

*Conference, 2000. Digest of Technical Papers. ISSCC. 2000 IEEE International*, IEEE, 2000, pp. 130–131.

[25] J. P. Uyemura, "Introduction to vlsi circuits and systems," 2002.

[26] R. Scheuerlein, W. Gallagher, S. Parkin, A. Lee, S. Ray, R. Robertazzi, and W. Reohr, "A 10 ns read and write non-volatile memory array using a magnetic tunnel junction and fet switch in each cell," in *Solid-State Circuits Conference, 2000. Digest of Technical Papers. ISSCC. 2000 IEEE International*, IEEE, 2000, pp. 128–129.

[27] D. Nikonov and I. Young, "Benchmarking of beyond-cmos exploratory devices for logic integrated circuits," *Exploratory Solid-State Computational Devices and Circuits, IEEE Journal on*, vol. 1, pp. 3–11, 2015.

[28] A. Imre, G Csaba, L Ji, A Orlov, G. Bernstein, and W Porod, "Majority logic gate for magnetic quantum-dot cellular automata," *Science*, vol. 311, no. 5758, pp. 205–208, 2006.

[29] D. B. Carlton, N. C. Emley, E. Tuchfeld, and J. Bokor, "Simulation studies of nanomagnet-based logic architecture," *Nano Letters*, vol. 8, no. 12, pp. 4173–4178, 2008.

[30] D. M. Bromberg, "Current-driven magnetic devices for non-volatile logic and memory," 2014.

[31] E. Varga, A. Orlov, M. T. Niemier, X. S. Hu, G. H. Bernstein, and W. Porod, "Experimental demonstration of fanout for nanomagnetic logic," *IEEE Transactions on Nanotechnology*, vol. 9, no. 6, pp. 668–670, 2010.

[32] E. Varga, M. T. Niemier, G. H. Bernstein, W. Porod, and X. S. Hu, "Non-volatile and reprogrammable mqca-based majority gates," in *Proceedings of the Device Research Conference (late results paper)*, 2009.

[33] S. Breitkreutz, J. Kiermaier, I. Eichwald, X. Ju, G. Csaba, D. Schmitt-Landsiedel, and M. Becherer, "Majority gate for nanomagnetic logic with perpendicular magnetic anisotropy," *IEEE Transactions on Magnetics*, vol. 48, no. 11, pp. 4336–4339, 2012.

[34] I Eichwald, A Bartel, J Kiermaier, S Breitkreutz, G Csaba, D Schmitt-Landsiedel, and M Becherer, "Nanomagnetic logic: Error-free, directed signal transmission by an inverter chain," *IEEE Transactions on Magnetics*, vol. 48, no. 11, pp. 4332–4335, 2012.

[35] D. Bhowmik, L. You, and S. Salahuddin, "Spin hall effect clocking of nanomagnetic logic without a magnetic field," *Nature nanotechnology*, vol. 9, no. 1, pp. 59–63, 2014.

[36] G. Csaba, W. Porod, and A. I. Csurgay, "A computing architecture composed of field-coupled single domain nanomagnets clocked by magnetic field," *International Journal of Circuit theory and applications*, vol. 31, no. 1, pp. 67–82, 2003.

[37] G. Csaba, P. Lugli, A. Csurgay, and W. Porod, "Simulation of power gain and dissipation in field-coupled nanomagnets," *Journal of Computational Electronics*, vol. 4, no. 1-2, pp. 105–110, 2005.

[38] M. S. Fashami, K. Munira, S. Bandyopadhyay, A. W. Ghosh, and J. Atulasimha, "Switching of dipole coupled multiferroic nanomagnets in the presence of thermal noise: Reliability of nanomagnetic logic," *Nanotechnology, IEEE Transactions on*, vol. 12, no. 6, pp. 1206–1212, 2013.

[39] D. C. Ralph and M. D. Stiles, "Spin transfer torques," *Journal of Magnetism and Magnetic Materials*, vol. 320, no. 7, pp. 1190–1216, 2008.

[40] D. Berkov and J Miltat, "Spin-torque driven magnetization dynamics: Micromagnetic modeling," *Journal of Magnetism and Magnetic Materials*, vol. 320, no. 7, pp. 1238–1259, 2008.

[41] J. C. Slonczewski, "Current-driven excitation of magnetic multilayers," *Journal of Magnetism and Magnetic Materials*, vol. 159, no. 1, pp. L1–L7, 1996.

[42] X. Waintal, E. B. Myers, P. W. Brouwer, and D. Ralph, "Role of spin-dependent interface scattering in generating current-induced torques in magnetic multilayers," *Physical Review B*, vol. 62, no. 18, p. 12 317, 2000.

[43] J. Xiao, A Zangwill, and M. D. Stiles, "Macrospin models of spin transfer dynamics," *Physical Review B*, vol. 72, no. 1, p. 014 446, 2005.

[44] M. Stiles and J Miltat, "Spin transfer torque and dynamics, spin dynamics in confined magnetic structures iii," *Topics Appl. Phys*, pp. 225–308, 2006.

[45] M. Stiles and A Zangwill, "Anatomy of spin-transfer torque," *Physical Review B*, vol. 66, no. 1, p. 014 407, 2002.

[46] E. O. Stejskal and J. E. Tanner, "Spin diffusion measurements: Spin echoes in the presence of a time-dependent field gradient," *The journal of chemical physics*, vol. 42, no. 1, pp. 288–292, 1965.

[47] F. J. Jedema, A. Filip, and B. Van Wees, "Electrical spin injection and accumulation at room temperature in an all-metal mesoscopic spin valve," *Nature*, vol. 410, no. 6826, pp. 345–348, 2001.

[48] Y Ji, A Hoffmann, J. Jiang, J. Pearson, and S. Bader, "Non-local spin injection in lateral spin valves," *Journal of Physics D: Applied Physics*, vol. 40, no. 5, p. 1280, 2007.

[49] T. Yang, T. Kimura, and Y. Otani, "Giant spin-accumulation signal and pure spin-current-induced reversible magnetization switching," *Nature Physics*, vol. 4, no. 11, pp. 851–854, 2008.

[50] Y. Huai, "Spin-transfer torque mram (stt-mram): Challenges and prospects," *AAPPS bulletin*, vol. 18, no. 6, pp. 33–40, 2008.

[51] B. Behin-Aein, D. Datta, S. Salahuddin, and S. Datta, "Proposal for an all-spin logic device with built-in memory," *Nature nanotechnology*, vol. 5, no. 4, pp. 266–270, 2010.

[52] S. Rakheja, S.-C. Chang, and A. Naeemi, "Impact of dimensional scaling and size effects on spin transport in copper and aluminum interconnects," *Electron Devices, IEEE Transactions on*, vol. 60, no. 11, pp. 3913–3919, 2013.

[53] S. Rakheja and A. Naeemi, "Roles of doping, temperature, and electric field on spin transport through semiconducting channels in spin valves," *Nanotechnology, IEEE Transactions on*, vol. 12, no. 5, pp. 796–805, 2013.

[54] N. Kani and A. Naeemi, "Pipeline design in spintronic circuits," in *Proceedings of the 2014 IEEE/ACM International Symposium on Nanoscale Architectures*, ACM, 2014, pp. 110–115.

[55] D. E. Nikonov, G. I. Bourianoff, and T. Ghani, "Proposal of a spin torque majority gate logic," *Electron Device Letters, IEEE*, vol. 32, no. 8, pp. 1128–1130, 2011.

[56] A. Hoffmann, "Spin hall effects in metals," *IEEE Transactions on Magnetics*, vol. 49, no. 10, pp. 5172–5193, 2013.

[57] E. H. Hall, "On a new action of the magnet on electric currents," *American Journal of Mathematics*, vol. 2, no. 3, pp. 287–292, 1879.

[58] E. Hall, "On the "rotational coefficient" in nickel and cobalt," *Proceedings of the Physical Society of London*, vol. 4, no. 1, p. 325, 1880.

[59] L Berger, "Side-jump mechanism for the hall effect of ferromagnets," *Physical Review B*, vol. 2, no. 11, p. 4559, 1970.

[60] T Jungwirth, Q. Niu, and A. MacDonald, "Anomalous hall effect in ferromagnetic semiconductors," *Physical review letters*, vol. 88, no. 20, p. 207 208, 2002.

[61] R. Karplus and J. Luttinger, "Hall effect in ferromagnetics," *Physical Review*, vol. 95, no. 5, p. 1154, 1954.

[62] I. M. Miron, G. Gaudin, S. Auffret, B. Rodmacq, A. Schuhl, S. Pizzini, J. Vogel, and P. Gambardella, "Current-driven spin torque induced by the rashba effect in a ferromagnetic metal layer," *Nature materials*, vol. 9, no. 3, pp. 230–234, 2010.

[63] Y. Kato, R. Myers, A. Gossard, and D. Awschalom, "Observation of the spin hall effect in semiconductors," *Science*, vol. 306, no. 5703, pp. 1910–1913, 2004.

[64] S. O. Valenzuela and M Tinkham, "Direct electronic measurement of the spin hall effect," *Nature*, vol. 442, no. 7099, pp. 176–179, 2006.

[65] S. O. Valenzuela and T. Kimura, *Experimental observation of the spin hall effect using electronic nonlocal detection.* Oxford University Press, 2012.

[66] L. Liu, C.-F. Pai, Y Li, H. Tseng, D. Ralph, and R. Buhrman, "Spin-torque switching with the giant spin hall effect of tantalum," *Science*, vol. 336, no. 6081, pp. 555–558, 2012.

[67] S. Manipatruni, D. E. Nikonov, and I. A. Young, "Energy-delay performance of giant spin hall effect switching for dense magnetic memory," *Applied Physics Express*, vol. 7, no. 10, p. 103 001, 2014.

[68] C.-F. Pai, L. Liu, Y Li, H. Tseng, D. Ralph, and R. Buhrman, "Spin transfer torque devices utilizing the giant spin hall effect of tungsten," *Applied Physics Letters*, vol. 101, no. 12, p. 122 404, 2012.

[69] C.-F. Pai, Y. Ou, L. H. Vilela-Leão, D. Ralph, and R. Buhrman, "Dependence of the efficiency of spin hall torque on the transparency of pt/ferromagnetic layer interfaces," *Physical Review B*, vol. 92, no. 6, p. 064 426, 2015.

[70] A Ganguly, K Kondou, H Sukegawa, S Mitani, S Kasai, Y Niimi, Y Otani, and A Barman, "Thickness dependence of spin torque ferromagnetic resonance in $Co_{75}Fe_{25}$/Pt bilayer films," *Applied Physics Letters*, vol. 104, no. 7, p. 072 405, 2014.

[71] J. Bass and W. P. Pratt Jr, "Spin-diffusion lengths in metals and alloys, and spin-flipping at metal/metal interfaces: An experimentalists critical review," *Journal of Physics: Condensed Matter*, vol. 19, no. 18, p. 183 201, 2007.

[72] W. Zhang, W. Han, X. Jiang, S.-H. Yang, and S. S. Parkin, "Role of transparency of platinum-ferromagnet interfaces in determining the intrinsic magnitude of the spin hall effect," *Nature Physics*, vol. 11, no. 6, pp. 496–502, 2015.

[73] H Liu, D Bedau, J. Sun, S Mangin, E. Fullerton, J. Katine, and A. Kent, "Dynamics of spin torque switching in all-perpendicular spin valve nanopillars," *Journal of Magnetism and Magnetic Materials*, vol. 358, pp. 233–258, 2014.

[74] J. Sun, "Spin-current interaction with a monodomain magnetic body: A model study," *Physical Review B*, vol. 62, no. 1, p. 570, 2000.

[75] L. D. Landau and E. Lifshitz, "On the theory of the dispersion of magnetic permeability in ferromagnetic bodies," *Phys. Z. Sowjetunion*, vol. 8, no. 153, pp. 101–114, 1935.

[76] C Tannous and J Gieraltowski, "The stoner–wohlfarth model of ferromagnetism," *European journal of physics*, vol. 29, no. 3, p. 475, 2008.

[77] D Spišák and J Hafner, "Theory of bilinear and biquadratic exchange interactions in iron: Bulk and surface," *Journal of magnetism and magnetic materials*, vol. 168, no. 3, pp. 257–268, 1997.

[78] D Spišák and J Hafner, "Surface and interface phase transitions in thin magnetic films with frustrated exchange interactions," *Physical Review B*, vol. 56, no. 5, p. 2646, 1997.

[79] J. Sun, M. Gaidis, G Hu, E. OSullivan, S. Brown, J. Nowak, P. Trouilloud, and D. Worledge, "High-bias backhopping in nanosecond time-domain spin-torque switches of mgo-based magnetic tunnel junctions," *Journal of Applied Physics*, vol. 105, no. 7, p. 07D109, 2009.

[80] G. Bertotti, *Hysteresis in magnetism: For physicists, materials scientists, and engineers*. Academic press, 1998.

[81] U. Gradmann, "Magnetic surface anisotropies," *Journal of magnetism and magnetic materials*, vol. 54, pp. 733–736, 1986.

[82] M. F. Toney, E. E. Marinero, M. F. Doerner, and P. M. Rice, "High anisotropy coptcrb magnetic recording media," *Journal of applied physics*, vol. 94, no. 6, pp. 4018–4023, 2003.

[83] S Ikeda, K Miura, H Yamamoto, K Mizunuma, H. Gan, M Endo, S. Kanai, J Hayakawa, F Matsukura, and H Ohno, "A perpendicular-anisotropy CoFeB–MgO magnetic tunnel junction," *Nature materials*, vol. 9, no. 9, pp. 721–724, 2010.

[84] L. Néel, R. Chastel, C Besset, J Horowitz, A Messiah, J Winter, G. Paquette, M. Bayet, M. Hoyaux, R. Bernas, *et al.*, "Magnetic surface anisotropy and superlattice formation by orientation. anisotropie magnétique superficielle et surstructures d'orientation p. 225," *Journal de Physique et le Radium*, vol. 15, no. 4, 1954.

[85] S Mangin, D Ravelosona, J. Katine, M. Carey, B. Terris, and E. E. Fullerton, "Current-induced magnetization reversal in nanopillars with perpendicular anisotropy," *Nature Materials*, vol. 5, no. 3, pp. 210–215, 2006.

[86] F. Den Broeder, W Hoving, and P. Bloemen, "Magnetic anisotropy of multilayers," *Journal of magnetism and magnetic materials*, vol. 93, pp. 562–570, 1991.

[87] H. Liu, "Spin transfer driven magnetization dynamics in spin valves and magnetic tunnel junctions," PhD thesis, New York University, 2013.

[88] M Beleggia, M De Graef, and Y. Millev, "The equivalent ellipsoid of a magnetized body," *Journal of Physics D: Applied Physics*, vol. 39, no. 5, p. 891, 2006.

[89] T. L. Gilbert, "A phenomenological theory of damping in ferromagnetic materials," *Magnetics, IEEE Transactions on*, vol. 40, no. 6, 2004.

[90] L Berger, "Emission of spin waves by a magnetic multilayer traversed by a current," *Physical Review B*, vol. 54, no. 13, p. 9353, 1996.

[91] J. M. Coey, *Magnetism and magnetic materials*. Cambridge University Press, 2010.

[92] W Brown Jr, "Thermal fluctuation of fine ferromagnetic particles," *Magnetics, IEEE Transactions on*, vol. 15, no. 5, pp. 1196–1208, 1979.

[93] C. W. Gardiner *et al.*, *Handbook of stochastic methods*. Springer Berlin, 1985, vol. 4.

[94] S.-C. Chang, S. Manipatruni, D. Nikonov, I. Young, and A. Naeemi, "Design and analysis of Si interconnects for all-spin logic," *Magnetics, IEEE Transactions on*, vol. 50, no. 9, pp. 1–13, 2014.

[95] H. Liu, D. Bedau, D. Backes, J. Katine, J. Langer, and A. Kent, "Ultrafast switching in magnetic tunnel junction based orthogonal spin transfer devices," *Applied Physics Letters*, vol. 97, no. 24, p. 242 510, 2010.

[96] W. Coffey, Y. P. Kalmykov, and J. Waldron, "The langevin equation: With applications to stochastic problems in physics," *Chemistry and Electrical Engineering. World Scientific*, 2004.

[97] I. Karatzas and S. Shreve, *Brownian motion and stochastic calculus*. Springer Science & Business Media, 2012, vol. 113.

[98] F. C. Klebaner, *Introduction to stochastic calculus with applications*. World Scientific Publishing Company, 2012.

[99] S. Bandyopadhyay and M. Cahay, *Introduction to spintronics*. CRC press, 2015.

[100] S. Ament, N. Rangarajan, and S. Rakheja, "A practical guide to solving the stochastic Landau-Lifshitz-Gilbert-Slonczewski equation for macrospin dynamics," *ArXiv preprint arXiv:1607.04596*, 2016.

[101] D. Pinna, "Spin-torque driven macrospin dynamics subject to thermal noise," PhD thesis, PhD thesis, New York University, 2015.

[102] S. C. Chapra and R. P. Canale, *Numerical methods for engineers*. McGraw-Hill New York, 1988, vol. 2.

[103] M d'Aquino, C Serpico, G Coppola, I. Mayergoyz, and G Bertotti, "Midpoint numerical technique for stochastic Landau-Lifshitz-Gilbert dynamics," *Journal of applied physics*, vol. 99, no. 8, 08B905, 2006.

[104] M. d'Aquino, C. Serpico, and G. Miano, "Geometrical integration of landau–lifshitz–gilbert equation based on the mid-point rule," *Journal of Computational Physics*, vol. 209, no. 2, pp. 730–753, 2005.

[105] A. Vansteenkiste and B. Van de Wiele, "Mumax: A new high-performance micromagnetic simulation tool," *Journal of Magnetism and Magnetic Materials*, vol. 323, no. 21, pp. 2585–2591, 2011.

[106] M. Donahue and D. Porter, "Oommf user's guide, version 1.0," *Interagency Report NISTIR 6376*, vol. National Institute of Standards and Technology, Gaithersburg, MD, 1999.

[107] M. Januszewski and M. Kostur, "Accelerating numerical solution of stochastic differential equations with cuda," *Computer Physics Communications*, vol. 181, no. 1, pp. 183–188, 2010.

[108] N Kani, A Naeemi, and S Rakheja, "Non-monotonic probability of thermal reversal in thin-film biaxial nanomagnets with small energy barriers," *AIP Advances*, vol. 7, no. 5, p. 056 006, 2017.

[109] D. Pinna, A. D. Kent, and D. L. Stein, "Thermally assisted spin-transfer torque dynamics in energy space," *Physical Review B*, vol. 88, no. 10, p. 104 405, 2013.

[110] D Pinna, A. Kent A., and D. Stein, "Thermally-assisted spin-transfer torque magnetization reversal of uniaxial nanomagnets in energy space," *Magnetics, IEEE Transactions on*, vol. 49, no. 7, pp. 3144–3146, 2013.

[111] N. Kani, S. Rakheja, and A. Naeemi, "A probability-density function approach to capture the stochastic dynamics of the nanomagnet and impact on circuit performance," *IEEE Transactions on Electron Devices*, vol. 63, no. 10, pp. 4119–4126, 2016.

[112] W. Scholz, T. Schrefl, and J. Fidler, "Micromagnetic simulation of thermally activated switching in fine particles," *Journal of Magnetism and Magnetic Materials*, vol. 233, no. 3, pp. 296–304, 2001.

[113] W. F. Brown Jr, "Thermal fluctuations of a single-domain particle," *Journal of Applied Physics*, vol. 34, no. 4, pp. 1319–1320, 1963.

[114] W Wernsdorfer, E. B. Orozco, K Hasselbach, A Benoit, B Barbara, N Demoncy, A Loiseau, H Pascard, and D Mailly, "Experimental evidence of the Néel-Brown model of magnetization reversal," *Physical Review Letters*, vol. 78, no. 9, p. 1791, 1997.

[115] L Nel, "Thorie du tranage magntique des ferromagntiques en grains fins avec applications aux terres cuites," *Ann. Gophys*, vol. 5, pp. 99–136, 1949.

[116] W. T. Coffey and Y. P. Kalmykov, "Thermal fluctuations of magnetic nanoparticles: Fifty years after brown," *Journal of Applied Physics*, vol. 112, no. 12, p. 121 301, 2012.

[117] Y. P. Kalmykov, "Evaluation of the smallest nonvanishing eigenvalue of the fokker-planck equation for the brownian motion in a potential. ii. the matrix continued fraction approach," *Physical Review E*, vol. 62, no. 1, p. 227, 2000.

[118] H.-J. Suh, C. Heo, C.-Y. You, W. Kim, T.-D. Lee, and K.-J. Lee, "Attempt frequency of magnetization in nanomagnets with thin-film geometry," *Physical Review B*, vol. 78, no. 6, p. 064 430, 2008.

[119] D. Pinna, D. L. Stein, and A. D. Kent, "Spin-torque oscillators with thermal noise: A constant energy orbit approach," *Physical Review B*, vol. 90, no. 17, p. 174 405, 2014.

[120] D Pinna, A. Kent, and D. Stein, "Spin-transfer torque magnetization reversal in uniaxial nanomagnets with thermal noise," *Journal of Applied Physics*, vol. 114, no. 3, p. 033 901, 2013.

[121] F. R. de Gusmão, E. M. Ortega, and G. M. Cordeiro, "The generalized inverse weibull distribution," *Statistical Papers*, vol. 52, no. 3, pp. 591–619, 2011.

[122] M. Gilli *et al.*, "An application of extreme value theory for measuring financial risk," *Computational Economics*, vol. 27, no. 2-3, pp. 207–228, 2006.

[123] D. G. Harlow, "Applications of the frechet distribution function," *International Journal of Materials and Product Technology*, vol. 17, no. 5-6, pp. 482–495, 2002.

[124] N. R. Mann, "Statistical estimation of parameters of the weibull and frechet distributions," in *Statistical Extremes and applications*, Springer, 1984, pp. 81–89.

[125] R. A. Johnson, "Probability and statistics for engineers," *Miller & Freunds,*, pp. 546–554, 2000.

[126] X. Yao, J. Harms, A. Lyle, F. Ebrahimi, Y. Zhang, and J.-P. Wang, "Magnetic tunnel junction-based spintronic logic units operated by spin transfer torque," *Nanotechnology, IEEE Transactions on*, vol. 11, no. 1, pp. 120–126, 2012.

[127] J. Rice, *Mathematical statistics and data analysis*. Nelson Education, 2006.

[128] V. Calayir, D. E. Nikonov, S. Manipatruni, and I. A. Young, "Static and clocked spintronic circuit design and simulation with performance analysis relative to cmos," *Circuits and Systems I: Regular Papers, IEEE Transactions on*, vol. 61, no. 2, pp. 393–406, 2014.

[129] J. C. Mallinson, "Damped gyromagnetic switching," *Magnetics, IEEE Transactions on*, vol. 36, no. 4, pp. 1976–1981, 2000.

[130] M. Dimian, "Nonlinear spin dynamics and ultra-fast precessional switching," PhD thesis, University of Maryland, Apr. 2005.

[131] R. Thornley, "Pulse response of recording media," *Magnetics, IEEE Transactions on*, vol. 11, no. 5, pp. 1197–1199, 1975.

[132] M. H. Kryder and F. B. Humphrey, "Micromagnetic characteristics of transverse diffuse domain boundaries in permalloy thin films," *Magnetics, IEEE Transactions on*, vol. 7, no. 3, pp. 725–728, 1971.

[133] N. Rizzo, T. J. Silva, and A. B. Kos, "Nanosecond magnetization reversal in high coercivity thin films," *Magnetics, IEEE Transactions on*, vol. 36, no. 1, pp. 159–165, 2000.

[134] C Serpico, I. Mayergoyz, and G Bertotti, "Analytical solutions of landau–lifshitz equation for precessional switching," *Journal of Applied Physics*, vol. 93, no. 10, pp. 6909–6911, 2003.

[135] K. Roy, S. Bandyopadhyay, and J. Atulasimha, "Hybrid spintronics and straintronics: A magnetic technology for ultra low energy computing and signal processing," *Applied Physics Letters*, vol. 99, no. 6, 2011.

[136] A. Khan, D. E. Nikonov, S. Manipatruni, T. Ghani, and I. A. Young, "Voltage induced magnetostrictive switching of nanomagnets: Strain assisted strain transfer torque random access memory," *Applied Physics Letters*, vol. 104, no. 26, p. 262 407, 2014.

[137] K. Roy, "Critical analysis and remedy of switching failures in straintronic logic using bennett clocking in the presence of thermal fluctuations," *Applied Physics Letters*, vol. 104, no. 1, p. 013 103, 2014.

[138] C. Serpico, M. d'Aquino, G. Bertotti, and I. D. Mayergoyz, "Analytical description of quasi-random magnetization relaxation to equilibrium," *Magnetics, IEEE Transactions on*, vol. 45, no. 11, pp. 5224–5227, 2009.

[139] G Bertotti, C Serpico, and I. Mayergoyz, "Probabilistic aspects of magnetization relaxation in single-domain nanomagnets," *Physical review letters*, vol. 110, no. 14, p. 147 205, 2013.

[140] G. Bertotti, I. D. Mayergoyz, M. d'Aquino, S. Perna, and C. Serpico, "Phase-flow interpretation of magnetization relaxation in nanomagnets," *Magnetics, IEEE Transactions on*, vol. 50, no. 11, pp. 1–4, 2014.

[141] J Atulasimha and S Bandyopadhyay, "Bennett clocking of nanomagnetic logic using multiferroic single-domain nanomagnets," *Applied Physics Letters*, vol. 97, no. 17, p. 173 105, 2010.

[142] A. Khitun and K. L. Wang, "Nano scale computational architectures with spin wave bus," *Superlattices and Microstructures*, vol. 38, no. 3, pp. 184–200, 2005.

[143] S. Dutta, S.-C. Chang, N. Kani, D. E. Nikonov, S. Manipatruni, I. A. Young, and A. Naeemi, "Non-volatile clocked spin wave interconnect for beyond-cmos nanomagnet pipelines," *Scientific reports*, vol. 5, 2015.

[144] R. Cowburn and M. Welland, "Room temperature magnetic quantum cellular automata," *Science*, vol. 287, no. 5457, pp. 1466–1468, 2000.

[145] V. Q. Diep and S. Datta, "The spin switch oscillator: A new approach based on gain and feedback," in *Device Research Conference (DRC), 2014 72nd Annual*, IEEE, 2014, pp. 293–294.

[146] G Zhang, W Hübner, E Beaurepaire, and J. Bigot, "Spin dynamics in confined magnetic structures i," *Topics in applied physics*, vol. 83, 2002.

[147] K. Ounadjela and B. Hillebrands, *Spin dynamics in confined magnetic structures ii*. Springer, 2003.

[148] L He, W. Doyle, and H Fujiwara, "High speed coherent switching below the stoner-wohlfarth limit," *Magnetics, IEEE Transactions on*, vol. 30, no. 6, pp. 4086–4088, 1994.

[149] S. Chikazumi and C. D. Graham, *Physics of ferromagnetism 2e*, 94. Oxford University Press, 2009.

[150] D. Xiao, M Tsoi, and Q. Niu, "Minimal field requirement in precessional magnetization switching," *Journal of applied physics*, vol. 99, no. 1, p. 013 903, 2006.

[151] A. Raychowdhury, D. Somasekhar, T. Karnik, and V. De, "Design space and scalability exploration of 1t-1stt mtj memory arrays in the presence of variability and disturbances," in *2009 IEEE International Electron Devices Meeting (IEDM)*, 2009.

[152] G Bertotti, I Mayergoyz, C Serpico, and M Dimian, "Comparison of analytical solutions of landau–lifshitz equation for damping and precessional switchings," *Journal of applied physics*, vol. 93, no. 10, pp. 6811–6813, 2003.

[153] H. Siegmann, E. Garwin, C. Prescott, J Heidmann, D Mauri, D Weller, R Allenspach, and W Weber, "Magnetism with picosecond field pulses," *Journal of magnetism and magnetic materials*, vol. 151, no. 1, pp. L8–L12, 1995.

[154] T. Gerrits, H. Van Den Berg, J Hohlfeld, L Bär, and T. Rasing, "Ultrafast precessional magnetization reversal by picosecond magnetic field pulse shaping," *Nature*, vol. 418, no. 6897, pp. 509–512, 2002.

[155] T Devolder and C Chappert, "Precessional switching of thin nanomagnets: Analytical study," *The European Physical Journal B-Condensed Matter and Complex Systems*, vol. 36, no. 1, pp. 57–64, 2003.

[156] G. Bertotti, I. D. Mayergoyz, and C. Serpico, "Critical fields and pulse durations for precessional switching of thin magnetic films," *Magnetics, IEEE Transactions on*, vol. 39, no. 5, pp. 2504–2506, 2003.

[157] A. Kent, B Özyilmaz, and E Del Barco, "Spin-transfer-induced precessional magnetization reversal," *Applied Physics Letters*, vol. 84, no. 19, pp. 3897–3899, 2004.

[158] C Serpico, A Quercia, G Bertotti, M d'Aquino, I Mayergoyz, S Perna, and P Ansalone, "Heteroclinic tangle phenomena in nanomagnets subject to time-harmonic excitations," *Journal of Applied Physics*, vol. 117, no. 17, 17B719, 2015.

[159] W. Scholz and S. Batra, "Micromagnetic modeling of ferromagnetic resonance assisted switching," *Journal of Applied Physics*, vol. 103, no. 7, 07F539, 2008.

[160] G Bertotti, I. Mayergoyz, C Serpico, M dAquino, and R Bonin, "Nonlinear-dynamical-system approach to microwave-assisted magnetization dynamics," *Journal of Applied Physics*, vol. 105, no. 7, 07B712, 2009.

[161] G. Bertotti, I. D. Mayergoyz, and C. Serpico, "Perturbation technique for llg dynamics in uniformly magnetized bodies subject to rf fields," *Magnetics, IEEE Transactions on*, vol. 38, no. 5, pp. 2403–2405, 2002.

[162] M. W. Hirsch, S. Smale, and R. L. Devaney, *Differential equations, dynamical systems, and an introduction to chaos*. Academic press, 2012.

[163] R. Engel-Herbert and T. Hesjedal, "Calculation of the magnetic stray field of a uniaxial magnetic domain," *Journal of Applied Physics*, vol. 97, no. 7, pp. –, 2005.

[164] M Beleggia, S Tandon, Y Zhu, and M De Graef, "On the magnetostatic interactions between nanoparticles of arbitrary shape," *Journal of magnetism and magnetic materials*, vol. 278, no. 1, pp. 270–284, 2004.

[165] O Dmytriiev, T Meitzler, E Bankowski, A Slavin, and V Tiberkevich, "Spin wave excitations of a magnetic pillar with dipolar coupling between the layers," *Journal of Physics: Condensed Matter*, vol. 22, no. 13, p. 136 001, 2010.

[166] A. J. Newell, W. Williams, and D. J. Dunlop, "A generalization of the demagnetizing tensor for nonuniform magnetization," *Journal of Geophysical Research: Solid Earth (1978–2012)*, vol. 98, no. B6, pp. 9551–9555, 1993.

[167] F. Battaglia and T. F. George, "Tensors: A guide for undergraduate students," *American Journal of Physics*, vol. 81, no. 7, pp. 498–511, 2013.

[168] H. Arnold and G. Elmen, "Permalloy, an alloy of remarkable magnetic properties," *Journal of the Franklin Institute*, vol. 195, no. 5, pp. 621–632, 1923.

[169] D. E. Nikonov, G. I. Bourianoff, G. Rowlands, and I. N. Krivorotov, "Strategies and tolerances of spin transfer torque switching," *Journal of Applied Physics*, vol. 107, no. 11, p. 113 910, 2010.

[170] H. Schumacher, C Chappert, R. Sousa, P. Freitas, and J Miltat, "Quasiballistic magnetization reversal," *Physical review letters*, vol. 90, no. 1, p. 017 204, 2003.

[171] E. D. Boerner and H. N. Bertram, "Dynamics of thermally activated reversal in nonuniformly magnetized single particles," *Magnetics, IEEE Transactions on*, vol. 33, no. 5, pp. 3052–3054, 1997.

[172] N. Kani, S. Dutta, and A. Naeemi, "Analysis of coupling strength in multi-domain magneto-systems," in *Device Research Conference (DRC), 2015 73rd Annual*, IEEE, 2015, pp. 111–112.

[173] N. Kani, S.-C. Chang, S. Dutta, and A. Naeemi, "A model study of an error-free magnetization reversal through dipolar coupling in a two-magnet system," *Magnetics, IEEE Transactions on*, 2015.

[174] N. Kani and A. Naeemi, "Analytic models for coupling reliability in identical two-magnet systems during slow reversals," *Journal of Applied Physics*, 2017, Accepted.

[175] J. R. Black, "Electromigrationa brief survey and some recent results," *IEEE Transactions on Electron Devices*, vol. 16, no. 4, pp. 338–347, 1969.

[176] S Krause, G Herzog, A Schlenhoff, A Sonntag, and R Wiesendanger, "Joule heating and spin-transfer torque investigated on the atomic scale using a spin-polarized scanning tunneling microscope," *Physical review letters*, vol. 107, no. 18, p. 186 601, 2011.

[177] T Min, J. Sun, R Beach, D Tang, and P Wang, "Back-hopping after spin torque transfer induced magnetization switching in magnetic tunneling junction cells," *Journal of Applied Physics*, vol. 105, no. 7, p. 07D126, 2009.

[178] A Thiaville, Y Nakatani, J Miltat, and N Vernier, "Domain wall motion by spin-polarized current: A micromagnetic study," *Journal of Applied Physics*, vol. 95, no. 11, pp. 7049–7051, 2004.

[179] H. Chang, "Coupled biaxial films," *Journal of Applied Physics*, vol. 35, no. 3, pp. 770–771, 1964.

[180] N. Kani, S. Rakheja, and A. Naeemi, "Analytic modeling of dipolar field requirements for robust coupling in a non-identical two-magnet system," *Journal of Applied Physics*, 2018, Submitted.

[181] T. Seki, Y. Hasegawa, S. Mitani, S. Takahashi, H. Imamura, S. Maekawa, J. Nitta, and K. Takanashi, "Giant spin hall effect in perpendicularly spin-polarized FePt/Au devices.," *Nature Materials*, vol. 7, no. 2, 2008.

[182] M Morota, Y Niimi, K Ohnishi, D. Wei, T Tanaka, H Kontani, T Kimura, and Y Otani, "Indication of intrinsic spin hall effect in 4d and 5d transition metals," *Physical Review B*, vol. 83, no. 17, p. 174 405, 2011.

[183] V. Vlaminck, J. E. Pearson, S. D. Bader, and A. Hoffmann, "Dependence of spin-pumping spin hall effect measurements on layer thicknesses and stacking order," *Physical Review B*, vol. 88, no. 6, p. 064 414, 2013.

[184] L. Liu, T. Moriyama, D. Ralph, and R. Buhrman, "Spin-torque ferromagnetic resonance induced by the spin hall effect," *Physical review letters*, vol. 106, no. 3, p. 036 601, 2011.

[185] M. Althammer, S. Meyer, H. Nakayama, M. Schreier, S. Altmannshofer, M. Weiler, H. Huebl, S. Geprägs, M. Opel, R. Gross, *et al.*, "Quantitative study of the spin hall magnetoresistance in ferromagnetic insulator/normal metal hybrids," *Physical Review B*, vol. 87, no. 22, p. 224 401, 2013.

[186] W. M. Haynes, *Crc handbook of chemistry and physics*. CRC press, 2014.

[187] S Ikeda, J Hayakawa, Y Ashizawa, Y. Lee, K Miura, H Hasegawa, M Tsunoda, F Matsukura, and H Ohno, "Tunnel magnetoresistance of 604% at 300k by suppression of ta diffusion in CoFeB/MgO/CoFeB pseudo-spin-valves annealed at high temperature," *Applied Physics Letters*, vol. 93, no. 8, p. 082 508, 2008.

[188] L. Tao, D. Liu, S. Liang, X. Han, and H. Guo, "Tunneling magnetoresistance of FePt/NaCl/FePt (001)," *EPL (Europhysics Letters)*, vol. 105, no. 5, p. 58 003, 2014.

[189] J. R. Childress, B. A. Gurney, and M. Schwickert, *Low resistance magnetic tunnel junction device with bilayer or multilayer tunnel barrier*, US Patent 6,347,049, Feb. 2002.

[190] K. Wang, J. Alzate, and P. K. Amiri, "Low-power non-volatile spintronic memory: Stt-ram and beyond," *Journal of Physics D: Applied Physics*, vol. 46, no. 7, p. 074 003, 2013.

[191] Y. Nagamine, H. Maehara, K. Tsunekawa, D. D. Djayaprawira, N. Watanabe, S. Yuasa, and K. Ando, "Ultralow resistance-area product of 0.4$\Omega$ ($\mu$m)$^2$ and high magnetoresistance above 50$\%$ in CoFeB/MgO/CoFeB magnetic tunnel junctions," *Applied physics letters*, vol. 89, no. 16, p. 162 507, 2006.

[192] A. B. Kahng, "The itrs design technology and system drivers roadmap: Process and status," in *Proceedings of the 50th Annual Design Automation Conference*, ACM, 2013, p. 34.

[193] K. Navi, M. H. Moaiyeri, R. F. Mirzaee, O. Hashemipour, and B. M. Nezhad, "Two new low-power full adders based on majority-not gates," *Microelectronics Journal*, vol. 40, no. 1, pp. 126–130, 2009.

[194] Z. Huo, Q. Zhang, S. Haruehanroengra, and W. Wang, "Logic optimization for majority gate-based nanoelectronic circuits," in *Circuits and Systems, 2006. ISCAS 2006. Proceedings. 2006 IEEE International Symposium on*, IEEE, 2006, 4–pp.

[195] A Roohi, M Kamrani, S Sayedsalehi, and K Navi, "A combinational logic optimization for majority gate-based nanoelectronic circuits based on ga," in *Semiconductor Device Research Symposium (ISDRS), 2011 International*, IEEE, 2011, pp. 1–2.

[196] S. Sayed, V. Q. Diep, K. Y. Camsari, and S. Datta, "Spin funneling for enhanced spin injection into ferromagnets," *Scientific reports*, vol. 6, 2016.

[197] S. Zhang, "Spin hall effect in the presence of spin diffusion," *Physical review letters*, vol. 85, no. 2, p. 393, 2000.

[198] S Mizukami, Y Ando, and T Miyazaki, "Effect of spin diffusion on gilbert damping for a very thin permalloy layer in cu/permalloy/cu/pt films," *Physical Review B*, vol. 66, no. 10, p. 104 413, 2002.

[199] P. Bonhomme, S. Manipatruni, R. M. Iraei, S. Rakheja, S.-C. Chang, D. E. Nikonov, I. A. Young, and A. Naeemi, "Circuit simulation of magnetization dynamics and spin transport," *IEEE Transactions on Electron Devices*, 2014.

[200] G. G. Lopez, *The impact of interconnect process variations and size effects for gigascale integration*. Georgia Institute of Technology, 2009.

[201] L. Su, Y. Zhang, J.-O. Klein, Y. Zhang, A. Bournel, A. Fert, and W. Zhao, "Current-limiting challenges for all-spin logic devices," *Scientific reports*, vol. 5, p. 14 905, 2015.

[202] S. Lim, H. Kim, S. Na, and S. Suh, "Application-related properties of giant magnetostrictive thin films," *Journal of magnetism and magnetic materials*, vol. 239, no. 1, pp. 546–550, 2002.

[203] A. Ludwig and E. Quandt, "Giant magnetostrictive thin films for applications in microelectromechanical systems," *Journal of Applied Physics*, vol. 87, no. 9, pp. 4691–4695, 2000.

[204] S. H. Lim, S. Han, H. Kim, Y. Choi, J.-W. Choi, and C. Ahn, "Prototype microactuators driven by magnetostrictive thin films," *IEEE transactions on magnetics*, vol. 34, no. 4, pp. 2042–2044, 1998.

[205] T Maruyama, Y Shiota, T Nozaki, K Ohta, N Toda, M Mizuguchi, A. Tulapurkar, T Shinjo, M Shiraishi, S Mizukami, *et al.*, "Large voltage-induced magnetic anisotropy change in a few atomic layers of iron," *Nature nanotechnology*, vol. 4, no. 3, pp. 158–161, 2009.

[206] J. Atulasimhaa and S. Bandyopadhyayb, "Hybrid spintronics/straintronics: A super energy-efficient computing paradigm based on interacting multiferroic nanomagnets," in *Spintronics in Nanoscale Devices*, Pan Stanford Publishing, 2013.

[207] N. Kani, J. T. Heron, and A. Naeemi, "Strain-mediated magnetization reversal through spin-transfer torque," *IEEE Transactions on Magnetics*, 2017.

[208] A. Tulapurkar, Y Suzuki, A Fukushima, H Kubota, H Maehara, K Tsunekawa, D. Djayaprawira, N Watanabe, and S Yuasa, "Spin-torque diode effect in magnetic tunnel junctions," *Nature*, vol. 438, no. 7066, pp. 339–342, 2005.

[209] S Zhang, P. Levy, and A Fert, "Mechanisms of spin-polarized current-driven magnetization switching," *Physical review letters*, vol. 88, no. 23, p. 236 601, 2002.

[210] D. Berkov and N. Gorn, "Magnetization precession due to a spin-polarized current in a thin nanoelement: Numerical simulation study," *Physical Review B*, vol. 72, no. 9, p. 094 401, 2005.

[211] C Serpico, R Bonin, G Bertotti, I. Mayergoyz, and M d'Aquino, "Thermal stability in uniaxial nanomagnets driven by spin-polarized currents," *IEEE Transactions on Magnetics*, vol. 42, no. 10, pp. 2679–2681, 2006.

[212] T. Wu, A. Bur, P. Zhao, K. P. Mohanchandra, K. Wong, K. L. Wang, C. S. Lynch, and G. P. Carman, "Giant electric-field-induced reversible and permanent magnetization reorientation on magnetoelectric Ni/(011)[Pb $(Mg_{1/3}Nb_{2/3})$ $O_3]_{(1-x)}$−$[PbTiO_3]_x$ heterostructure," *Applied Physics Letters*, vol. 98, no. 1, p. 012 504, 2011.

[213] A. Rushforth, E De Ranieri, J Zemen, J Wunderlich, K. Edmonds, C. King, E Ahmad, R. Campion, C. Foxon, B. Gallagher, *et al.*, "Voltage control of magnetocrystalline anisotropy in ferromagnetic-semiconductor-piezoelectric hybrid structures," *Physical Review B*, vol. 78, no. 8, p. 085 314, 2008.

[214] M Weiler, A Brandlmaier, S Geprägs, M Althammer, M Opel, C Bihler, H Huebl, M. Brandt, R Gross, and S. Goennenwein, "Voltage controlled inversion of magnetic anisotropy in a ferromagnetic thin film at room temperature," *New Journal of Physics*, vol. 11, no. 1, p. 013 021, 2009.

[215] H Boukari, C Cavaco, W Eyckmans, L. Lagae, and G. Borghs, "Voltage assisted magnetic switching in $Co_{50}Fe_{50}$ interdigitated electrodes on piezoelectric substrates," *Journal of Applied Physics*, vol. 101, no. 5, p. 054 903, 2007.

[216] J.-W. Lee, S.-C. Shin, and S.-K. Kim, "Spin engineering of CoPd alloy films via the inverse piezoelectric effect," *Applied physics letters*, vol. 82, no. 15, pp. 2458–2460, 2003.

[217] S. Goennenwein, M Althammer, C Bihler, A Brandlmaier, S Geprägs, M Opel, W Schoch, W Limmer, R Gross, and M. Brandt, "Piezo-voltage control of magnetization orientation in a ferromagnetic semiconductor," *Physica status solidi (RRL)-Rapid Research Letters*, vol. 2, no. 3, pp. 96–98, 2008.

[218] J.-M. Hu and C. Nan, "Electric-field-induced magnetic easy-axis reorientation in ferromagnetic/ferroelectric layered heterostructures," *Physical Review B*, vol. 80, no. 22, p. 224 416, 2009.

[219] Q. Wang, X. Li, C.-Y. Liang, A. Barra, J. Domann, C. Lynch, A. Sepulveda, and G. Carman, "Strain-mediated 180° switching in CoFeB and Terfenol-D nanodots with perpendicular magnetic anisotropy," *Applied Physics Letters*, vol. 110, no. 10, p. 102 903, 2017.

[220] D. Parkes, L. Shelford, P Wadley, V Holỳ, M Wang, A. Hindmarch, G van der Laan, R. Campion, K. Edmonds, S. Cavill, *et al.*, "Magnetostrictive thin films for microwave spintronics.," *Scientific reports*, vol. 3, pp. 2220–2220, 2012.

[221] E. W. Lee, "Magnetostriction and magnetomechanical effects," *Reports on progress in physics*, vol. 18, no. 1, p. 184, 1955.

[222] H. K. Lachowicz and H. Szymczak, "Magnetostriction of amorphous magnetic materials," *Journal of Magnetism and Magnetic Materials*, vol. 41, no. 1, pp. 327–334, 1984.

[223] T. Brintlinger, S.-H. Lim, K. H. Baloch, P. Alexander, Y. Qi, J. Barry, J. Melngailis, L. Salamanca-Riba, I Takeuchi, and J. Cumings, "In situ observation of reversible nanomagnetic switching induced by electric fields," *Nano letters*, vol. 10, no. 4, pp. 1219–1223, 2010.

[224] D. Hunter, W. Osborn, K. Wang, N. Kazantseva, J. Hattrick-Simpers, R. Suchoski, R. Takahashi, M. L. Young, A. Mehta, L. A. Bendersky, *et al.*, "Giant magnetostriction in annealed $Co_{1-x}Fe_x$ thin-films," *Nature communications*, vol. 2, p. 518, 2011.

[225] W. D. Armstrong, "Magnetization and magnetostriction processes in $Tb_{(0.27-0.30)}$ $Dy_{(0.73-0.70)}$ $Fe_{(1.9-2.0)}$," *Journal of Applied Physics*, vol. 81, no. 5, pp. 2321–2326, 1997.

[226] J. A. Heuver, A. Scaramucci, Y. Blickenstorfer, S. Matzen, N. A. Spaldin, C. Ederer, and B. Noheda, "Strain-induced magnetic anisotropy in epitaxial thin films of the spinel $CoCr_2O_4$," *Physical Review B*, vol. 92, no. 21, p. 214 429, 2015.

[227] D. Parkes, S. Cavill, A. Hindmarch, P Wadley, F McGee, C. Staddon, K. Edmonds, R. Campion, B. Gallagher, and A. Rushforth, "Non-volatile voltage control of magnetization and magnetic domain walls in magnetostrictive epitaxial thin films," *Applied Physics Letters*, vol. 101, no. 7, p. 072 402, 2012.

[228] J. Atulasimha, A. B. Flatau, and E. Summers, "Characterization and energy-based model of the magnetomechanical behavior of polycrystalline iron–gallium alloys," *Smart materials and structures*, vol. 16, no. 4, p. 1265, 2007.

[229] J. Lou, R. Insignares, Z. Cai, K. S. Ziemer, M. Liu, and N. X. Sun, "Soft magnetism, magnetostriction, and microwave properties of FeGaB thin films," *Applied Physics Letters*, vol. 91, no. 18, p. 182 504, 2007.

[230] M. Liu, S. Li, Z. Zhou, S. Beguhn, J. Lou, F. Xu, T. Jian Lu, and N. X. Sun, "Electrically induced enormous magnetic anisotropy in terfenol-d/lead zinc niobate-lead titanate multiferroic heterostructures," *Journal of Applied Physics*, vol. 112, no. 6, p. 063 917, 2012.

[231] R. Van Dover, M Hong, E. Gyorgy, J. Dillon Jr, and S. Albiston, "Intrinsic anisotropy of Tb-Fe films prepared by magnetron Co sputtering," *Journal of applied physics*, vol. 57, no. 8, pp. 3897–3899, 1985.

[232] S. Rafique, J. R. Cullen, M. Wuttig, and J. Cui, "Magnetic anisotropy of FeGa alloys," *Journal of Applied Physics*, vol. 95, no. 11, pp. 6939–6941, 2004.

[233] J. Atulasimha, A. B. Flatau, and J. R. Cullen, "Analysis of the effect of gallium content on the magnetomechanical behavior of single-crystal FeGa alloys using an energy-based model," *Smart Materials and Structures*, vol. 17, no. 2, p. 025 027, 2008.

[234] P. Grundy, D. Lord, and P. Williams, "Magnetostriction in TbDyFe thin films," *Journal of Applied Physics*, vol. 76, no. 10, pp. 7003–7005, 1994.

[235] J. Lou, D. Reed, M. Liu, C. Pettiford, and N. X. Sun, "Novel electrostatically tunable FeGaB/(Si)/PMN-PT multiferroic heterostructures for microwave application," in *Microwave Symposium Digest, 2009. MTT'09. IEEE MTT-S International*, IEEE, 2009, pp. 33–36.

[236] J Walowski, M. D. Kaufmann, B Lenk, C Hamann, J McCord, and M Münzenberg, "Intrinsic and non-local gilbert damping in polycrystalline nickel studied by ti: Sapphire laser fs spectroscopy," *Journal of Physics D: Applied Physics*, vol. 41, no. 16, p. 164 016, 2008.

[237] P. G. Gowtham, G. E. Rowlands, and R. A. Buhrman, "A critical analysis of the feasibility of pure strain-actuated giant magnetostrictive nanoscale memories," *Journal of Applied Physics*, vol. 118, no. 18, p. 183 903, 2015.

[238] K. Roy, S. Bandyopadhyay, and J. Atulasimha, "Switching dynamics of a magnetostrictive single-domain nanomagnet subjected to stress," *Physical Review B*, vol. 83, no. 22, p. 224 412, 2011.

[239] M d'Aquino, S Perna, C Serpico, G Bertotti, and I. Mayergoyz, "Analysis of reliable sub-ns spin-torque switching under transverse bias magnetic fields," *Journal of Applied Physics*, vol. 117, no. 17, 17B716, 2015.

[240] S Rakheja and N Kani, "Spin pumping driven auto-oscillator for phase-encoded logicdevice design and material requirements," *AIP Advances*, vol. 7, no. 5, p. 055 905, 2017.

[241] B. Lambson, D. Carlton, and J. Bokor, "Exploring the thermodynamic limits of computation in integrated systems: Magnetic memory, nanomagnetic logic, and the landauer limit," *Physical review letters*, vol. 107, no. 1, p. 010 604, 2011.

[242] A. Brataas, A. D. Kent, and H. Ohno, "Current-induced torques in magnetic materials," *Nature materials*, vol. 11, no. 5, pp. 372–381, 2012.

[243] L. Rogers and D. Williams, "Diffusions, markov processes and martingales, vol 2: Ito calculus," 1987.

[244] K. Itô, "Multiple wiener integral," *Journal of the Mathematical Society of Japan*, vol. 3, no. 1, pp. 157–169, 1951.

[245] K. Itô, *On stochastic differential equations*. American Mathematical Soc., 1951, vol. 4.

[246] K. Itô, "109. stochastic integral," *Proceedings of the Imperial Academy*, vol. 20, no. 8, pp. 519–524, 1944.

[247] R. Stratonovich, "A new representation for stochastic integrals and equations," *SIAM Journal on Control*, vol. 4, no. 2, pp. 362–371, 1966.

[248] R. L. Stratonovich, *Topics in the theory of random noise*. CRC Press, 1967, vol. 2.

[249] R. Stratonovich, "On a method of calculating quantum distribution functions," in *Soviet Physics Doklady*, vol. 2, 1957, p. 416.

[250] E. Wong and M. Zakai, "On the convergence of ordinary integrals to stochastic integrals," *The Annals of Mathematical Statistics*, vol. 36, no. 5, pp. 1560–1564, 1965.

[251] S. E. Shreve, *Stochastic calculus for finance ii: Continuous-time models*. Springer Science & Business Media, 2004, vol. 11.

[252] T. Sauer, "Numerical solution of stochastic differential equations in finance," in *Handbook of computational finance*, Springer, 2012, pp. 529–550.

# VITA

Nickvash Kani was born in New York in October of 1988. In May of 2010 he received a Bachelor of Science in Computer Engineering from Boston University. In August of 2010 he began his PhD studies at the Georgia Institute of Technology. During the course of his 7+ year tenure, his research interests changed from embedded system design and programming to modeling of physical systems using high-performance computing methods. Having studied the complete spectrum of computing systems has afforded him a unique perspective on the philosophy of computing. He eventually received Master of Science and Doctor of Philosophy in Electrical and Computer Engineering from the Georgia Institute of Technology in August of 2013 and December of 2017, respectively.